2019

Highly efficient single atom based materials in energy conversion

Weihong Lai
University of Wollongong

UNIVERSITY
OF WOLLONGONG
AUSTRALIA

Highly efficient single atom based materials in energy conversion

Weihong Lai

Supervisors: Dr. Shulei Chou & Prof. Jiazhao Wang

This thesis is presented as part of the requirement for the conferral of the degree:

DOCTOR of PHILOSOPHY

The University of Wollongong

Institute for Superconducting and Electronic Materials

Australian Institute of Innovative Materials

Faculty of Mechanical, Material and Mechatronics Engineering

8 June 2019

Abstract

Since the size of metal components plays a pivotal role in determining the reactivity and selectivity of the heterogeneous catalysts; enormous efforts are invested in downsizing the metal particles to atomic level for ultimate catalysis over last decade. Single atoms (SAs) become an interesting research field towards material synthesis and performance optimization for diverse catalytic reactions. Significantly, various single atoms show remarkable catalytic activity and selectivity toward a variety of electrocatalytic reactions, including hydrogen evolution reaction (HER), oxygen evolution reaction (OER), oxygen reduction reaction (ORR), CO oxidation reaction, CO_2 reduction reaction, water gas shift reaction, and hydrogenation with a high efficiency. It is noteworthy that the same foreign isolated substitutions can be tuned to show distinguishing catalytic activities via anchoring on different supports.

Thus, three different strategies have been developed to fabricate a series of sustainable catalysts. We prepared a quasi-Pt-allotrope nanostructure, which is composed of metallic Pt_3Co hollow core (H-PtCo) and a N-doped carbon shell, which is modified with single-atom Pt on it (Pt_1N-C). An ordered intermetallic PtBi clusters with the monatomic Pt layer (PtBi@Pt) is also constructed and uniformly dispersed over cross the graphene. In addition, single-atom sites (M_1), including platinum (Pt_1), ruthenium (Ru_1), iridium (Ir_1), iron (Fe_1), palladium (Pd_1), and nickel (Ni_1), on two distinct domains of the hybrid support, four-fold N/C atoms (M_1@NC) and center of Co octahedral (M_1@Co) have been synthesized in this thesis.

First of all, the Quasi-Pt-allotrope catalyst: Hollow PtCo@single-atom Pt_1 nanoarchitecture enables the inner and exterior spaces easily accessible, exposing

extra-high active surface area and active sites for the penetration of both aqueous and organic electrolytes. Moreover, the novel Pt_1N-C shells not only effectively protects the H-PtCo cores from agglomeration, but also increase the efficiency of the ORR in virtue of the isolated Pt atoms. These advanced features endow it with overwhelming ORR performance, so that it exhibits stable ORR without any fade over a prolonged 10000 cycle test at 0.9 V in $HClO_4$ solution. Density functional theory calculations reveal that the single atom Pt, forming part of the $PtNC_3$ structure, can provide a comparable highly active ORR efficiency to Pt (111). Furthermore, this material can offer efficient and stable ORR activities in various organic electrolytes, indicating its great potential for next-generation lithium-air batteries as well.

For the second work, the ordered PtBi intermetallic (PtBi@Pt) supported on graphene matrix, which is fabricated from single-atom Pt mixed with PtBi catalyst (PtBi/SA Pt) *via* a single-atom self-assembling (SAS) method. The PtBi@Pt with ultrafine size (~2 nm) delivers an extremely high mass activity of 9.01 mA μgPt^{-1}, which is 8-fold more active than commercial Pt/C; significantly, in-situ Fourier transform infrared spectroscopy indicates that ethanol is completely oxidized to CO_3^{2-} on the PtBi@Pt, accompanied by 12 electron transfer, as is further demonstrated by the density functional theory results, which significantly outperforms other reported catalysts for the EOR under alkaline conditions.

For the third work, we report a general π-electron assisting strategy to anchor diverse single-atom sites (M_1), including platinum (Pt_1), ruthenium (Ru_1), iridium (Ir_1), iron (Fe_1), palladium (Pd_1), and nickel (Ni_1), on a heterogeneous support. It is confirmed that the π-electrons of the precursor (pentagon imidazole) are vital for the formation of M_1 active sites on the support, which could significantly immobilize metal ions and prevent them from aggregation with each other during initial process. It is novel that

the M_1 can simultaneously anchor on two distinct domains of the hybrid support, four-fold N/C atoms (M_1@NC) and center of Co octahedral (M_1@Co), which are expected to serve as bi-functional electrocatalysts towards HER and OER, respectively. Amongst, a catalyst of Ir_1 exhibits the most excellent water splitting performance, showing a low applied potential of 1.603 V to achieve 10 mA cm^{-2} in 1.0 M KOH solution with cycling over 5 h. The density functional theory (DFT) calculations speculate that the Ir_1@Co (Ir) sites can accelerate the OER and Ir_1@ NC_3 sites are responsible for the enhanced HER, clarifying the unprecedented performance of this bi-functional catalyst toward full water splitting.

It can be concluded that the three strategies have been developed in this thesis, which successfully broaden the practical applications in proton exchange membrane fuel cells, EOR, water splitting, and lithium-air batteries, which are all considered as the most efficient and clean next-generation technology for the conversion of chemical energy. Our works are of significance to show the mechanism of preparation of single atoms, atomic structures of the prepared materials, theoretically and experimentally explain the mechanism of how the interaction between single atom and varieties of supports affects their surface chemistry, catalytic performance as well. Thus, I believe this thesis work can provide more insights on the design of efficient ORR, OER, EOR, and HER electrocatalysts.

Acknowledgements

It is a quite happy time to have my four years PhD in the Institute for Superconducting and Electronic Materials (ISEM) at the University of Wollongong in Australia. With the supports from my supervisors, families, and friends, I overcome challenges, tough time and soon, will finish my thesis.

Firstly, I am grateful to Prof. Shixue Dou, and Prof. Huakun Liu to build up such a great platform to have me learn, get training, financial supports and many chances to attend a high level seminar form all over the world.

Furthermore, I wish to express my deepest gratitude to my research supervisors, Professor Shulei Chou, for his academic supervision and guidance, constant support and encouragement, invaluable advice throughout my doctoral degree. He spent amounts of time to mentor me in the construction of self-confidence and future orientation as well. I would like to express my utmost appreciation to my co-supervisor, Prof. Jiazhao Wang, for her financial supports, professional suggestions and inculcation, including designing experiments and imparting new research techniques. I also wish to thank Dr. Yunxiao Wang, for her help in the design of experiments, manuscript revision, and polish of my writing. I would also like to thank Dr. Tania Silver for her critical reading of my manuscripts and thesis.

Furthermore, I wish to express my appreciation to Gilberto, and David, who spent his valuable time on TEM test for my samples and manuscript reversion. I would also like to thank for their kind assistance from staffs and technicians in ISEM, including Dr. Germanas Peleckis (XRD), Dr. Kosta Konstantinov (BET, TGA/DTA), Mr. Tony (SEM), Mr. Tony Romeo (SEM, EDS), Mrs. Crystal Login, Mrs. Narelle Badger, Mrs.

Joanne George (OH&S), Mr. Robert Morgan, Mr. Mathew Davis, Mrs. Candace Gabelish.

My deep gratitude goes to my co-workers, Prof. Zhenpeng Hu, Prof. Qiao Sun, Prof. Jin Xiao, Dr. Binwei Zhang, Dr. Weibo Hua, Dr. Zhe Hu, Dr. Mingzhe Chen, Dr. Lifu Zhang, Dr. Zichao Yan, Dr. Li Wang, Dr. Yaru liang, Dr. Zili Zhang, and Ms. Yanfei Xu, who have been very helpful, sharing their experiences and knowledge.

Moreover, many thanks to Dr. Min Liu, Dr. Yi Du, Dr. Xun Xu, Dr. Qi Li, Daniel Li, Michelle Li, Dr. Lili, Liu, Bo Zhang, Dr. Lei Zhang, Lijia Chen, Qiannan Liu, Wanlin Wang, Nv Wang, Yanfang Zhu, Weijie Li, Enhui Wang, Florian Gebert, Yajie Liu, Zhixin Tai, Fang Li, Yuyang Hou, Prof. Jie Xiao, Prof. Li Li, Yaojie Lei, Long Ren, Yundan Liu, Liang Wang, Yanxia Wang, Hanwen Liu, Yong Gang, Longfei Zhao, Yanxia Wang, Prof. Zongcheng Miao, Peng Li, Jiayi Chen, Yani Liu, Zhongfei Xu, Haifeng Feng, Ningyan Cheng, Nana Wang, Zhi Zheng, Prof. Nengfei Xu, Prof. Jincheng Zhuang, Haipeng Guo, Xiaobo Zheng, Dandan Cui, Dr. Boyang Ruan, and other students and staff at, for their kind help and valuable advice.

Finally, I would like to express my deep appreciation and love to my families, who are standing by me and encouraging me to move forward all the time.

Certification

I, Weihong Lai, declare that this thesis submitted in fulfilment of the requirements for the conferral of the Doctor of Philosophy Degree, from the University of Wollongong, is wholly my own work unless otherwise referenced or acknowledged. This document has not been submitted for qualifications at any other academic institution.

_____

Weihong Lai

25 Feb 2019

Lists of Nomenclature

Abbreviations

3D	Three-dimensional
ADF	Annular dark-field imaging
AFM	Atomic force microscopy
CV	Cyclic voltammetry
DFT	Density functional theory
DOS	Density of states
EOR	Ethanol Oxidation Reaction
EXAFS	Extended X-ray absorption fine structure
EDS	Energy dispersive X-ray spectroscopy
EELS	Electron energy loss spectroscopy
FIB-SEM	Focus ion beam scanning electron microscopy
FFT	Fast Fourier Transform
HER	Hydrogen evolution reaction
HRTEM	High resolution transmission electron microscopy
ICP-AES	Inductively coupled plasma optical emission spectrometry
LSV	Linear sweep voltammetry
ORR	Oxygen reduction reaction
OER	Oxygen evolution reaction
RRDE	Rotating ring-disk electrode
SIMS	Secondary ion mass spectrometer

SEM	Scanning electron microscopy
STEM	Scanning transmission electron microscpy
TEM	Transmission electron microscopy
TGA	Thermogravimetric analysis
UV	Ultraviolet
UV-Vis	UV-Visible
XRD	X-ray diffraction
XPS	X-ray photoelectron spectroscopy
SPV	Surface photovoltage spectra
TEM	Transmission electron microscopy
TGA	Gravimetric analysis
2D	Two-dimensional
UCNP	Upconversion nanoparticle
UV	Ultraviolet
VB	Valence band
XPS	X-ray photoelectron spectroscopy
XRD	X-ray diffraction

List of Symbols

θ	Angle of incidence with the lattice plane	°/degree
λ	Wavelength	nm
j	Current density	mA cm^{-2}
η	Over-potential	mV
θ	Angle of incidence with the lattice plane	°/degree
λ	Wavelength	nm
j	Current density	mA cm^{-2}

List of Organisations

ISEM	Institute for Superconducting and Electronic Materials
EMC	Electron Microscopy Centre
AIIM	Australian Institute of Innovative Materials
UOW	University of Wollongong
ARC	Australian Research Council
UOW	University of Wollongong

Table of Contents

List of Figures

depletion of electron density while green represents accumulation. The isosurface level is ± 0.005 e $Bohr^{-3}$. Reproduced with the permission. Copyright 2018, Nature Publishing Group.

Figure 2-2. (a) Carbon nanocones doped with Ni(II) and N atoms. Structures 1–6 tetradentate nanocone ligand. (b) Schematic diagrams of the molecular orbitals that contain major Ni dz2 and s atomic orbital contributions for the cones of structures 1-6. (c) Electron spin density (ESD) surface (e/bohr3) of capsules 7, nanocapsule 7 is obtained from a 180° cone frustrated by three pyrrole defects (top left); 8 is obtained by twelve B and six N atom doping of 7 (top middle); Nanocapsule 9 is obtained from 180° and 120° bottom cones, fused as in (12,0) CNT. The top portion differs from the carbon 180° cone in three N–C substitutions and a Ni atom at the tip instead of a C atom. The bottom portion differs from the carbon 120° cone in four N–C substitutions and a Ni atom at the tip instead of two C atoms (top right). Nanocapsule 10 contains Fe(II) and Ni(II). The octahedral coordination of Fe(II) is completed by the addition of a 2,2'-bipyridine (bpy) ligand (bottom left). Electrostatic potential (ESP) of capsule 10 in the interval e mapped on the 0.0004 e/bohr3 total electron density surface (bottom right). Reproduced with the permission. Copyright 2009, Elsevier.

Figure 2-3. (a) Optimized structures of different substrates: (I) Pristine graphene (g). (II) Pyridinic N1-doped graphene (g-P-N_1). Optimized structures of (III) Pt1 adsorption on pristine graphene (g-Pt_1), (IV) Pt_1 adsorption on g-P-N_1 (g-P-N_1-Pt_1). The grey, blue and cyan balls denote the carbon, nitrogen and platinum atoms, respectively. Reproduced with permission. Copyright 2015, Nature Publishing Group. (b) The EXAFS fitting curves of Pt-ISA/NG at R space. Copyright 2018, American Chemical Society. (c) Comparison between the experimental Ru K-edge XANES

spectrum of Ru-N/G-750 and the theoretical spectrum calculated from the depicted structures using the full-potential FDM. Copyright 2017, American Chemical Society. (d) The proposed Co/Ni/Fe-N_x architectures. Reproduced with permission. Copyright 2016, Wiley-VCH; Reproduced with permission. Copyright 2017, American Chemical Society; Reproduced with permission. Copyright 2017, Wiley-VCH. (e) The fitting results of the EXAFS spectra of Ru SAs/N−C. Copyright 2017, American Chemical Society.

Figure 2-4. (a) Structural model of an ideal, truncated octahedral nanoparticle with an optimal single-atomic-site coverage. Although strictly not representative of the nanoparticles synthesized here, this model provides a reasonable estimate of the upper concentration limit for such single-atom Pt sites. I-IV, Models that depict the proposed evolution of PtAu surface structures from single-atom Pt sites (II) to few-atom Pt clusters (III) to a complete Pt shell (IV) as a result of increased Pt content. (b) DFT-calculated binding of CO at PtAu surfaces. I–III, Illustration of CO adsorption modes on model (111) lattices of pure (I), few-atom (II) and single-atom (III) Pt surfaces that shows the apical (i), bridging (ii), hexagonal close-packed hollow (iii) and face-centred cubic hollow (iv) coordination sites. IV,Calculated adsorption energies for the indicated CO adsorption sites. Copyright 2018, Nature Publishing Group. (c) The measured valence photoemission spectra ($h\nu = 150$ eV) of an AgCu alloy that contained 0.3 at% Cu and metallic Ag reveal the narrow Cu 3d states at a binding energy of ~2.5 eV. (d) The difference spectrum of AgCu and Ag, plotted with a Cu reference spectrum, demonstrate that the Cu 3d states in AgCu are one-fifth the width they are in bulk Cu. (e) Spin density isosurfaces of substituted 1H-MoS_2 at Θ=1/48. The dashed line denotes the 4 × 4 supercell used in the calculations, green and gray

distributions correspond to positive and negative values, respectively. Copyright 2018, Nature Publishing Group.

Figure 2-5. (a) Structure and energetics of the anchored Pt^{2+} species on ceria nanoparticles determined by theory. The Pt^{2+} is strongly bound at the (100) nanofacets of the ceria nanoparticle. Color coding of atoms: red O, beige Ce^{4+}, brown Ce^{3+}, blue Pt, white H. Reproduced with permission. Copyright 2014, Wiley-VCH. (b) Illustration of Pt nanoparticle sintering, showing how ceria can trap the mobile Pt to suppress sintering. Cubes appear to be less effective than rods or polyhedral ceria. Reproduced with permission. Copyright 2016, American Association for the Advancement of Science (AAAS). (c) Illustration of the different ability on oxidizing CO via altering the relative chemical potentials between SAs and metal nanoparticles (NPs) on ceria. Reproduced with permission. Copyright 2017, American Chemical Society. (d) Schematic illustration of the 0.2Pt/m-Al_2O_3-H_2 synthesis process: Aluminum isopropoxide, P123, and H_2PtCl_6 mixture ethanolic solution self-assembled into a gel after ethanol evaporation at 60 °C. The gel was calcined at 400 °C and reduced in 5% H_2/N_2 at 400 °C, forming the single atom catalyst 0.2Pt/m-Al_2O_3-H_2. Reproduced with permission. Copyright 2017, Nature Publishing Group.

Figure 2-6. (a-c) HAADF-STEM images of Ir_1/FeO_x sample, Au_1/FeO_x sample and Pt_1/FeO_x sample. Reproduced with permission. Copyright 2014, American Chemical Society; Reproduced with permission. Copyright 2015, Springer; Reproduced with permission. Copyright 2011, Nature Publishing Group. (d) The k3-weighted Fourier transform spectra (the above) and the normalized XANES spectra (the bottom) of sample A (Pt_1/FeO_x), sample B (Pt_1/FeO_x with loading mass of 2.5 wt% Pt), PtO_2 and Pt foil. Reproduced with permission. Copyright 2011, Nature Publishing Group. (e)

The proposed reaction pathways for CO oxidation on the Pt_1/FeO_x catalyst (sample A). Reproduced with permission. Copyright 2011, Nature Publishing Group.

Figure 2-7. (a) Schematic illustration of the synthetic process for the $Ru_1/Co_1/Fe_n$ catalysts on nitrogen-doped graphene (NG). Reproduced with permission. Copyright 2015, Nature Publishing Group; Reproduced with permission. Copyright 2017, American Chemical Society; Reproduced with permission. Copyright 2018, Wiley-VCH; respectively. (b) STEM image of Co1-NG, inset is the SEM image of NG. (c) Left: Wavelet transforms for the Co_1-NG and Co-containing graphene (Co-G). Reproduced with permission. Copyright 2015, Nature Publishing Group. Right: Fourier transform magnitudes of the experimental Ru K-edge EXAFS spectra of the Ru-N/G samples prepared under different conditions along with reference materials. (d) The Fourier transforms are not corrected for phase shift. WT for the k^3-weighted EXAFS signal of sample Ru-N/G-750. The maximum at 5.5 $Å^{-1}$ is associated with the Ru-N(O) contributions. Reproduced with permission. Copyright 2017, American Chemical Society and (e) The STEM image of high density atomic Fe dispersion on NG. Reproduced with permission. Copyright 2018, Wiley-VCH (f) Theoretical calculations and proposed mechanism on the nitrogen-coordinated Fe catalytic site. a) Free energy diagram for electrochem-ical CO_2 reduction to CO on $Fe–N_4$ moieties embedded on graphene sheets. The proposed associative mechanism involves the following steps: (1) $CO_2 + * + H^+ + e- \rightarrow COOH*$, (2) $COOH* + H^+ + e- \rightarrow CO* + H_2O$, (3) $CO* \rightarrow CO + *$, where * denotes the active site on the catalyst surface. b) Top view of the optimized structures for Fe–N4 moieties embedded on graphene layer and potential nitrogen-substitution. Reproduced with permission. Copyright 2018, Wiley-VCH (g) The schematic illustration of the formation of Co_1/N-C (900).

Reproduced with permission. Copyright 2016, Wiley-VCH. (h) Schematic illustration of the synthetic process for the Fe-SAs/CN and Ni-SAs/CN. Reproduced with the permission. Copyright 2017, American Chemical Society; (i) Schematic illustration of the synthetic process for single-Co-atom catalysts via pyrolyzing Fe-Co prussian blue analogue. Reproduced with the permission. Copyright 2018, American Chemical Society.

Figure 2-8. STM images showing atomically dispersed Pd atoms in a Cu(111) surface and hydrogen atoms that have dissociated and spilled over onto the Cu surface. (a) Pd alloys into the Cu(111) surface preferentially above the step edges as evidenced by the rumpled appearance of the upper terrace (scale bar indicates 5 nm). (Inset) Atomic resolution of the Pd/Cu alloy on the upper terrace showing individual, isolated Pd atoms in the surface layer appearing as protrusions (scale bar, 2 nm). (b) Schematic showing H_2 dissociation and spillover at individual, isolated Pd atom sites in the Cu surface layer. (c) Islands of H atoms imaged after hydrogen uptake appear as depressed regions on the clean Cu(111) lower terrace (scale bar, 5 nm). (Inset) High-resolution image of individual hydrogen atoms on Cu(111) (scale bar, 2 nm). Images recorded at 5 K. Reproduced with permission. Copyright 2012, American Association for the Advancement of Science (AAAS). (d-g) STM images of Pd/Cu alloys with a range of stoichiometries: (d) 0.01 ml Pd, (e) 0.1 ml Pd, (f) 1 ml Pd and (g) 2 ml Pd. Scale bars: 5nm. Imaging conditions 0.05–0.15 V, 0.1–1.0 nA. Pd/Cu alloys were formed at 380 K. Reproduced with permission. Copyright 2013, Royal Society of Chemistry. (h) Proposed reaction pathway for semi-hydrogenation of acetylene over silica-supported Cu alloyed Pd SAC: dissociation of H_2 and Spill over of H atoms (left), adsorption and

the Advancement of Science (AAAS). (b) The proposed Co-N-C architecture toward the target reactions and stability of this catalyst paralysed at different temperatures and acid leaching. Reproduced with permission. Copyright 2015, American Chemical Society. (c) TEM image and HRTEM images of a Ag-HMO nanorod with a [001] growth direction with Auto-correlation function analysis showing a corresponding simulated image; (d) Single-atom Ag chains inside the tunnels of the HMO viewed from the [011] and [001] directions, respectively, and atom arrangement on the (001) facet of Ag-HMO; (e) in situ XRD patterns of the formation of Ag-HMO at different temperature. Reproduced with permission. Copyright 2012, Wiley-VCH.

Figure 2-12. (a) Schematic illustration of the reduction of CO_2 with H_2 on Pd/Al_2O_3 and Pd/MWCNT catalysts. Reproduced with permission. Copyright 2013, American Chemical Society. (b) Support effect for selectivity of ORR reaction with Pt_1 catalysts. Reproduced with permission. Copyright 2016, American Chemical Society. (c) CO Faradaic efficiency at various applied potentials with different catalysts for CO_2 reduction in aqueous solution. Reproduced with permission. Copyright 2018, Nature Publishing Group. (d) Faraday efficiency (%) to the products of CO_2 reduction under applied voltage of -0.5, -1, and -1.5 V vs Ag/AgCl (3M KCl) for Fe_1-N-C sample and corresponding turnover frequency (h^{-1} cm^{-2}). Reproduced with permission. Copyright 2018, Nature Publishing Group.

Figure 3-1. The general procedure of this thesis project.

Figure 4-1. (a) Schematic illustration of the fabrication process for H-PtCo@Pt_1N-C. (b) Scanning electron microscope (SEM) image of ZIF-67-50. (c) Annular bright field (ABF) image of Co@PtCo@Co@Pt_1N-C. (d) Annular bright field (ABF) image of H-PtCo@Pt_1N-C.

List of Tables

Chapter 1

1. Introduction

1.1. Research Background

Heterogeneous catalysts by supported metal nanostructures are extensively used in most industrial processes. In order to make use of alternative energy sources, including biomass, solar or nuclear for the future, it is imperative to explore favourable heterogeneous catalysts for fuel cells and photovoltaic cells. A heterogeneous catalyst is consisted of metal components finely dispersed/coordinated/stabilized on a variety of supports. Unless one very specialized synthesis techniques are utilized, it is extremely challenging to obtain metal nanoclusters dispersed onto high-surface-area supports with exactly the same atomic configuration and number of atoms. Since the size of metal components plays a pivotal role in determining the reactivity and selectivity of the heterogeneous catalysts; enormous efforts are invested in downsizing the metal particles to atomic level for ultimate catalysis over last decade. Single atoms (SAs) become an interesting research field towards material synthesis and performance optimization for diverse catalytic reactions.

Practically, when the metal loading ratio is high (>1 wt %) with conventional methods, for example wet chemical methods, the supported metal catalysts are usually presented as broad size distributions with irregular morphology, such as nanoparticles, nanoclusters, and isolated metal single atoms. As shown in Figure 1-1a, an atomic resolution electron micrograph clearly displays the Pt nanoclusters deposited onto the

surfaces of ZnO nanobelts via a modified deposition-precipitation method. It is evident that there are diverse architectures of Pt nanoclusters, including single atoms (A), faceted clusters (B), highly disordered or amorphous-like clusters (C), large Pt clusters (D), and strained clusters (E). Accordingly, a schematic illustration presents the various types of Pt clusters, trimers, dimers and monomers on the ZnO surfaces.[1] During catalytic processes, these nanoparticles and sub-nanoclusters possess multiple active sites and surface defects including steps, edges, and kinks, which can affect the selectivity and activity toward different reaction paths. In order to elucidate and understand reaction pathways, the most effective strategy is to take advantages of well-defined atomically distributed metal active centers.[2]

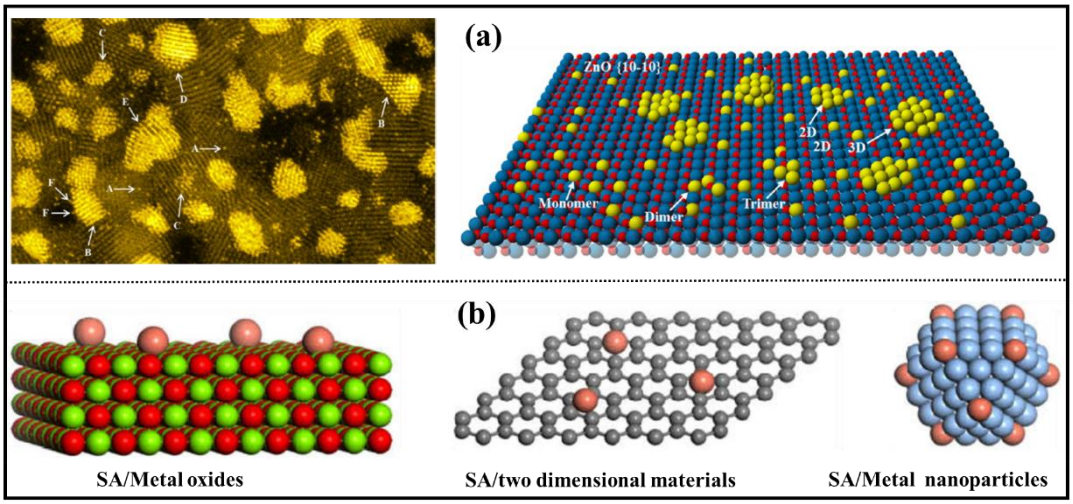

Figure 1-1. (a) Left panel: aberration-corrected HAADF-STEM image of a Pt/ZnO nanobelt model catalyst shows the presence of Pt single atoms (A), faceted Pt clusters (B), highly disordered Pt subnano clusters (C), reconstructed surface atoms of Pt nanoparticles (D), strained lattices of Pt (E), and highly unsaturated Pt atoms attached to the Pt nanocrystal (F); Right panel: schematic illustration of the various types of metal clusters, trimers, dimers, and monomers dispersed onto the ZnO $\{10\bar{1}0\}$ surface. During a catalytic reaction, all these various "sites" may contribute to the observed

catalytic performance. Reproduced with permission.[1] Copyright 2016, American Chemical Society. (b) Schematic diagrams illustrating SAs on different supports: metal oxides, two-dimensional materials, and the surface of metal NCs (from left to right). Reproduced with permission.[3] Copyright 2017, Elsevier.

The low-coordination environment of metal SAs could expose more catalytically active sites, achieving the ultimate specific activity of per metal atom. The terminology, single-atom catalysts (SACs), was firstly introduced in 2011 by Zhang and co-workers, in which they reported Pt SAs (Pt_1) dispersed on FeO_x with high CO oxidation activity.[2b] Unique single-atom metals are expected to deliver extraordinary catalytic performance. Meanwhile, the intrinsic quantum size effects with electrons confinement are responsible for discrete energy level distributions and distinctive HOMO-LUMO gaps. More importantly, it is found that the supports not only act as physical carriers to support the SAs but also catalytically or chemically impact on the catalytic properties of SACs. The understanding on atomic-local environments of SAs due to the nature of the interactions between metal SAs and supports is essential but still very ambiguous.

The concept of strong metal-support interaction (SMSI) was brought out in heterogeneous catalysis field in 1980s,[4] which can describe the huge changes in chemisorption properties of Pt and other group VIII metals when they were dispersed on titanium oxide. This SMSI that produced large electronic perturbations for small Pt particles in contact with $CeO_2(111)$ can significantly enhance the ability of the admetal to dissociate the O−H bonds in water.[5] Similarly, this SMSI effect is believe to alter the charge state of the metal by electron transfer between metal SAs and a support, which is responsible for the activated reactants and enhanced catalytic properties of

the SAs.[6] Later on, another hypothesis, electronic metal-support interactions (EMSI), was brought out by Rodriguez *et al.* based on the results of valence photoemission measurements and density functional theory (DFT) calculations.[5] Campbell concluded that the electronic perturbations can lead to upshift in the d-band centres (εd) relative to the Fermi level based on the EMSI, thus enhancing chemical and catalytic properties.[7] Even though the understanding has been deepened from SMSI to EMSI,[8] a thorough theory only could be built up via developing a perfect catalyst with structurally fixed and spatially uniform single-atom active sites, in which the intrinsic metal effects, including the electronic quantum size effect[9] and structure-sensitivity geometric effect[10], could be tactfully avoided. On the other hand, the metal-support interaction is associated with the charge transfer between metal species and supports, having a great influence on catalytic effects. Therefore, it is essential to understand the SMSI for tuning the activity, selectivity and stability of heterogeneous SACs.

SACs have been extensively investigated in the past several years. Comprehensive information has been provided in terms of the dispersion of the atoms, the interaction between single atoms and the support, and even in-situ dynamics of single atoms during catalysis. The developments on both atomic-resolution characterization techniques and theoretical modelling are unveiling the mysteries of SACs. Some reviews on SACs have been published in recent years,[11] but, to the best of our knowledge, none of them underlines the critical roles of supports. Over decades, research community has devoted to find effective approaches to strongly anchor the metal SAs to form highly stable and reactive catalytic active centres for desired

catalytic reactions, yet, it remains a grand challenge to guide the prediction and design of highly stable and reactive SACs under realistic conditions.

1.2. Objectives of the Research

The main science initiatives of preparing single atoms is to maximize the size effect of catalysts so that the use of single atoms would be more sustainable and extremely reduces the cost. However, the catalytic capability of single atom is dependent on the correlation with support surface, which leads to the polarization of these heteroatomic bonds and substantial charge transfer from the active metal to the support through strong metal-support interactions. These efforts have been focused on both developing and deploying technologies capable of distinctive catalytic properties, as well as those capable of improving the efficiency of the activity and selectivity with combining traditional metallic materials.

The objectives of the research are to (1) design single atoms on the carbon shell to improve the ORR activity of the ultra-refined metallic Pt_3Co particles; (2) prepare a superior catalyst with Pt-skin on order PtBi intermetallic (PtBi@Pt) supported on graphene matrix with Pt single atoms to increase the efficiency on EOR; (3) successfully stabilize the single metal atom species (M_1= Pt_1, Ir_1, Pd_1, Ru_1, Fe_1, and Ni_1) on distinc substrate, leading to the formation of a serials of M_1@Co/NC catalysts, which subsequently corresponds to two different active sites of M_1@Co and M_1@NC, simultaneously accelerating OER and HER.

1.3. Thesis Structure

In this thesis, we highlight the roles of supports and understand the atomic-local

environments of SACs based on SMSI effects in terms of theoretical calculation and practical experiments. This review will involve the significant progress on the synthesis of novel SACs on various supports. We will then primarily focus on understanding the selection of supports on synthesis of SACs that are stable against sintering. Moreover, the underlying mechanisms for various SACs fabrication and corresponding electrocatalytic applications are summarized, which lead to a better understanding of the role of single-atom species, supports selection, and SMSI effects for catalytic properties. Besides, in order to study the influence of the single atom and heterostructures in energy conversion applications, detailed structural characterizations, electro-catalytic properties are performed, and their relationship is also discussed in depth in this thesis. The scope of this thesis work is briefly outlined as follows:

Chapter 1 introduces the background of single-based materials and extends their importance and significance in catalyst area.

Chapter 2 presents a literature review on recent progress in preparation of single atoms on variety support, showing their strong and alternative interaction, which impact their intrinsic catalytic properties.

Chapter 3 presents the detailed preparation methods, as well as the structural and electrochemical characterization techniques for materials with heterostructures.

Chapter 4 investigates the performance of the hollow PtCo@single-atom Pt1 on nitrogen doped carbon towards superior oxygen reduction reaction.

Chapter 5 introduces the fabrication of Ordered Platinum-Bismuth Intermetallic Clusters with Pt-skin, which is utilized for High Efficient Electrochemical Ethanol

Oxidation Reaction.

Chapter 6 introduces a general method of π-electron assisting preparation of single-atom sites on a heterogeneous support as bi-functional electrocatalysts towards full water splitting.

Chapter 7 summarizes the works in this thesis and provides some outlooks for the design and synthesis of materials and for applications in catalytic areas.

Chapter 2

2. Literature Review

2.1. The synergistic electronic effects between atomic dopants and supports

The foreign atoms implanted on a specific supports could change the electronic structure through the lattice distortion. These changes are based on the field of condense matter physics and will result in the materials features in a vast array of practical applications. However, the electronic structures are affected over the type and quantity of dopants. Recently, tremendous types of metal atoms have been employed as dopants in atomic level and investigated through attaching with various host materials, including metal compounds, carbon, modified carbon, and nano-sized metal particles over the years. The different local structure of these substrates provides alternative coordination environment and electronic correlation with atomic dopants. These effects play an essential role in a wide range of applications and must be investigated in advance. We listed the change of electronic structure with showing how the different metal atoms change the physical properties of the host materials.

2.1.1 The electronic structure of atomic dopants on metal oxides

The metal oxides were considered a very important class, which provides a controlled method for studying fundamental details concerning metal/oxide interfaces and also

creates a vast array of technologically significant applications. With the development of advances in the nanotechnical engineering of metal oxides, the modification on metal oxides were widely investigated from particle to single atom. The atomic dopants shown the unique quantum size effects, allowing modification and control of the electronic structure, and consequently the surface chemistry, chemical reactivity of the supports through incorporation of judiciously selected impurity atoms in otherwise inert substrates. Over the past decades, plenty of works theoretically and experimentally confirmed that the atomic-level metal doped metal oxides significantly affected their electronic structures, such as the absorption edges, fermi level, and band gap, which indeed further change their functionality in energy conversion system[12-15]. For example, the dopants change the band bending associated with the Fermi level can be very different even on the same face of same materials, because the position of Fermi level highly depended on the doped impurities and defects at very low concentrations[16]. If we use the TiO_2 as a prototype, the impurity doping or ion implantation on TiO_2 can narrow its wide band gap in order to create fascinating photocatalysts which is not only operated under ultraviolet (UV) light but also natural light. It has been found that the metal, such as 3d transition metal (V, Cr, Mn, Co, Ni, Fe), doped TiO_2 can tune the localized structure and energy level. For instance, the dopants, including V, Cr, Mn, or Fe had the localized level of the t_{2g} state lying in the band gap, the Co was even situated at the top of the valance band (VB). However, the Ni dopant are rather delocalized, thus significantly contributing to the formation of the Valance band with the O p and Ti 3D electrons[16]. Similarly, the 3d metal doped ZnO can alter the magnetic states form the spin-glass state to the ferromagnetic state, and also stabilize the ferromagnetic state due to the double-exchange mechanism[17]. Thus,

we believed that it is significant to have the reasonable localized structure and design new functional material through coordinating metal dopants with suitable metal oxides in atomic level. Quantum mechanical calculations also support the model proposed above, wherein the individual transition metal adatoms, such as Cu, Co, and Ni, are to be highly cationic on oxide surfaces. The isolated Cu on a cluster model of ZnO $(000\bar{1})$-O show the Cu is with charge and electronic character as same as the bulk CuO, forming oxidation state of Cu^{2+} ions[12].

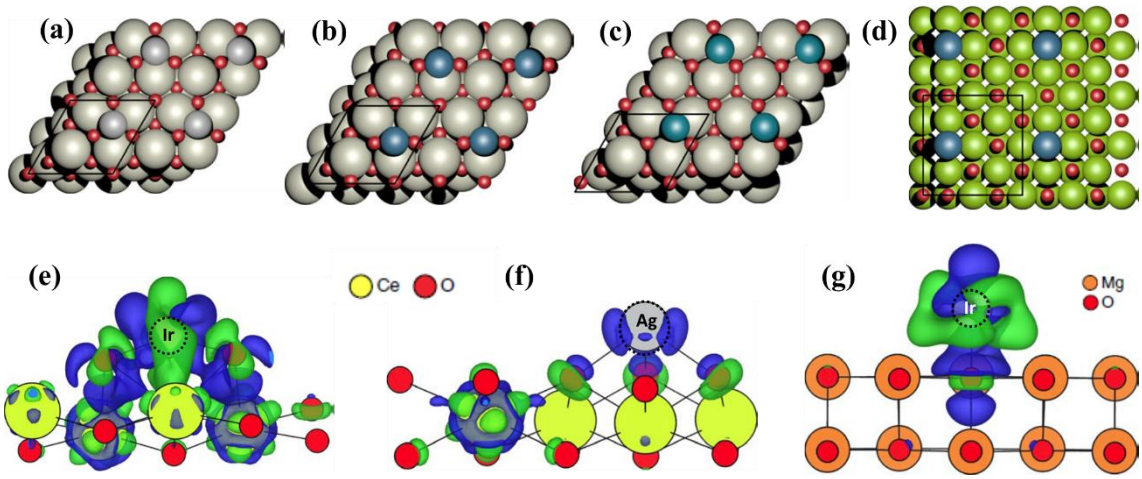

Figure 2-1. Adsorption geometries of metals on CeO_2(111) and MgO(100). (a–c) Top view of adsorbed late transition metals on the CeO_2(111) surface at the threefold hollow site (Ag) (a), twofold oxygen bridge site (Ir) (b) and oxygen side-bridge site (Pd) (c). (d) Adsorbed metals on MgO(100) all prefer the anionic oxygen site. The black rectangle represents the unit cell used in the study. Metal–support interactions on CeO_2(111) and MgO(100) supports. a–c, Isostructural charge density difference plots of Ir/CeO_2(111) (e), Ag/CeO_2(111) (f) and Ir/MgO(100) (g). Blue denotes depletion of electron density while green represents accumulation. The isosurface level is ± 0.005 e $Bohr^{-3}$. Reproduced with the permission.[18] Copyright 2018, Nature Publishing Group.

As discussed above, detailed discussion of atomic dopants on metal oxide is of high significance and recently, Senftle's group did a systematic study on the interaction between single atoms and oxide supports via DFT.[18] They concluded that the adsorption sites of single-atom transition metals on metal oxides supports includes threefold hollow sits, twofold oxygen bridge sites, oxygen side-bridge sites, and anionic oxygen sites. For example, based on energetically favourable configurations, Ag is favourably adsorbed at a threefold hollow site, Ir is bonded at a twofold oxygen bridge site, while Pd is located at an oxygen side-bridge site on the CeO_2(111) substrate (Figure 2-1a-c); In contrast, all metal single atoms are adsorbed above the anionic oxygen on the MgO(100) surface (Figure 2-1d). To better understand the electronic mechanism of SMSIs, they simulated the electronic structures of two metal atoms with two oxide support: low oxygen affinity Ag and high oxygen affinity Ir and reducible CeO_2(111) and irreducible MgO (100). As illustrated in Figure 2-1e, significant charge transfer takes place between Ir and the surface, which results in the charge redistribution from Ir adatom towards neighbouring oxygen and cerium atoms, thereby the formation of an Ir^{2+} states. Figure 2-1f demonstrates that the charge transfer between Ag and CeO_2(111) are less, only forming an Ag^+ state by reducing one Ce atom. By comparing the charge density difference plots of Ir_1/CeO_2(111) and Ag_1/CeO_2(111), green band linking Ir and Ce atoms is observed, which indicated a charge accumulation and revealed the presence of metal-metal binding. For the irreducible MgO (100), it is unable to readily accept electron density from a metal adatom but instead reduces the metal adatoms. The metal-support interactions are localized onto one surface oxygen via transferring electron density from the support to

the adsorbed Ir (Figure 2-1g). Therefore, the metal-oxide supports effect can be determined by factors as fellows. (1) Oxide formation enthalpy of metals: metals with high oxygen affinity, such as vanadium, would bind to any oxide supports stronger than those with low oxygen affinity, such as silver. (2) The adsorption strength of supports: typically, the reducible surface is able to accept donated electrons upon single-atom adsorption. The irreducible oxide supports do not interact strongly with metals. (3) Metal-metal interactions: besides the presence of metal-oxygen-metal bonds, the metal-metal interactions between the adatom metal and the support metal should be considered, which also play a role in determining the overall metal-support effects. These properties can be used to empirically screen interaction strengths between metal-support pairs, thus aiding the design and synthesis of single-atom catalysts on oxide supports.

2.1.2 The electronic structures of single atoms on carbonaceous supports

Carbonaceous nanostructures were intensively used as supports to coordinate with boron, nitrogen and metal atoms since their rigid skeletons possess planar sp^2 molecular orbitals sandwiched between overlapping unsaturated delocalized electrons[19]. Also, the modified carbonaceous materials, which were functionalized by physisorption, impurity dopants and covalent bonding, have been widely used in molecular sensing, controlling, drug delivering, catalysts, and batteries[20-23]. Especially, developing stable metal-doped carbon nanostructures are highly attractive in catalytic applications.

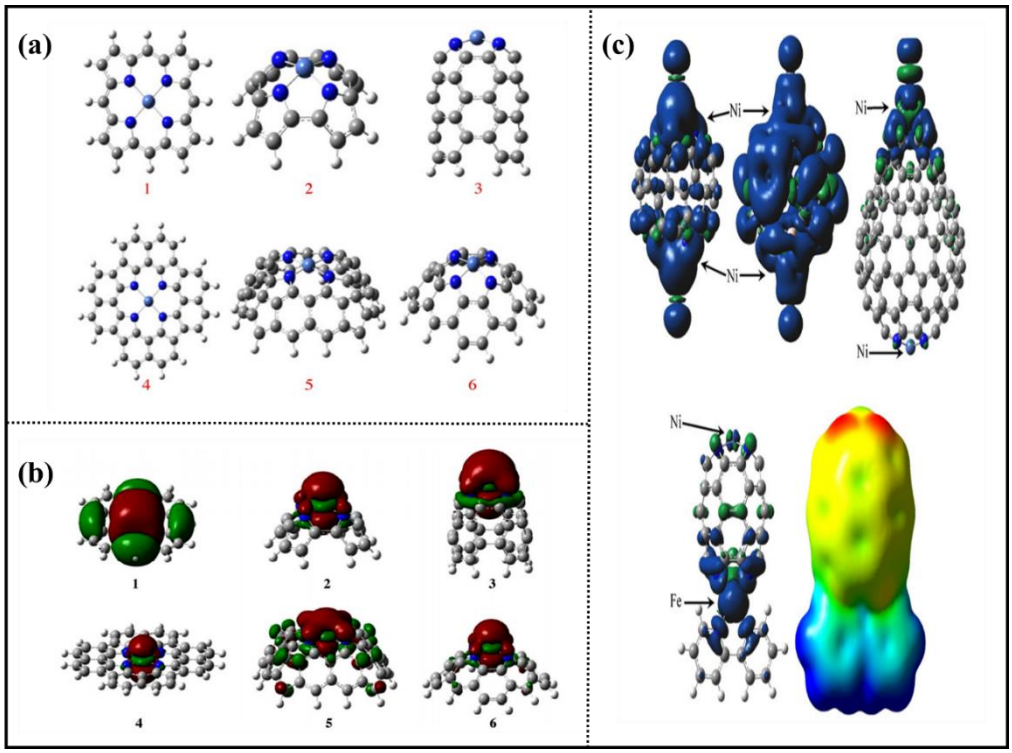

Figure 2-2. (a) Carbon nanocones doped with Ni(II) and N atoms. Structures 1–6 tetradentate nanocone ligand. (b) Schematic diagrams of the molecular orbitals that contain major Ni dz2 and s atomic orbital contributions for the cones of structures 1-6. (c) Electron spin density (ESD) surface (e/bohr3) of capsules 7, nanocapsule 7 is obtained from a 180° cone frustrated by three pyrrole defects (top left); 8 is obtained by twelve B and six N atom doping of 7 (top middle); Nanocapsule 9 is obtained from 180° and 120° bottom cones, fused as in (12,0) CNT. The top portion differs from the carbon 180° cone in three N–C substitutions and a Ni atom at the tip instead of a C atom. The bottom portion differs from the carbon 120° cone in four N–C substitutions and a Ni atom at the tip instead of two C atoms (top right). Nanocapsule 10 contains Fe(II) and Ni(II). The octahedral coordination of Fe(II) is completed by the addition of a 2,2'-bipyridine (bpy) ligand (bottom left). Electrostatic potential (ESP) of capsule 10 in the interval e mapped on the 0.0004 e/bohr3 total electron density surface (bottom right). Reproduced with the permission.[24] Copyright 2009, Elsevier.

At the early stage, researchers were looking into the catalytic activity of metal-ligands complex, such as Co-phtalocyanines[25]. With the further development, these complexes were sintered as metal-nitrogen-carbon catalysts. In particularly, when the metal atoms formed isolated metallic center, these metal atoms were called single atom. Interestingly, the host carbonaceous materials were strongly affected by the metal dopants in ground states, axial coordination, stability, electric field, spin and charge density. For instance, the different binding sites caused by metal dopants have different geometrical and electronic environment, because the distortion of metal atoms breaks the plane of symmetry and makes themselves coordinationally unsaturated, binding with different types of ligands. As shown in Figure 2-2a, the charges slightly decrease from the flat 1 and 4 to the buckled 3 and 6, but the buckling of the structure results in an asymmetric distribution of the Ni *4s* and *3d* orbital lobes, meaning that the ligands approached different electronic environment from the top and from the bottom (Figure 2-2b). Although the two ligand binding sites of cones 5 possess different geometries, they have similar electronic structure due to its unique bowl –shaped ligand. These results shows that even same metal atom doped on the same materials, once they have different geometries, the electronic structures and the bonding environment would hugely affected. In the real applications, nitrogen doped carbon was always used to anchor single atoms, the co-doped nitrogen and metal atom (capsule 8) would spread the spin density over large part of the capsule of the undoped one (capsule 7) and theoretically, the induce of two different metal coordination (capsule 9) can further increase the spin polarization (Figure 2-2c). The largest metal atom charge is obtained for the Fe atom of capsule 10 due to its highly charge polarized[24].

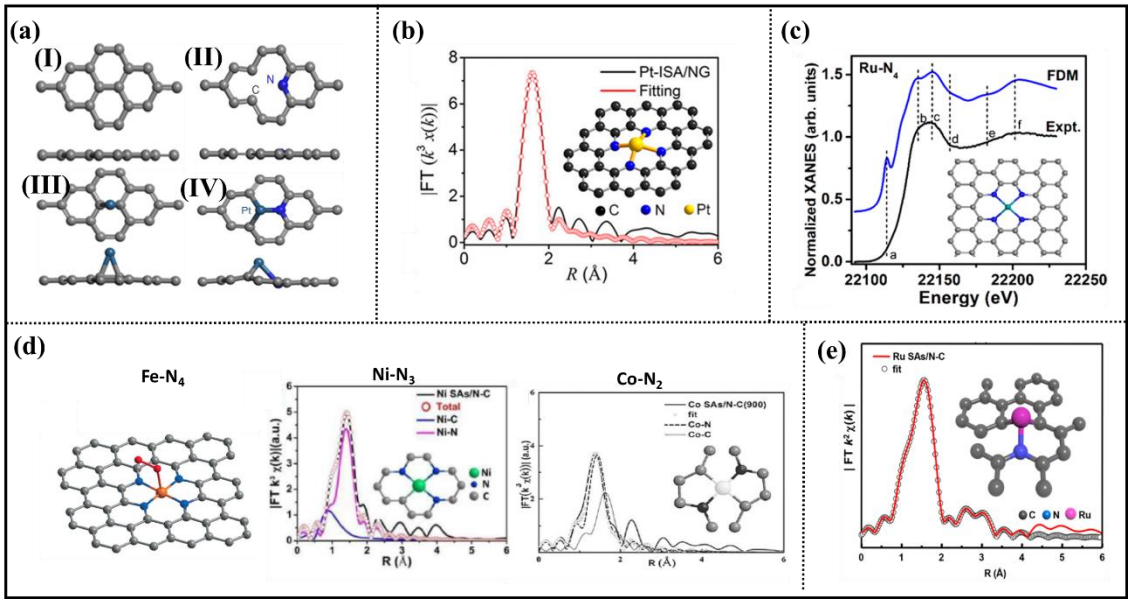

Figure 2-3. (a) Optimized structures of different substrates: (I) Pristine graphene (g). (II) Pyridinic N1-doped graphene (g-P-N_1). Optimized structures of (III) Pt1 adsorption on pristine graphene (g-Pt_1), (IV) Pt_1 adsorption on g-P-N_1 (g-P-N_1-Pt_1). The grey, blue and cyan balls denote the carbon, nitrogen and platinum atoms, respectively. Reproduced with permission.[26] Copyright 2015, Nature Publishing Group. (b) The EXAFS fitting curves of Pt-ISA/NG at R space.[27] Copyright 2018, American Chemical Society. (c) Comparison between the experimental Ru K-edge XANES spectrum of Ru-N/G-750 and the theoretical spectrum calculated from the depicted structures using the full-potential FDM.[28] Copyright 2017, American Chemical Society. (d) The proposed Co/Ni/Fe-N_x architectures. Reproduced with permission.[29] Copyright 2016, Wiley-VCH; Reproduced with permission.[30] Copyright 2017, American Chemical Society; Reproduced with permission.[31] Copyright 2017, Wiley-VCH. (e) The fitting results of the EXAFS spectra of Ru SAs/N−C.[32] Copyright 2017, American Chemical Society.

Furthermore, the co-doped nitrogen can stabilize these metal atoms from aggregating, forming metal particles. Typically, there are three types of N in the N-doped C, including graphitic-N, pyrrolic-N, and pyridinic-N.[27,32,33] The pyrrolic-N and pyridinic-N are located in a π conjugated system,[34] and their p-electrons are believed to stabilize metal single atoms. In order to understand the electronic and structural properties between single metal atoms and N-doping supports. X-ray absorption spectroscopy (XAS) has been utilized to probe metal-support interface. For the Pt_1, Liu *et al.* found that individual Pt single atoms could be homogeneously anchored on N-doped carbon black (N: 2.7 wt. %). In contrast, when the carbon support without N-doping, besides the Pt_1 atoms, Pt nanoparticles co-existed as well with the same Pt loading ratio (0.4 wt.%) and synthesis procedures. This result indicated that the N-doping of carbon support plays a critical role in effectively anchoring Pt_1 atoms and prevent their aggregation. As illustrated in the Figure 2-3a, the pyridinic (P)-N has been identified as the strong anchoring sites for Pt single metal atoms due to the modified interfacial interaction. The adsorption energy of Pt_1 on g-P-N_1 is -5.35 eV, which is much lower than that on pristine graphene (-1.56 eV). This suggests that the Pt_1 can be selectively trapped strongly by g-P-N_1 site and thus improve and stabilize the dispersion of Pt single atoms on N-doped graphene surface, confirming the vital role of support properties on the formation of single atoms.[35] Recently, Li's group achieved a high Pt_1 loading ratio up to 5.3 wt. % on N-doped graphene via a Na_2CO_3 salt-assisted one-pot pyrolysis strategy[27]. A main peak at 1.61 Å in the FT-EXAFS curve for this sample corresponds to Pt-N coordination and can be further calculated to be Pt-N_4 configuration (Figure 2-3b). On the N-graphene support, Ru-N_4 moieties are represented by a porphyrinic or pyridinic geometry (Figure 2-3c)[28]. The ZIF-8-

derived Fe_1/NC and Ni_1/NC, and Zn/Co-ZIF-67-derived Co_1/NC show a 4, 3, and 2 metal coordination number with surrounding N atoms, respectively (Figure 2-3d)[29-31]. With precise N-coordination, the high metal loadings of 1.5-4 wt % is achieved. For the Ru_1/N-C from UiO-66-NH_2, the Ru loading ratio is only 0.3 wt %, which corresponds a coordination environment of Ru-N(C_2) in Figure 2-3e[32].

2.1.3 The electronic structures of single atoms on alloy and other supports

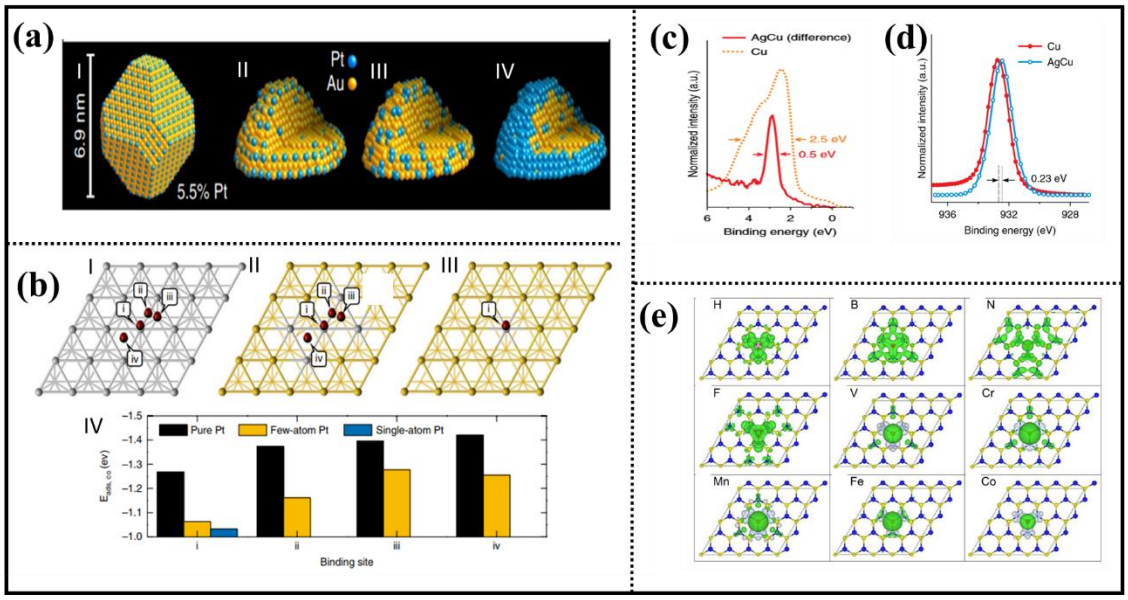

Figure 2-4. (a) Structural model of an ideal, truncated octahedral nanoparticle with an optimal single-atomic-site coverage. Although strictly not representative of the nanoparticles synthesized here, this model provides a reasonable estimate of the upper concentration limit for such single-atom Pt sites. I-IV, Models that depict the proposed evolution of PtAu surface structures from single-atom Pt sites (II) to few-atom Pt clusters (III) to a complete Pt shell (IV) as a result of increased Pt content. (b) DFT-calculated binding of CO at PtAu surfaces. I–III, Illustration of CO adsorption modes

on model (111) lattices of pure (I), few-atom (II) and single-atom (III) Pt surfaces that shows the apical (i), bridging (ii), hexagonal close-packed hollow (iii) and face-centred cubic hollow (iv) coordination sites. IV,Calculated adsorption energies for the indicated CO adsorption sites. [36] Copyright 2018, Nature Publishing Group. (c) The measured valence photoemission spectra (hν = 150 eV) of an AgCu alloy that contained 0.3 at% Cu and metallic Ag reveal the narrow Cu 3d states at a binding energy of ~2.5 eV. (d) The difference spectrum of AgCu and Ag, plotted with a Cu reference spectrum, demonstrate that the Cu 3d states in AgCu are one-fifth the width they are in bulk Cu.[37] (e) Spin density isosurfaces of substituted 1H-MoS_2 at Θ=1/48. The dashed line denotes the 4 × 4 supercell used in the calculations, green and gray distributions correspond to positive and negative values, respectively.[38] Copyright 2018, Nature Publishing Group.

In general, the surface metal-matal bond created large perturbations in the electronic, chemical, and catalytic properties of metal center[39]. Especially, it is believed that the dissimilar metal atoms can produce charge transfer, which is the key role in modifying the chemical properties of the metal matrix layers and determining the cohesive energy, comparing with the bulk alloys. Since the isolated metal atom shown a tendency to fully use of the large number of valence orbitals, controlling the donation and acceptance of electrons, the single atom would provide a useful way to tune a metal catalyst's electronic structure and thus enhance its performance via its isolating activation ad desorption steps[40]. For instance, Peng's group compared the adsorption energy of CO on pure Pt surface, few Pt atoms and single Pt atom on Au particles as shown in Figure 2-4a. The results shown that the CO adsorption is weakened and reduced from -1.268Ev on bulk Pt to -1.063 eV and -1.032eV on few-atom and single-

atom surfaces (Figure 2-4b). Thus, this weakened CO adsorption can keep CO from poisoning the surface and enhance the formic acid oxidation (FAO) reaction[36]. Also, scientists found that the d band of 0.5eV for the single metal Cu (solute atom) doped on Ag (matrix atom) became several times narrower than those of 2.5eV for bulk material Cu (Figure 2-4c). The computational calculation and photoemission spectroscopy measurements revealed that the solute's d states resemble those of a free atom, whereby the d-electron orbitals are nearly degenerated, showing a clear charge transfer (Figure 2-4d). Especially, when it is in dilute concentrations, the solute-solute bonding disappeared and exhibited a weak interaction with the electronic states of the matrix element due to the minimal energetic and spatial overlap between the solute and matrix atoms[37].

Besides metal oxides, carbon-based materials, and metal alloy, there are other supports, which was also used as host materials, including metal sulphides, metal nitrides, and metal carbides. The different host materials provides varieties of local structures due to the change of thickness, phases, and strains. The alternation of the local environment of foreign atoms arise a series of differences of the surface engineering, such as orbital exchange-coupling interaction, the electronic band gap, electron density, and adsorption energy. For instance, Li's group calculated the change of structural, electronic, and magnetic properties of MoS_2 through using a full range of substitutional dopants form non-metal to metal atoms. As shown in Figure 2-4e, both of the non-metal and metal doping shows a more stable configurations compared with the pristine ones. The spin resolved densities of the non-metal substitutions (H, B, N, F) indicated that the spin polarizations are mainly localized on dopants and adhesive atoms, while the polarizations of metal substitutions (V, Cr, Mn, Fe, Co) are

mostly localized on the metal atoms. Also, based on the TDOS and PDOS, it is suggested that the impurity states of non-metal are hybridized between 2*p* states of non-metal atom and 4*d* states of nearest Mo atoms, rarely contribution from the 3*p* states of S atom. The impurity states of metal atoms, however, origin form both the 4*d* orbital of metal atoms and Mo atoms[38].

Thus, the theoretical predictions have many times confirmed that the heterogeneous dopants hugely affected the local structure of host materials, changing their performance in various potential applications as well. It is of highly significance to prepare these promising single-atom based materials in the real use. Fortunately, researchers have developed ways to achieve these ideal single atom structures through considering the unique properties of varieties of supports, such as metal oxide, carbon, modified carbon, and metal particles.

2.2. Support effects for SACs synthesis

The SACs is hardly stable since the surface energy is ultimately high due to the smallest particle size. The strong interaction between metal and support plays an essential role in creating stable and finely dispersed SACs and prevents them from aggregation. Three factors, including precursors, supports, and synthetic procedures, are ultimately critical in controlling the interactions and optimizing the dispersion of isolated metal atoms. The essential prerequisite of SACs fabrication is to rationally select supports with specific adsorption sites, which could stabilize single atoms under realistic reaction conditions with elevated temperatures and pressures. Three representative supports with different local environments have been displayed, including metal oxides, two-dimensional materials, and the surface of metal

nanoclusters. Correspondingly, we displayed the commonly used supports and devoted to understand the interaction between single atoms and these classic supports, which lays significant foundation for the design and synthesis of single-atom catalysts. Table 2-1 provides a partial list of the supports and synthesis methods for producing supported SACs.

2.2.1 Metal oxides

The study of metal particles on oxide supports have received intensive attentions in heterogeneous catalysis, owing to the key role of the nature of the interaction of a metal particle with an oxide support in catalytic activity and selectivity. Low-index oxide facets of oxide supports are conducive to adsorption of metal catalyst, such as CeO_2 (111)[41,42] and Fe_3O_4 (001)[43-45], in which the surface cation vacancy structures render extraordinary thermal stability of precious metal adatoms and prevent them agglomeration into clusters at high temperature (700 K)[46-48]. The support with oxidic defects is preferred with surface oxygen anions and OH^- groups as ligands, which lone electron pairs on oxygen for dative coordination and lead to the stronger interaction of unsaturated surface centres with isolated metal species, such as on ZnO,[64,90] MgO,[91] Fe_2O_3,[90] Al_2O_3,[90] and TiO_2.[92] To design SACs, it is crucial to select a support which allows creation of defined metal sites on the surface and inhibits the aggregation of the metal atoms toward nanoparticles. A single metal atom could substitutionally replace a surface cation of a metal oxide support, stabilizing the single metal atoms via a charge-transfer mechanism. Many studies suggest that surface defects of oxide-supported metal clusters could provide anchoring sites for metal clusters and even single atoms.[93-95] The single metal atom might strongly anchor into the support due to its interaction with the neighbouring oxygen anions in a form of metal-O-support

bonding, leading to the realization of isolated single atoms. Moreover, the metal-metal interactions between the adatom metal and the support metal can partially determine metal atom adsorption energy as well.

Table 2-1. A partial list of the supports and synthesis methods for producing supported SACs towards various catalytic reactions.

Support	**SAs**	**Methods**	**Applications**	**Ref**
CeO_2	Au_1 Pt_1	Coprecipitation-calcination; Atom trapping; Deposition-precipitation;	Preferential oxidation of CO (PROX); CO oxidation;	49-51
Al_2O_3	Pt_1 Au_1	Mass-selected soft-loading; Sol-gel calcination method; Impregnation-precipitation; Laser ablation;	CO oxidation; Hydrosilylation reactions; NO oxidation;	52-56
FeO_x	Ir_1 Au_1 Pt_1	Coprecipitation-calcination; Adsorption method	Water gas shift (WGS) reaction; CO oxidation;	57-61

		Coprecipitation-calcination	Reduction of NO by H_2; Hydorogeneation of nitroarenes	
TiO_2	Pd_1 Pt_1	Impregnation-calcination	Styrene hydrogenation; CO oxidation;	[62,63]
ZnO	Pt_1 Au_1	Adsorption method	Methanol Steam Reforming	[64]
$ZnZrO_x$	Au_1	Impregnation-calcination	Ethanol dehydrogenation	[65]
MnO_2	Ag_1	Annealing method	HCHO oxidation	[66]
SiO_2	Pt_1	Impregnation-calcination	CO oxidation; WGS	[67]
VO_2	Rh_1	Adsorption method	Ammonia–borane hydrolysis	[68]
WO_x	Pt_1	Impregnation-calcination	Selective hydrogenolysis of glycerol	[69]
MoS_2	Pt_1 Ni_1 Co_1	Hydrothermal method; Hydrothermal method- calcination;	hydrogen evolution reaction (HER); Hydrodeoxygenation reaction (HDO)	[70,71]

TiN, TiC	Pt_1	IWI method	Oxygen reduction reaction (ORR)	[72,73]
Graphene (G)	Pt_1 Co_1 In_1 Pd_1 Ni_1	Electron beam; Atomic layer deposition (ALD); Sputtering tool; Chemical exfoliation	Methanol oxidation reaction (MOR); Hydrogenation of 1,3-butadiene; HER;	[74-77]
Carbon	Nb_1 Au_1	Arc-discharge approach; Impregnation-calcination	ORR; Acetylene hydrochlorination	[78,79]
N-doped Graphene/ carbon black	Co_1 Ru_1 Pt_1	Iyophilization-annealing; Impregnation-calcination;	HER; CO_2 reduction; ORR;	[26,28,35]
C_3N_4	Pd_1 Pt_1 Co_1	Deposition-precipitation; Impregnation-calcination;	Hydrogenations; Photocatalytic H_2 Evolution; Visible-light CO_2 reduction;	[80-82]

		Iyophilization-annealing;	ORR; OER;	
ZIF-67 derivatives	Co_1	Hydrothermal method-pyrolysis; Dielectric barrier discharge plasma treatment;	ORR; OER;	29,83
ZIF-8 derivatives	Fe_1 Ni_1	Hydrothermal method-pyrolysis; Precipitation-pyrolysis;	ORR; CO_2 electroreduction;	30,31
UiO-66 derivatives	Ru_1	Impregnation-calcination	Hydrogenation of Quinoline	32
Porphyrinic Triazine-based frameworks	Fe_1	Ionothermal synthesis- pyrolysis	ORR;	84
Cu particle	Pd_1 Ni_1	Galvanic replacement method;	Hydrogenation of butadiene to butenes; Selective hydrogenation of phenylacetylene;	85-89

	Incipient wetness coimpregnation method;	Semihydrogenation of acetylene; Non-oxidative dehydrogenation of ethanol to acetaldehyde;

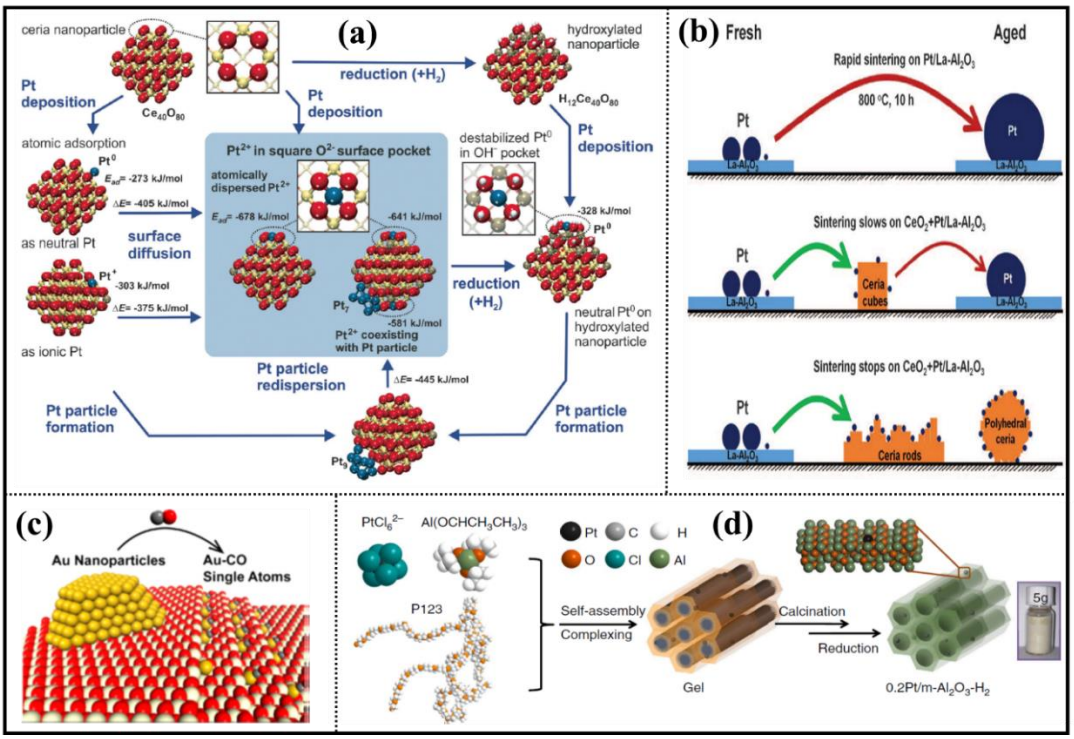

Figure 2-5. (a) Structure and energetics of the anchored Pt^{2+} species on ceria nanoparticles determined by theory. The Pt^{2+} is strongly bound at the (100) nanofacets of the ceria nanoparticle. Color coding of atoms: red O, beige Ce^{4+}, brown Ce^{3+}, blue Pt, white H. Reproduced with permission.[96] Copyright 2014, Wiley-VCH. (b) Illustration of Pt nanoparticle sintering, showing how ceria can trap the mobile Pt to suppress sintering. Cubes appear to be less effective than rods or polyhedral ceria. Reproduced with permission.[51] Copyright 2016, American Association for the

Advancement of Science (AAAS). (c) Illustration of the different ability on oxidizing CO via altering the relative chemical potentials between SAs and metal nanoparticles (NPs) on ceria. Reproduced with permission.[97] Copyright 2017, American Chemical Society. (d) Schematic illustration of the 0.2Pt/m-Al_2O_3-H_2 synthesis process: Aluminum isopropoxide, P123, and H_2PtCl_6 mixture ethanolic solution self-assembled into a gel after ethanol evaporation at 60 °C. The gel was calcined at 400 °C and reduced in 5% H_2/N_2 at 400 °C, forming the single atom catalyst 0.2Pt/m-Al_2O_3-H_2. Reproduced with permission.[53] Copyright 2017, Nature Publishing Group.

2.2.1.1. CeO_2

Ceria surfaces with a limited amount of low coordinated surface sites can adsorb noble metal atoms and remain them stable in real reaction conditions.[42,96] *Via* the DFT simulation (Figure 2-5a), Bruix *et al.* selected the cuboctahedral $Ce_{40}O_{80}$ nanoparticles as a representative model of nanostructured ceria, which features a truncated octahedral shape with O-terminated (111) and a fraction of (100) nanofacets. The (100) surface is much less stable than the (111) surface of ceria.[98] They identified (100) nanofacets as an effective surface to achieve atomically stabilized dispersion without bulk diffusion. The Pt^{2+} (*d*8) ions are well confined in square O^{2-} surface pocket at a (100) nanofacet of CeO_2, forming a square-planar PtO_4 unit as a Pt^{2+}-containing moiety. The theoretical calculation speculated that the adsorption energy of the anchored Pt_1 is high enough to withstand thermally-induced agglomeration into large nanoparticles and activity loss by diffusion into the CeO_2 bulk.[96] Dvorak and colleagues emphasized the importance of defect sites on oxide support for single-atom catalyst stabilization. They realized the single Pt^{2+} dispersion at the step edges of highly defined monolayer ceria (111) surfaces. Jones and colleagues found that

conditions under which nanoparticles emit mobile species are ideal to form single atoms if the mobile species can be effectively captured. Initially, a vapor-phase was utilized to transfer Pt from a metal foil to alumina.[99] As shown in Figure 2-5b, when the Pt/La-Al_2O_3 was physically mixed and sintered at 800 ^oC in flowing air, the ceria rods and polyhedrals can similarly trap the mobile Pt at the surface to effectively suppress sintering. In contrast, the cubic CeO_2 shows the lowest reactivity. They demonstrated that the Pt single atoms were randomly anchored on the ceria surfaces without any preference for specific facets. Atom trapping is feasible for preparing single-atom catalysts, which requires a supply of mobile atoms, a support that can bind the mobile species, and reaction conditions that are favourable to Ostwald ripening.[51] Qiao *et al.* prepared two CeO_2-supported Au SAs with loading ratio of 0.05 and 0.3% Au by a simple adsorption strategy, which were denoted as $0.05Au_1/CeO_2$ and $0.3Au_1/CeO_2$, respectively The atomic high-angle annular dark-field scanning transmission electron microscopy (HAADF-STEM) images showed that Au_1 atoms were situated on the Ce columns of CeO_2 nanocrystallites, implying that the Au_1 atoms were very likely anchored onto the surface Ce vacancy sites.[49] Most recently, Li's group revealed that Au_1 prefer to anchor at CeO_2 step sites rather than terrace surface or on Au NPs (Figure 2-5c). Moreover, for CO oxidation, they found that Au_1 exhibit little redox coupling with the irreducible support and only weakly bind CO; but the positively charged Au^+ could be formed due to the strong coupling with the reducible support, leading to vastly stable CO adsorption.[97]

2.2.1.2. Al_2O_3

Various modification has been made on Al_2O_3 to accommodate single atoms, such as porous Al_2O_3, θ-Al_2O_3, and γ-Al_2O_3.[52-56] Comparing with FeO and MgO, single atoms

doped on Al_2O_3 can modify Langmuir−Hinshelwood (L-H) mechanism due to the inert nature of Al_2O_3, which was considered to be favorable to keep the high active single atoms from agglomeration. Noble metals, such as Pt and Au, have been successfully trapped on these Al_2O_3 based materials. It was reported that the single atoms, like Pt_1, can be anchored in the inner surface of the support, allowing these atomic species stable under oxidative and reductive atmospheres at high temperatures. It is believed that these trapped single atoms can modify the inert Al_2O_3 and show exceptional catalytic performance.[52]

Significantly, they developed a modified sol-gel solvent vaporization self-assembly method (Figure 2-5d), which spontaneously assembled into a highly ordered, hexagonally arranged mesoporous structure with Pt precursor encapsulated in the matrix.[42] Besides the single Pt atoms, Au single atoms modified the inert Al_2O_3. It is found that the aluminium oxide clusters can react with single atom Au, attracting O_2, forming $AuAl_3O_3^+$, $AuAl_3O_4^+$, and $AuAl_3O_5^+$ cluster under thermal collision conditions. The attracted O_2 molecular on the gold-aluminium bond plays a key role on the catalytic oxidation of carbon monoxide (CO). Specifically, the extra O atom on the $AuAl_3O_5^+$ clusters make the Au-Al bond cleave and release valence electrons, which reduce oxygen and break the O-O bond, assisting to improve the cycling performance of CO.[56] These results indicate that Al_2O_3 support is very vital to form unique active bonds with these single atoms in the oxidized catalytic reaction.

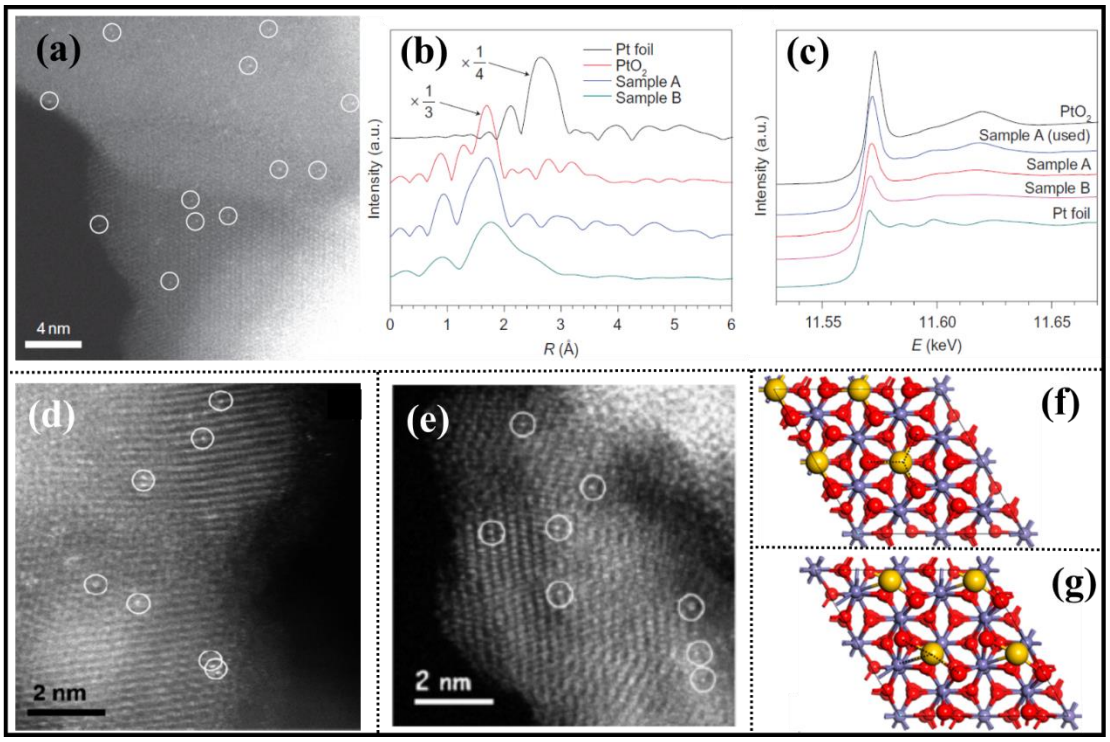

Figure 2-6. (a-c) HAADF-STEM images of Ir_1/FeO_x sample, Au_1/FeO_x sample and Pt_1/FeO_x sample. Reproduced with permission.[100] Copyright 2014, American Chemical Society; Reproduced with permission.[58] Copyright 2015, Springer; Reproduced with permission.[61] Copyright 2011, Nature Publishing Group. (d) The k3-weighted Fourier transform spectra (the above) and the normalized XANES spectra (the bottom) of sample A (Pt_1/FeO_x), sample B (Pt_1/FeO_x with loading mass of 2.5 wt% Pt), PtO_2 and Pt foil. Reproduced with permission.[61] Copyright 2011, Nature Publishing Group. (e) The proposed reaction pathways for CO oxidation on the Pt_1/FeO_x catalyst (sample A). Reproduced with permission. [61] Copyright 2011, Nature Publishing Group.

2.2.1.3. FeO_x

As early as 1999, Boccuzzi *et al.* reported that $FeO(OH)_x$ surfaces are necessary for the preparation of active Au_1/FeO_x catalysts via FTIR study.[101] *Via* a co-precipitation

method, Ir_1/FeO_x catalysts were synthesised with loading ratio of 0.01 wt. %, which were denoted as $0.01Ir_1/FeO_x$ and $0.22Ir_1/FeO_x$, applying into water-gas shift (WGS) and CO oxidation. The $0.01Ir_1/FeO_x$ achieved one of the most active catalysts reported for WGS. On the other hand, the 0.22 Ir_1/FeO_x was verified a higher energy barrier than Pt_1/FeO_x catalysts for CO oxidation, which is responsible for its lower activity. This work revealed the fundamental mechanism of isolated surface atoms and could contribute to design various single-atom catalysts with high activity.[57,102] A similar $0.03Au_1/FeO_x$ (Au loading ratio of 0.03 wt.%) was prepared via the modified co-precipitation method by the same group, serving as an important catalyst candidate for CO oxidation. In spite of high activity, it is surprising that it is extremely stable, even at a high temperature (400 ^oC). They further elucidated the mechanism for the formation of ultrastable single gold atoms, in which the concept of strong covalent metal-support interactions (CMSI) was firstly introduced. They proposed that Au_1 atoms were positively charged by occupying Fe vacancy sites of the FeO_x support, realizing the strong CMSI between Au atoms and the lattice O atoms of the support surface.[58] Qiao *et al.* pioneeringly reported the synthesis of sing-atom Pt supported on iron oxide (Pt_1/FeO_x) via a co-precipitation method. The Pt loading ratio is 0.17 weight percent (wt.%). The low Pt loading ratio and high surface area of FeO_x nanocrystallite support simultaneously promote the isolated single atoms dispersion. A serial of the-state-art-of techniques are exploited to discern the only dispersion of isolated Pt, including aberration-corrected high-angle annular dark-field scanning transmission electron microscopy (HAADF-STEM) images and X-ray absorption (XAS) spectra. As displayed in Figure 2-6a-c, for $Pt_1/FeOx$ catalyst, they demonstrated that the structure defects and the hydroxyl groups derived from poorly crystallized and large-

surface area FeO_x support plays a critical role in stabilizing the Pt single atoms. Furthermore, extended X-ray absorption fine structure (EXAFS) and X-ray adsorption near-edge structure (XANES) spectra were measured and analysed to reveal the presence of Pt-O coordination and the positive charges of Pt single atoms due to the SMSI effect between Pt and FeO_x support. They concluded that the electron transfer from Pt atoms to the FeO_x surface leads to the positive charge of Pt atoms; The strong electrostatic and covalent interactions between high-valent single Pt atoms and the FeO_x surface are responsible for the stability of the single Pt atoms on the FeO_x support, ultimately accounting for the excellent catalytic activity of the Pt_1/FeO_x catalyst on CO oxidation.[61] The HAADF-STEM images visually show the dispersion and configuration of Ir_1 and Au_1 single atoms (marked by the white circles) on the surface of FeO_x supports (Figure 2-6d-e). Inspired by these works, Li *et al.* investigated the catalytic properties of various single-atom catalysts M_1/FeO_x (M = Au, Rh, Pd, Co, Cu, Ru, and Ti) by means of density functional theory (DFT) computations, which shed light on developing superior catalysts for CO oxidation. As illustrated in Figure 2-6f, the most stable sites for all the single metal atoms are vacancy-free 3-fold hollow sites, which induced significant charge transfers from the single-metal atoms to iron-oxide surface. The DFT calculation verified that the high stability could be indicated by the strong binding energies and diffusion barriers of the single-metal atoms on the FeO_x support. Generally, oxygen vacancies are inevitable, in which the binding strengths of the single metal atoms to the less coordinated oxygen (two M-O bonds) are weakened and the electron transfers from metal atoms to the surface are reduced as well (Figure 2-6g).[103]

2.2.1.4 TiO_2

Defects on reducible oxides, such as TiO_2, can stabilize atomically dispersed metal atoms and attract researchers to develop various strategies of doping single noble atoms. For instance, it has been reported that the ethylene glycolate (EG)-stablized ultrathin TiO_2 nanosheets can uniformly load Pd single atoms with a high ratio of 1.5%. The EG modified TiO_2 nanosheets were critical to anchor Pd single atom and induce strong Pd-O interfaces to activate H_2 in a heterolytic pathway rather than the homolytic pathway on conventional Pd heterogeneous catalysts. Pd_1/TiO_2 demonstrated a better hydrogenation of polar unsaturated bonds, owing to the yields of $H^{\delta-}$ and $H^{\delta+}$. The Pd_1/TiO_2 were also considered as an excellent catalyst for removing nitrogen oxides (NO).[62] Alternatively, Phillip's group used these ultra-refined nanosized TiO_2 particles (~5 nm) to separate Pt atoms via depositing precious metal atom on each TiO_2 particles to prevent the agglomeration. To use different ratio of additive, the Pt atoms were successfully loaded on TiO_2 particles with morphology of single atom, clusters, and particles. This work provided a characterization approach to evaluation the catalytic activity of each Pt single atom site, that is, using the correlated scanning transmission electronic microscopy (STEM) imaging and CO probe molecule infrared spectroscopy (IR), the strong IR signatures of CO bound from Pt single atoms shows a two-fold great than these Pt peroxided clusters.[52] Besides the coordination of single atoms on TiO_2, He's group demonstrated that Au single atoms can be obtained via the reaction between Au^{3+} with TiO_2, forming $AuTi_2O_5^-$. The closed-shell gold containing heteronuclear oxide $AuTi_2O_5^-$ are reactive toward CO oxidation than the corresponding open-shell titanium oxide cluster anions. The essential role of Au single atoms have been confirmed by theoretical calculations, indicating that gold atom can act as a CO trapper and electron acceptor.[104]

2.2.1.5 Other metal oxides

Besides these popular metal-oxides based substrates mentioned above, variety of other metal oxides, including manganese oxide (MgO), vanadium oxide (VO_2), amorphous silica (SiO_2), and tungsten oxide (WO_x), have also been realized that can use for coordinating single atoms. For instance, ZnO NWs consisted primarily of (1010) facets were utilized for the single Pt_1 and Au_1 atomic dispersion. The single atoms were identified to anchor at the surface Zn lattice sites and stabilized by the lattice oxygen. Moreover, the theoretical calculations confirmed that the coordination binding between single precious metal atoms and oxygen can largely enhance the reaction activity, and change the reaction selectivity. When utilized in methanol steam reforming (MSR), the Pt_1/ZnO exhibited 1000 times higher turnover frequency than the pristine ZnO. The MSR experiments showed that Au_1/ZnO and Pt_1/ZnO catalyst delivered much higher conversion than the ZnO NWs, which was 28 %, 43%, and ~10%, respectively. By contrast, the Pt_1/ZnO outperformed due to its high selectivity of ~88% toward CO_2.[64] Wang *et al.* reported a $ZnZrO_x$ support by incorporating ZnO_2 to modulate the acidity of the ZrO_2 surface, which could provide more binding sites for atomic gold and much better stabilizes them against growth than either of the neat oxides. With the loading ratio of ~0.5 wt%, the active Au-O_x suface species could suppress undesired dehydration reaction and form acetaldehyde and hydrogen with 100% selectivity for ethanol at low temperature (200 ^oC), even in the presence of water.[65] The isolated Au-O_x species, therefore, play a key role in the activation of ethanol and its subsequent dehydrogenation reaction. Significantly, hollandite-type manganese oxide nanorods (HMO) can insert with Ag chains to expose the terminal Ag site, forming Ag single atom. This strategy was elaborately designed with the

amount of Ag to open the HMO tunnels to expose catalytically active sites of Ag atoms. Also, the strong intrinsic EMSI played a key role in improving the activation ability towards oxidation, due to the high depletion of the *d* electronic state of the silver active sites.[66]

2.2.2. N-doped Carbonaceous supports

It is ideal to utilize carbonaceous supports in SACs with the viewpoint of low cost. Direct single-atom adoption on graphene by ion implantation is of limited success. Meanwhile, the strong covalent C−C bonds render a substitutional doping by diffusion less efficient and compatible with tight thermal budget.[105] Thus, utilization of surface uncapped sites or aggregation inhibitors on the carbonaceous supports is vital to successfully stabilize the single metal atom species. Several reports have achieved single-atom doping on graphene *via multi*-step procedures with complex graphene modifications and inaccessible loading techniques, such as Pt_1, Co_1, In_1, Pd_1, and Ni_1.[74-77] Additionally, the single-atom niobium and gold realized atomically dispersion in graphitic layers of carbon.[78,79] Since the anchoring sites on the C supports are acquired with limit but not always abundant, which is prone to result in extremely low concentrations of single metal atoms, thus depriving the general utilization of this type of support.

2.2.2.1 Nitrogen-doped graphene

It is ideal to atomically disperse single atoms on thin two-dimensional substrate, which represents the ultimate low-end limit for SACs, exposing the most active sites with enlarged active surface area. Practically, nitrogen-doped graphene with rich anchoring sites and ideal 2D graphitic framework served as the most accessible support. As

shown in Figure 2-7a, Tour's Fannealing graphene oxide (GO) and small amounts of Co, Ru, and Fe salts in a gaseous NH_3 atmosphere.[26,28,106] A hybrid with atomically dispersed Co onto nitrogen-doped graphene (Co_1-NG) was obtained (Figure 2-7b), which showed that the Co_1-NG possessed the similar morphology to graphene without any particles. The presence of Co_1 atoms was confirmed by the bright dots. They performed extended X-ray absorption fine structure (EXAFS) analysis at the Co *K*-edge. The wavelet transform (WT) analysis (Figure 2-7c) indicated that Co single atoms are in the ionic state with nitrogen atoms. Hence, nitrogen doping on the graphene could serve as sites for Co atomic dispersion. The maximal efficiency of Co SAs enables the Co_1-NG as a highly active and robust HER catalyst in both acid and base media. Combined with the low-cost and scalable preparation method, the Co_1-NG is expected to be a promising candidate to replace Pt for water splitting applications.[26] For the Ru_1-NG, the EXAFS Fourier transforms and WT in Figure 2-7d displayed the signal at ~1.5 Å and one WT intensity maximum at 5.4 $Å^{-1}$, which are associated with the presence of Ru-N(O).[28] Meanwhile, atomic Fe single atoms and clusters on NG (Fe_n-NG) was fabricated via the similar process, which was estimated for CO_2 reduction to CO (Figure 2-7e). With Fe-N_4 moieties embedded in N-doped graphene. The high selectivity and activity of CO_2 to CO is ascribed to the synergetic effect of the Fe-N_4 moieties and N-doping on the graphene surface (Figure 2-7f).[106] In addition, it is reported that there are some other organic group can be used to modify the carbon, showing a strong interaction with single atoms. Yan's group demonstrated that the phosphomolybdic acid (PMA)-modified active carbon stabilized the Pt single atoms with a high Pt loading mass (close to 1%). It shown that the same loading mass of Pt atoms were severely aggregated without the modification of PMA, forming

particles. The thermodynamic and kinetic control were considered as the key role to successfully synthesize single atom materials, that is, the various sites can provide vacancy to accommodate Pt atoms and the kinetic barrier of agglomeration for atoms anchored on spatially separated PMA species is substantially higher than those on support without modification.[107]

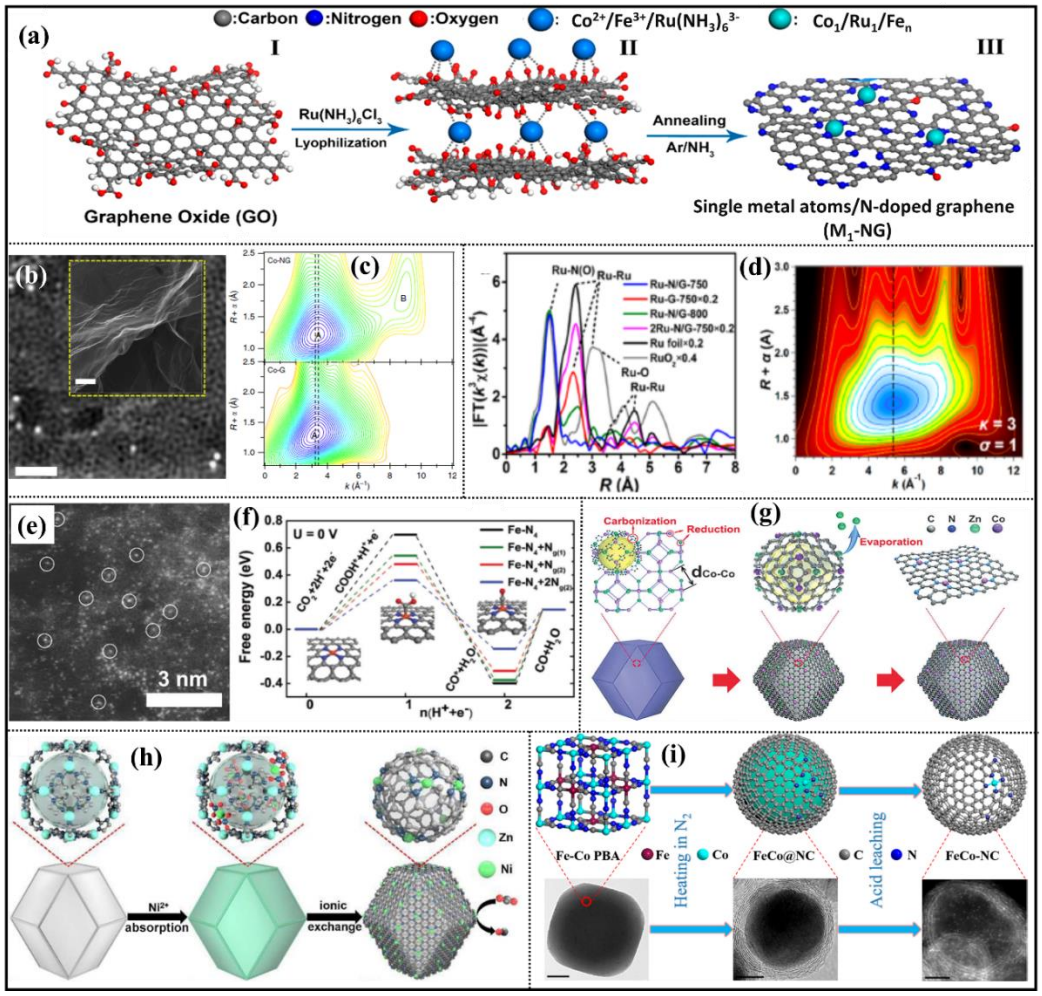

Figure 2-7. (a) Schematic illustration of the synthetic process for the $Ru_1/Co_1/Fe_n$ catalysts on nitrogen-doped graphene (NG). Reproduced with permission.[26] Copyright 2015, Nature Publishing Group; Reproduced with permission.[28] Copyright 2017, American Chemical Society; Reproduced with permission.[106] Copyright 2018, Wiley-VCH; respectively. (b) STEM image of Co1-NG, inset is the SEM image of NG. (c)

Left: Wavelet transforms for the Co_1-NG and Co-containing graphene (Co-G). Reproduced with permission.[26] Copyright 2015, Nature Publishing Group. Right: Fourier transform magnitudes of the experimental Ru K-edge EXAFS spectra of the Ru-N/G samples prepared under different conditions along with reference materials. (d) The Fourier transforms are not corrected for phase shift. WT for the k^3-weighted EXAFS signal of sample Ru-N/G-750. The maximum at 5.5 $Å^{-1}$ is associated with the Ru-N(O) contributions. Reproduced with permission.[32] Copyright 2017, American Chemical Society and (e) The STEM image of high density atomic Fe dispersion on NG. Reproduced with permission.[106] Copyright 2018, Wiley-VCH (f) Theoretical calculations and proposed mechanism on the nitrogen-coordinated Fe catalytic site. a) Free energy diagram for electrochem-ical CO_2 reduction to CO on $Fe–N_4$ moieties embedded on graphene sheets. The proposed associative mechanism involves the following steps: (1) $CO_2 + * + H^+ + e– \rightarrow COOH*$, (2) $COOH* + H^+ + e– \rightarrow CO* + H_2O$, (3) $CO* \rightarrow CO + *$, where * denotes the active site on the catalyst surface. b) Top view of the optimized structures for $Fe–N_4$ moieties embedded on graphene layer and potential nitrogen-substitution. Reproduced with permission.[106] Copyright 2018, Wiley-VCH (g) The schematic illustration of the formation of Co_1/*N*-C (900). Reproduced with permission.[29] Copyright 2016, Wiley-VCH. (h) Schematic illustration of the synthetic process for the Fe-SAs/CN and Ni-SAs/CN. Reproduced with the permission.[30] Copyright 2017, American Chemical Society; (i) Schematic illustration of the synthetic process for single-Co-atom catalysts via pyrolyzing Fe-Co prussian blue analogue. Reproduced with the permission.[108] Copyright 2018, American Chemical Society.

2.2.2.2 Metal organic frameworks-derived nitrogen-doped carbon

It remains challenge to fully control the synthesis of well-defined isolated atoms. Because the concentration of metal atoms is supposed to be extremely low to avoid aggregation, especially on the incorporated support. A strategy considered to solve this situation is to assembly organic ligands, which is expected to anchor single atoms and show thermal stability. It is believed that MOF structure is the best option, owing to the easy accessibility and numerous ligands dispersed on the architectural structures. It is well known that metal-organic frameworks (MOFs) are consisted with metal-containing nodes and organic linkers, in which the metal sites are atomically dispersed. Direct pyrolysis of MOFs are expected to be an ideal route for preparing various single atoms based on the versatility of metal ions and ligands. However, this approach is highly challenging due to the high-temperature pyrolysis tends to rapidly convert single-atom metal ions into aggregated nanoparticles. Li's group has made significant breakthrough on this direction, in which they utilized low-boiling-point Zn atoms (mp 420 ºC, bp 907 ºC) as a template so that to free abundant N-rich defects after Zn evaporated at high temperature. As a result, another metal can closely anchored through N-coordination to form isolated metal single atoms without aggregation during pyrolysis.[109] Specifically, as illustrated in Figure 2-7g, a ZIF-67-like Zn/Co bimetallic MOF (BMOF) was synthesized, in which Zn^{2+} replaced a certain proportion of Co^{2+} sites, thereby expanding the distances of adjacent Co atoms. The Zn^{2+} ions can be used as separators to adjust the distance of adjacent Co atoms and prevent the formation of Co-Co bond. Also, the leaving Zn^{2+} sites generate free N sites during

pyrolysis, which can further provide thermal stability for these active single atoms. The single atom Co nodes are in-situ reduced and anchored into the nitrogen-doped porous carbon with Zn evaporated at high temperature. It is impressive that the Co loading ratio is as high as 4 wt%.[29] Furthermore, zeolitic imidazolate frameworks (ZIF-8) served as an effective precursor for the synthesis of Fe and Ni single atoms in an N-carbon matrix (Fe-SAs/CN and Ni-SAs/CN).[30,31] $Fe(acac)_3$ and $Ni(NO_3)_2$ were selected as metal sources, which could be trapped into molecular-scale cages of ZIF-8 with cavity diameter (d_c) of 11.6 angstrom and pore diameter (d_p) of 3.4 angstrom. As illustrated in Figure 2-7h, after pyrolysis at 1000 ^oC under Ar atmosphere, ZIF-8 transformed into nitrogen-doped porous carbon with the evaporation of Zn. Meanwhile, $Ni(NO_3)_2$ within the cage were reduced by carbonization of the organic linker, leading to the formation of isolated single iron atoms anchored on nitrogen species.[30] All MOF-derived single atoms showed superior electrocatalytic activities, owing to the synergistic effect between transition metals and N species, which will be discussed in details later. The broad range of ligands on MOFs has variety of selectivity. For example, the numerous free amine groups ($-NH_2$) at the skeleton of UiO-66-NH_2 are considered as a critical role to access the atomically isolated dispersion of single atom sites of Ru. It is suggested that Ru metal ions can be adsorbed within the MOFs channels by the strong coordination interaction between the electron lone pair of nitrogen and *d*-orbital of Ru atoms. The Ru SAs/N-C shows a selectivity of 99% toward chemoselective hydrogenation of functionalized quinolones, which is much more effective than that of Ru nanoparticles on NC (Ru NCs/C).[32] The successful synthesis of single atom material and applications on catalytic reaction via coordination of organic ligands attracts more investigation on MOFs structures.

Wang's group reported a feasible method to produce coordinative unsaturated metal sites through dielectric barrier discharge plasma treatment. The irradiated ZIF-67 create single Co atoms as catalytic centres for oxygen evolution reaction (OER). Both of experimental results and theoretical calculation demonstrated these unsaturated Co sites plays a critical role to achieve high activity of OER.[83] Also, Cao's group reported that the atomic Fe species can be anchored on porous porphyrinic triazine-based frameworks (FeSAs/PTF) with a high loading of 8.3 wt. %. The FeSAs/PTF shows excellent ORR activity, long-term durability, and good methanol tolerance in both alkaline and acidic media.[84] Most recently, Zhang's group produced single-Co-atom catalysts via pyrolyzing Fe-Co prussian blue analogue followed by acid leaching. They utilized Fe doping and different calcination temperature to modulate the contents of pyrrolic N in the obtained N-doped graphene shells, which are favourable to form abundant CoN_4 sites (Figure 2-7i).[33]

Thus, the strategy of using MOFs structure as substrates has been proved that it can effectively coordinate with variety of atoms with a high loading mass (>1%), indicating its easy control and huge potential for broader applications.

2.2.2.3 Graphitic carbon nitride (g-C_3N_4)

Graphitic carbon nitride (g-C_3N_4) consists of 2D conjugated planes packed together with tri-*s*-triazine repeating units through interlayer van der Waals interactions with lattice-hole structure. The characteristic N-coordinating cavities formed by the tri-*s*-triazine structure serve as potential scaffold for firmly anchoring isolated single atoms. Stable single-site Pd species was strongly trapped into the six-fold cavities of mesoporous g-C_3N_4, which offered the first stable single-site heterogeneous catalyst

for hydrogenations of alkynes and nitroarenes. This $Pd_1/g\text{-}C_3N_4$ catalyst exhibited high activity and selectivity (>90 %), which is associated to the facile hydrogen activation and alkyne adsorption on the atomically dispersed Pd1 sites.[80] Li *et al.* successfully dispersed isolated single Pt atoms on $g\text{-}C_3N_4$ with loading amount of 0.16 wt %. Since $g\text{-}C_3N_4$ itself is a promising stable and active catalyst for photocatalytic water splitting,[110-112] the $Pt_1/g\text{-}C_3N_4$ represents a new and highly efficient photocatalytic system for H_2 evolution. The synergistic co-catalyst of single-atom and $g\text{-}C_3N_4$ provides a new strategy to modulate the electronic structure, leading to a prolonged lifetime of photogenerated electrons due to the isolated single Pt atoms induced, intrinsic change of the surface trap states. The $Pt_1/g\text{-}C_3N_4$ eventually achieves tremendously enhanced photocatalytic H_2 generation performance, showing 8.6 times higher than that of Pt nanoparticles on the per Pt atom basis, and nearly 50 times of that for bare $g\text{-}C_3N_4$.[81] Furthermore, DFT calculation was applied to investigate the $Pd_1/g\text{-}C_3N_4$ and $Pt_1/g\text{-}C_3N_4$.

For phtocatalytic CO_2 reduction, which concluded that HCOOH is the preferred product on the $Pd_1/g\text{-}C_3N_4$ catalyst with a rate-determining barrier of 0.66 eV, while the $Pt_1/g\text{-}C_3N_4$ catalyst prefers to reduce CO_2 to CH_4 with a rate-determining barrier of 1.16 eV.[113] Qiao's group developed a range of molecule-level $g\text{-}C_3N_4$ coordinated single Co atoms ($Co_1/g{-}C_3N_4$) as a new-generation catalysts for these oxygen electrode reactions, including ORR and OER in alkaline media. The high activity of $Co_1/g{-}C_3N_4$ catalyst with a desired molecular configuration originates from the precise $Co{-}N_2$ coordination in the $g\text{-}C_3N_4$ matrix. Moreover, the reversible ORR/OER activity trend for a wide variety of transition metals/$g{-}C_3N_4$ complexes has been

constructed to provide guidance for the molecular design of this promising class of catalysts.[82]

2.2.3 Single atom alloys (SAAs)

One alloying method has been developed to stabilize the single atoms with another metal to form an alloyed SAs, in which one metal is completely isolated by the second one. By virtue of the synergistic effect of the bimetallic catalysts, the alloyed SAs exhibit geometric and electronic structures different from those of the single atoms that was prepared by anchoring on the support. Sykes's group has done significant contribution in this system by both theoretical model and real catalytic experiments. As revealed via the scanning tunnelling microscopy (STM), Figure 2-8a clearly displayed rumpled appearance of the upper terrace, indicating Pd preferentially alloys into the Cu(111) surface above the step edges. The atomic resolution of the Pd/Cu alloy on the upper terrace (inset) shows the isolated Pd atoms in the surface layer appearing as protrusions. They found that a single atom alloy, with individual Pd atoms in a Cu (111) surface, could show lower energy barrier for both hydrogen dissociation and subsequent desorption (Figure 2-8b and c). The facile hydrogen dissociation at Pd SAs and weak binding on Cu substrate synergistically result in high hydrogenation selectivity of styrene and acetylene in contrast to pure Cu or Pd metal alone.[85] A PdCu SAA with trace amount of Pd (0.18 at%) was reported to demonstrate high activity and selectivity for the hydrogenation of butadiene to butenes. As shown in Figure 2-8d, the concentration of the Pd relative to the host Cu surface is critical. When the Pd coverage is low, Pd could exsit in the form of individual, isolated atoms into the Cu surface layer. The larger scale bar image in Figure 2-8e indicates that the alloying site is the ascending step edges. When Pd coverages increase, Pd islands could

be observed on the surface as seen in Figure. 2-8f and g.[86] By the same method, they also synthesized Cu-alloyed Pd single atoms supported on Al_2O_3 via the galvanic replacement method, which exhibited both high conversion and styrene selectivity for selective hydrogenation of phenylacetylene.[87] More recently, Pei *et al.* successfully synthesized silica gel supported Cu-alloyed Pd SAA by a simple incipient wetness coimpregnation method (Figure 2-8h). They found that this $PdCu/SiO_2$ exhibited a high selectivity of ~85% with 100 % complete acetylene elimination toward the semihydrogenation of acetylene. The IB-metal-alloyed Pd SACs were also systematically compared with Cu-alloyed Pd SAC, in which similar active sites and catalytic mechanisms were revealed for the three catalysts. The further DFT calculation results indicated that the distinct conversion and selectivity of Pd atoms in the IB metal alloys is ascribed to the electron transfer between the IB mentals and Pd.[88] Similarly, it is reported that a trace amount of Ni was employed to atomically disperse on Cu particles forming NiCu alloy (NiCu SAA). In-situ diffused reflectance infrared Fourier transform spectroscopy (DRIFTS) was employed in this work and identified that the C-H activation is the rate determining step of the dehydrogenation reaction on all the copper catalysts. The presence of Ni single atoms shown unique catalytic activities in the selective non- oxidative ethanol dehydrogenation reaction, owing to the exceptional low C-H bond activation barrier achieved via the effects between Ni isolated atoms and Cu particles. Also, comparing with Cu/SiO_2 monometallic nanoparticles, the NiCu SAA facilitated the formation of acetaldehyde in a low temperature of 150 ℃, showing a direct evidence of the key role in C-H bond scission of ethanol dehydrogenation.[89]

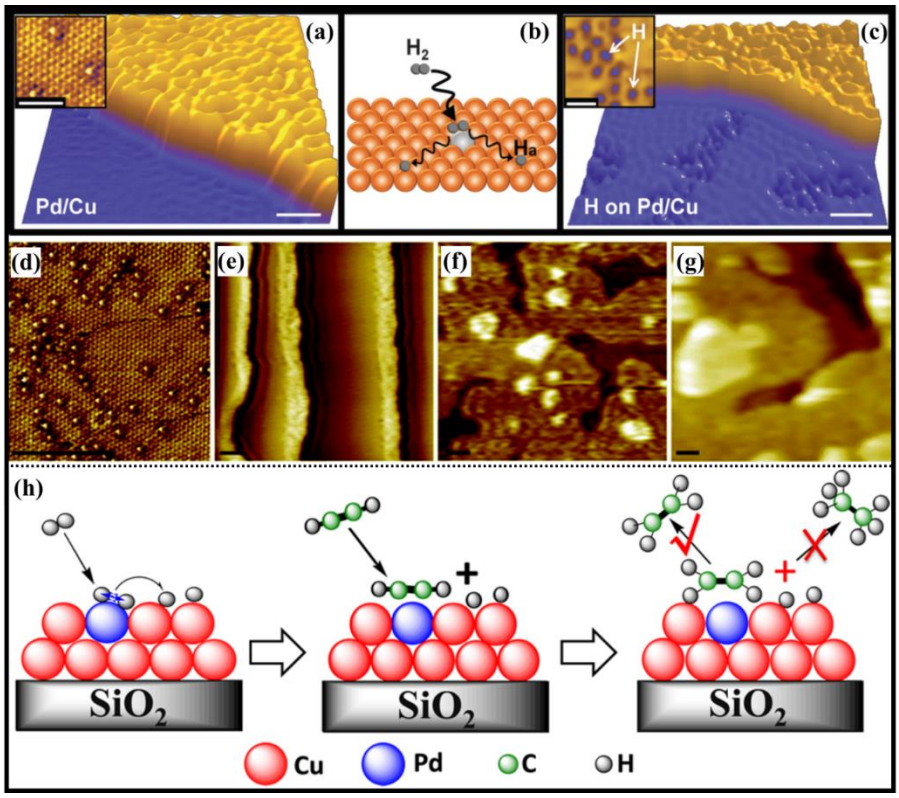

Figure 2-8. STM images showing atomically dispersed Pd atoms in a Cu(111) surface and hydrogen atoms that have dissociated and spilled over onto the Cu surface. (a) Pd alloys into the Cu(111) surface preferentially above the step edges as evidenced by the rumpled appearance of the upper terrace (scale bar indicates 5 nm). (Inset) Atomic resolution of the Pd/Cu alloy on the upper terrace showing individual, isolated Pd atoms in the surface layer appearing as protrusions (scale bar, 2 nm). (b) Schematic showing H_2 dissociation and spillover at individual, isolated Pd atom sites in the Cu surface layer. (c) Islands of H atoms imaged after hydrogen uptake appear as depressed regions on the clean Cu(111) lower terrace (scale bar, 5 nm). (Inset) High-resolution image of individual hydrogen atoms on Cu(111) (scale bar, 2 nm). Images recorded at 5 K. Reproduced with permission. [85] Copyright 2012, American Association for the Advancement of Science (AAAS). (d-g) STM images of Pd/Cu alloys with a range of stoichiometries: (d) 0.01 ml Pd, (e) 0.1 ml Pd, (f) 1 ml Pd and (g) 2 ml Pd. Scale bars:

5nm. Imaging conditions 0.05–0.15 V, 0.1–1.0 nA. Pd/Cu alloys were formed at 380 K. Reproduced with permission. [86] Copyright 2013, Royal Society of Chemistry. (h) Proposed reaction pathway for semi-hydrogenation of acetylene over silica-supported Cu alloyed Pd SAC: dissociation of H_2 and Spill over of H atoms (left), adsorption and hydrogenation of Acetylene (middle), and desorption of π-Bonded Ethylene (right). Reproduced with permission. [88] Copyright 2017, American Chemical Society.

2.2.4 Metal sulphides, nitrides, and carbides

2.2.4.1 MoS_2

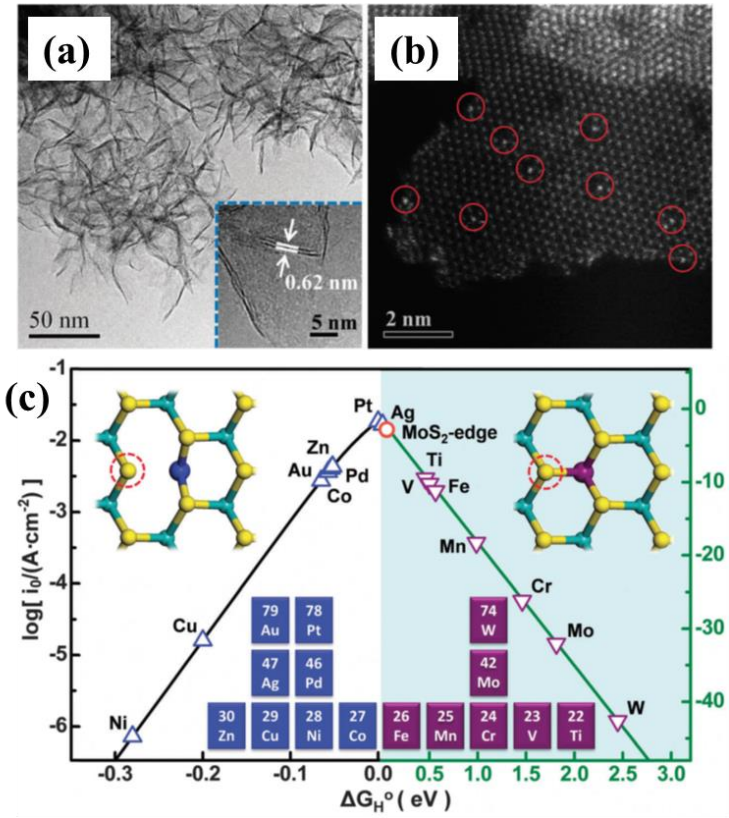

Figure 2-9. (a) TEM image of Pt–MoS_2 with the inset showing a typical MoS_2 layer distance of 0.62 nm. (b) HAADF-STEM images of Pt–MoS_2 showing that the single Pt uniformly disperse in the 2D MoS_2 plane. (c) The relation between currents ($\log(i_0)$)

and ΔG_H^0 presents a volcano curve. The left and right sides of the volcano plot adopt two sets of scales for better visibility. The inserted graphs point to different configurations of doped MoS_2 as coordinated with four (left) and six (right) S atoms. The adsorption sites for H atoms are marked by the red dashed circles. The studied metal atoms are located in the Periodic Table as shown by the inset at the bottom. Green balls: Mo; yellow balls: S; blue and purple balls: doped metal atoms. Reproduced with permission.[70] Copyright 2015, Royal Society of Chemistry.

In some case, though the single atoms are not catalytically active, they unexpectedly play important role in enhancing the catalytic activity of support. Liu *et al.* reported atomic Co dispersed on MoS_2 monolayers, in which the Co-doping create many sulfur vacancy sites in MoS_2 basal planes, leading to excellent activity, selectivity, and stability for the hydrodeoxygenation reaction (HDO) of 4-methylphenol at 180 °C with no detectable sulfur loss from the catalyst system.[71] Bao's group reported that the catalytic activity of in-plane S atoms of MoS_2 can be trigged via single-atom Pt doping for hydrogen evolution reaction (HER). The significant enhancement was attributed to the tuned adsorption behaviour of H atoms on the in-plane S sites neighbouring the doped Pt single atoms. The Pt_1/MoS_2 was synthesised by a one-pot hydrothermal method, leading to the formation of flower-like 2D MoS_2 nanosheets with uniform dispersion of bright Pt SAs shown in Figure 2-9a and b. The triggering mechanisms of various metal SAs have been investigated via DFT calculations. As shown in Figure 2-9c, the metal atoms could substitute the Mo atoms in the MoS_2 matrix, leading to two different configurations of doped MoS_2. Some metal atoms, including V, Ti, Fe, Mn, Cr, etc., tend to remain in the middle to bond with six S atoms, which can be anticipated to possess low activity due to their weak binding ability with H. While

other metal atoms, such as Pt, Ag, Pd, Co, Ni, etc., are prone to shift toward one side and bond with only four S atoms but with other two S atoms unsaturated, leading to distinctly high adsorption behaviours of H atoms on the two unsaturated S atoms and thereby high HER activity. It is clear the Pt-MoS_2 shows higher HER activity than Ni- and Cu-doped MoS_2, which are owing to the overly strong adsorption of H* by the unsaturated S atoms neighbouring the dopants (Ni and Cu) on the left side of the volcano plot.[70]

2.2.4.2 TiC and TiN

TiN and TiC were considered as promising candidates for the metallic support material in PEMFCs, and methanol direct fuel cells, demonstrating clear advantages over traditionally used acidic susceptible carbon-based supports, including good electrical conductivity and its high resistance to corrosion and acid attack. In a view of combination of the high-efficiency single atom material and stable TiN, Soon's group developed a theoretical strategy to anchor Pt single atoms via producing N-vacancy on the surface. Comparing to the clean TiN surface, TiN surface vacancies is energetically favourable of Pt atoms. The author also further shown the charge density differences, when Pt bonded with N vacancies and Ti vacancies. For the N vacancy, it demonstrated that Pt atoms embedded into the TiN surface experiences a significant increase in the occupation of the 5d states due to coordination by the four neighboring surface Ti atoms, where the electronegativity of Pt (Pauling value of 2.28) is large than that of Ti (Pauling value of 1.54). For Pt atom adsorption on Ti vacancies, the charge redistribution is directional and both N and Ti atoms are involved in the charge transfer, leading to the depletion of the planar Pt 5d states and the unfavourable Pt adsorption energy.[114,73] Via DFT calculation, Back et al. explored a range of SACs, where

transition-metal atoms (M=Ag, Au, Co, Cu, Fe, Ir, Ni, Os, Pd, Pt, Rh, and Ru) are doped at surface defect sites of TiC and TiN. The iridium-doped TiC (Ir1@d-TiC) was theoretically evaluated as highly active and selective CO_2 reduction catalysts.[115]

2.3. Support effects for catalytic reactions

Properties of supports, including nanocrystal shape and exposed facet, would strongly influence the catalytic performance of SACs.

2.3.1 Activity

SACs can typically accelerate a wide range of reaction, such as CO oxidation,[52,61] methane conversion,[116] water-gas shift (WGS) reaction,[57,92] and other important reactions,[78,117] which could achieve orders of magnitude higher activity than their NP counterparts. For the WGS reaction, it is impressive that SACs on oxide supports are always more active than their NP counterparts based on turnover frequency (TOF),[57,67,118,119] since the NPs only serve as spectators during the WGS reaction. In contrast, some SACs might be inferior in catalytic activity than their NP counterparts for CO oxidation, and it should be pointed out that the advantages of SACs are multifarious and not always limited to activity but depend on a variety of factors on a case-by-case basis.[61,67,120]

It is readily comprehensible that the types of SACs directly determine the catalytic performance when anchored on the same support. Taking M_1/FeO_x as examples, when anchored on FeO_x support for CO oxidation. Pt_1 could deliver 2-3 times more active than Pt NPs;[61] Au_1 is comparable to its NP counterpart,[58] while Ir_1 and Rh_1 are less active than their NP counterparts.[102,103] The catalytic activity for single atoms on the same FeO_x support show a trend with the order $Au_1 > Pt_1 > Ir_1 \approx Rh_1$, which is oppositely

corresponding to the absorption strength of CO on metal sites because the weak CO adsorption is favourable and could significantly enhance the adsorption and activation of O_2. On the other hand, the stabilization of SACs and catalytic properties are closely related to the support effect. It is noticeable that surface of the FeO_x support is dominated by Fe_3O_4 with abundant oxygen vacancies and hydroxyl groups, which are believed to provide reactive O atoms for the reactions and play critical roles in the oxidation reactions, especially for WGS and CO oxidation.[121] The impact of surface O atoms is revealed via in-situ spectroscopy that surface lattice O atoms of the FeO_x support could assist the single atoms to directly participate in CO oxidation.[122] Meanwhile, the research on Pt_1/CeO_2 also confirmed the important role of surface O atoms. A steam treatment at 750 ^oC was conducted, which was expected to afford active surface lattice O atoms in the vicinity of Pt^{2+}, leading to high activity for low-temperature CO oxidation.[123] Moreover, the applications of SACs are extended to electrocatalytic reactions.[124-126] Besides the requirements on the nature and number of active sites as these in thermocatalytic reactions, the activity of the catalysts in electrocatalysis additionally relies on the properties with high electrical conductivity. For the application, N-doped C is considered as one of the most promising supports to synthesis a serials of atomically dispersed metal single atoms, leading to M_1-N-C electrocatlysts, including Co_1-N-C,[26,29,127,128] Fe_1-N-C,[129,130] Ni_1-N-C,[77] and Cu_1-N-C[131] materials. Li's group has developed a general method for the preparation of single atoms via N coordination with the assistance of ZIF-8 and ZIF-67. Impressively, the ZIF-derived Co_1-N-C and Fe_1-N-C could exhibit superior ORR performance than commercial Pt/C catalysts in alkaline electrolyte, which achieve half-wave potentials of 0.881 and 0.900 V, respectively. The high activity is ascribed to that the single Co

and Fe atoms could transport electrons to absorbed OH species.[29,129] Moreover, a catalyst consisted of Pt_1 on N-doped graphene nanosheets also outperform the Pt NP and commercial Pt/C catalysts for HER in acidic media. The superior activity of Pt_1 was proven to result from the partially unoccupied Pt *5d*-like orbitals, which are favourable to absorb H and resulted H_2.[132] In addition, Pt_1 on N-doped carbon black can be utilized as a high-active catalyst for four-electron ORR in an acidic media, in which the Pt single atoms are bonded with single pyridinic N atoms to form Pt_1-N_1 active sites. This active sites surprisingly cleave O_2 on one Pt atom *via* 4e- transfer but poor binding for CO.[35] The application of supported single atoms has recently extended to photocatalytic conversions. Ideally, the supports are supposed to absorb solar light and also stabilize the anchored single atoms. The g-C_3N_4 is accordingly regarded as a promising candidate owing to its high stability, excellent visible-light absorption, and capability to bind noble metal centres through N donor atoms. Pt_1 on g-C_3N_4 (Pt_1/g-C_3N_4) exhibited 50 times higher photocatalytic HER activity than g-C_3N_4 and eight times higher TOF per atom than Pt NP/g-C_3N_4. It is ascribed to that the Pt single atoms could change the surface trap states of g-C_3N_4, thereby enhancing photo-generated electron–hole separation.[81] Additionally, g-C_3N_4 support is believed to deliver H atoms to Pt_1 and Pd_1 single atoms via DFT calculation, which render them high active catalysts for CO_2 phtoreduction.[113] Due to the unknown nature of the active sites, the N donor atoms vary from two to six, in which the materials typically have metals bound to four N atoms. Beyond the intrinsic activity of M_1-N_x active sites, the pore structure and electrical conductivity of the carbon matrixes could impact on mass and electron transport of the catalysts, leading to case-by-case performance. In some

case, they even are inactive in reactions that require two or more neighbouring metal atoms to activate these conversions.

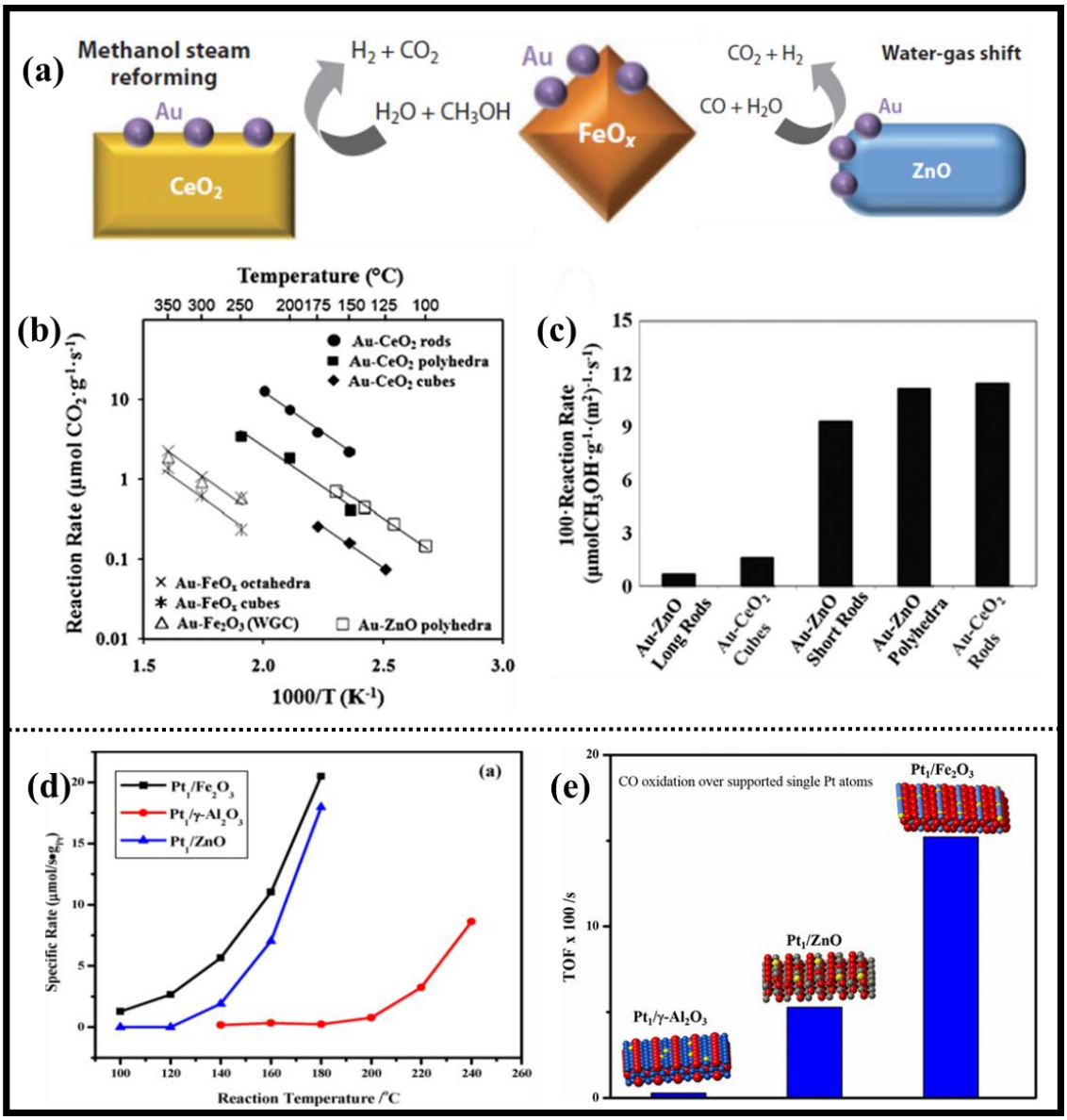

Figure 2-10. (a) The schematic illustration of Au catalysts on different supports: CeO_2, FeO_x, and ZnO for methanol steam reforming and water-gas shift; (b) Steady-state WGS reaction rates over gold–metal oxide catalysts on various substrates; (c) Comparison of SRM rates at 250 °C over Au–ZnO and Au–CeO_2 nanoshapes. Reproduced with permission.[133] Copyright 2011, Royal Society of Chemistry. (d)

Specific rate of wet CO oxidation over dry Pt_1/Fe_2O_3, Pt_1/ZnO, and $Pt_1/\gamma\text{-}Al_2O_3$ SACs; (e) The turn over frequency (TOF) comparison of Pt_1 single atoms on different metal oxide supports for dry CO oxidation at 140 ^oC. Reproduced with permission.[90] Copyright 2017, American Chemical Society.

Impressively, when anchored on different shapes of the same supports or different supports, the same type of single atoms could exhibit different activity and selectivity. For instance, ceria with various shapes, including rods, cubes, and polyhedral, were utilized as supports of 1% Au. Gold was poorly dispersed and aggregated into nanoparticles when deposited on the CeO_2 nanocubes (100), which was inactive for the low-temperature WGS reaction. In contrast, most of the gold on the (110) facets of CeO_2 nanorods was atomically dispersed with high activity. This results manifests that the (110) have more binding sites for gold than the (100) polar surfaces of CeO_2.[134] Furthermore, as illustrated in Figure 2-10a, various oxide supports, including CeO_2, ZnO and FeO_x single crystal, are utilized to compare the substrate effect.[133] Boucher *et al.* found that ZnO (0001) surfaces are the favourable supports for the active Au sites toward water-gas shift (WGS).[133,135] It is evident that activation energy and conversion rates of the Au-FeO_x are lower compared to Au-CeO_2 and Au-ZnO for WGS reaction tests. The possible reason for the lower activity is a weaker interaction of the Au with iron oxide surface. They suspect an instability/deactivation of the Au–FeO_x nanoshapes under reaction conditions (Figure 11b). Moreover, the "shape effect" of oxide supports is examined for both WGS and MSR reaction. The WGS reaction of Au/FeO_x catalysts depends on the iron oxide shape in experiments with gold deposited on single crystals of nano-Fe_3O_4, (i.e., octahedra (111) and cubes (100), Figure 2-10b).[133] As shown in Figure 11c, both Au-CeO_2 and Au-ZnO are active catalysts for

the SRM reaction. It is evident that Au-CeO_2 delivered higher reaction rates, which is attributed to the better dispersion of Au on CeO_2 (110) surfaces, leading to more Au-O active sites. This Au-O species serve as the active sites for methanol reactions, in which the CeO_2 (110) surfaces that can disperse gold atomically are also superior to CeO_2 nanocubes presenting (100) surfaces.[135-137] Au–ZnO samples with a large fraction of ZnO (0001) surfaces exposed (polyhedra and short rods) are active for the MSR reaction (Figure 2-10c). Liu *et al.* carried out a systematic investigation on support effects via dispersing single Pt_1 on highly reducible Fe_2O_3, reducible ZnO, and irreducible γ-Al_2O_3. It was proven that Pt_1/Fe_2O_3, Pt_1/ZnO, and Pt_1/γ-Al_2O_3 are all active for CO oxidation and the reducibility of the supports determine the catalytic performance of Pt_1 SACs (Figure 2-10d and e). At 140 ^oC, the TOF value of that Pt_1/Fe_2O_3 is larger than that of the Pt_1/ZnO, which are much larger than that of Pt_1/γ-Al_2O_3. The TOF of a Pt_1 atom supported on Fe_2O_3 and ZnO is about 50 and 18 times higher than that of a Pt_1 atom supported on γ-Al_2O_3.[90] Such a huge difference in the TOF value of one Pt_1 atom suggests that that the interaction between single metal atoms and support as well as surface properties of supports control the catalytic behaviour of SACs.

2.3.2 Stability

Stability of SACs is an important factor that often hinders the application of SACs. Due to their high surface-free energy and the low coordination number, SACs are prone to sinter/ripen with time and catalytic processes, agglomerating into their thermodynamically stable state, such as particles.[95,138]

Thermally stable SACs can be successfully synthesized. Campbell and his co-workers found that small particles have a much lower heat adsorption than large particles, indicating the lower onset temperature for Ostwald ripening.[139,140] Moreover, they measured the energies of Ag atoms in Ag NPs supported on CeO_2 and MgO surfaces, which demonstrated that Ag NPs with any sizes below 1000 atoms had much higher stability on reduced CeO_2(111) than on MgO(111) (Figure 2-11a). This effect was found to be a result of strong bonding to both defects and CeO_2(111) terraces.[141] Single metal atoms are in principle easier to aggregate than metal NPs, and thus stronger metal–support interactions (SMSI) are required for the stability of SACs. For instance, both experimental results and DFT calculations revealed that Pt atoms prefer to be on the four-fold hollow sites. Flytzani-Stephanopoulos's group introduced alkali ions (Na or K) on zeolites and mesoporous oxides, to stable the single-site cationic An-O(OH)$_x$ - species.[142] They also prepared single-atom-centric Pt sites stabilized by sodium through –O ligands, which are active and stable in WGS reaction from ~120 to 400 ^{o}C.[143] Qiao *et al.* reported that the Au_1/FeO_x catalysts were not only highly active but also extremely stable, even at temperatures as high as 400 °C; they proposed the single Au_1 atoms located at Fe vacancy sites of the FeO_x nanocrystallites via strong covalent metal-support interaction (CMSI), thus immobilizing the Au_1 atoms on the support surface.[58] Additionally, atomically dispersed Au on FeO_x supports also were proven to show a remarkable stability in heat treatments up to 500 °C.[144]

Even though thermally stable SACs can be successfully synthesized on various supports, it is predictable that chemical or reaction stabilization of these surface single atoms remains to be a challenge due to the presence of oxidative or reducing reactants and high temperature under operating conditions. Reaction stability of SACs is of great

importance to design more robust catalysts. For instance, reactants, such as CO, NO, H_2, and O_2, were confirmed to affect or induce dramatically the sintering, disruption, and re-dispersion of supported metal particles and single atoms.[47,145,146] CO induced the coalescence of Pd adatoms supported on Fe_3O_4(001) surfaces at room temperature.[47] For the Pt/Fe_3O_4 system, the CO-induced mobility leads to the agglomeration of Pt into subnanometer clusters, but on the other hand the presence of CO stabilizes the smallest clusters against decay.[145] The strong interaction between the reactant and the metal adatom is essential for the synthesis of a catalyst with high thermal and chemical stability. Kyriakou *et al.* anchored single Pd atoms in the lattice matrix on Cu(111) surfaces to obtain an extremely stable SAC with strong Pd–Cu bonds.[85] Zhang's group prepared a series of single-atom Co–N–C catalysts with single Co atoms strongly bonded with four pyridinic N atoms, which showed high stability for the chemoselective hydrogenation of nitroarenes and aerobic oxidative cross-coupling of primary and secondary alcohols.[147,148] As shown in Figure 2-11b, the single atom Co-N-C catalyst was derived from pyrolysis of Co-phenanthroline complexes on a mesporous carbon support, which was proposed to be Co_1 bonded with N within graphitic sheets. This catalyst showed high catalytic activity toward the target reactions with turnover frequency of 3.8 s^{-1}. Impressively, the Co single atoms in the Co-N-C structure are highly stable against sintering during pyrolysis (< 800 ^oC) and acid leaching.[147] Tang's group developed Ag_1-hollandite manganese oxide (HMO) catalyst with excellent thermal and chemical stability by initially depositing Ag NPs on HMO surfaces, and then annealing the sample at 500 °C in air. As revealed by Figure 2-11c, the HRTEM images confirmed that single-atom Ag linear chains were successfully synthesized via a simple thermal process. Figure 2-11d illustrated several

models of this sample viewed from different directions with atom arrangement on the (001) facet of Ag-HMO. Moreover, temperature-dependent in situ XRD recorded the formation of this single atom Ag chain from 50 to 380 °C, in which the diffraction intensity of Ag(111) gradually decreases along shifting to lower Bragg angles and then totally disappears after 230 °C. The hollandite crystal structure remains unchanged in the whole process. Thus, Ag atoms can diffuse into the HMO tunnels to form a Ag atom chain inside, which exposed the end atoms on the surfaces to achieve SAC (Figure 2-11e).[66,149] This Ag_1-HMO catalyst possessed four strong Ag–O bonds and one Ag–Ag bond, thereby showing high thermal stability at a temperature as high as 500 °C. Even when part of Ag–O bonds were broken during reactions such as HCHO oxidation, strong Ag–Ag bond can maintain the exposed single Ag atoms to be at a steady state after high temperature annealing or chemical reactions (Figure 12c). [66]

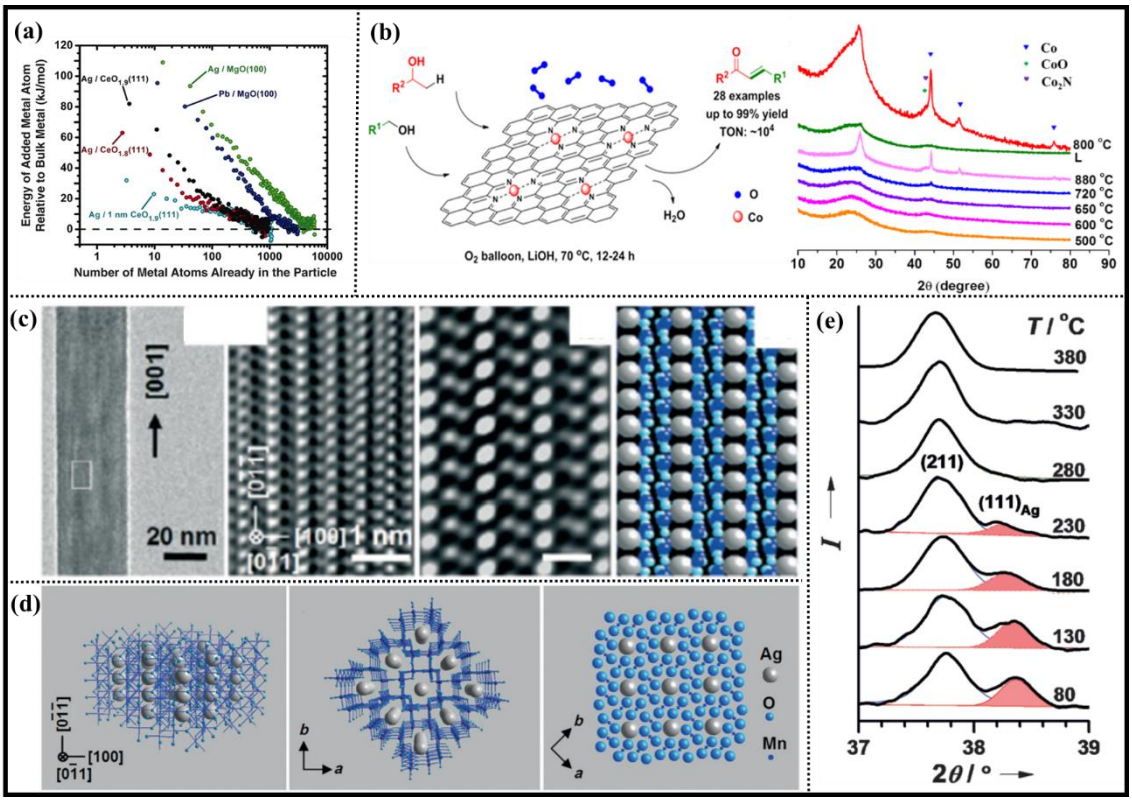

Figure 2-11. (a) Measured energy of a Ag atom, relative to its energy in bulk Ag (solid), versus the Ag particle size to which it adds, for Ag particles on the four substrates. Reproduced with permission. [141] Copyright 2010, American Association for the Advancement of Science (AAAS). (b) The proposed Co-N-C architecture toward the target reactions and stability of this catalyst paralysed at different temperatures and acid leaching. Reproduced with permission. [147] Copyright 2015, American Chemical Society. (c) TEM image and HRTEM images of a Ag-HMO nanorod with a [001] growth direction with Auto-correlation function analysis showing a corresponding simulated image; (d) Single-atom Ag chains inside the tunnels of the HMO viewed from the [011] and [001] directions, respectively, and atom arrangement on the (001) facet of Ag-HMO; (e) in situ XRD patterns of the formation of Ag-HMO at different temperature. Reproduced with permission.[66] Copyright 2012, Wiley-VCH.

2.3.3 Selectivity

Selectivity becomes crucial when molecules present two or more reacting groups and only one of them has to be transformed. Thus, a selective catalyst has to "recognize" and preferentially interact with the desired chemical group, while avoiding the transformation of the others. Single atoms feature with the uniformly dispersed, strongly anchored, and typically electron-deficient nature, which determine the regulable selectivity via changing the mode and strength of the reactant, intermediate and/or product adsorption or by changing the reaction pathway.

The tuning of SACs has been to the benefit of many reactions, especially selective hydrogenation. The frequently used catalysts hydrogenations are noble metals. Facile

dissociation of reactants and week binding of intermediates are key requirements for efficient and selective catalysis. Unfortunately, the highly active noble metals are not chemoselective, which is usually addressed by utilizing stoichiometric reducing agents, realizing high chemoselectivity in the expense of lowering catalytic activity. The heterogeneous catalysts with high chemoselecitivity and activity are highly desired. Based on the uniform geometry of single atoms and their good capability for H_2 dissociation,[85] Zhang's group reported novel FeO_x supported Pt single-atom and pseudo-single-atom structure as highly active and chemoselective catalyst on hydrogenation of functionalized nitroarenes. The strong metal-support interaction leads to significant electron transfer from the Pt atoms or ensembles to the FeO_x support. The presence of positively charged Pt centers, the absence of Pt-Pt metallic bonding and the reduced metal oxide surfaces are synetically favourable to the absorption of nitro groups, which determines significantly improved performance.[49] The selectivity of a nitro group into an amino group has been investigated by catalysing with various heterogeneous single atoms. The Pt_1/FeO_x shows outstanding activity and chemoselectivity with low Pt_1 loading ratio (0.08 wt.%),[60] giving rise to a TOF of ~1500 h^{-1} and 99% selectivity to 3-aminostyrene from 3-nitrostyrene. The high chemoselectivity is due to the partially anionic O atoms of the $–NO_2$ group can strongly binds with the isolated cationic Pt centers. This favourable phenomenon is more effective when introducing alkali metal cations to Pt_1/FeO_x with high Pt loadings, leading to >20-fold mass activity with similarly high TOF values and chemoselectivities.[150] It should be pointed out that the support plays a critical role in tuning selectivity for hydrogenation of nitroarenes. On the other hand, Pd_1 exhibited high activity and selectivity for the selective hydrogenation of C≡C bonds, C=C bonds,

and other unsaturated systems.[76,80,85,87,88,151,152] Interestingly, no matter what supports are, the Pd_1 without the Pd-Pd bonding always show superior performance, which is due to the multinuclear sites could strongly bind ethylene and promote the further hydrogenation to ethane. The product selectivity of hydrogenation of CO_2 is very sensitive to the size the active sites. The single atoms can easily release CO with relatively few H atoms present to further reduce CO; while NPs surface with many H atoms is favourable to the formation of CH_4. Despite of the size effect, the strong metal-support interaction (SMSI) could tune the chemical state of single atoms and thus have significant impact on the reaction selectivity. For instance, Kwark *et al.* demonstrated fundamentally different activity and selectivity via comparing Pd_1 and traditional 3D Pd cluster on different supports for the reaction of CO_2 reduction. **(**Figure 2-12a). For instance, Pd_1,[117] Ru_1,[153] and Rh_1[154] are highly selective for the pathway of CO formation as part of the reverse WGS reaction. In contrast, the corresponding particles tend to induce CH_4 as the major product due to the size effect .This support effect can be emphasized by Yang *et al*. via anchoring single-atom Pt catalyst on two different supports of titanium carbide and titanium nitride toward ORR reaction (Figure 2-12b). Experimentally, they and co-workers synthesized two platforms: TiC and TiN to anchor Pt single atoms, showing there were big difference in catalytic activity, selectivity and stability. The oxygen reduction current density of Pt_1/TiC was almost two times larger than that of Pt_1/TiN at all potential ranges. Also, the Pt_1/TiC catalyst showed higher activity and higher selectivity toward H_2O_2 than Pt_1/TiN. However, unlike the single-atom catalysts, Pt particles on TiC and TiN demonstrated a similar performance of ORR activity and selectivity toward H_2O_2, indicating that support effect had essential role on their unique catalytic ability and

selectivity. The DFT calculation was performed in this work to further explain the reason how the atomic dispersed active sites synergistically affect the ORR chemistry combining with support. Pt_1/TiN facilitate the dissociation of OOH* to O and OH rather than to the molecularly intact state, indicating the oxygen-oxygen bond would be dissociated more easily on Pt_1/TiN than on Pt_1/TiC. The energy profile shown that Pt/TiN (100) requires two successive energy uphill steps (0.52 and 0.94 eV) to produce H_2O_2, opposite to the case for Pt/TiC (100) at the same reaction coordinates. The adsorption energies of oxygen species on TiC and TiN predicted that there is less formation of H_2O_2 on than that on Pt/TiC, resulting in differences on activity and selectivity. The obtained Pt_1/TiC showed higher activity, stability, and selectivity for electrochemical oxygen reduction to H_2O_2 production than Pt_1/TiN. DFT calculations indicated that oxygen species preserved as oxygen–oxygen bonds on the Pt_1/TiC catalyst, which leads to high selectivity toward H_2O_2 production. In contrast, Pt_1/TiN have strong affinity into oxygen species, possibly resulting in surface poisoning species. The work clearly confirms that the supports in SACs could actively participate in the surface reaction but not just provide anchoring sites for single atoms.[73] DFT calculations found that the catalytic activity of TiC is expected to be active and selective for CO_2 reduction to CH_4, while TiN is limited for this process due to strong oxygen affinity.[104]

Similarly, single atom catalysts are also conclusive to the electrochemical reduction of CO_2 over the HER due to the stronger surface absorption for CO_2 reduction intermediates than that of H atoms and being cationic of the active metal atoms.[30,115,155-158] In particular, Ni_1-N-C catalysts are highly selective for the $2H^+/2e^-$ electro-reduction of CO_2 to CO with high Faradaic efficiency (> 90%). [30,158] Figure

2-12c showed that the single-atom A-Ni-NSG (single nickel atoms dispersed on nitrogenated graphene with a sulphur precursor) electrode exhibits a maximum Faradaic efficiency (CO) of about 97% at around−0.5 V (versus RHE). Further reduction of CO to methane is completely suppressed because of the weak binding of CO to the single Ni atom site. Notably, the two single-Ni-atom catalysts maintain greater than 80% selectivity towards CO formation, even at very negative applied potentials, and this selectivity is almost independent of the proton concentration.[158] Fe_1-N-C catalysts are active and selective toward the formation of CH_3CO_2H with selectivity of 61% and Faradaic efficiency of 97.4% (Figure 2-12d) at very low potential.[159] The selectivity of ORR reactions could be deliberately tuned from a $4e^-$ ($4H^+ + 4e^- + O_2 \rightarrow 2H_2O$) to a $2e^-$ ($2H^+ + 2e^- + O_2 \rightarrow H_2O_2$) pathway via taking advantage of single atoms. For instance, Pt_1-TiN,[72] Pt_1-Hg,[160] and Pd_1-Hg-C[161] exhibit high selectivity of H_2O_2, which is due to the absence of metal-metal bonding. Thus, these SACs do not possess the reducing equivalents to reduce O_2 to H_2O, which generally requires at least two adjacent active metal sites. Also, Gu et al. has proposed that the interaction between Pt1/Au1 atoms and Zn (10-01) nanofacets leads to positively charged Pt1 and Au1 atoms, which could facilitate the adsorption of reaction intermediates during MSR and thus modify the reaction pathways.[64]

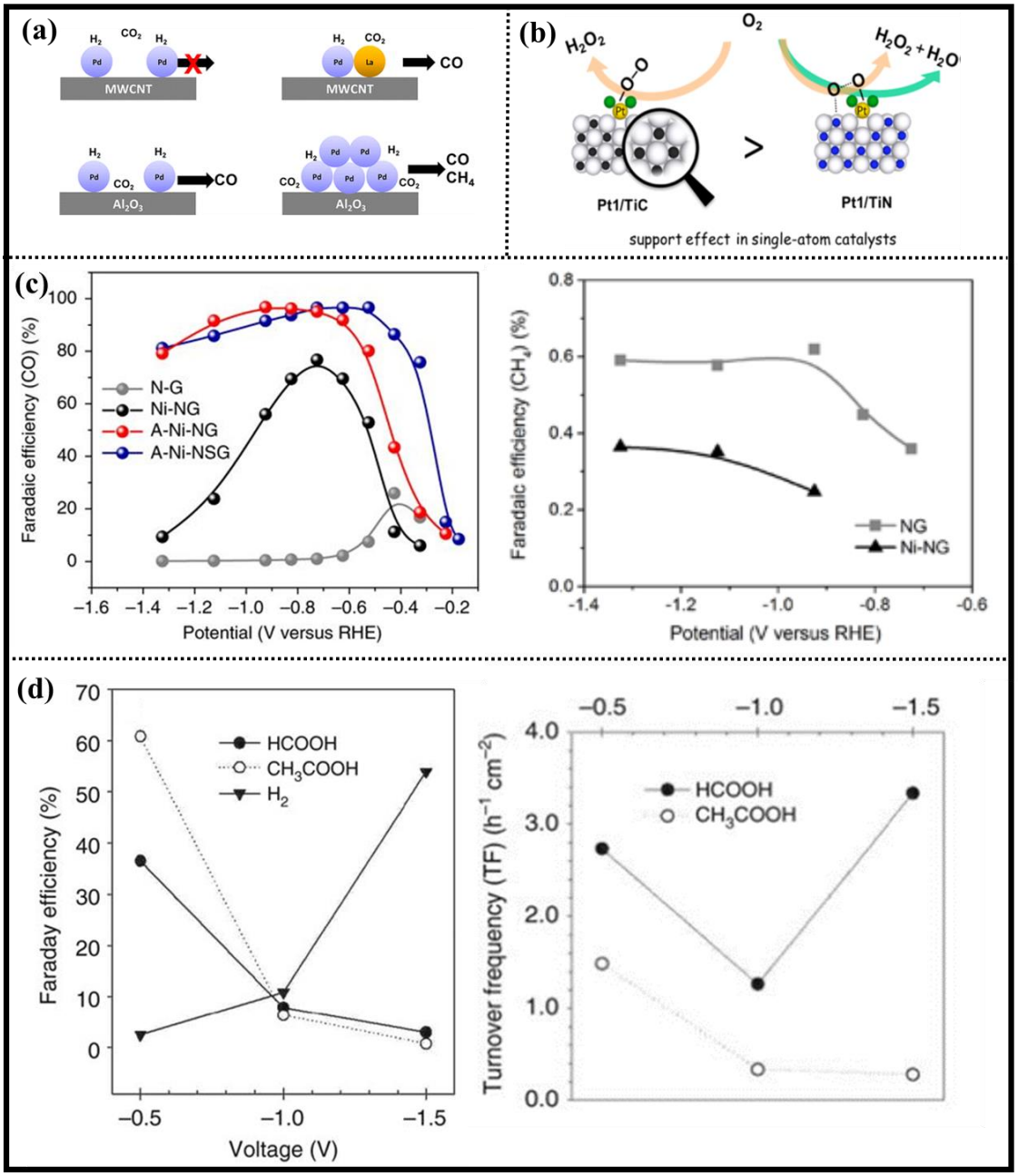

Figure 2-12. (a) Schematic illustration of the reduction of CO_2 with H_2 on Pd/Al_2O_3 and Pd/MWCNT catalysts. Reproduced with permission.[117] Copyright 2013, American Chemical Society. (b) Support effect for selectivity of ORR reaction with Pt_1 catalysts. Reproduced with permission.[73] Copyright 2016, American Chemical Society. (c) CO Faradaic efficiency at various applied potentials with different catalysts for CO_2 reduction in aqueous solution. Reproduced with permission.[158]

Copyright 2018, Nature Publishing Group. (d) Faraday efficiency (%) to the products of CO_2 reduction under applied voltage of -0.5, -1, and -1.5 V vs Ag/AgCl (3M KCl) for Fe_1-N-C sample and corresponding turnover frequency (h^{-1} cm^{-2}). Reproduced with permission.[159] Copyright 2018, Nature Publishing Group.

2.4. Conclusions

SACs have gained increasing interest due to very different catalytic behaviours from that of nanoparticles and bulk counterparts. In this review, the support effect has been emphasized both on SACs fabrication and catalytic behaviours. A variety of supports have been explored, on which diverse single metal sites can be successfully anchored on these substrates without agglomeration. For instance, the metal oxides, such as ZnO, MgO, [91] Fe_2O_3, Al_2O_3, and TiO_2, can modify with lone electron pairs oxygen defects, such as oxygen vacancies, the ethylene glycolate and hydroxyl groups, to define metal species. The coordination between supports and metal species leads to strong interaction, inhibiting the aggregating of anchored metal sites. Thus, various ingenious designs have been developed *via* creation of defects, introducing organic ligands, and their inert surface structure of materials, the favour facets as well. Similarly, carbon-vacancy, sulphur-vacancy, and the nitrogen-vacancy in supports, such as graphene, MoS_2 and TiN, were also found to show strong interactions with metal ions forming single atom sites. Also, the nitrogen-doped carbon is the most commonly used carbon based supports to stabilize single atoms. Fortunately, these nitrogen doped carbon supports have a plenty of carbonaceous sources, meaning that the metal species can be coordinated via many ways, such as nitrogen sources-sintering carbon, graphitic carbon nitride, metal organic frameworks. The nitrogen sources-sintering carbon, such as NH_3, has been considering that the formed pyridinic (P)-N has the strong anchoring

sites for single metal atoms due to the modified interfacial interaction. This suggests that the metal atoms can be selectively trapped strongly by C-N site and thus stabilize the dispersion of single atoms on carbon surface, confirming the vital role of support properties on the formation of single atoms. The pyrolysis process of the nitrogen contained organic structure can strongly stabilize varieties of metal species, forming metal-N_x-C structure. Compared with carbon-based supports, the formation of single atoms on metal-based surface exhibits different geometric and electronic structures, that is, only a trace amount of heterogeneous metal species can be doped to form bimetallic catalysts.

On the other hand, the support surface through strong metal-support interactions leads to the polarization of these heteroatomic bonds and substantial charge transfer from the active metal to the support. These electron-deficient single metal sites are responsible for distinctive catalytic properties. It has been clear that the coordination environments, quantum size effect, and the strong electronic interaction between the SACs and the supports were building the bridge to probe more advanced functional catalysts in atomic level. The supports were definitely playing an essential role to determine those key catalytic characters and showing how to rationally design an efficient support-SACs structure to enhance the activity and selectivity in each special reaction. For instance, oxygen surface chemistry remains a key challenge for the design of a number of important future electrochemical conversion and storage devices, such as fuel cells, Li-air batteries, or electrolysers. It has been proved that single atom dopants are the underlying causes for activity enhancements on oxygen reduction reaction and oxygen evolution reaction (ORR and OER), owing to their electronic metal-support interaction. The unique electronic structure of different elements,

however, needs suitable coordination atoms to conduct their activity and reduce the energy barriers.

Chapter 3

3. Experimental Procedure

3.1. Overview

The general procedure of this thesis work is demonstrated in Figure 3.1. Generally, the aiming elements were uniformly dispersed on support precursor, these elements were followed by reducing in high temperature, forming single-atom based materials. The structural properties of the as-prepared samples were characterized by a series of techniques, such as XRD, Raman spectroscopy, SEM, XPS, FT-IR, AFM, TEM and DFT. Their electrochemical catalytic performances were evaluated by measuring the ORR, EOR, and water splitting.

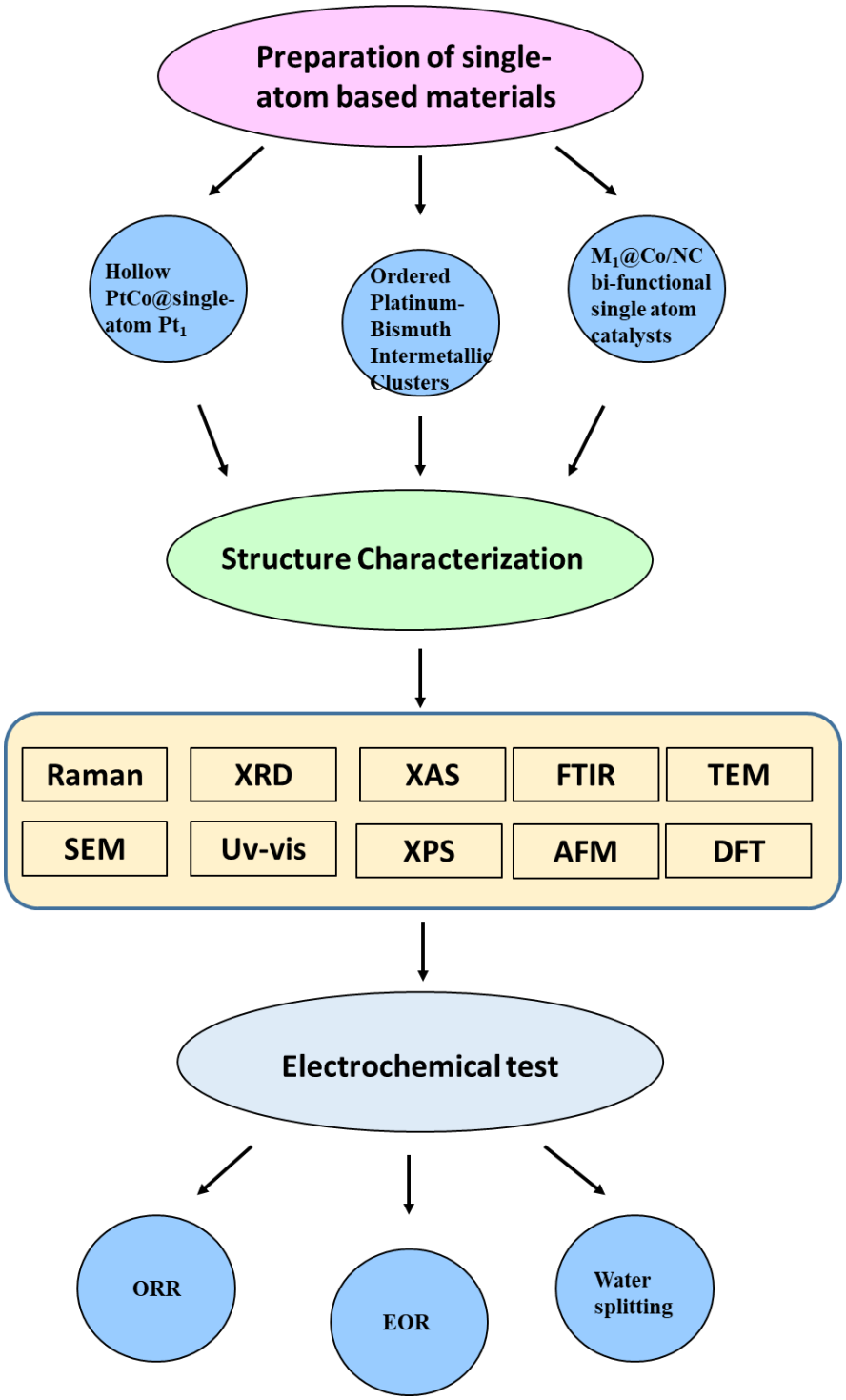

Figure 3-1. The general procedure of this thesis project.

3.2. Chemicals and Materials

The chemicals and materials used in this thesis are listed in Table 3.1.

Table 3-1. Chemicals and materials used in this thesis.

Chemicals	Formula	Purity (%)	Supplier
Ethanol	C_2H_5OH	100	Chem-Supply Pty. Ltd.
Ethanol	C_2H_5OH	96	Chem-Supply Pty. Ltd.
Cobalt(II) nitrate hexahydrate	$Co(NO_3)_2 \cdot 6H_2O$	>98	Sigma-Aldrich
Potassium tetrachloroplatinate(II)	K_2PtCl_4	>98	Sigma-Aldrich
2-methylimidazole	$C_4H_6N_2$	>99	Sigma-Aldrich
Nafion@117		5 % in H_2O	Sigma-Aldrich
Potassium hydroxide	KOH	>90	Sigma-Aldrich
Zinc nitrate hexahydrate	$Zn(NO_3)_2 \cdot 6H_2O$	99	Sigma-Aldrich
Platinum(II) acetylacetonate	$C_{10}H_{14}O_4Pt$	99	Sigma-Aldrich
Iridium(II) acetylacetonate	$C_{10}H_{14}O_4Ir$	99	Sigma-Aldrich
Palladium(II) acetylacetonate	$C_{10}H_{14}O_4Pd$	99	Sigma-Aldrich
Ruthenium (III) acetylacetonate	$C_{15}H_{21}O_6Ru$	97	Sigma-Aldrich
Iron(III) acetylacetonate	$Fe(C_5H_7O_2)_3$	99	Sigma-Aldrich

Nickel (II) acetylacetonate	$C_{10}H_{14}O_4Ni$	99	Sigma-Aldrich
Bismuth(III) nitrate pentahydrate	$Bi(NO_3)_3 \cdot 5H_2O$	98	Aldrich
Chloroplatinic acid	H_2PtCl_6	8 wt. % in H_2O	Sigma-Aldrich
Methanol	CH_3OH	>99.9%	Sigma-Aldrich

3.3. Materials Preparation

The methods used to prepare materials in this thesis mainly are carbonization method.

3.3.1. Carbonization Method

ZIF-67 were used as carbonization precursor to prepare single atom materials in the first and third work. In a typical synthesis, 2-methylimidazole (1.97 g) was dissolved in a mixed solution of 30 ml methanol and 10 ml ethanol. $Co(NO_3)_2 \cdot 6H_2O$ (1.746 g) was dissolved in another mixed solution of 30 ml methanol and 10 ml ethanol. 0.125 mmol K_2PtCl_4 was dissolved in 2.56 ml deionized water. The above three solutions were then mixed under continuous stirring for 30 mins, and the final solution was kept for 20 h at room temperature. The purple precipitate was collected by centrifugation, washed in ethanol several times, and dried at 80 °C. Finally, the purple precipitate was then annealed at 600 °C under 5% hydrogen/argon for 3 h. This resultant product was denoted as Co@PtCo@Co@Pt_1N-C. The Co@PtCo@Co@Pt_1N-C which was immersed in a certain concentration of hydrochloric acid solution (37 wt %) to remove the cobalt oxide. The final product was then formed, denoted as H-PtCo@Pt_1N-C.

Also, for preparing single atom on heterogeneous support (Co and carbon), 100 mg ZIF-67 powders mixed with 50 ml ethanol by ultra-sonification for 30 mins to form a homogeneous dispersion. 0.0075 mmol platinum (II) acetylacetonate, iridium (II) acetylacetonate, palladium acetylacetonate, ruthenium (III) acetylacetonate, nickel (II) acetylacetonate, and iron (III) acetylacetonate were then added into the dispersion with rigorously stirring until ethanol were evaporated out, forming ZIF-67-Pt/Ir/Pd/Ru/Fe/Ni mixtures respectively. Finally, the mixture was annealed at 600 °C (Pt/Ir/Pd/Ru)/700 °C (Fe/Ni) under argon for 2 h. These resultant products were denoted as $(Pt/Ir/Pd/Ru/Fe/Ni)_1$@Co/CN.

Similarly, for the preparation of single-atom Pt mixed with PtBi catalyst (PtBi/SA Pt), the H_2PtCl_6 and $Bi(NO_3)_3 \cdot 5H_2O$ precursors, containing 0.68 mL of 0.039 M H_2PtCl_6 ethanol solution and 0.88 mL of 0.01 M $Bi(NO_3)_3 \cdot 5H_2O$ ethanol solution, respectively, were mixed, and 0.02 g of GO was dispersed in the mixture. The mixture, containing GO, Pt and Bi precursors, were ultrasonicated until ethanol was evaporated; then the mixture was heated 12 h in an oven at 80 °C. Then, the precursors were first reduced at 600 °C in 5 vol % H_2 in nitrogen for 12 h, denoted as PtBi/SA Pt. When further reduced at 600 °C in 5 vol % H_2 in nitrogen for another 12 h, novel monatomic Pt layer on ordered PtBi intermetallic clusters (PtBi@Pt) was formed.

3.4. Characterization Techniques

3.4.1. XRD

XRD is a general and rapid analytical technique primarily used to identify the composition and crystal structures of the materials via analyzing the diffraction

patterns. The analyzed sample needs to be finely grounded and uniformly mixed before testing.

X-rays are a kind of light radiation which is induced by the atomic inner electrons under the bombardment of the high-speed electrons. Typically, the crystals can be used as gratings for the X-rays since the wavelengths of the X-rays are comparable with the interplanar spacings of the crystals. When the X-rays arrive at the lattice planes of the crystal materials, interference will occur if the Bragg's law ($2d\sin\theta = n\lambda$) is satisfied. Here, d refers to the lattice spacing, θ represents the angle between the incidence X-ray and the lattice plane, n is any integer, and λ is the wavelength of the incident X-ray. In this doctoral work, the composition and the crystal structures of the as-prepared powders were characterized by a GBC MMA X-ray diffractometer (Scientific Equipment LLC, Hampshire, IL, USA) in UOW. The radiation used in the XRD measurement was Cu-Kα1 (40 kV, 25 mA, λ=0.15418 nm).

3.4.2. Raman Spectroscopy

Raman spectroscopy is a kind of spectroscopic techniques which can be used to investigate the molecular vibration, rotation and a series of other low-frequency modes of a material. Raman scattering is a type of the inelastic scattering, and the typical laser light used in the Raman scattering could be visible light, near-infrared light or the near-ultraviolet light. The energy of the laser photons will be shifted down and up when the laser light interacts with the system phonons. The information on the phonon modes, which reflect the symmetry of molecules and chemical bonds, can be obtained by the energy shift. In this work, the mapping mode (one spectrum per 250 seconds) was adopted to capture the Raman spectra (Lab RAM HR, Horiba Jobin Yvon SAS) of the

samples one by one.

3.4.3. SEM

The SEM is a type of electron microscope. It can create images for the surfaces of the materials by scanning the surfaces with a focused electron beam. The information on the surface morphology and composition of the materials can be produced via the interaction between the electrons and the atoms in the materials. Generally, the electron beam scans in a raster scan pattern, and the images are generated by combining the beam's position with the detected signal. In this work, the morphology of the as-prepared samples was detected by a field emission scanning electron microscope (JSM-7500FA, JEOL, Tokyo, Japan) in UOW.

3.4.4. XPS

XPS is a type of quantitative spectroscopic technique. It can be used to determine the elemental composition, experimental formula as well as the chemical and electronic states of the elements contained in the tested materials. XPS spectra are collected by irradiating a sample with X-rays while simultaneously measuring the kinetic energy and amount of escaped electrons with the depth in the range from 1 nm to 10 nm ejected from surface of the tested samples. In this work, XPS was conducted at the Photoelectron Spectroscopy Station (Beamline 4W9B, Tsinghua University) with the resolution of 0.05 eV. All the XPS data were analyzed using the commercial CasaXPS 2.3.15 software package. Before analysis, the spectra were calibrated by C 1s = 284.8 eV.

3.4.5. FT-IR

FT-IR is a spectroscopic technique which can be used to analyze the molecular structures and chemical compositions via detecting the materials' characteristic absorption of infrared radiation with different wavelengths. For the molecules, especially the organic molecules, the atoms that make up the chemical bonds or functional groups are in the state of constant vibration. As the frequency of the vibration is comparable to the frequency of the infrared vibration, vibration absorption can be occurred for the chemical bonds or functional groups in the molecules when the molecules are irradiated by the infrared light. Different chemical bonds or functional groups present different absorption frequencies which are located at different position in the FT-IR spectrum, hence, information on the chemical bonds or functional groups in the molecules can be obtained. In this work, the FT-IR spectrum was characterized by using a Shimadzu FTIR Prestige-21 in UOW with the range from 4000 cm^{-1} to 500 cm^{-1}.

3.4.6. AFM

AFM is a very high resolution type of scanning probe microscopy, with demonstrated resolution on the order of fractions of a nanometer. The information is gathered by touching the surface with a sharp tip. It has three major abilities: force measurement, imaging, and manipulation. Herein, in this work, an atomic force microscope (MPF-3D, Asylum Research, Santa Barbara, USA) was utilized to generate topographic images and evaluate the thickness of the atomically thin transition metal oxide nanosheets.

3.4.7. TEM and STEM

TEM is a microscopy technique in which the beam of accelerated and focused electrons is transmitted through a sufficiently thin specimen to form an image. TEM can be employed to investigate the morphology, crystal structure, and electronic structure of a specimen. SAED is a crystallographic experimental technique that can be used inside the TEM. As a diffraction technique, SAED can be employed to examine crystal defects and crystal structures. SAED is distinguished from conventional TEM in that the electron beam is focused on a size-limited spot which scans over the sample in a raster pattern. The rastering of the beam across the sample makes it available for various analysis techniques such as mapping by EDS, EELS, and HAADF imaging. These signals can be obtained simultaneously, allowing direct correlation of the image and quantitative data. In this doctoral work, the TEM observations of the samples were carried out using a JEM-2011F (JEOL, Tokyo, Japan) and a probe-corrected JEOL ARM200F (equipped with a cold field emission gun, a high resolution pole-piece, and a Centurio EDS detector) at 80 kV for upconversion nanoparticles and 200 kV for other samples in UOW.

3.4.8. DFT

Density functional theory is a quantum mechanical modelling method used in the investigation of the electronic structures for the multiple electronic systems. It has wide application in physics and chemistry, especially in investigating the properties of the molecules and condensed matt. The objective of the DFT method is the electronic density instead of the wavefunctions, hence, it is more convenient than the classic modelling method like the Hartree-Fock. The common application of DFT is achieved

via Kohn-Sham method. In the frame of Kohn-Sham DFT, the complicated many-body system is simplified to a system in which the electron with no interaction with others moves in the effective potential field. The effective potential field includes the external potential field and the influence of Coulomb interactions between electrons. DFT is the most versatile and popular computational method in condensed matt, computational physics and computational chemistry.

3.4.9. XAS

X-ray absorption spectroscopy (XAS) is a widely used technique for determining the local geometric and/or electronic structure of matter. The experiment is usually performed at synchrotron radiation facilities, which provide intense and tunable X-ray beams. Samples can be in the gas-phase, solution, or as solids. The X-ray Absorption Near-Edge Structure XANES introduced in 1980 and later in 1983 called also NEXAFS (Near-edge X-ray Absorption Fine Structure) which are dominated by core transitions to quasi bound states (multiple scattering resonances) for photoelectrons with kinetic energy in the range from 10 to 150 eV above the chemical potential, called "shape resonances" in molecular spectra since they are due to final states of short life-time degenerate with the continuum with the Fano line-shape. In the high kinetic energy range of the photoelectron the scattering cross-section with neighbor atoms is weak and the absorption spectra are dominated by EXAFS (Extended X-ray Absorption Fine Structure) where the scattering of the ejected photoelectron of neighboring atoms can be approximated by single scattering events. In this work, X-ray absorption spectroscopy (XAS) experiments were carried out at the applied X-ray absorption fine structure spectroscopy (XAFS) beamline P65 at the PETRA III (Deutsches Elektronen-Synchrotron, DESY, Hamburg). The storage rings of PETRA

III were operated at the electron energy of 6 GeV with a beam current of 100 mA. XAS spectra were recorded in quick-XAFS (QXAFS) method in transmission mode using an ionization chamber of Pt foil. The intensity of the monochromatic X-ray beam was monitored respectively by three consecutive ionization detectors. All the XAS spectra were processed using DEMETER software package. The data was normalized and analyzed via using Athena and Artemis software.

3.5. Electrochemical Measurements

3.5.1. Linear Sweep Voltammetry (LSV)

LSV is a commonly used method to detect catalytic activity towards the OER/ORR/HER, which is performed on a rotating ring-disk electrode (RRDE). LSV is a voltammetric method where the potential between the working electrode and a reference electrode is swept linearly in time, and the current at the working electrode is recorded simultaneously. Oxidation or reduction of the species is registered as a peak at the potential where the species begins to be oxidized or reduced.

3.5.2. Cyclic Voltammetry (CV)

CV is a commonly used technique to study the redox reactions in a catalysis (EOR) or battery system, through which the following can be determined: the intermediates participating in the redox reaction, the stability of the reaction products, the electron stoichiometry, the electron transfer kinetics, and the reversibility of a reaction. CV curves usually display a hysteresis in the absolute potential between the anodic and cathodic peaks due to the polarization that is caused by a slow diffusion rate and the

intrinsic activation barrier obstructing the electron transfer between the electrodes. In a typical CV measurement, the potential of the cell is scanned at a specified rate with the response current collected. Herein in this work, the CV data were recorded on a Biologic VPM3 electrochemical workstation in UOW.

3.5.3. Li-O_2 Battery Measurements

The electrochemical performances of lithium oxygen batteries were investigated using 2032 coin-type cells with air holes on the cathode side. For the preparation of the H-PtCo@Pt_1N-C cathode electrode, 90 wt % catalyst and 10 wt % poly(1,1,2,2-tetrafluoroethylene) (PTFE) were mixed in an isopropanol solution. The resulting homogeneous slurry was coated on carbon paper. After that, the electrodes were dried at 120 ºC in a vacuum oven for 12 h. All the Li-O_2 batteries were assembled in an Ar-filled glove box (Mbraun, Unilab, Germany) with water and oxygen contents below 0.1 ppm. They contained lithium metal foil as the counter electrode and a glass fiber separator (Whatman GF/D). One electrolyte consisted of 1 M $LiCF_3SO_3$ in tetraethylene glycol dimethyl ether (TEGDME), and the other one consisted of 0.1 M $LiClO_4$, redox mediator tetrathiafulvalene (TTF) in dimethylsulfoxide (DMSO). All the assembled coin cells were stored in an O_2 purged chamber which was connected to a LAND CT 2001 instrument. The galvanostatic discharge-charge tests were then conducted on the battery testing system with the specific capacity of 200 mAh g^{-1}, and the capacity was calculated based on the mass of active materials in the cathode.

Chapter 4

4. The Quasi-Pt-allotrope catalyst: Hollow PtCo@single-atom Pt_1 on nitrogen doped carbon towards superior oxygen reduction

4.1. Introduction

Electrocatalysis plays a pivotal role in electrochemical energy conversion and storage technologies, including water electrolysers, metal-air batteries, and proton-exchange membrane fuel cells[162]. The exploration of low-cost and high-performance electrocatalysts is playing the most essential and imperative role in the development of fuel cells. Platinum-based bimetallic nanomaterials have been considered as efficient catalysts for the oxygen reduction reaction (ORR)[162d, 163]. In contrast to monometallic Pt catalysts, the Pt_3Ni (111) surface has a much lower overpotential and is 10-fold more active toward the ORR than the Pt (111)[164]; similarly, Pt_3Co[165], PtCu[166], and PtFe[167] have shown enhanced ORR performance compared to commercial Pt/C. Researchers are struggling to boost the ORR activity by optimizing the nanostructures of PtM alloys, where M is a metal, such as by decreasing particle sizes[168] or dealloying PtM to expose increased active sites[169], as the electrocatalytic reactions only take place on the catalyst surface[170]. Unfortunately, even though they have favorable structures, high activity Pt-based catalyst materials are easily degraded and are extremely vulnerable to agglomeration during annealing and cycling tests,

leading to the rapid failure of their catalytic performance[171]. For example, Mallika et al.[172] pointed out a common trend: although Pt_3Co nanoparticles with a smaller size initially show higher ORR performance than these with a larger size, the smaller nanoparticles are more unstable against agglomeration compared to the larger particles and will lead to more rapid activity decay during cycling. On the other hand, combinations of noble metals such as Pd@Pt are formed into core@shell structures to increase the ORR efficiency and simultaneously maintain the stability of their nanostructure over time,[173] but this greatly increases the expense, and there is still a significant drop from their initial ORR performance. It is still a huge challenge to fabricate efficient and stable nanostructures for the next-generation electrocatalysts.

Carbon, as one of the most widely used frameworks in composites, is essential to increase the conductivity and stabilize the nanoarchitectures of samples, such as metal organic frameworks[174]. Significantly, it has been reported that the carbon-based core@shell structure, such as FeS@C[175], and Si@C[176], can very effectively protect these highly active materials from agglomeration and collapse, leading to optimized electrochemical performance over prolonged cycling. Also, the modification of the carbon, with different dopants, is a general strategy to improve the ORR performance of the carbon. Recently, single-atom Pt, as a new frontier of functional materials, has been received intensive attention in ORR advancement due to its superior size effect[177]. The synergistic effect between single atom and carbon can accelerate the sluggish ORR kinetics, so that this combination is being recognized as one of the most promising strategies in the design of the potential affordable catalysts. The calculated overpotential of single atom Pt-N/C (1.74 V), however, is still higher than that of Pt (111), which is generally 0.69-1.69 V. Thus, from the fundamental perspective, it is

rational to construct a stable nanostructure by virtue from low overpotential bimetallic PtM alloy, protective carbon, and single atom dopants, achieving a high active composite towards superior ORR performance.

Herein, we demonstrate the synthesis of a quasi-Pt-allotrope: Pt_3Co nanospheres with an internal hollow structure (H-PtCo), which, in turn, are surrounded by an N-doped carbon shell with single-atom Pt anchored to it (Pt_1N-C). The intermetallic H-PtCo with its internal cavities and uneven surface can expose abundant active sites and efficiently achieve high ORR activity. The Pt_1N-C is critical, because it not only can provide accessible tunnels for electrolyte penetration and fast electron diffusion, but also stabilizes the hollow structure in the center and protects these highly-active fine nanoparticles from agglomeration. *In-situ* synthesis of the multifunctional C shell and the creation of internal cavities for ultra-refined Pt-based nanoparticles are difficult and have only now been realized. When tested in 0.1 M $HClO_4$ solution, the mass activity of H-PtCo@Pt_1N-C is 1.2 mA μg_{Pt}^{-1} at 0.9 V vs. reversible hydrogen electrode (RHE), which is one of the most remarkable ORR performance among all reported Pt-Co/C systems. After 10000 cycles, the mass activity of H-PtCo@Pt_1N-C at 0.9 V remains 1.26 mA μg_{Pt}^{-1} without any fade. These results indicate that H-PtCo@Pt_1N-C can boost the ORR activity with greatly enhanced durability. More importantly, the single atoms Pt in shells forming Pt-NC_3 is confirmed that they are favorable to prompt ORR performance via the DFT calculation. Also, when tested in tetraethylene glycol dimethyl ether (TEGDME) and dimethylsulfoxide (DMSO)-based organic electrolytes, the discharge overpotential of H-PtCo@Pt_1N-C was only 0.05 V, indicating that this sample has an efficient ORR capability in organic electrolytes as well. Furthermore, this synthesis method sheds light on a plausible strategy for various ultra-refined

bimetallic catalysts; the superior ORR performance of H-PtCo@Pt_1N-C holds great promise for its practical applications in next-generation proton exchange membrane fuel cells and lithium-air batteries.

4.2. Experimental Section

4.2.1. Materials

Potassium tetrachloroplatinate(II) (K_2PtCl_4, 98%), Cobalt(II) nitrate hexahydrate ($Co(NO_3)_2$ $6H_2O$, ACS reagent grade, ≥ 98%), 2-methylimidazole ($C_4H_6N_2$, 99%), Nafion@117 solution (5 wt %, dispersed in a binary solvent of water and lower aliphatic alcohols), potassium hydroxide (KOH, reagent grade, 90%), and commercial Pt black (20 wt. % Pt loading on Vulcan XC72) were purchased from Sigma-Aldrich. All the chemical reagents were used as received without any further purification.

4.2.2. Materials Preparation

4.2.2.1. Synthesis of H-PtCo@Pt_1N-C

In a typical synthesis, 2-methylimidazole (1.97 g) was dissolved in a mixed solution of 30 ml methanol and 10 ml ethanol. $Co(NO_3)_2 \cdot 6H_2O$ (1.746 g) was dissolved in another mixed solution of 30 ml methanol and 10 ml ethanol. 0.125 mmol K_2PtCl_4 was dissolved in 2.56 ml deionized water. The above three solutions were then mixed under continuous stirring for 30 mins, and the final solution was kept for 20 h at room temperature. The purple precipitate was collected by centrifugation, washed in ethanol several times, and dried at 80 °C. Finally, the purple precipitate was then annealed at 600 °C under 5% hydrogen/argon for 3 h. This resultant product was denoted as Co@PtCo@Co@Pt_1N-C. The Co@PtCo@Co@Pt_1N-C which was immersed in a

certain concentration of hydrochloric acid solution (37 wt %) to remove the cobalt oxide. The final product was then formed, denoted as H-PtCo@Pt_1N-C.

4.2.2.2. Synthesis of Pt1N-C.

In a typical synthesis, 2.5 mg H_2PtCl4 was mixed with 50 mg ZIF-8 forming mixture. Then, the mixture was dried up via stirring and sintered at 900 °C for 3 hours in argon.

4.2.2.3. Synthesis of nitrogen doped carbon (NPC).

Zinc acetate, oleic acid, and benzimidazole were used as the ZnO template, the carbon source, and the nitrogen source, respectively. 0.2 g and 0.8 g benzimidazole were respectively ground with 2 g oleic acid and 2 g anhydrous zinc acetate to obtain uniform mixtures, and the mixtures were annealed at a ramp rate of 3 °C min^{-1} under flowing argon gas as the temperature was increased from room temperature to 700°C, at which they were held for 2 h. The resulting products were immersed in a certain concentration of hydrochloric acid solution (37 wt %) to remove the resultant zinc oxide, and they were then dried in an oven at 80 °C, after the pH was adjusted to neutral with distilled water, to yield nitrogen-doped porous carbon (NPC).

4.2.2.4. Synthesis of Pt/NPC.

In a typical synthesis, 0.02 g of NPC was mixed in 0.68 mL of an aqueous solution of 0.039 M K_2PtCl_4. The mixture was ultra-sonicated until the solvents were fully evaporated. The mixture with NPC-containing K_2PtCl_4 was typically heated overnight in a blast oven at 80 °C. The precursors then solidified and shrank to form crystals. Finally, the precursors were reduced at 300 °C in forming gas (10 vol % H_2 in argon) for 3 h, and the temperature was then raised to 700 °C for 3 h. A Pt/NPC sample was collected when the product was Coled down to room temperature.

4.2.2.5. Synthesis of PtCo/NPC.

The fabrication method for PtCo/NPC was the same as that for Pt/NPC, except for the addition of $Co(NO_3)_2 \cdot 6H_2O$. 0.02 g of NPC was mixed in the precursors K_2PtCl_4 and $Co(NO_3)_2 \cdot 6H_2O$, consisting of 0.68 mL of 0.039 M K_2PtCl_4 water solution and 0.88 mL of 0.01 M $Co(NO_3)_2 \cdot 6H_2O$ ethanol solution.

4.2.3. Structural characterization.

The morphologies of the samples were investigated by field-emission scanning electron microscopy (FESEM; JEOL JSM-7500FA) and transmission electron microscopy (TEM, JEOL 2011, 200 kV). The high-angle annular dark-field scanning TEM (HAADF-STEM) images and the scanning TEM energy dispersive X-ray spectroscopy (STEM-EDS) data were acquired on the transmission electron microscopy system (TEM, JEOL ARM-200F, 200 kV). The XRD patterns were collected by powder X-ray diffraction (XRD; GBC MMA diffractometer) with Cu Kα radiation at a scan rate of $4\,^\circ\,min^{-1}$. The bonding on H-PtCo@Pt_1N-C was determined by XPS (PHOIBOS 100 Analyser from SPECS, Berlin, Germany; Al Kα X-rays).

4.2.4. Electrochemical Measurements.

Before the glassy carbon electrode (GCE) was used, it was consecutively polished with 1.0 and 0.05 μm alumina powder, rinsed with deionized water, and sonicated first in ethanol and then in water. Electrochemical experiments were carried out in 0.1 M $HClO_4$ by using a computer-controlled potentiostat (Princeton 2273 and 616, Princeton Applied Research) in a conventional three-electrode cell at room temperature. Typically, working electrodes were prepared by mixing the catalyst with deionized water + isopropanol + 5% Nafion® (v/v/v = 4/1/0.05). For all Pt-based catalysts, the Pt

loading on the rotating disk electrode (RDE) was calculated as 10.1 μg_{Pt} cm^{-2}. A Pt wire was used as the counter electrode and Ag/AgCl (KCl, 3M) was used as the reference electrode, with all potentials referred to reversible hydrogen electrode (RHE). Thus, the potential with respect to RHE can be calculated as follows: E(RHE) = E(Ag/AgCl) + 0.059 × pH + 0.210. Before testing, flowing N_2/O_2 was bubbled through the electrolyte in the cell to achieve an N_2/O_2-saturated solution. The cyclic voltammetry (CV) profiles were obtained in N_2- or O_2-saturated 0.1 M $HClO_4$ solution at a scan rate of 50 mV s^{-1}. The electrochemical surface area (ECSA) was determined by the integrating the hydrogen desorption charge on CVs. The oxygen reduction reaction (ORR) testing was carried out in O_2-saturated 0.1 M $HClO_4$ solution at different rotation rates with a scan rate of 10 mV s^{-1}. Accelerated durability tests were performed at room temperature in O_2-saturated 0.1 M $HClO_4$ solution by applying cyclic potential sweeps between 0.6 and 1.1 V versus RHE at a scan rate of 50 mV s^{-1} for 10000 cycles or 5000 cycles. The kinetic current (I_k) can be calculated using the Koutecky-Levich (K-L) equation, which is expressed by

$$\frac{1}{I} = \frac{1}{I_k} + \frac{1}{I_d}$$

where I is the measured current and I_d the diffusion limited current.

The K-L plot is based on the Levich equation:

$$I_d = 0.62nFAD^{2/3}\upsilon^{-1/6}\omega^{1/2}C_{O_2}$$

where n is the number of electrons transferred; F is Faraday's constant (96,485 C mol^{-1}); A is the area of the electrode (0.196 cm^2); D is the diffusion coefficient of O_2 in 0.1 M $HClO_4$ solution (1.93 × 10^{-5} $cm^2 \cdot s^{-1}$); υ is the kinematic viscosity of the electrolyte (1.01 × 10^{-2} $cm^2 \cdot s^{-1}$); ω is the angular frequency of rotation, $\omega = 2\pi f/60$, where f is

the RDE rotation rate in rpm and C_{O_2} is the concentration of molecular oxygen in 0.1 M $HClO_4$ solution (1.26×10^{-6} mol·cm^{-3}).

4.2.5. Li-O_2 Battery Measurements.

The electrochemical performances of lithium oxygen batteries were investigated using 2032 coin-type cells with air holes on the cathode side. For the preparation of the H-PtCo@Pt_1N-C cathode electrode, 90 wt % catalyst and 10 wt % poly(1,1,2,2-tetrafluoroethylene) (PTFE) were mixed in an isopropanol solution. The resulting homogeneous slurry was coated on carbon paper. After that, the electrodes were dried at 120 ºC in a vacuum oven for 12 h. All the Li-O_2 batteries were assembled in an Ar-filled glove box (Mbraun, Unilab, Germany) with water and oxygen contents below 0.1 ppm. They contained lithium metal foil as the counter electrode and a glass fiber separator (Whatman GF/D). One electrolyte consisted of 1 M $LiCF_3SO_3$ in tetraethylene glycol dimethyl ether (TEGDME), and the other one consisted of 0.1 M $LiClO_4$, redox mediator tetrathiafulvalene (TTF) in dimethylsulfoxide (DMSO). All the assembled coin cells were stored in an O_2 purged chamber which was connected to a LAND CT 2001 instrument. The galvanostatic discharge-charge tests were then conducted on the battery testing system with the specific capacity of 200 mAh g^{-1}, and the capacity was calculated based on the mass of active materials in the cathode.

4.2.6. DFT calculation.

The first-principles calculations were performed under the framework of density functional theory (DFT) calculations as implemented in the Vienna Ab initio Simulation Package (VASP)[178]. The Perdew-Burke-Ernzerhof(PBE)[179] exchange-correlation functional within the generalized gradient approximation (GGA) is used in

this study. The projector augmented wave pseudopotential was employed for describing the electron-core interactions, combining the plane-wave basis set of 520 eV energy cut-off for the valence electrons. The vacuum is set about 20 Å in a perpendicular direction to avoid the interaction between the periodic images. The Brillouin zone is sampled with a 5 × 5 × 1 k-point grid. The convergence criteria for the energy and residual force are set to 10-5 eV and 0.02 eV / Å, respectively.

The free energy change of reaction was defined by,

$$\Delta G_{(U,\,pH)} = \Delta G + \Delta G_{pH} + \Delta G_U \quad (1)$$

$$\Delta G = \Delta E + \Delta ZPE - T\Delta S \quad (2)$$

$$\Delta G_{pH} = -kT\cdot\ln[H^+] = kT\cdot\ln10\cdot pH \quad (3)$$

$$\Delta G_U = eU \quad (4)$$

where ΔE is the total energy change of the reaction, ΔZPE is the difference on zero-point-energy of the system during the reaction, ΔS is the entropy change during the reaction. And all these parameters can be obtained by routine calculations[180].

The ORR half-reaction was considered by four elementary steps:

1) $O_{2(g)}+H^++*\text{-->}OOH*\text{-}e$

2) $OOH*+ H^+\text{-->}O*+H_2O\text{-}e$

3) $O*+ H^+\text{-->}OH*\text{-}e$

4) $OH*+ H^+\text{-->}*+H_2O\text{-}e$

4.3. Results and Discussion

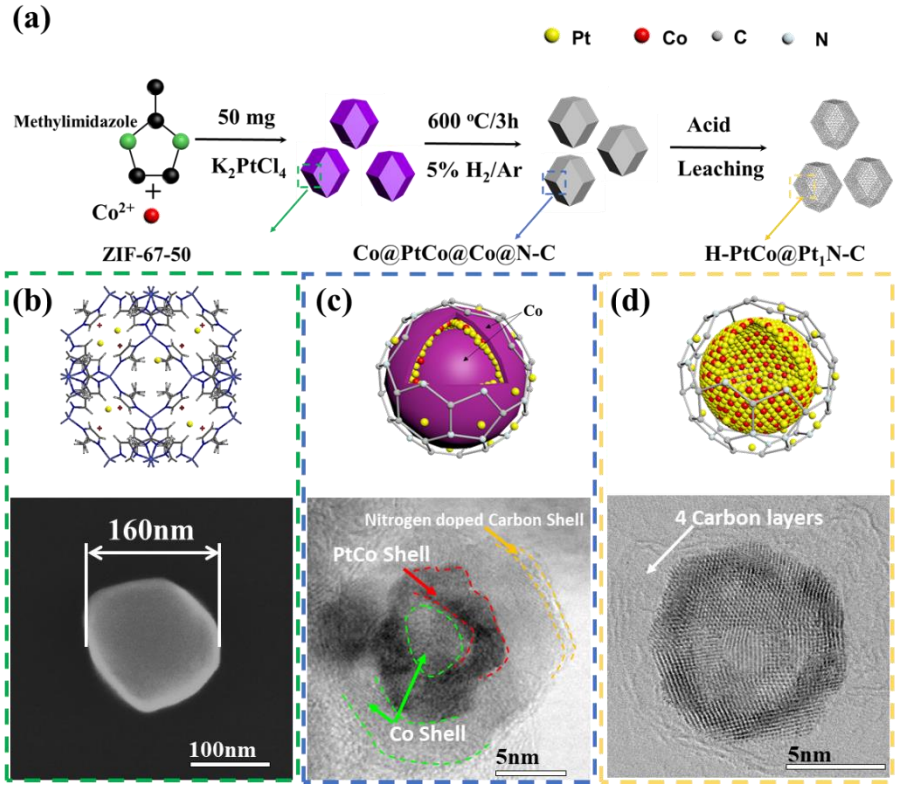

Figure 4-1. (a) Schematic illustration of the fabrication process for H-PtCo@Pt_1N-C. (b) Scanning electron microscope (SEM) image of ZIF-67-50. (c) Annular bright field (ABF) image of Co@PtCo@Co@Pt_1N-C. (d) Annular bright field (ABF) image of H-PtCo@Pt_1N-C.

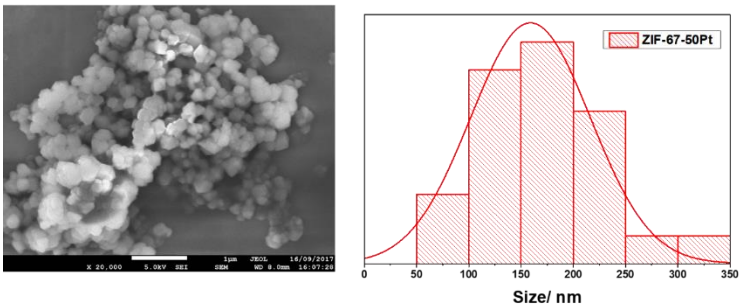

Figure 4-2. SEM image and histogram of the diameters of ZIF-67-50 particles.

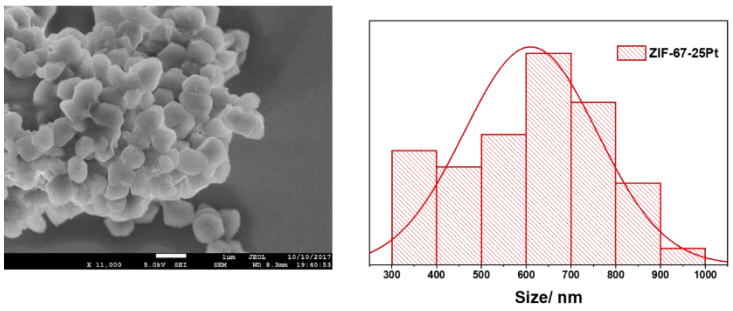

Figure 4-3. SEM image and histogram of the diameters of ZIF-67-25 particles.

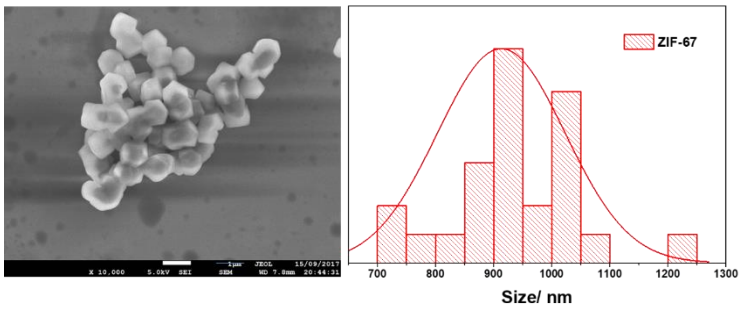

Figure 4-4. SEM image and histogram of the diameters of ZIF-67-0 particles.

Inspired by the synthesis of zeolitic imidazolate framework-67 (ZIF-67)[181], H-PtCo@Pt_1N-C was fabricated as illustrated in Fig. 4-1a. Pt salts (K_2PtCl_4) was added at the beginning, which can modify the coordination between methylimidazolate anions and cobalt cations, leading to a decrease in the particle size. The smallest average diameter of the modified ZIF-67 was around 100-250 nm (ZIF-67-50), obtained by adding 50 mg Pt salt (Fig. 4-1b, Fig. 4-2 in the Supporting Information). In a sharp contrast, when the Pt salts was decreased to 25 and 0 mg, the diameter of products increase to 500-800 (ZIF-67-25) and 850-1050 nm (ZIF-67-0) (Fig. 4-3 and 4-4), respectively. We thus believe that the decrease in the particle size is mostly due to the change of the pH value, which is consistent with previous work reported by Ming Hu's group[182]. The increased concentration of OH^-, which is provided by the

dissociation of Pt salt (K_2PtCl_4), probably forms prenucleation clusters with Co^{2+}, so that it prevents the Co^{2+} from supporting the growth of ZIF-67[183].

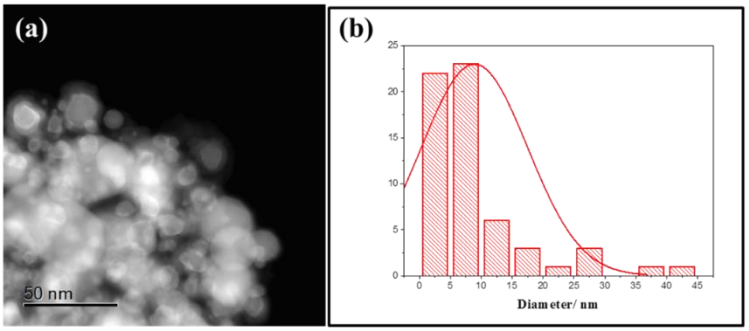

Figure 4-5. (a) HAADF-STEM image at low magnification, and (b) Histogram of the diameters of Co@PtCo/Pt@Co@Pt_1N-C particles.

When the ZIF-67-50 was calcinated at 600 °C, ultra-refined intermediate nanoparticles, denoted as Co@PtCo@Co@Pt_1N-C, were produced, with main particle size around 10 nm in a range from 2 to 45 nm according to the low magnification scanning transmission electron microscope (STEM) images (Fig. 4-5). The high-angle annular dark field (HAADF) image and energy dispersive spectroscopy (EDS) mapping analysis provide evidence that the Pt phase is well ring-dispersed in the middle of Co with nitrogen doped carbon as shell (Fig. 4-1c, Fig. 4-5a). The synchronous increase in the Co prior to Pt also confirms that the Pt atoms are rare on the external Co shell and restricted in the middle only (Fig. 4-5b).

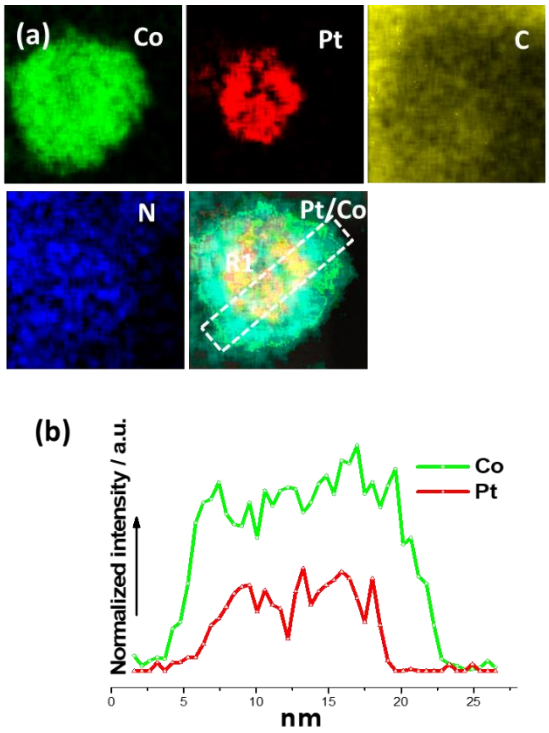

Figure 4-6. (a) STEM-EDS elemental maps of Co, N, C, and Pt for the selected Co@PtCo@Co@Pt_1N-C particle. (b) Line profile analysis from the indicated white rectangle R1 in (a), where the increased intensity of Co prior to Pt indicates that the Co shell wraps the PtCo core.

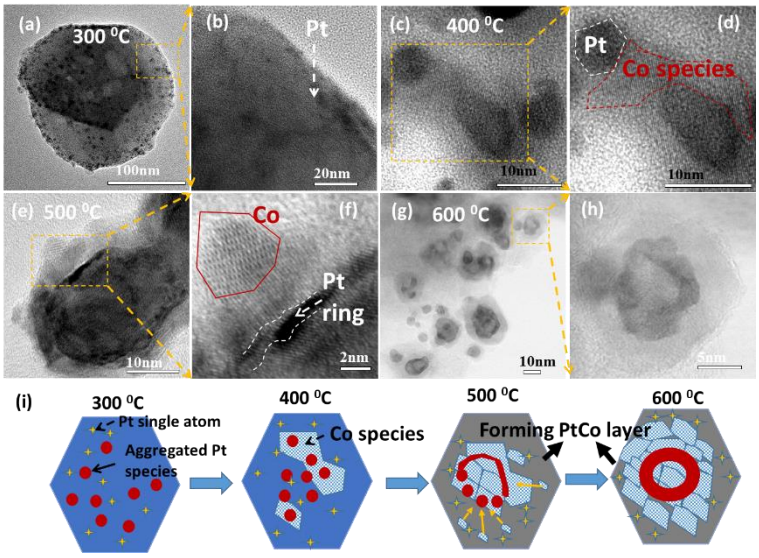

Figure 4-7. (a, b) TEM images at different magnifications of Co@PtCo@Co@Pt_1N-C obtained at 300 ℃; (c, d) TEM images of Co@PtCo@Co@Pt_1N-C at different magnifications obtained at 400 ℃; (e, f) TEM images of Co@PtCo@Co@Pt_1N-C at different magnifications obtained at 500 ℃; (g, h) TEM images of Co@PtCo@Co@Pt_1N-C at different magnification obtained at 600 ℃; (i) Schematic illustration of the evolution of intermediate Co@PtCo@Co@Pt_1N-C particles.

To reveal the mechanism behind the formation of Co@PtCo@Co@Pt1N-C intermediate, we further investigated the morphology of the intermediates obtained at the different temperature. The Pt phase, which is not connected to imidazole groups, tends to aggregate into nanoparticles at a lower temperature (300^{o}C) with a possible slight amount of Co species to form the PtCo@Co core (Fig. 4-7). With inceasing temperature, more Co fragments begin to aggregate and wrap the PtCo@Co core, subsequently leading to the the external Co shells and the formation of Co@PtCo@Co@Pt_1N-C. Co serves as a hard template and matrix to create inner cavities/active sites and accommodate Pt phases. Subsequently, the final product, elaborate H-PtCo@Pt_1N-C nanoparticles with well-constructed hollow structures, could be obtained after acid etching the Co away. The high resolution annular bright field (ABF) image of H-PtCo@Pt_1N-C indicates that the carbon shell coated on the particle surface is only 4 atomic layers thick (Fig. 4-1d).

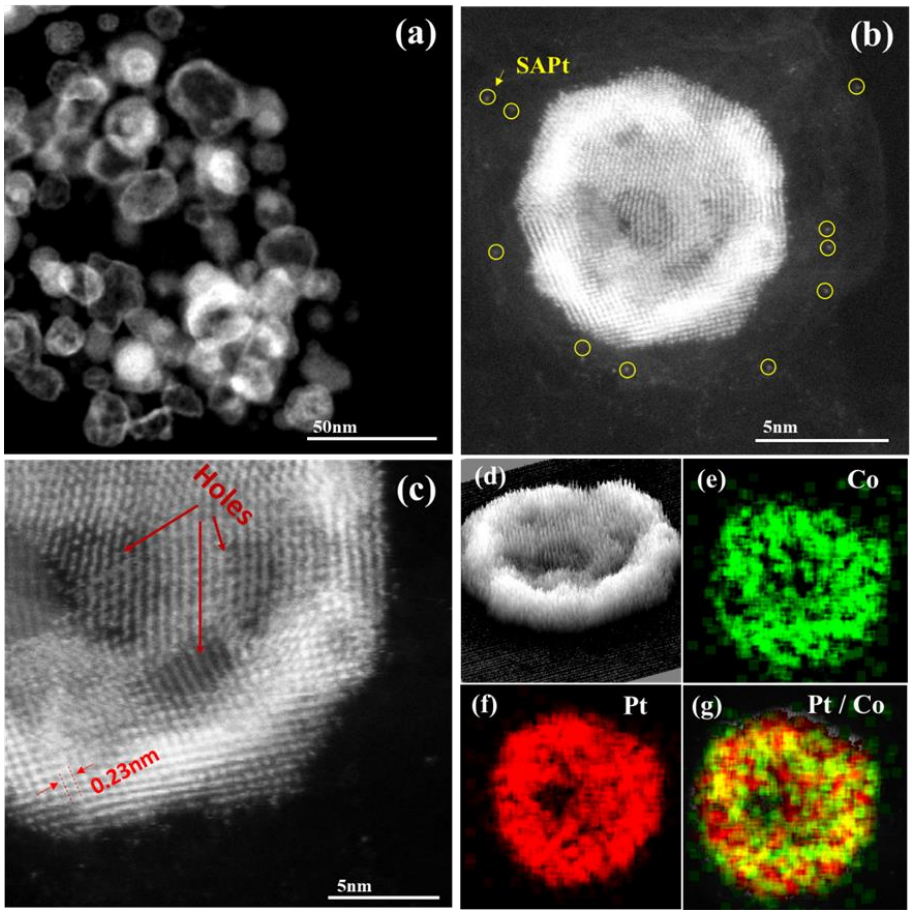

Figure 4-8. (a) Low-magnification high-angle annular dark field (HAADF) image of H-PtCo@Pt_1N-C. (b) High-resolution HAADF image of H-PtCo@Pt_1N-C. (d) The corresponding 3D electron signal intensity, and (e-g) STEM-EDS maps of elemental distributions of H-PtCo@Pt_1N-C. SA: single atom.

Specifically, the low magnification HAADF image of H-PtCo@Pt_1N-C shows that this approach can achieve uniform hollow structures with bright shells (Fig. 4-8a). The high-resolution HAADF image clearly shows the presence of the porous carbon shell, which can directly provide physical segregation from other particles and protect the particles from agglomeration, thus maintaining excellent structural stability of the interior core. In addition, it is interesting that bright spots with high contrast (yellow circles) can be clearly seen on the carbon shell, indicating the isolated single Pt atoms

(Pt_1) were doped into the carbon lattice (Fig. 4-8b), so that the whole image resembles looks like a moon hanging in the sky surrounded by stars. Moreover, Fig. 4-8c presents a hollow structure with holes and shows lattice spacing of 0.23 nm, which is indexed to the (111) planes of PtCo alloy.

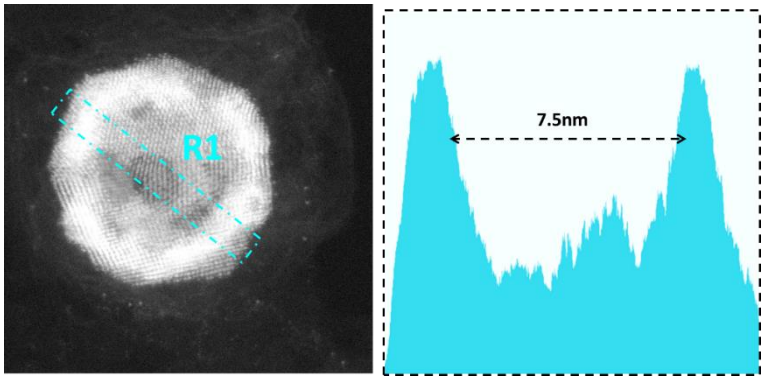

Figure 4-9. The electronic intensity measured along R1 on the hollow PtCo alloy shows there is an intensity-collapse, which is 7.5 nm, corresponding to the inner diameter of the hollow structure.

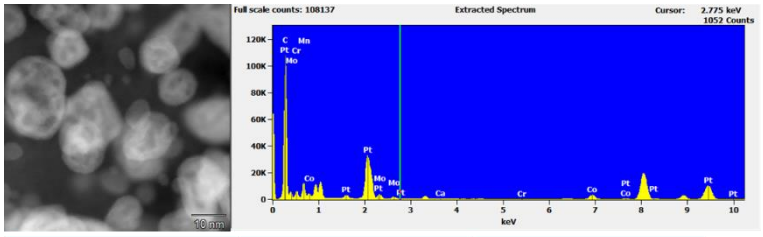

Pt	Co	PtCo
0.47	0.16	2.75

Figure 4-10. Annular dark field (ADF)-STEM image of H-$PtCo_{core}$@Pt_1N-C_{shell} and its corresponding EDS spectrum, revealing that the atomic ratio of Pt to Co is 2.75.

The holey structure of H-PtCo@Pt_1N-C assists in providing tunnels for O_2 to flow in and form internal-external double active layers, which can enhance the catalytic performance. The collapse of the electron signal intensity measured along H-PtCo@Pt_1N-C further confirms the hollow structure with an inner diameter of 7.5 nm

(Fig. 4-9). Also, the uneven intensity of H-PtCo@Pt_1N-C shows that the particle has a rugged surface, which further increases the active sites in combination with the hollow nanostructure (Fig. 4-8d). The STEM-energy dispersive spectroscopy (EDS) elemental mapping shows the Pt and Co projected distributions within the particle (Fig. 4-8e-f), and further STEM-EDS analysis reveals an average Pt/Co atomic ratio of about 2.75, indicating that the main phase in H-PtCo@Pt_1N-C is Pt_3Co (Fig. 4-10). Also, a line profile extracted from the particle, as shown by the blue arrow in Fig. 4-11, confirms that the Pt has a synchronous change with Co.

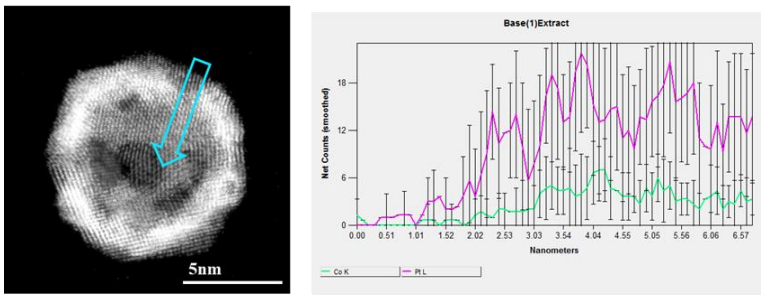

Figure 4-11. Line profile analysis along the indicated blue rectangle in H-PtCo@Pt_1N-C_{shell}.

The high-resolution HAADF as shown in Fig. 4-12a illuminates that the high-contrast bright spots, which are considered as Pt_1, are uniformly dispersed on the carbon shell at a high density without any aggregation. The focused and under-focused Pt atoms in the HAADF image (bright and dark one as shown in Figure 4-12a) indicate that Pt_1 atoms are doped in different depths, implying a three-dimensional distribution of Pt_1 in H-PtCo@Pt_1N-C. The inverse fast Fourier transform (FFT) image, which was taken from a small area (red rectangle in Fig. 4-12a), shows that the bright Pt atoms are each evenly anchored in middle of a quadrangle of the nitrogen-doped carbon (the yellow rectangles), indicating the synergistic super lattice between Pt and N-C support (Fig.

4-12b). The formation of Pt_1 is likely determined by the on N-doped C support, in which there is strong electronic metal-support interactions (EMSI) in the form of Pt-N-C bonding. Also, the measured distance of the bond of C(N)-Pt-C(N) on the first shell was around 3.6 Å (Fig. 4-12d), which is very near the value from the theoretical simulated atomic model as shown in Figure 4-12c. The elemental mapping further confirmed that the element Pt evenly distributed in the C matrix (Fig. 4-12e-h).

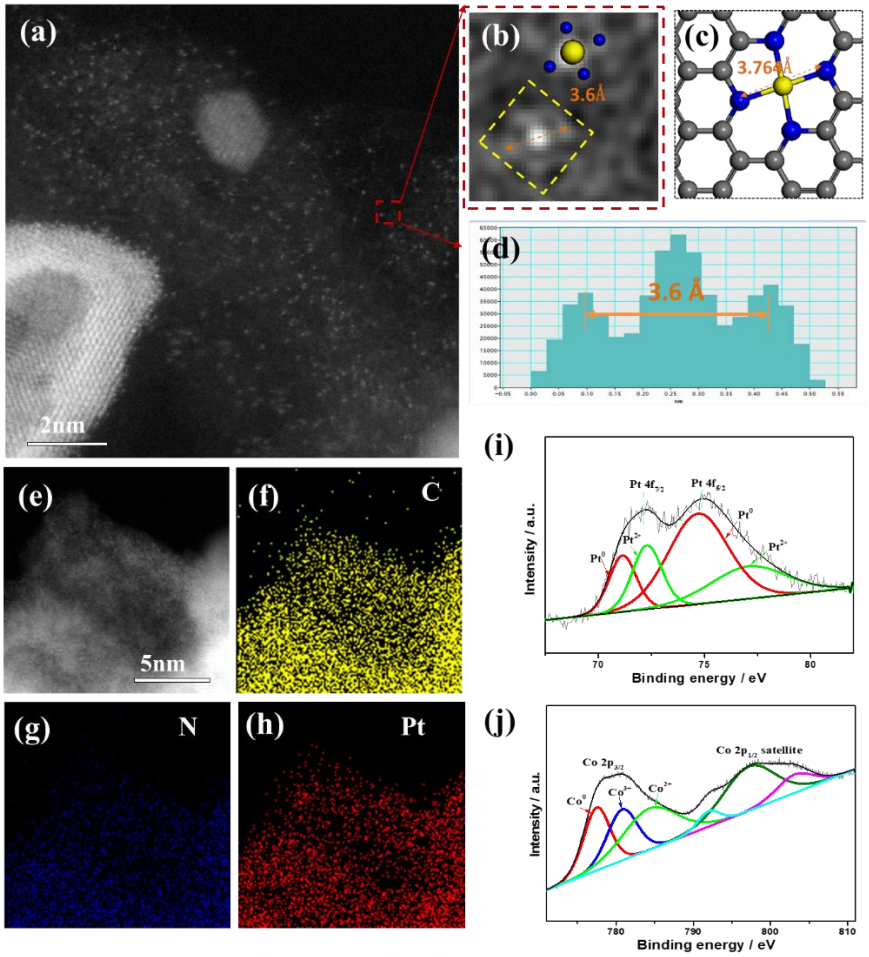

Figure 4-12. (a) HAADF image of H-PtCo@Pt_1N-C focused on single Pt atoms doped on carbon shell. (b) The FTTI-HAADF image of H-PtCo@Pt_1N-C derived from the red rectangle in Figure 4-12a, with the inset showing the arrangement of atoms. (c) Simulated model of carbon/nitrogen-Pt single atoms. The blue ball represents

nitrogen/carbon atoms, the yellow ball represents Pt atoms. (d)The electronic intensity profile the distance diagonal atoms in first shell is 3.6 Å. (e-h) STEM-EDS maps of elemental distributions. High resolution (i) Pt 4f and (j) Co 2p XPS spectra of H-PtCo@Pt_1N-C.

As is well-known, Pt_1 as a new frontier in heterogeneous catalysis could exhibit unexpected properties due to its atomic scale and superior activity, which is expected to play an active role in synergistically boosting ORR properties of the sample. The surface composition and valence state of H-PtCo@Pt_1N-C were investigated by X-ray photoelectron spectroscopy (XPS). As shown in Fig. 4-12i, the binding energies at 72.13 eV and 74.89 eV in the Pt spectrum correspond to the Pt $4f_{2/7}$ and Pt $4f_{5/2}$ peaks of the H-PtCo@Pt_1N-C, which can be deconvoluted into four peaks at 71.19 eV, 72.27 eV, 74.68 eV, and 77.21 eV, respectively, indicating the presence of metallic Pt and oxidized Pt[184]. This result is consistent with the co-existed status of metallic Pt in the PtCo alloy and oxidized Pt_1 single atoms. Also, the high resolution XPS spectrum of Co2p shows the coexistence of Co^0, Co^{3+}, and Co^{2+}, indicating the presence of metallic Co and possibly the residue of cobalt oxides (Fig. 4-12j).

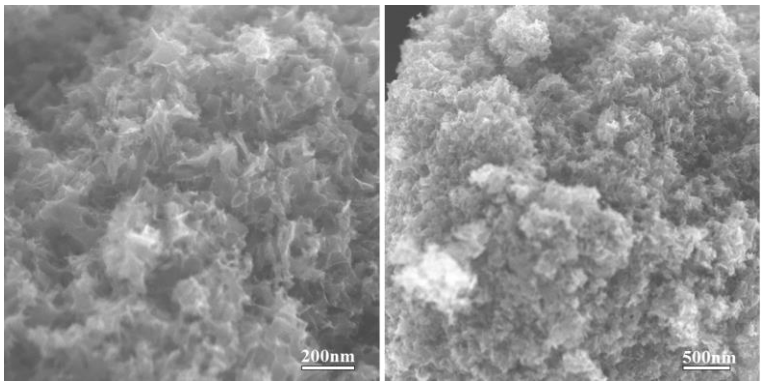

Figure 4-13. Typical SEM images of NPC at different magnifications.

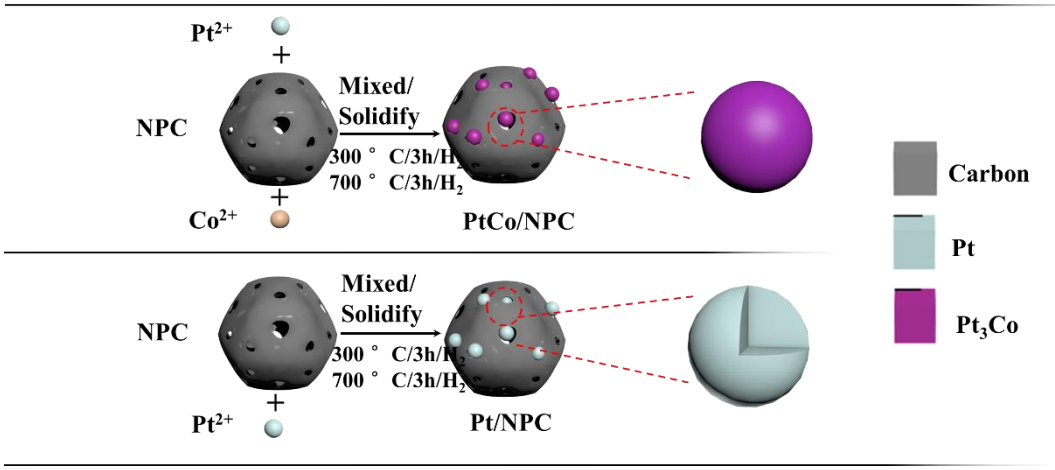

Figure 4-14. Schematic illustration for of fabrication processes for PtCo/NPC and Pt/NPC.

To verify the functions of the hollow structure and bimetallic effect, ultra-refined solid Pt_3Co alloy nanoparticles (PtCo/NPC) and solid Pt nanoparticles (Pt/NPC) were respectively prepared as comparison, respectively. A new Nitrogen-doped porous carbon (NPC) with nanopores was synthesized as a framework for both samples (Fig. 4-13), as it has been reported that the nanoporous carbon can prevent the Pt particles from growing big size[185]. The fabrication process was shown in Fig. 4-14.

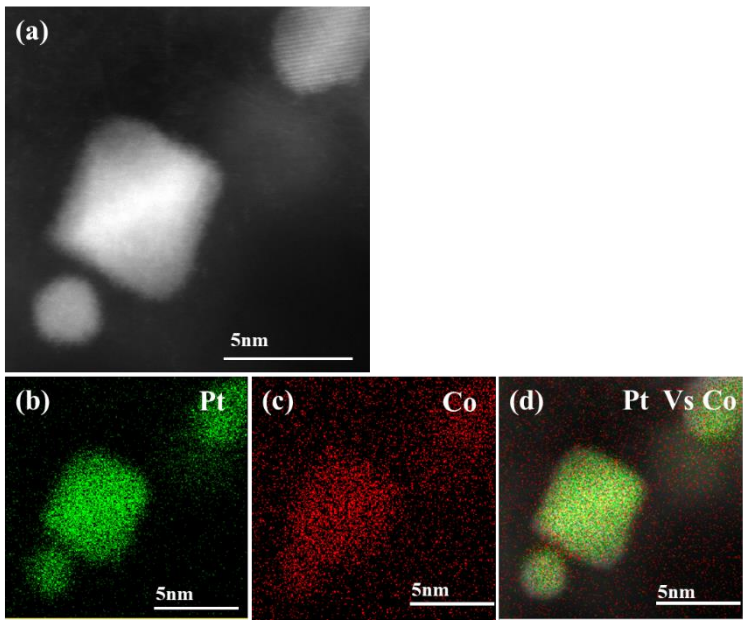

Figure 4-15. HAADF-STEM image and STEM-EDS maps of PtCo/NPC. (a) HAADF-STEM image. (b-d) STEM-EDS maps.

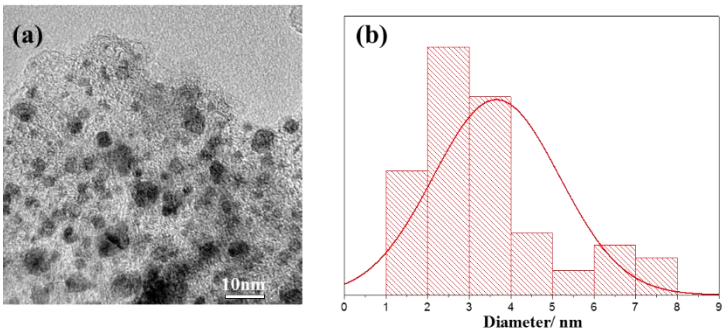

Figure 4-16. (a) TEM image of PtCo/NPC at low magnification. (b) Histogram of the diameters of PtCo/NPC particles based on Fig. 4-16a.

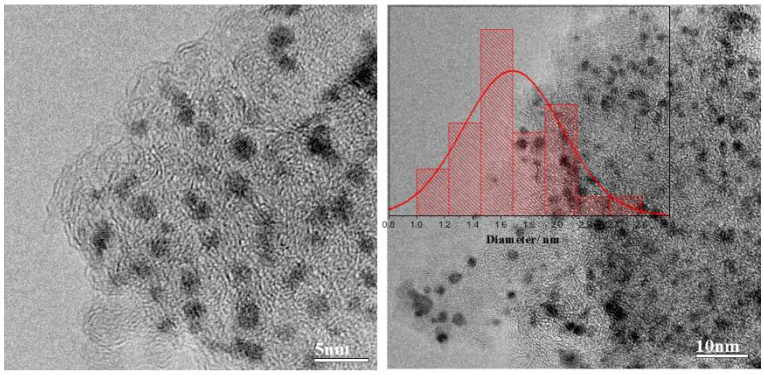

Figure 4-17. (a, b) Typical TEM images of Pt/NPC at different magnifications. Inset of (b) is a histogram of the diameters of Pt/NPC particles based on Fig. 4-17a.

The experimental details for all the samples are presented in the Supporting Information. The HAADF-STEM images show the nanoparticles sizes of PtCo/NPC and Pt/NPC varying between 4 and 8 nm (Fig. 4-15, 4-16, and 4-17), which are comparable to those of H-PtCo@Pt_1N-C. Additionally, the structure-simulation models confirm that there are structural differences amongst these three samples in terms of hollow structures and metallic Pt_3Co phase (Fig. 4-18). As shown in Figure

S16, H-PtCo@Pt_1N-C, PtCo/NPC, and Pt/NPC have particles of a similar size, varying between 4 and 8 nm. Also, the random intensity variations observed between the atomic columns suggest that the alloyed Pt-Co face-centered cubic phase is disordered. Compared to the typical hexagonal structure of Pt/NPC (Fig. 4-18c), the H-PtCo@Pt_1N-C (Fig. 4-18a) and PtCo/NPC (Fig. 4-18b) possess a more spherical appearance, indicating that they are smoother, with a smaller extent of low-Cordination surface atoms. The structure-simulation models show the structural differences between H-PtCo@Pt_1N-C (Fig. 4-18d), PtCo/NPC (Fig. 4-18e), and Pt/NPC (Fig. 4-18f). There is a cavity in the center of the H-PtCo@Pt_1N-C particle, but not in the PtCo/NPC. In particular, to gain better insight into the structure of the dark-contrasted nanoparticles, the three-dimensional (3D) variations of HAADF intensity were compared between H-PtCo@Pt_1N-C (Fig. 4-18g) and PtCo/NPC (Fig. 4-18h). In this model, the contrast varies linearly with the mass and the thickness of the analyzed area, and is proportional to the square of the mean atomic number Z of the specimen. Thus, the observed color-contrast difference may come from the different structures: hollow and solid.

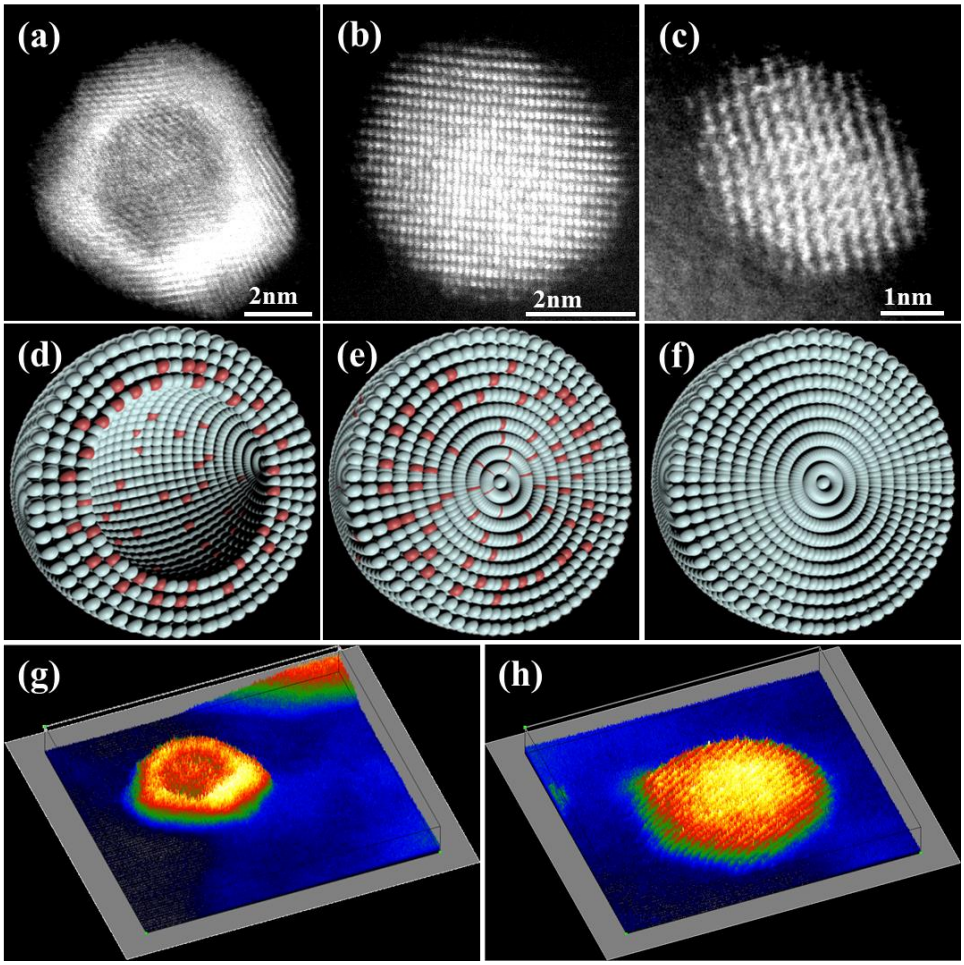

Figure 4-18. HAADF-STEM images of (a) H-PtCo@Pt_1N-C, (b) PtCo/NPC, and (c) Pt/NPC. Structure-simulation models of (d) H-PtCo@Pt_1N-C, (e) PtCo/NPC, and (f) Pt/NPC. Variations of HAADF intensity for (g) H-PtCo@Pt_1N-C and (h) PtCo/NPC.

The X-ray diffraction (XRD) patterns of all these samples are indexed to a face-centered cubic (fcc) structure, corresponding to the (111), (200), (220), and (311) planes of Pt metal and Pt_3Co alloy, respectively (Fig. 4-19). As shown in the X-ray diffraction (XRD) patterns, the peaks at 39.7, 46.2, 67.4, and 85.7° of Pt/NPC and Pt/C are indexed to pure Pt metal with a face-centered cubic (fcc) structure, corresponding to the (111), (200), (220), and (311) planes, respectively. These peaks in H-PtCo@Pt_1N-C and PtCo/NPC are shifted to higher angles, suggesting that Pt has been

incorporated with Co to form an alloy phase with concomitant lattice construction. The four broad diffraction peaks at 40.5, 47.1, 68.8, and 87.6°are indexed to the Pt_3Co alloy (JCPDF no. 29-0499), showing typical fcc Pt features as well.

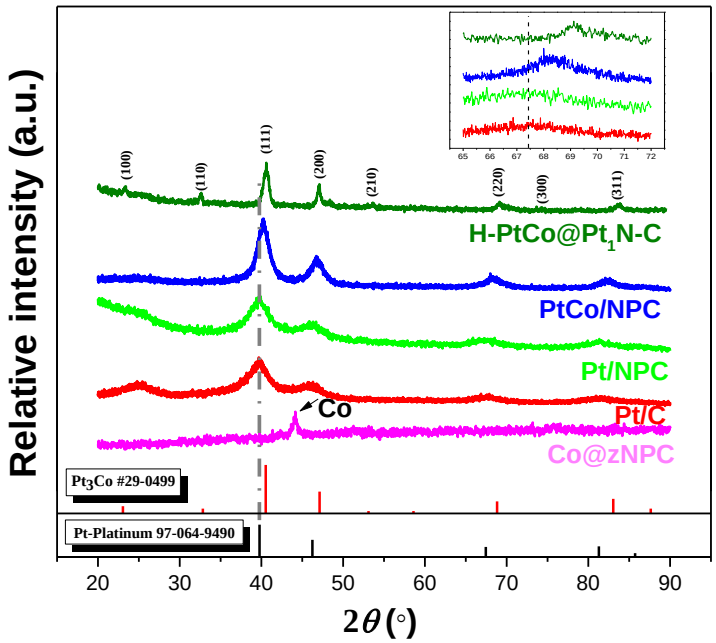

Figure 4-19. XRD patterns of H-PtCo@Pt_1N-C, PtCo/NPC, Pt/NPC, Pt/C, and Co@zNPC, with the inset showing an enlargement of the indicated range.

Fig. 4-20a shows the ORR polarization curves of different catalysts recorded at room temperature at a sweep rate of 10 mV s^{-1} with a rotation rate of 1600 rpm in O_2-saturated 0.1 M $HClO_4$ solution. It is evident that H-PtCo@Pt_1N-C has the highest onset potential, which is 60 mV higher than that of commercial Pt/C. The onset potential increases in the sequence: Pt/NPC < Pt/C < PtCo/NPC < H-PtCo@Pt_1N-C. This result unambiguously proves the critical functions of both the bimetallic alloy and the cavities in the unique sample. The highest onset potential for H-PtCo@Pt_1N-C is partially attributed to the interior cavities, which are likely to provide more active sites and modify the electronic and structural properties of PtCo alloy. Compared with the

current density of Pt/C, the H-PtCo@Pt_1N-C has a comparable diffusion-limited value, ~5.4 mA cm^{-2}. The rotation-rate-dependent current-potential curves of H-PtCo@Pt_1N-C are presented in Fig. 4-20b (inset). The number of electrons transferred (n) is estimated to be ~4.0 at 0.75-0.9 V from the slopes of the Koutecky-Levich plots, indicating the nearly complete reduction of O_2 to H_2O on the surface of the H-PtCo@Pt_1N-C. As shown in Fig. 4-20c, the mass activity of H-PtCo@Pt_1N-C can be calculated to be 1.2 mA μg_{Pt}^{-1} at 0.9 V, which corresponds to 3.4, 10, and 8 times higher than those of PtCo/NPC (0.35 mA μg_{Pt}^{-1}), Pt/NPC (0.12 mA μg_{Pt}^{-1}), and Pt/C (0.15 mA μg_{Pt}^{-1}), respectively. Moreover, the mass activity comparison of these catalysts at 0.85 V also demonstrates that H-PtCo@Pt_1N-C could deliver the best electrocatalytic performance. The kinetic current (I_k) can be calculated using the Koutecky-Levich equation (for details, see the electrochemical testing section in the Supporting Information). Fig. 4-20d compares the specific activity (I_k) for H-PtCo@Pt_1N-C, PtCo/NPC, Pt/NPC, and Pt/C. At 0.9 V, the specific activity of H-PtCo@Pt_1N-C is 2.39 mA cm_{Pt}^{-2}, which is much higher than that for PtCo/NPC (0.7 mA cm_{Pt}^{-2}), Pt/NPC (0.24 mA cm_{Pt}^{-2}), and Pt/C (0.3 mA cm_{Pt}^{-2}). The superior performance of H-PtCo@Pt_1N-C toward the ORR was further evaluated in a lithium-O_2 cell with different organic electrolytes. One electrolyte consists of 1 M $LiCF_3SO_3$ in tetraethylene glycol dimethyl ether (TEGDME); the other one consists of 0.1 M $NaClO_4$ in dimethylsulfoxide (DMSO). Fig. 4-20e shows the discharge-charge profiles of H-PtCo@Pt_1N-C in TEGDME and DMSO, respectively. At a current density of 20 mA g^{-1}, the average discharging voltage is ~2.91 V in both TEGDME and DMSO. The extremely low overpotential of 0.05 V implies that the practical ORR potential is very close to the thermodynamic potential of the reaction, $2Li^+ + 2e^- + O_2 \rightarrow Li_2O_2$,

indicating the excellent ORR performance of H-PtCo@Pt_1N-C in organic electrolytes. Furthermore, the H-PtCo@Pt_1N-C possesses durability towards the ORR over 5 cycles, with only a minor increase in the overpotential (Fig. 4-20f). All these results verify that the unique H-PtCo@Pt_1N-C nanoparticles could achieve outstanding ORR performance in both aqueous and organic electrolytes.

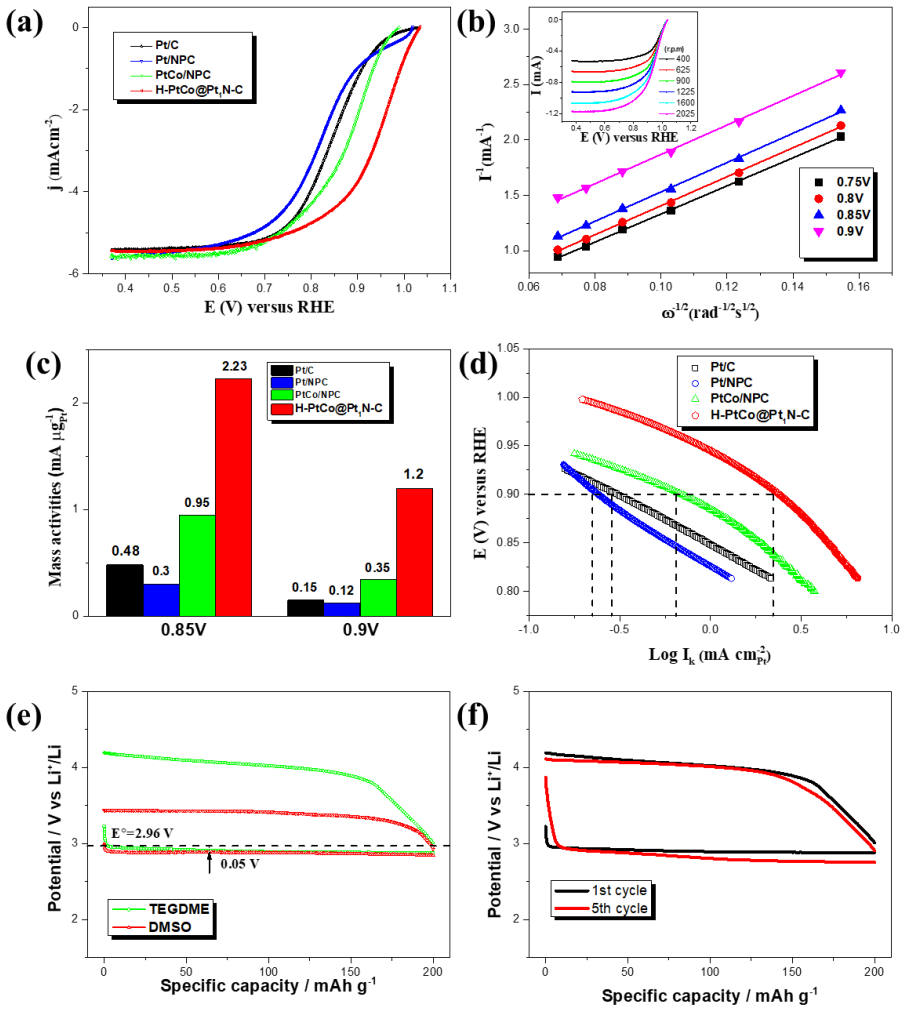

Figure 4-20. (a) ORR polarization curves for H-PtCo@Pt_1N-C, PtCo/NPC, Pt/NPC, and Pt/C in O_2-saturated 0.1 M $HClO_4$ solution at room temperature, collected with a rotation rate of 1,600 rpm at a sweep rate of 10 mV s^{-1}. (b) Koutecky-Levich plots from the ORR data for H-PtCo@Pt_1N-C at different potentials, with the inset in (b) showing the rotation-rate-dependent current-potential curves. (c) Comparison of mass

activities for H-PtCo@Pt_1N-C, PtCo/NPC, Pt/NPC, and Pt/C at 0.85 and 0.9 V. (d) Comparison of specific activities (I_k) for these samples. (e) Discharge-charge profiles of H-PtCo@Pt_1N-C in TEGDME and DMSO. (f) Cycling stability of H-PtCo@Pt_1N-C in TEGDME.

For further investigated the synergistic effect between PtCo hollow structure and single Pt atoms, H-PtCo@Pt_1N-C were processed at a higher-temperature 750 °C (ZIF-67-50-750). Compared with H-PtCo@Pt_1N-C, the diffusion-limited current density for the ORR polarization curves of ZIF-67-50-750 increased to 6.0 mA cm^{-2}, which is probably accounted for the increased conductivity (Fig. 4-21). The specific activity of ZIF-67-50-750 at 0.9V, however, had a minor decreased. The deformation of hollow structure and agglomeration of single Pt atoms on carbon surface were observed via the STEM-HAADF image of ZIF-67-50-750 (Fig. 4-22), which was considering as the reason of fading ORR performance of ZIF-67-50-750. Also, Pt_1N-C were synthesized to confirm the special role of Pt atom in ORR reaction (Fig. 4-23 and 4-24).

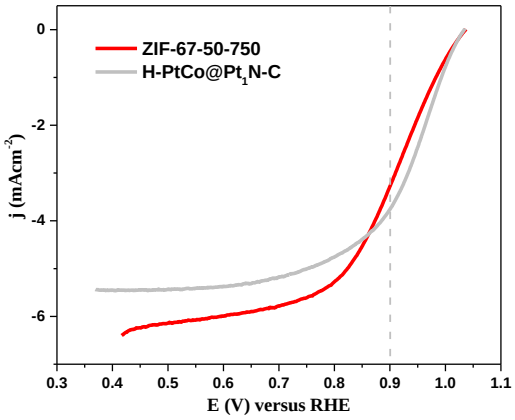

Figure 4-21. The ORR activities of ZIF-67-50-750.

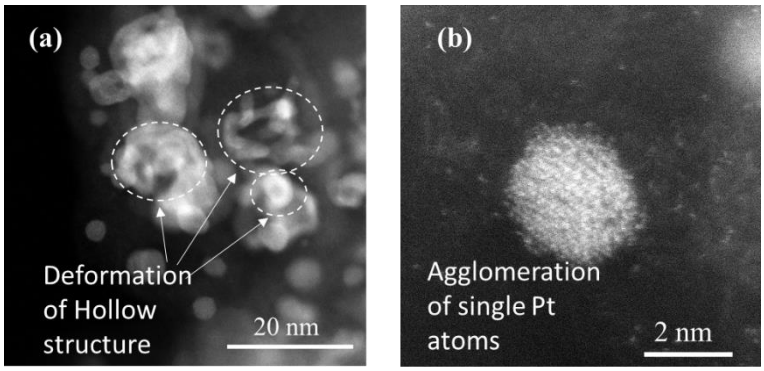

Figure 4-22. The HAADF image of ZIF-67-50-750 on hollow structure (a) and carbon surface (b).

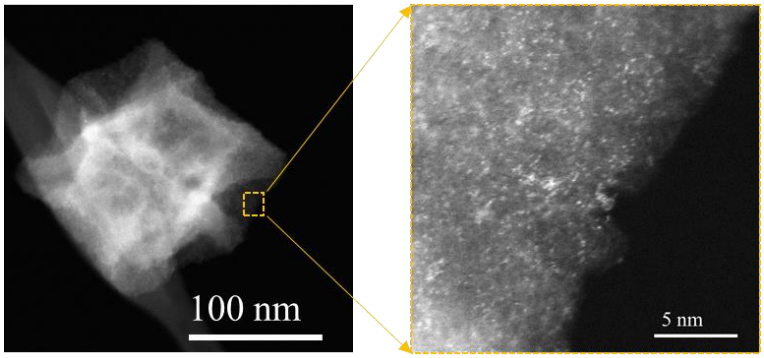

Figure 4-23. The HAADF images of Pt_1N-C with low and high magnifications.

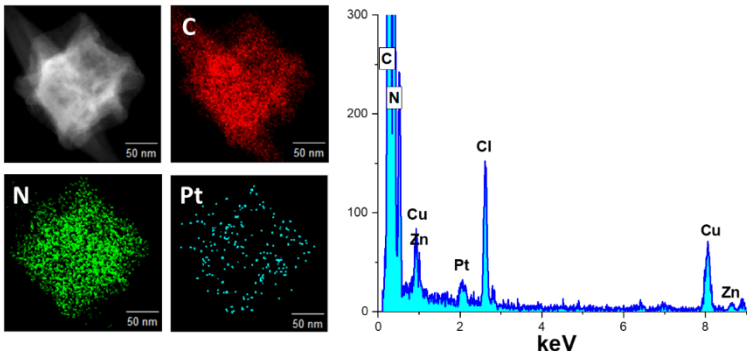

Figure 4-24. The STEM elemental mapping and EDS spectrum on Pt_1N-C.

The onset ORR potential of Pt_1N-C had a severe decrease compared with H-PtCo@Pt_1N-C, but still shown a better ORR performance than the ZIF-67 derived nitrogen doped carbon (Co-NC) (Fig. 4-25). The Koutecky-Levich plots of Pt_1-N-C at

different potentials were further tested, which suggested that the Pt_1-N-C had a four electrons ORR pathway (Fig. 4-26). These results indicated that the unique nanostructure, including the ultra-fined PtCo alloy, and effective C shell with Pt_1, synergistically endows the H-PtCo@Pt_1N-C with enhanced ORR performance.

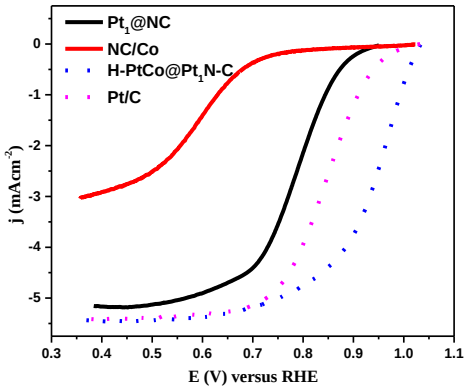

Figure 4-25. The ORR activity of Pt_1@N-C.

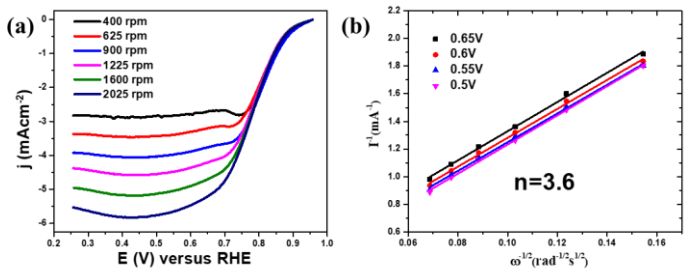

Figure 4-26. The rotation-rate-dependent current-potential curves of Pt_1N-C and the Koutecky-Levich plots from the ORR data for Pt_1N-C at different potentials.

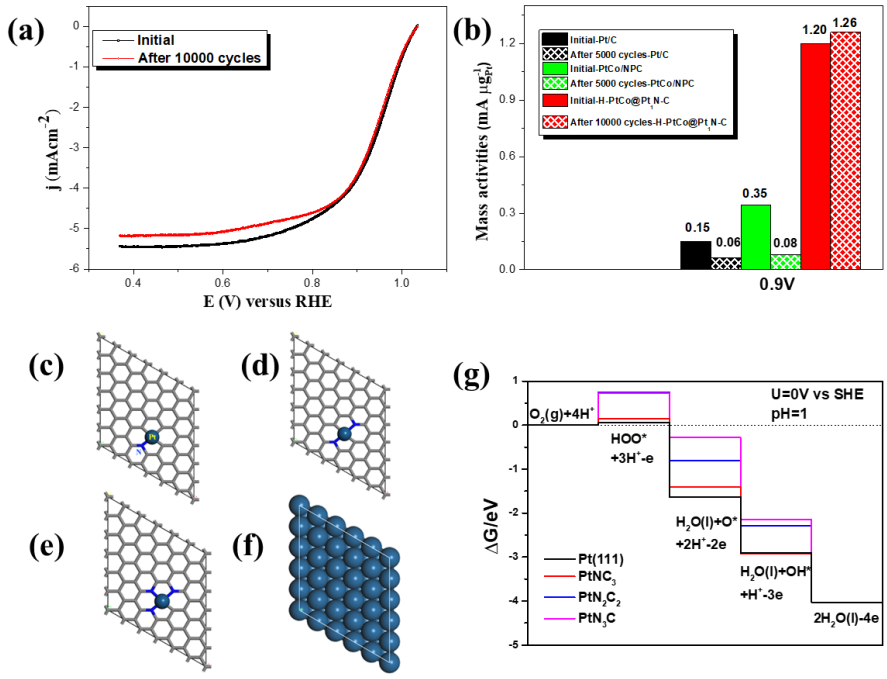

Figure 4-27. (a) ORR polarization curves for H-PtCo@Pt_1N-C before and after 10000 potential cycles. (b) Comparative ORR mass activities of H-PtCo@Pt_1N-C, PtCo/NPC, and Pt/C before and after 10000/5000 potential cycles respectively. (c-g) Structure models used in DFT calculation. The single atom Pt is modelled as a four-coordinated structure, which is $PtNC_3$ (c), PtN_2C_2 (d), and PtN_3C (e) respectively. Pt(111) (f) also was used for comparison. (g) Free energy diagram of the ORR on $PtNC_3$ (a), PtN_2C_2 (b), PtN_3C, and Pt(111).

When tested in O_2-saturated 0.1 M $HClO_4$ solution, an accelerated durability test between 0.6 and 1.1 V shows that there is no obvious shift at 0.9 V and only a 4.5% loss of diffusion-limited current density for the ORR polarization curves of H-PtCo@Pt_1N-C after 10000 cycles (Fig. 4-27a). In stark contrast, the PtCo/NPC and Pt/C show a larger negative shift in their ORR polarization curves, with 77% and 60% loss of mass activity (Fig. 4-27b, Fig. 4-28).

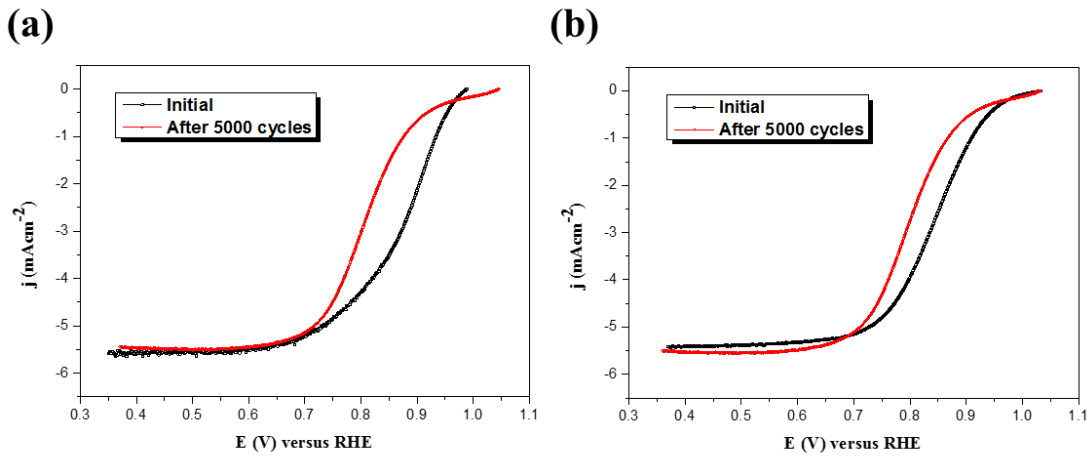

Figure 4-28. (a) Comparative ORR activities of PtCo/NPC before and after 5000 potential cycles. (b) Comparative ORR activities of Pt/NPC before and after 5000 potential cycles.

Table 4-1. Detailed information on the samples in Fig. 4-29.

Number	catalyst	electrolyte	MA@0.9V/mA·μg^{-1}	Reference
1	$PtCo_3$	0.1M $HClO_4$	0.34	[2]
2	$PtCu_3Co$	0.1M $HClO_4$	0.37	[2]
3	$PtCu_2Co_2$	0.1M $HClO_4$	0.37	[2]
4	$PtCuCo_3$	0.1M $HClO_4$	0.49	[2]
5	Acid-treated Pt_3Co	0.1M $HClO_4$	0.35	[3]
6	Annealed Pt_3Co	0.1M $HClO_4$	0.31	[3]
7	Pt_3Co -700	0.1M $HClO_4$	0.52	[1]
8	Pt_3Co -400	0.1M $HClO_4$	0.16	[1]
9	Pt_3Co /C	0.1M $HClO_4$	0.136	[4]
10	Pt_3Co /C-200	0.1M $HClO_4$	0.129	[4]
11	Pt_3Co /C-500	0.1M $HClO_4$	0.217	[4]
12	Pt_3Co /C-800	0.1M $HClO_4$	0.34	[5]
13	$Pt_{75}Co_{25}$ /C (500)	0.1M $HClO_4$	0.33	[6]
14	$Pt_{75}Co_{25}$ /C (500)	0.1M $HClO_4$	0.97	[6]

15	$Pt_{75}Co_{25}$/C (500)	0.1M $HClO_4$	0.96	[6]
16	D-$PtCo_3$/HSC	0.1M $HClO_4$	0.46	[7]
17	D-PtCo/HSC	0.1M $HClO_4$	0.49	[7]
18	PtCo hollow nanowires	0.1M $HClO_4$	0.17	[8]
19	PtCo nanowires	0.1M $HClO_4$	0.793	[9]
20	Pt_9Co/C	0.1M $HClO_4$	0.103	[10]
21	Pt_7Co/C	0.1M $HClO_4$	0.129	[10]
22	Pt_5Co/C	0.1M $HClO_4$	0.229	[10]
23	Pt_3Co/C	0.1M $HClO_4$	0.434	[10]
24	Pt_2Co/C	0.1M $HClO_4$	0.322	[10]
25	Pt-Co/C-S	0.1M $HClO_4$	0.154	[11]
26	Pt-Co/C-T	0.1M $HClO_4$	0.109	[11]
27	Pt-Co/C-SB	0.1M $HClO_4$	0.151	[11]
28	Pt-Co/C-TB	0.1M $HClO_4$	0.102	[11]
29	Pt-Co/C-SH	0.1M $HClO_4$	0.054	[11]
30	Pt-Co/C-TH	0.1M $HClO_4$	0.093	[11]
31	PtNiCo nanowires	0.1M $HClO_4$	4.2	[12]
32	Pt_3Co nanowires	0.1M $HClO_4$	3.4	[13]
33	H-PtCo@Pt_1N-C	0.1M $HClO_4$	1.2	this work
34	H-PtCo@Pt_1N-C After 10000	0.1M $HClO_4$	1.26	this work

Reference

[1] D. Wang, H. L. Xin, R. Hovden, H. Wang, Y. Yu, D. A. Muller, F. J. DiSalvo, H. D. Abruña, Nature materials 2013, 12, 81.

[2] R. Srivastava, P. Mani, N. Hahn, P. Strasser, Angewandte Chemie International Edition 2007, 46, 8988.

[3] S. Chen, P. J. Ferreira, W. Sheng, N. Yabuuchi, L. F. Allard, Y. Shao-Horn, Journal of the American Chemical Society 2008, 130, 13818.

[4] Z. Liu, C. Yu, I. A. Rusakova, D. Huang, P. Strasser, Topics in Catalysis 2008, 49, 241.

[5] H. Schulenburg, E. Muller, G. Khelashvili, T. Roser, H. Bonnemann, A. Wokaun, G. Scherer, The Journal of Physical Chemistry C 2009, 113, 4069.

[6] D. S. Choi, A. W. Robertson, J. H. Warner, S. O. Kim, H. Kim, Advanced Materials 2016, 28, 7115.

[7] Q. Jia, K. Caldwell, K. Strickland, J. M. Ziegelbauer, Z. Liu, Z. Yu, D. E. Ramaker, S. Mukerjee, ACS catalysis 2014, 5, 176.

[8] Y. Huang, M. Garcia, S. Habib, J. Shui, F. T. Wagner, J. Zhang, J. Jorné, J. C. Li, Journal of Materials Chemistry A 2014, 2, 16175.

[9] S. M. Alia, S. Pylypenko, K. C. Neyerlin, D. A. Cullen, S. S. Kocha, B. S. Pivovar, ACS Catalysis 2014, 4, 2680.

[10] S.-I. Choi, S.-U. Lee, W. Y. Kim, R. Choi, K. Hong, K. M. Nam, S. W. Han, J. T. Park, ACS applied materials & interfaces 2012, 4, 6228.

[11] Q. He, S. Mukerjee, Electrochimica Acta 2010, 55, 1709.

[12] K. Jiang, D. Zhao, S. Guo, X. Zhang, X. Zhu, J. Guo, G. Lu, X. Huang, Sci. Adv. 2017, 3, e1601705;

[13] L. Bu, S. Guo, X. Zhang, X. Shen, D. Su, G. Lu, X. Zhu, J. Yao, J. Guo, X. Huang, Nat. Comm. 2016, 7. 11850.

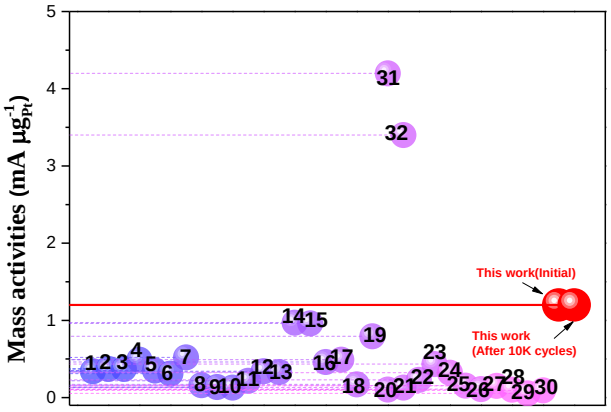

Figure 4-29. Comparison of the mass activities of Pt-Co systems from reports in the literature and this work. The numbers in the figure represent the different samples. Detailed information on the samples is shown in Table 4-1.

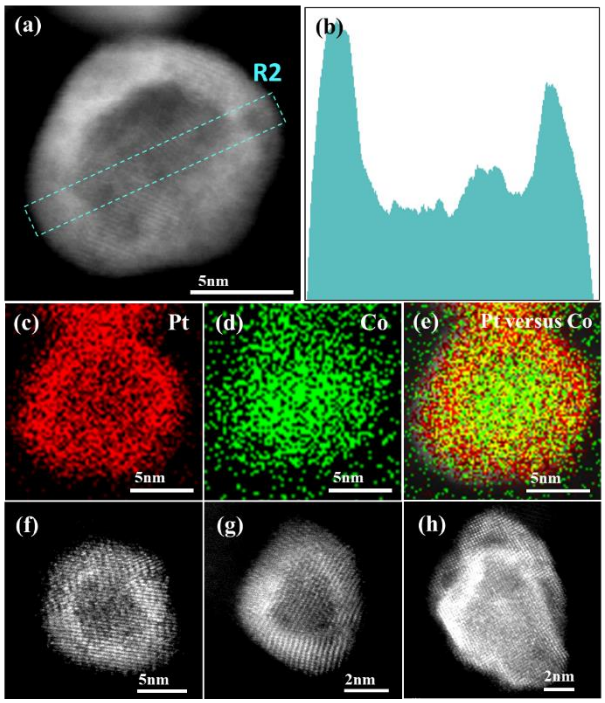

Figure 4-30. (a) HAADF-STEM image of a H-PtCo@Pt_1N-C nanoparticle after 10000 electrochemical cycles. (b) Electron signal intensity measured along the rectangle R2

in Fig. 4-30a. (c-e) STEM-EDS elemental maps. (f-h) Further particles demonstrate the stability of H-PtCo@Pt_1N-C after electrochemical cycling.

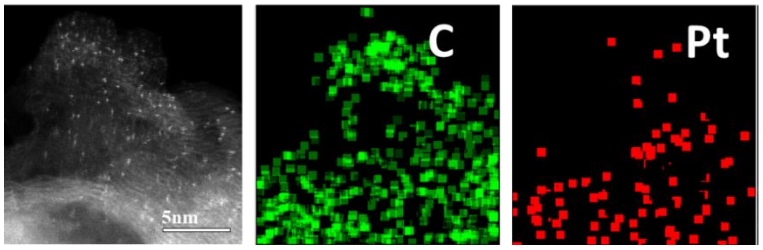

Figure 4-31. The HAADF image of single atom Pt and its corresponding elemental mapping.

Compared with the mass activity of Pt-Co/C systems reported in the literature that were tested under similar conditions at +0.9 V, it is impressive that H-PtCo@Pt_1N-C in both the initial cycle and the 10000^{th} cycle exhibits excellent electrocatalytic ORR performance (Table 4-1, Fig. 4-29). It is clear that the nanostructures and components of the H-PtCo@Pt_1N-C are well preserved after 10000 cycles (Fig. 4-30), leading to the sustainable ORR durability. Slight Co loss (Fig. 4-30c-e) because of the acid environment suggests that these zones were practically effective, as they are shown to be electronically and ionically connected and accessible to oxygen. Also, these single Pt atoms are well maintain, showing their strong bonding with the carbon shell and high stability (Fig. 4-31). By sharp contrast, both commercial Pt/C and PtCo/NPC exhibit large size changes and substantial aggregation after 5000 cycles (Fig. 4-32, Fig. 4-33) in agreement with their severe activity loss. This unique nanostructure, including the ultra-refined PtCo alloy, abundant cavities, and effective C shell with Pt_1 and N codoping, synergistically endows the H-PtCo@Pt_1N-C with enhanced ORR performance.

It has been confirmed many times in the previous reports that that Pt_3Co can enhance the ORR activity in the previous reports via experiments and theoretical calculations[165, 186]. For further revealing the synergistic effects of the Pt-4N/C structure on the enhancement of ORR activity, first-principles calculations were performed and compared on different models of Pt-N/C coordination. The Pt single-atom catalysts were modelled by a p(6×6) graphene slab with two C atoms substituted by a Pt atom to form a four-coordinated structure, where the C atoms adjacent to Pt could be substituted by N atoms to simulate the reaction centers in the experiments (Figure 4-27c, d, and e). The Pt(111) surface was modelled by a p(5×5) Pt(111) slab consisting of four atomic layers (Figure 4-27f). As shown in Figure 4-27g, the free energy change on the four elementary steps of the oxygen reduction reaction (ORR) suggest that the rate limiting step is the hydrogenation of the O_2 molecule. The less number of N atoms adjacent to Pt in the four-coordinated structure corresponds to the smaller over-potential. In particular, the $PtNC_3$ structure has the smallest over-potential, which is 0.10 V higher than the Pt(111) in the calculations. The XPS result indicated that the atom ratio of carbon and nitrogen (C/N) was estimated as 5.2, implying that the $PtNC_3$ was the most favored coordination in Pt-quadrangle structure (Fig. 4-34). These data are essentially in good agreement with the experimental observations on the comparable on-site potential with Pt/C (Figure 4-20) and Pt_1N-C (Fig. 4-25). It also suggests that the limiting amount of N atoms adjacent to Pt to a low level may benefit the reactivity of the materials.

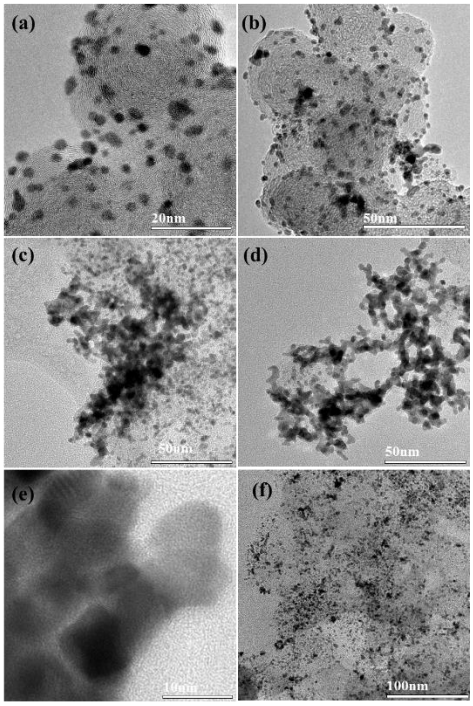

Figure 4-32. (a,b) Typical TEM images of Pt/C before cycling. (c-f) Representative TEM images of Pt/C after 5000 cycles.

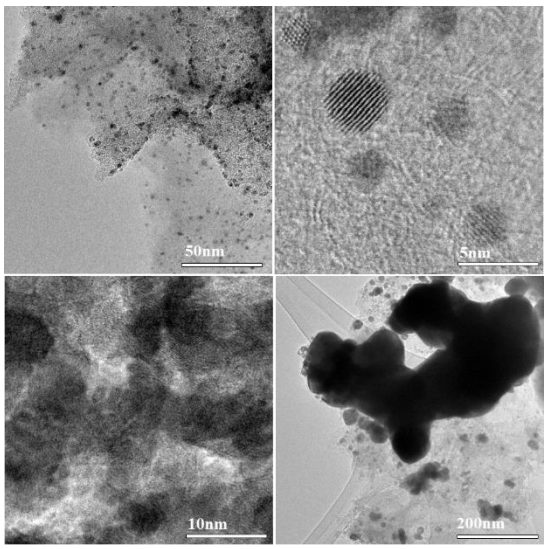

Figure 4-33. (a, b) Typical TEM images of PtCo/NPC before cycling. (c-d) Representative TEM images of PtCo/NPC after 5000 cycles.

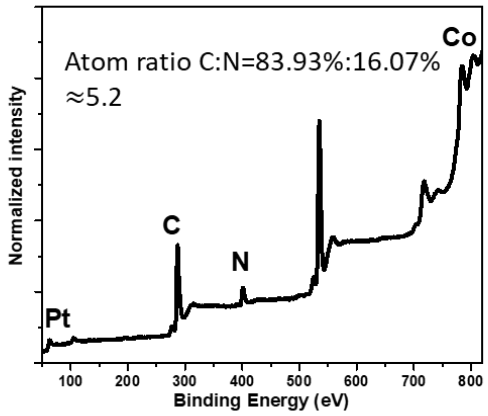

Figure 4-34. The XPS spectrum of H-PtCo@Pt_1N-C.

4.4. Conclusion

In summary, based on the participation of Pt salt in the coordination between methylimidazolate anions and cobalt cations, ultra-refined H-PtCo@Pt_1N-C has been successfully constructed. Due to the synergistic effects between the hollow PtCo alloy cores and Pt single atoms/N co-doped C shells, the H-PtCo@Pt_1N-C shows high mass activity over 10000 cycles in $HClO_4$ solution and excellent ORR performance in organic electrolytes as well. This pioneering strategy will be expanded in attempts to develop a range of bimetallic catalysts via introducing noble metal compounds during the fabrication of various metal-organic frameworks (MOFs). More efforts will be subsequently devoted to discerning the synthesis mechanisms and investigating their ORR performance for practical applications.

Chapter 5

5. Ordered Platinum-Bismuth Intermetallic Clusters with Pt-skin for Highly Efficient Electrochemical Ethanol Oxidation Reaction

5.1. Introduction

Fuel cells have been gaining increasing attention because they are efficient and green power sources suitable for portable electronic devices and automotive applications.[187-190] In comparison with H_2 fuel cells, direct ethanol fuel cells (DEFCs), as one of the most promising renewable energy applications, have many obvious advantages, such as high energy density and inexhaustible availability from biomass.[191-192] It is widely accepted that the ethanol oxidation reaction (EOR) involves two parallel oxidation pathways: complete oxidation and partial oxidation. The complete electro-oxidation of ethanol with the transfer of 12 electrons is accompanied by breaking the C-C bond, leading to the formation of CO_2 (acid media) or CO_3^{2-} (alkaline solutions), which is the C1 pathway. For incomplete oxidation (C2 pathway), the final oxidation product of ethanol is acetate, which the reaction is involved with the transfer of $4e^-$. Despite C1 pathway possessing higher electro-efficiency, most EOR electrocatalysts prefer the C2 pathway, which incompletely utilizes ethanol to form acetate as the final oxidation

product;[193-194] According to previous reports, the proportion of Pt-based EOR electrocatalysts favoring the C1 pathway at room temperature is only 1% as the split of the C-C bond is kinetically hindered.[195-197] To improve the ability on splitting the C-C bond and its selectivity, the most effective strategy is the modification of the electronic structure of Pt based electrocatalysts by introducing Rh;[198-199] it is widely believed that synergistic reactions exist in such multicomponent systems, which could weaken the bonding of intermediates and offer additional adsorbed hydroxyl groups, OH_{ads}, to aid in the further oxidation of carbonaceous intermediates.[200] Nevertheless, the production of Rh is extremely rare, even lower than that of Pt. Rational design of electrocatalysts can reduce cost and simultaneously allow them to work via the C1 pathway, showing a very powerful objective for the EOR.

It is a remarkable fact that those electrocatalytic reactions only take place on the surface of the catalysts;[201] thus, intensive studies have been carried out to tuning the surface composition of bimetallic electrocatalysts.[202-205] The most successful bimetallic electrocatalysts for controlling surface composition is the Pt-skin structure,[206-208] which boosts the activity of electrocatalysts. Despite the fact that Pt-skin of Pt_3Co could enhance activity of EOR, it still goes through the incomplete oxidation pathway. Nevertheless, the prosperity of Pt-skin surface is dependent on the inner atoms, which cause the compressive or tensile strain of the Pt-surface; these strain effect will open up new idea to design electrocatalysts. A good example is that the PtPb/Pt core/shell nanoplates exhibit amazing activity when the materials is prepared with large biaxial tensile strain.[209] Besides, the structure of catalysis also affect their electrochemical performance; thus great attention on the morphology of electrocatalysis such as nanowires,[210, 211] nanoporous,[212, 213] and nanoclusters[214-216]

materials, are paid. Based on this view, tuning the strain effect of the Pt-skin via exploiting favorable inner atoms and controlling the structure of electrocatalysis may achieve electro-oxididation ethanol via C1 pathway without a loss of catalytic performance.

Herein, by introducing relatively cheap element Bi in the core, we report a superior catalyst with Pt-skin on ordered PtBi intermetallic (PtBi@Pt) supported on graphene matrix, which is fabricated from single-atom Pt mixed with PtBi catalyst (PtBi/SA Pt) *via* a single-atom self-assembling (SAS) method. The electrochemical performance towards the EOR of PtBi@Pt was first studied. It delivers a peak current density of 9.01 mA μg_{pt}^{-1} with much higher activity than PtBi/SA Pt and Pt/C even after stability testing, which significantly outperforms other reported catalysts for the EOR under alkaline conditions. Moreover, *in-situ* Fourier transform infrared spectroscopy (FTIR) demonstrates that the final product of the EOR is CO_3^{2-}, confirming the selectivity of the C1 pathway.

5.2. Experimental Section

5.2.1. Materials Preparation

5.2.1.1. Synthesis of *PtBi/SA Pt and PtBi@Pt*

Graphene oxide (GO) was synthesized by Hummers' method. For the preparation of single-atom Pt mixed with PtBi catalyst (PtBi/SA Pt) , the H_2PtCl_6 and $Bi(NO_3)_3{\cdot}5H_2O$ precursors, containing 0.68 mL of 0.039 M H_2PtCl_6 ethanol solution and 0.88 mL of 0.01 M $Bi(NO_3)_3{\cdot}5H_2O$ ethanol solution, respectively, were mixed, and 0.02 g of GO was dispersed in the mixture. The mixture, containing GO, Pt and

Bi precursors, were ultrasonicated until ethanol was evaporated; then the mixture was heated 12 h in an oven at 80 °C. Then, the precursors were first reduced at 600 °C in 5 vol % H_2 in nitrogen for 12 h, denoted as PtBi/SA Pt. When further reduced at 600 °C in 5 vol % H_2 in nitrogen for another 12 h, novel monatomic Pt layer on ordered PtBi intermetallic clusters (PtBi@Pt) was formed.

5.2.1.2. Synthesis of *PtBi/C-12 and PtBi/C-24*.

For synthesis of PtBi supported on XC-72, GO is replaced by carbon black XC-72, and the following processes are the same with PtBi/SA Pt, PtBi@Pt. The 12 h and 24 h thermal treatment are named as PtBi/C-12 and PtBi/C-24, respectively.

5.2.2. Characterization

The XRD experiments were carried out on a Rigaku Dmax-3C diffractometer using Cu Kα radiation (40 kV, 30 mA, λ = 0.15408 nm). The X-ray photoelectron spectroscopy (XPS) measurements were conducted on using Al Kα radiation and fixed analyzer transmission mode. The morphology of PtBi/SA Pt and PtBi@*Pt* were investigated by field emission scanning electron microscopy (SEM; JEOL JSM-7500FA), transmission electron microscopy (TEM) and high-angle annular dark field – scanning TEM (HAADF-STEM; JEOL ARM-200F, 200 keV). The sizes of the PtBi/SA Pt and PtBi@*Pt* particles were measured from about 200 nanoparticles. The loadings of Pt and Bi in the PtBi/SA Pt were determined by nergy dispersive X-ray spectroscopy (EDX) to be about 5.43% and 5.63%; and the loading of Pt and Bi for PtBi@*Pt* was 5.70% and 5.85%, respectively.

5.2.3. Electrochemical Measurements.

A glassy carbon electrode (GC) is polished by Al_2O_3 powder with 5, 1, and 0.3 mm, washed with water under the ultrasonic bath. A certain amount of catalyst (PtBi/SA Pt or PtBi*@Pt*) ink is dropped on a GC electrode, and then left it to dry. Nafion® solution is applied to form a thin layer on the surfaces of the catalysts. For comparison, the commercial Pt/C is prepared by the same process. The electrochemical measurements are conducted on a three-electrode electrochemical cell, a Pt foil as counter electrode, and linked to a PAR 263A potentiostat (EG&G). All electrode potentials have been quoted versus the mercury/mercury oxide reference electrode (Hg/HgO). The solution was de-aerated by bubbling high purity N_2 through it for 15 min before measurements; meanwhile during the experiment, a flow of N_2 is over it to form protection gas atmosphere. The electrochemical experiments are conducted at room temperature.

Electrochemical *in-situ* Fourier transform infrared (FTIR) reflection spectroscopy measurements are carried out on a Nexus 870 spectrometer (Nicolet), and the detector is a cooled MCT equipped with a liquid nitrogen. A CaF_2 disk is applied for the IR window. A thin layer configuration between the IR window with the working electrode by pushing the working electrode against the IR window before *in-situ* FTIR experiments.[217] *In-situ* FTIR spectra are collected via multi-stepped FTIR spectroscopy (MSFTIR) and single potential alteration FTIR processes. The result spectra are transferring to the relative change in reflectivity, counted as below:

$$\frac{\Delta R}{R} = \frac{R(E_S) - R(E_R)}{R(E_R)}$$

Where R(E_R) and R(E_S) are the independent beam spectra gathered at samples potential E_S and reference potential E_R.

Density functional theory (DFT) calculations

DFT are carried out on a Perdew-Burke-Ernzerhof (PBE) generalized gradient approximation (GGA) exchange-correlation functional through a Vienna Ab-initio Simulation Package (VASP) code.[218-221] A projector-augmented-wave (PAW) pseudopotential is applied to describe the core electron interaction. The cut-off energy was set as 400 eV and the *k*-point sampling for Brillouin zone was 4x4x1. Significantly, the vacuum region layers are built more than 12 Å to make sure the slab interaction is eliminated. Since PtBi is in hexagonal P63/mmc phase, the (0001) surface would be the most stable. The PtBi(0001) surface with single Pt atom site, was used as a p(2x2) supercell including 16 Pt and 12 Bi atoms. The Pt(0001) surface with two adjacent Pt atoms was modelled by adding one extra Pt atom on the single Pt atom exposed surface. The bottom two layer Pt atoms and one layer Bi atoms are fixed in the slab; meanwhile the other atoms are relaxed under the optimization process. The transition states lie in a constrained optimization approach, forcing converge criteria under the 0.05 eV/Å in modified VASP.[222-224]

5.3. Results and Discussion

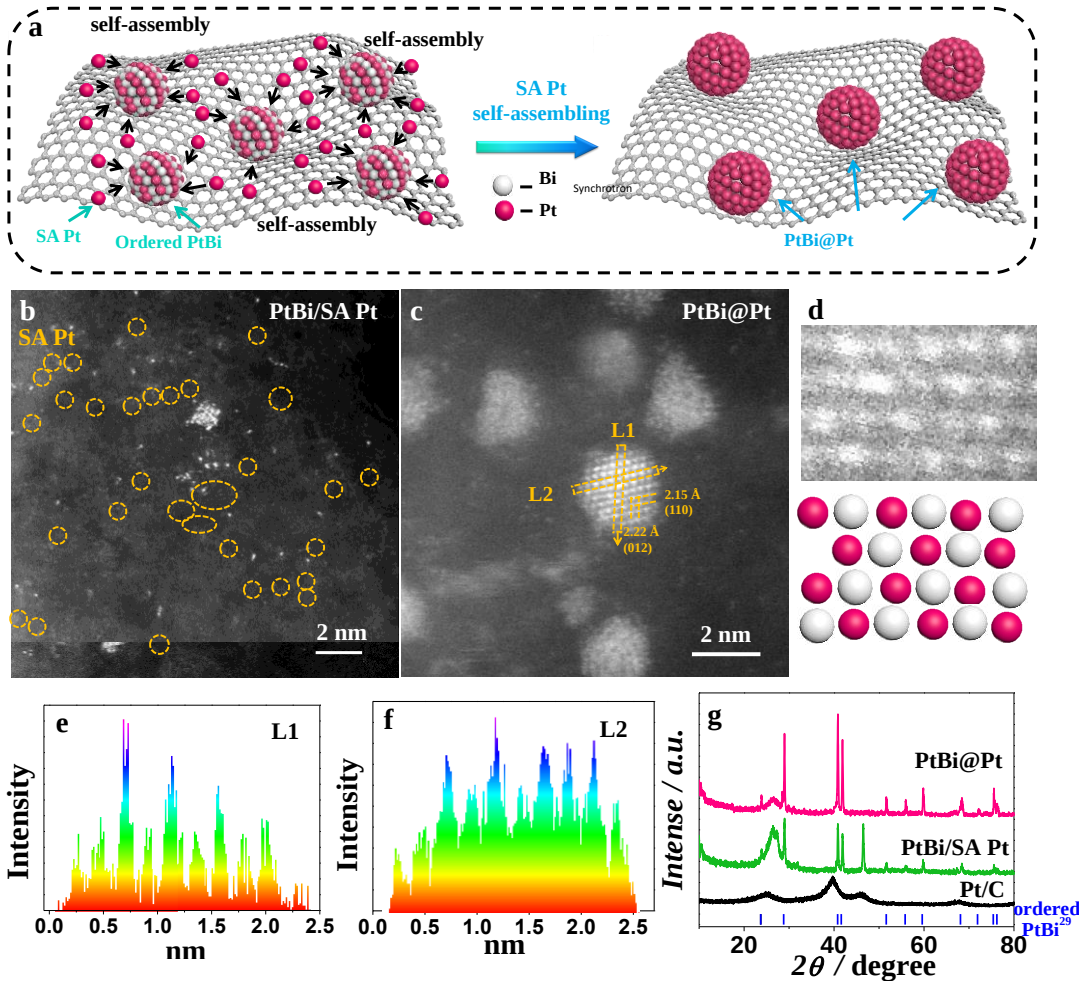

Figure 5-1. (a) Schematic illustration of the SAS method: single Pt atoms self-assembling on the surfaces of ordered PtBi intermetallic clusters to form PtBi@Pt. (b)-(c), HAADF-STEM images of PtBi/SA Pt and PtBi@Pt. (d) Superlattice feature from (c), with its model structure. (e) Intensity of L1 and L2 in (c) across the clusters. (f) XRD patterns of Pt/C, PtBi/SA Pt and PtBi@Pt, and ordered PtBi intermetallic.[215]

The core-skin PtBi@Pt was gradually synthesized by controlling thermal treatment temperatures without using any surfactant or organometallic precursors. Firstly, an

intermediate, PtBi/SA Pt, is prepared by controlled thermal treatment method at 600 ºC for 12 h. By increasing the thermal treatment time to 24 h, as illustrated in Figure 5-1a, these single Pt atoms stabilized by graphene will migrate to the surface of the ordered PtBi intermetallic, and then self-assemble to form Pt-skin on the ordered PtBi intermetallic clusters. The formation of single Pt atoms in PtBi/SA Pt is mostly ascribed to that the functional groups of graphene could stabilize the single Pt atoms;[225] and part of the Pt will be reduced together with Bi by H_2 at 600 ºC to form an ordered PtBi intermetallic. Figure 5-1b and Figure 5-2 show atomic resolution high-angle annular dark field (HAADF) scanning transmission electron microscope (STEM) images of PtBi/SA Pt, which demonstrate that isolated Pt single atoms are uniformly distributed at high density throughout the graphene, and PtBi clusters are also detected, with dimensions of ~1.3 ± 0.5 nm. There are so many single Pt atoms in the Figure 5-1b and 5-2 that we have just circled some of them, demonstrating the presence of SA Pt in PtBi/SA Pt. In particular, the Bi columns could show higher intensity than the Pt columns, due to the fact that the atomic number *Z* of Bi is 83, which is higher than that of Pt ($Z = 78$).[226] By comparing the brightness variation of Pt and Bi intensities in the HAADF images, we concluded that these single atoms were Pt. There are some Pt clusters (< 0.5 nm), containing 2-3 Pt atoms, in PtBi/SA Pt; the reason why PtBi/SA Pt exists in clusters is that it is difficult to stabilize pure metal atoms in graphene due to their mobility and instability;[217] and at such high Pt loading level (~8.24%), it is easy to form clusters.[227]

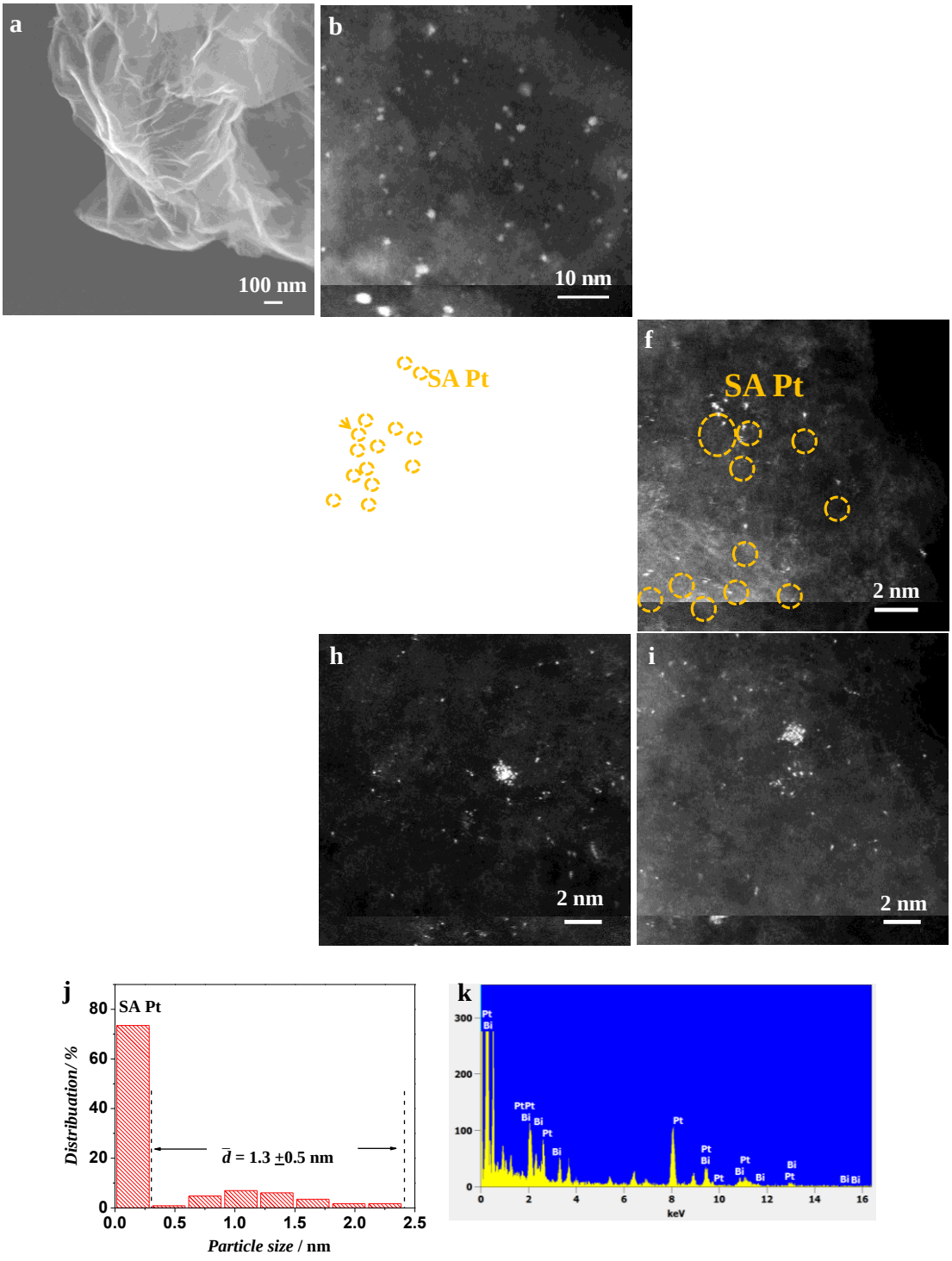

Figure 5-2. (a) SEM image and (b-i) HAADF-STEM images of PtBi/SA Pt. (j) Histogram of nanoparticle sizes of PtBi/SA Pt. (k) EDS spectrum of PtBi/SA Pt.

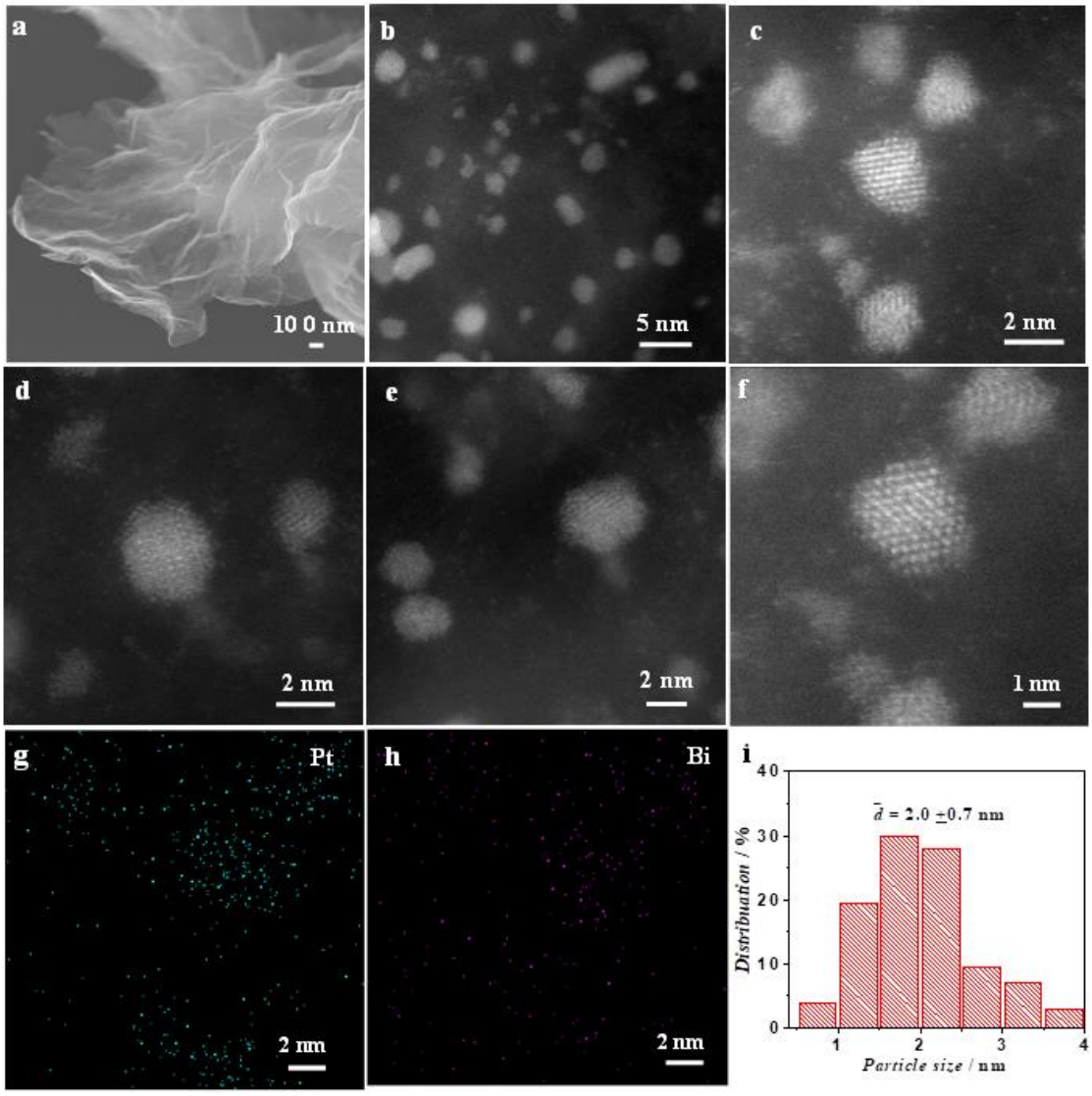

Figure 5-3. (a) SEM and (b-h) HAADF-STEM images of PtBi@Pt with elemental mapping of Pt and Bi from f; (i) histogram of nanoparticle sizes of PtBi@Pt.

The image of PtBi@Pt (Figure 5-1c) demonstrates that most of these clusters are well dispersed on the graphene, accompanied by the SA Pt self-assembling on PtBi intermetallic. To determine the monatomic nature of the Pt layer on PtBi@Pt, we examined two sites by intensity analysis, which are shown in Figure 1e. Both sites have 1-2 atomic layer of Pt; Pt and Bi appear to be distributed alternately, as shown by the alternating brightness and darkness in Figure 5-1d, indicating that these PtBi

intermetallic clusters are ordered. Furthermore, the *d*-spacings of 2.15 Å and 2.22 Å correspond to the (110) and (012) planes of PtBi intermetallic, respectively, indicating that the clusters are viewed along the [001] zone axis.[228] This inner PtBi intermetallic certain will have a tensile strain on the Pt-skin surface. The mean size of PtBi@Pt is evaluated to be ~2.0 ± 0.7 nm, as analyzed from 200 clusters (Figure 5-3), which indicates that after long time thermal treatment, SA Pt and Pt cluster could self-assemble on the surface of PtBi cluster, and form bigger clusters. We also examined many areas of PtBi@Pt, and they do not present single Pt atoms, which suggests that most of the PtBi particles were converted to PtBi@Pt. When the support is replaced by XC-72, these SA Pt, Pt clusters and PtBi clusters agglomerated to PtBi nanoparticles (Figure 5-4, 5-5, 5-6).

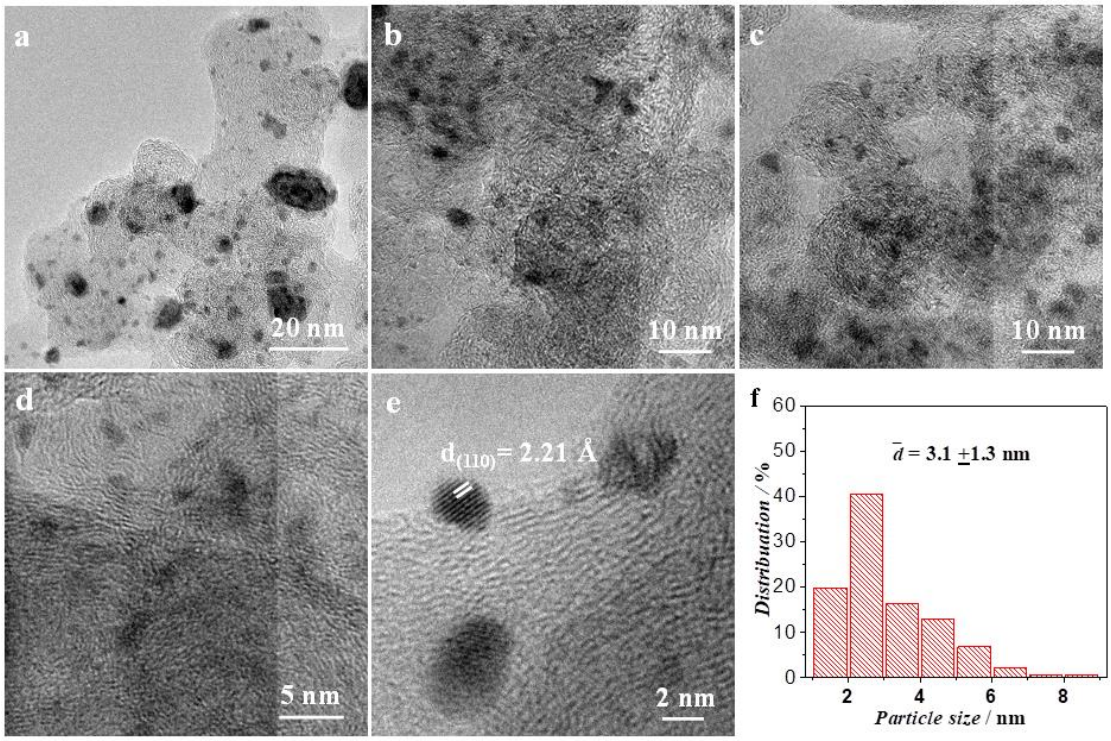

Figure 5-4. (a)-(b) TEM images of PtBi/C-12; (c) histogram of nanoparticle sizes of PtBi/C-12.

To investigate whether the single Pt could be obtained on the carbon black XC-72, which is used as support in commercial Pt/C, we prepared the PtBi/C-12 and PtBi/C-24, as shown in Figure 5-4 and Figure 5-5. However, unlike PtBi/SA Pt and PtBi@Pt, it could be clearly seen that both the nanoparticle size of PtBi/C-12 and PtBi/C-24 are inhomogeneous. Nevertheless, most of these two nanomaterials are small nanoparticle; the mean particle size of PtBi/C-12 was determined to be 2.1± 1.3 nm and PtBi/C-24 was 3.3± 2.2 nm. It also indicates that under longer thermal treatment, the nanoparticles will sinter to form large particles. This result is corresponding to the self-assembly phenomena in the PtBi/SA Pt and PtBi@Pt: via 24 h thermal treatment, the SA Pt would self-assemble on the surface of ordered PtBi nanoparticles, formation PtBi@Pt. The XRD of commercial Pt/C, PtBi/C-12, PtBi/C-24, and ordered PtBi of the reference[196] are shown in Figure 5-6. It demonstrates that the PtBi phase in PtBi/C-12 and PtBi/C-24 are also in ordered PtBi intermetallic phase, indicating that this method is an efficient way to prepare order PtBi intermetallic. From HRTEM in Figure 5-4 and Figure 5-5, the crystal grains both these two PtBi/C-12 and PtBi/C-24 were clearly observed and the lattice spacing of 0.221 nm was corresponded to the [110] planes of PtBi.

The X-ray diffraction (XRD) results in Figure 5-1f demonstrate that the PtBi phase in PtBi/SA Pt and PtBi@Pt is in good agreement with the ordered PtBi intermetallic phase.[229] The broad peak at ~26º is assigned to the graphene.

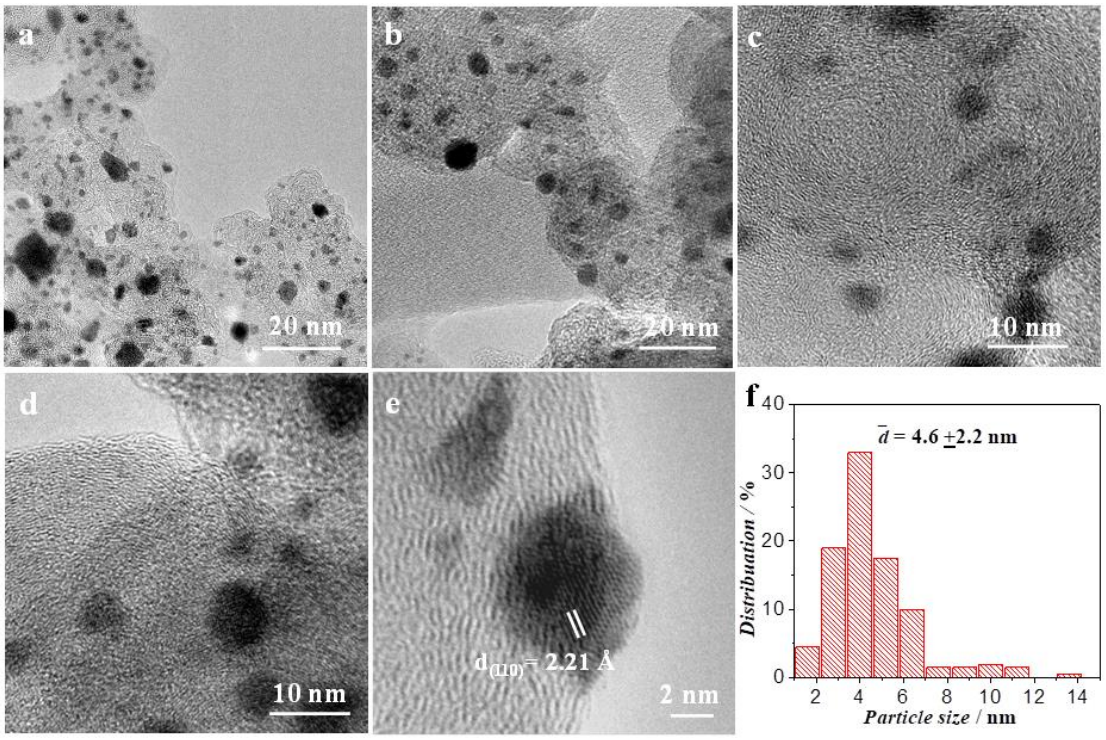

Figure 5-5. (a)-(b) TEM images of PtBi/C-24; (c) histogram of nanoparticle sizes of PtBi/C-24.

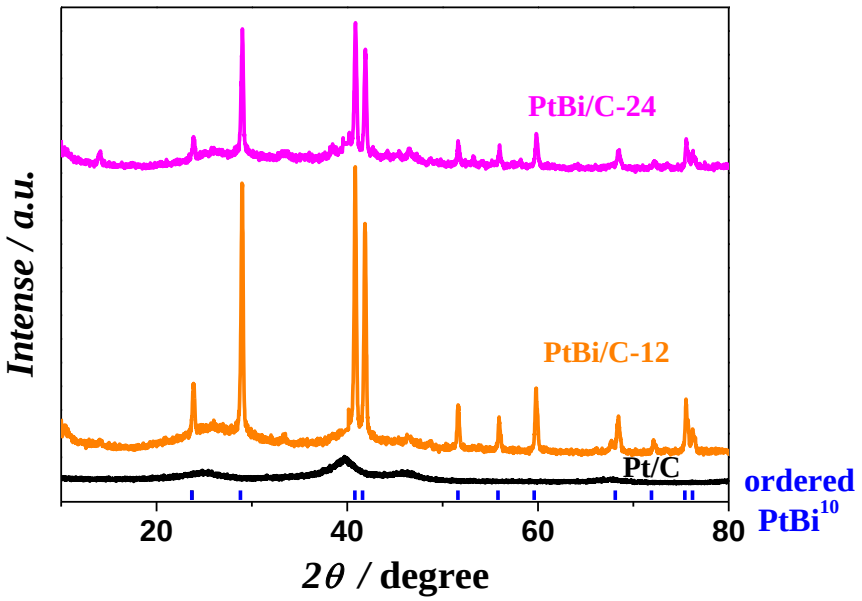

Figure 5-6. (d) Wide-angle XRD patterns of commercial Pt/C, PtBi/C-12, PtBi/C-24, and ordered PtBi of the reference[33].

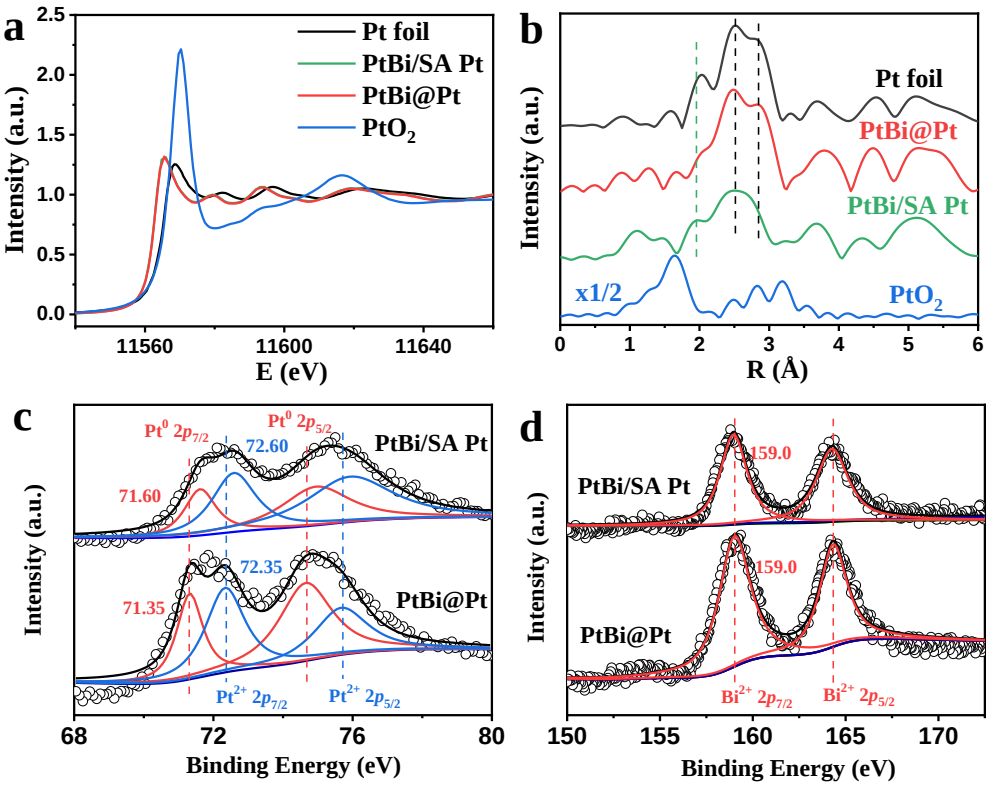

Figure 5-7. (a) XANES spectra, and (b) Fourier transform EXAFS spectra at the Pt L_3-edge for the PtBi/SA Pt, PtBi@Pt, PtO_2, and Pt foil. XPS spectra of Pt 4f (c) and Bi 4f (d) for PtBi/SA Pt and PtBi@Pt.

X-ray absorption fine structure (XAFS) can probe the local atomic and electronic structures of absorbing atoms, as shown in Figure 5-7a and 5-7b. The X-ray absorption near edge structure (XANES) spectra of PtBi@Pt and PtBi/SA Pt were similar to that of Pt foil (Figure 5-7a), suggesting that the Pt species in PtBi@Pt and PtBi/SA Pt may be mainly in the metallic state. Note that the first peaks of PtBi@Pt and PtBi/SA Pt both were at 11565.5 eV, left shifted towards that of Pt foil (11568.4 eV) and PtO_2 (11570.3 eV). This result may be attributed to the formation of Pt-Bi bonds. As shown

in the Extended X-Ray absorption fine structure (EXAFS) spectrum in R space (Figure 5-7b), PtBi/SA Pt presented a weak peak at 1.96 Å from the Pt-O shell, suggesting the presence of single Pt atoms.[230, 231] Another prominent peak at 2.52 Å was observed in PtBi/SA Pt, which was attributed to the presence of Pt-Pt bonds.[231,232] It also suggested that the PtBi/SA Pt contains both single Pt atoms and PtBi clusters. Noted that the spectrum of PtBi@Pt is similar to that of Pt foil, indicating that there were no single Pt atoms, in correspondence with the STEM results. X-ray photoelectron spectroscopy (XPS) is applied to investigate the chemical states of Pt and Bi, as shown in Figure 5-7. The Pt $4f_{7/2}$ spectrum can be deconvoluted into pure Pt (Pt^0) and Pt^{2+}; the binding energy (BE) of Pt^0 in PtBi/SA Pt and PtBi@Pt are 71.60 and 71.35 eV, respectively. Interestingly, the BE of Pt^0 in PtBi@Pt is near to that in pure Pt (71.2 eV), which indicates that the states of PtBi@Pt are close to those of metallic Pt. In contrast, the BE of Pt^0 in PtBi/SA Pt is the highest; the difference in the values indicates that Pt in the ordered PtBi intermetallic has a strong interaction with Bi and that single Pt atoms are oxidized as Pt^{2+} (i.e. PtO).[233] The XPS reflects the overall state of materials, thus demonstrating that it is mainly single Pt atoms that self-assemble to form the Pt-skin on PtBi@Pt. The Bi XPS spectrum in PtBi/SA Pt and PtBi@Pt is similar (Figure 5-7b). Both of them only have Bi^{3+}, and the BE is 159.0 eV; this also demonstrates that there is a strong interaction between Pt and Bi in the ordered PtBi intermetallic.[234]

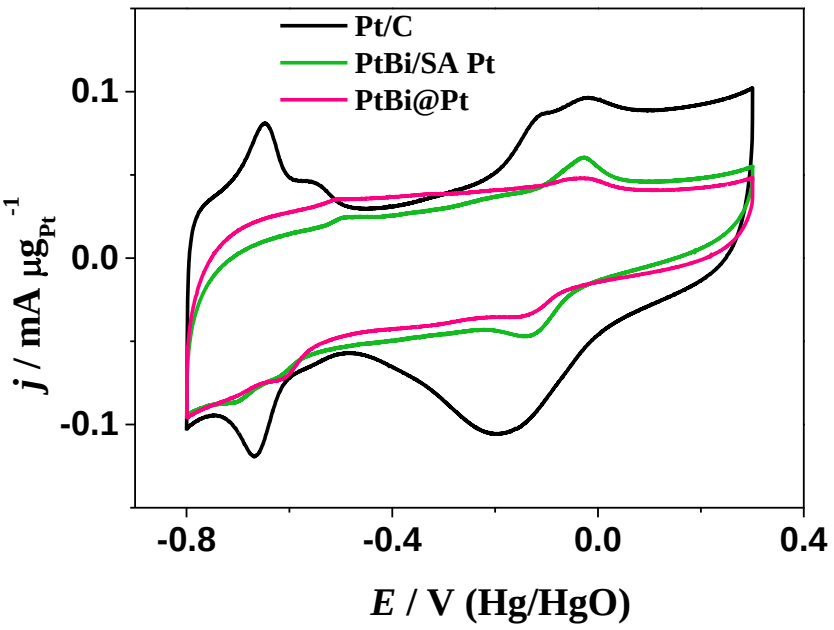

Figure 5-8. (a) Cyclic voltammograms of catalysts in 1 M KOH, 50 mV s^{-1}: Pt/C (black line), PtBi/SA (green line), and PtBi@Pt (red line).

Cyclic voltammograms (CVs) of Pt/C, PtBi/SA Pt and PtBi@Pt in 1 M KOH solution are shown in Figure 5-8, where neither of the PtBi catalysts show any apparent hydrogen adsorption or desorption compared with Pt/C. This result indicates that the presence of Bi in the core would modify the electron state of the Pt surface and block the sites for adsorbing monatomic hydrogen, H_{ads}. A similar characteristic has also been observed for the Pt-skin of Pt_3Co and Pt_3Ni, [193,201] which also suggests the presence of Pt-skin on the PtBi@Pt. Thus, the CV properties of both PtBi/SA Pt and PtBi@Pt could be assigned to the formation of ordered PtBi intermetallic.[221, 201]

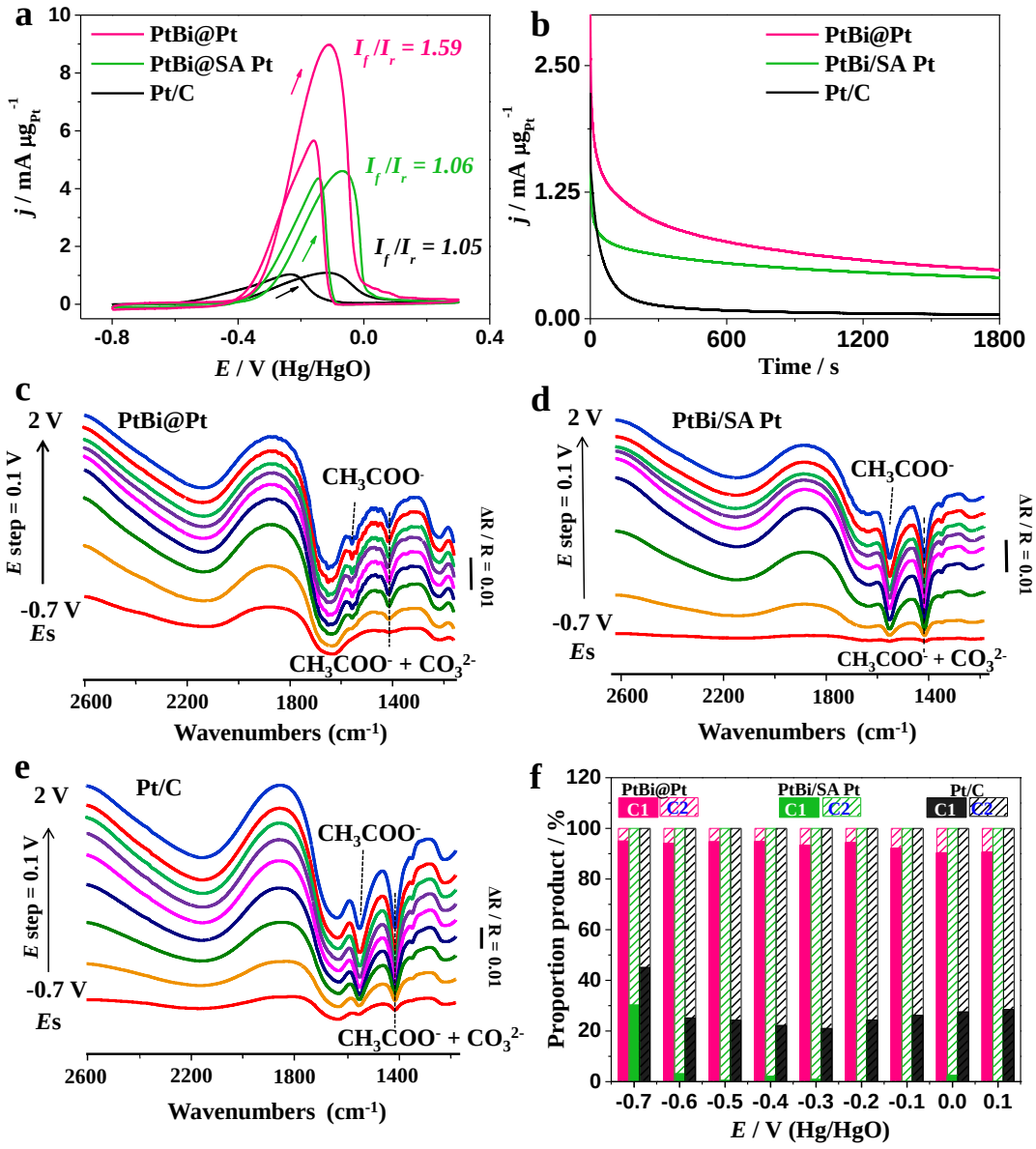

Figure 5-9. CVs (a) and current-time curves (b) of PtBi@Pt, PtBi/SA Pt, and Pt/C in 1 M KOH + 1 M CH_3CH_2OH solution, 50 mV s^{-1}. (c)-(e), *in-situ* mass spectroscopy (MS) FTIR spectra of PtBi@Pt (c), PtBi/SA Pt (d), and Pt/C (e) in 1 M KOH + 1 M CH_3CH_2OH. (f) Proportions of production from the C1 or C2 pathways estimated based on the *in-situ* MS-FTIR reaction products.

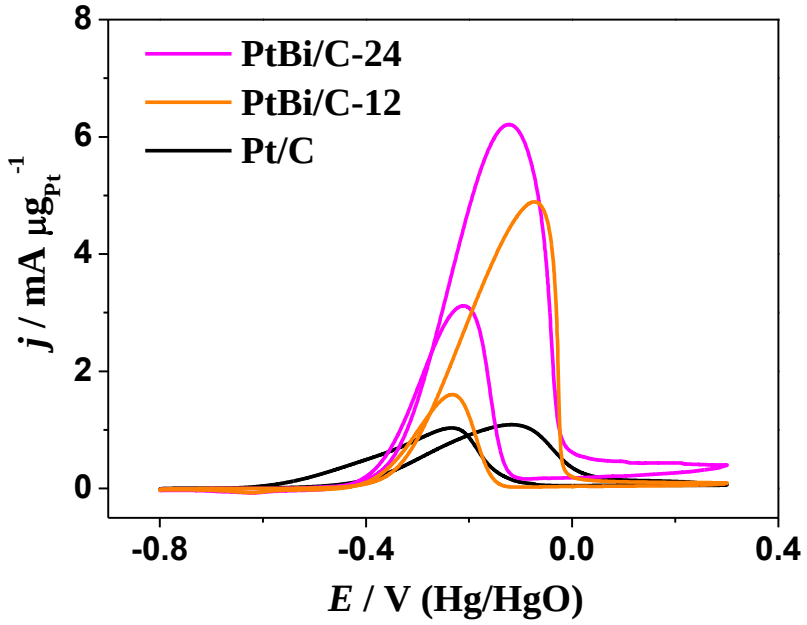

Figure 5-10. Cyclic voltammograms of catalysts in 1 M KOH + 1 M CH_3CH_2OH, 50 mV s^{-1}: Pt/C, PtBi/C-24, and PtBi/C-12.

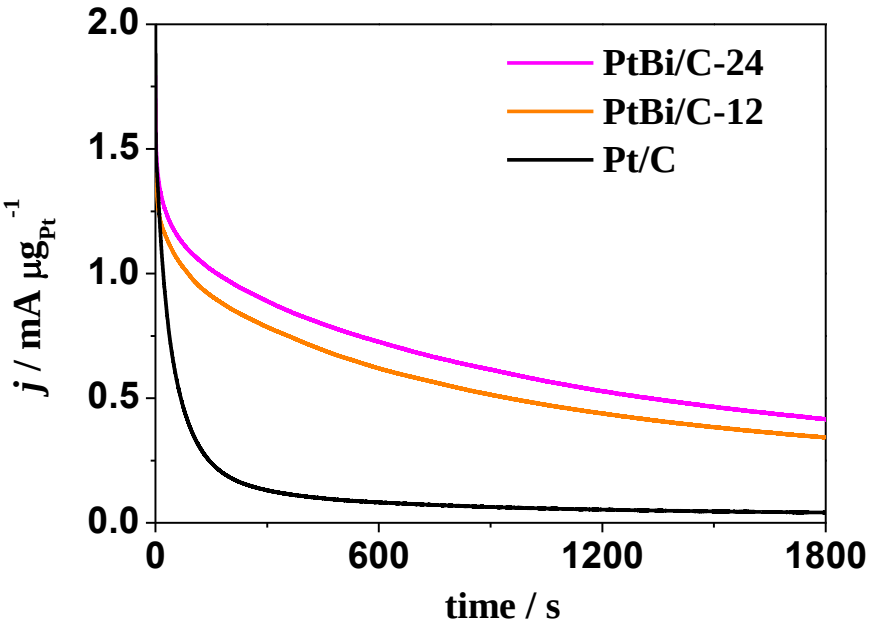

Figure 5-11. The current-time curves of catalysts in 1 M KOH + 1 M CH_3CH_2OH, 50 mV s^{-1}: Pt/C, PtBi/C-12, and PtBi/C-24.

The electrocatalytic characteristics of the EOR for these three catalysts were investigated in a basic medium (1 M CH_3CH_2OH and 1 M KOH), as shown in Figure 5-9a, Figure 5-10 and 5-11. All of them exhibited one forward scan peak, corresponding to the oxidation of CH_3CH_2OH to intermediate products[235, 236] and one reverse scan peak, typically assigned to the further oxidation of intermediate products.[235, 236] Significantly, PtBi@Pt shows the highest peak current in the forward anodic scan of 9.01 mA μg_{pt}^{-1} at -0.114 V, when compared with PtBi/SA Pt (4.69 mA μg_{pt}^{-1} at -0.067 V), Pt/C (1.09 mA μg_{pt}^{-1} at -0.119) (Figure 5-12), and results in the recent literatures (Table 5-1).

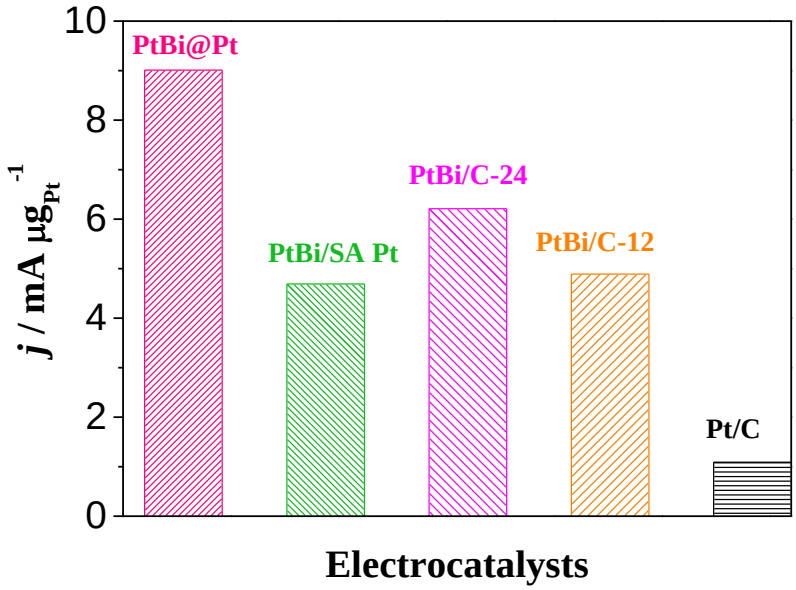

Figure 5-12. The comparison of mass activities for these electrocatalysts: PtBi@*Pt*, PtBi/SA Pt, PtBi/C-24, PtBi/C-12, and Pt/C at their peak current.

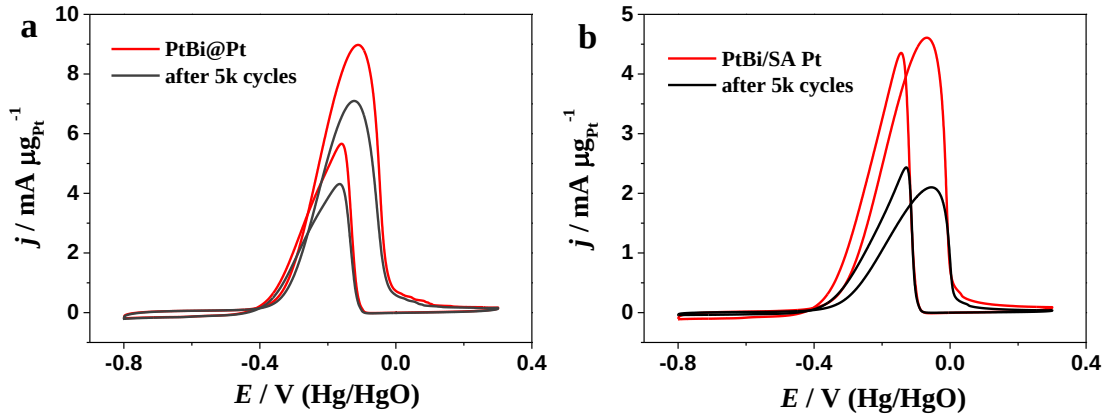

Figure 5-13. CVs of PtBi@Pt (a) and PtBi/SA Pt (b) before and after 5000 potential cycles between -0.4 and 0.1 V versus Hg/HgO in 1 M KOH + 1 M CH_3CH_2OH solution; scan rate: 50 mV s^{-1}.

The electrocatalytic characteristics of the EOR for PtBi/C-24 and PtBi/C-12 in 1 M CH_3CH_2OH and 1 M KOH is shown in Figure 5-10. Significantly, the PtBi/C-24 electrocatalyst shows the higher peak current in the forward anodic scan of 6.21 mA μg_{pt}^{-1} at -0.123 V, when compared with PtBi/C-12 (4.89 mA μg_{pt}^{-1} at -0.074 V), Pt/C (1.09 mA μg_{pt}^{-1} at -0.119). The current-time curves at -0.3 V (Hg/HgO) on PtBi/C-24 and PtBi/C-12 catalysts at room temperature are shown in Figure S8. After 1800 s, the activity of PtBi/C-24 is still higher than those of PtBi/C-12 and Pt/C, demonstrating that PtBi/C-24 possesses better operation stability. The high activity of PtBi/C-24 could be attributed that the surface composition of PtBi/C-24 may via a similar thermal treatment, formation of Pt-rich surface. To get a better understanding of the catalytic activity of these five catalysts for EOR, the current peak of mass activity at 0.90 V was calculated in Figure 5-12. The mass activity increased in the sequence: Pt/C < PtBi/SA Pt ≈ PtBi/C-12 < PtBi/C-24 < PtBi@Pt. This result also indicates that the PtBi@Pt, with well-sized-distribute, shows better electrochemical performance than that of uneven distributed of PtBi/C-24. It is widely acknowledged that the ratio of the

forward peak current (I_f) to the reverse peak current (I_r) reflects the toleration of electrocatalyst against poisoning.[237] The value of I_f / I_r for PtBi@Pt is 1.59, which is higher than those of PtBi/SA Pt (1.06) and Pt/C (1.05), indicating that the PtBi@Pt electrocatalyst has the best tolerance to intermediate accumulation. The current-time curves at -0.3 V (Hg/HgO) on these three catalysts at room temperature are shown in Figure 5-9b. After 1800 s, the activity of PtBi@Pt is still higher than those of PtBi/SA Pt and Pt/C, demonstrating that PtBi@Pt possesses better operation stability. To further investigate the electrochemical durability of the PtBi@Pt and PtBi/SA Pt, they were evaluated in the potential range between -0.4 and 0.1 V versus Hg/HgO for 5,000 cycles in 1 M KOH solution, as shown in Figure 5-13. After 5,000 sweeping cycles, PtBi@Pt also maintains a high mass activity of 7.08 mA μg_{Pt}^{-1}; under the same conditions, however, the PtBi/SA Pt only retains 2.10 mA μg_{Pt}^{-1}, representing almost 50 % loss of mass activity. This high activity of PtBi@Pt could be attributed to the tensile strain of the Pt-skin surface arising from the inner ordered PtBi intermetallic,[229,238] which may promote ethanol dehydrogenation; meanwhile, the better stability of PtBi@Pt may also originate from its special structure, in which the Pt-skin structure could prevent the loss of the interior Bi during CV and durability testing.

Unlike Pt-skin surface of Pt_3Co@Pt only enhancing the activity via C2 pathway,[7] the Pt-skin surface of PtBi@Pt may both improve the acitivity and selectivity of EOR. To evaluate the selectivity towards ethanol oxidation, *in-situ* FTIR was applied to identify the intermediate and final products of these three samples, as shown in Figure 5-9c-e. The signature peak at 1550 cm^{-1}, found in all three samples, is attributed to the asymmetric stretching vibrations of the carboxyl group in CH_3COOH, which is usually

applied to the analysis of incomplete oxidation of CH_3CH_2OH.[193, 239] Notably, in none of these three samples can the signature peak of CO_2 (2345 cm^{-1}) be detected, suggesting that the KOH in solution reacts with CO_2, leading to the formation of CO_3^{2-}. Therefore, the symmetric stretching band of COO at 1415 cm^{-1} is coming from the superposition of bands from CO_3^{2-} and CH_3COO^-, which represents the overall electro-oxidation of CH_3CH_2OH.[239] To investigate the capability for C-C bond breaking in CH_3CH_2OH, we compared the ratio of integrated intensities associated with total electro-oxidation (1415 cm^{-1}) and incomplete electro-oxidation (1550 cm^{-1}) at various working potentials, as shown in Figure 5-9f. The results show that the value in PtBi@Pt for the C1 pathway is above 90%, demonstrating that the compressive strain of the Pt-skin surface influenced by inner PtBi intermetallic could enhance the selectivity towards the C1 pathway. Remarkably, the values for the C1 pathway in PtBi/SA Pt and Pt/C are reduced to 30% and 50%, respectively, indicating that the activity of both of them towards ethanol electro-oxidation is primarily via the C2 pathway, especially at high potential (> -0.7 V). This result suggests that, although single Pt atoms and ordered PtBi intermetallic have high reactivity, they show very poor EOR selectivity; when single Pt atoms are segregated on the surface of PtBi intermetallic, PtBi@Pt not only has high activity, but also could completely oxidize ethanol to CO_3^{2-}.

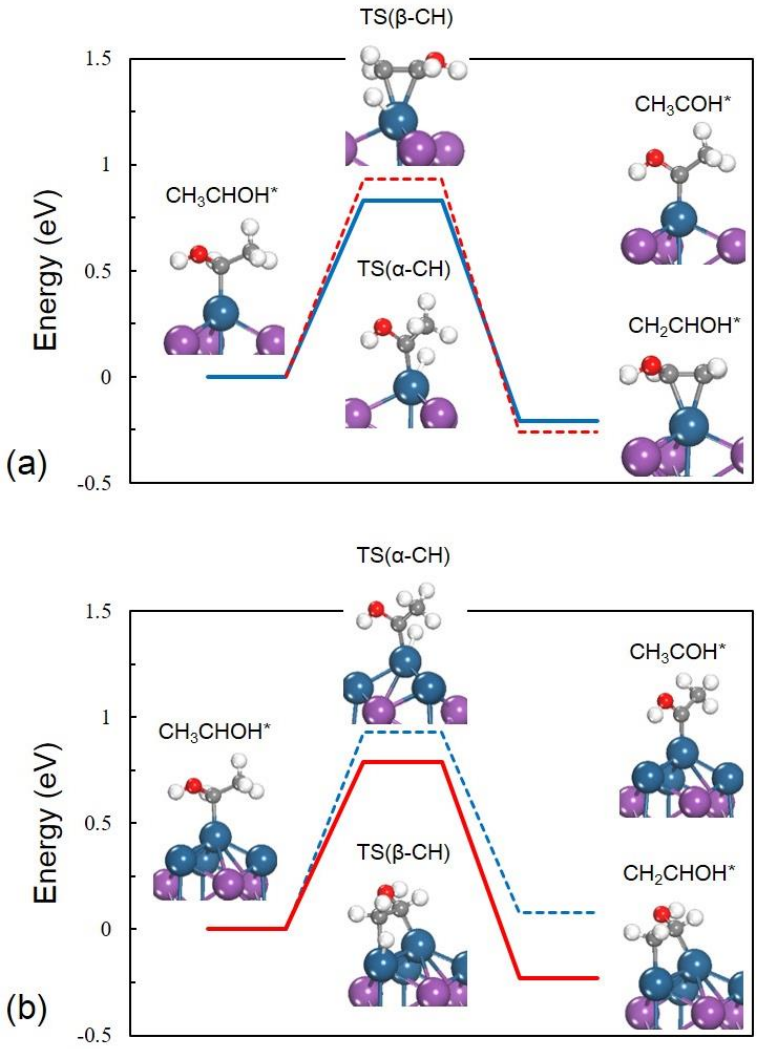

Figure 5-14. Energy profiles for the competitive α- (in blue) and β- (in red) dehydrogenation pathways on (a) PtBi(0001) and (b) Pt-PtBi(0001), respectively. The favored kinetic pathway is illustrated by a solid line and the unfavored one by a dashed line. The optimized intermediates and transition states are inserted. Blue: Pt; purple: Bi; red: O; grey: C; white: H.

According to the theoretical model proposed in the literature,[240] the C1 product selectivity can be estimated quantitatively by comparing the barrier difference between α-dehydrogenation and β-dehydrogenation, i.e., $\Delta E_a = E_{a,\alpha\text{-CH}} - E_{a,\beta\text{-CH}}$, where E_a is the activation energy. As shown in Figure 5-14 and Figure 5-15, on the PtBi(0001) surface

with a single Pt site, the α-C-H bond breaks to form CH_3COH* ($E_{a,\alpha\text{-}CH}$ = 0.83 eV), which is more kinetically favored than the β-C-H bond ($E_{a,\ \beta\text{-}CH}$ = 0.93 eV), formation of CH_2CHOH*; as a result, the ΔE_a of the PtBi(0001) surface with a single Pt site is -0.1 eV, indicating that CH_3CO* would be the predominate product on the surface derived from ethanol decomposition, which could then be oxidized to acetate. When more Pt atoms are adsorbed at the adjacent position near the single Pt site, impressively, the new surface is found to be very reactive towards the β-C-H bond breaking process; the calculated barrier for CH_2CHOH* formation is 0.79 eV, which is lower than 0.93 eV for CH_3COH* formation. Therefore, the ΔE_a of the Pt-PtBi(0001) is 0.14 eV, indicating that it mainly product is CH_2CHOH*, which will form CH_2CO*; this result also confirms that the tensile strain of the Pt-skin surface from the inner PtBi intermetallic would help the dehydrogenation of ethanol. Significantly, the CH_2CO* acts as a further precursor for C-C bond splitting, demonstrating that it could proceed via the C1 pathway. This result is corresponding to the *in situ* FTIR results, demonstrating that ethanol will be oxidized to CO_2 on PtBi@Pt.

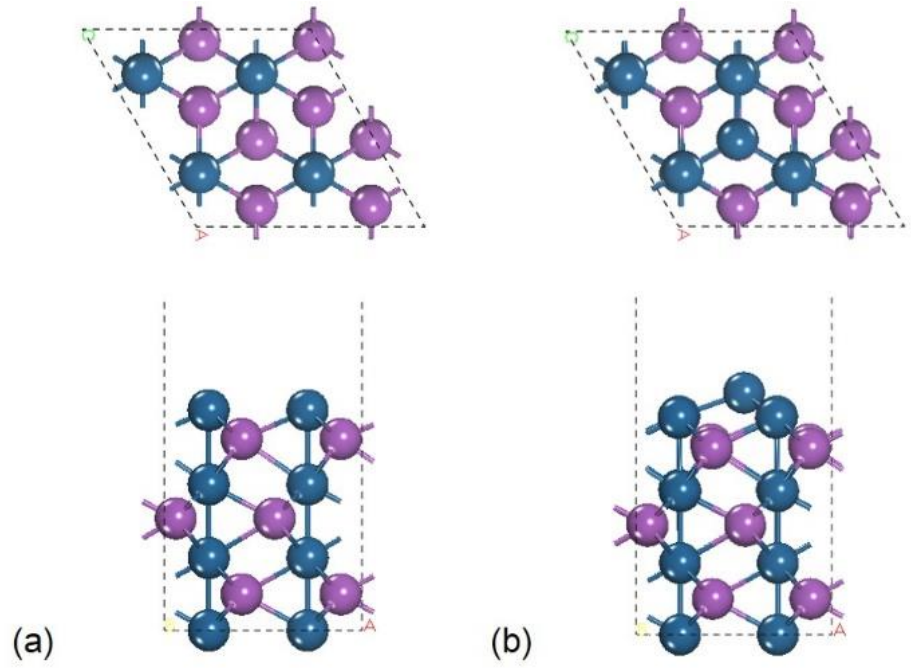

Figure 5-15. Top and side views of models of PtBi(0001) surface (a) with single Pt atom site, and (b) with two adjacent Pt atoms site. Blue: Pt; purple: Bi.

Table 5-1. A recent literature survey of the activity of EOR electrocatalysts in alkaline electrolytes.

Electrocatalyst	**Electrolyte**	**Mass activity of Peak current (mA μg_{Pt}^{-1})**	**References**
PtBi@Pt	**1 M KOH + 1 M CH_3CH_2OH**	**9.01**	**This work**
Pd/Ni(OH)$_2$/rGO	1 M KOH + 1 M CH_3CH_2OH	1.546	*Adv. Mater.* **2017**, *29*, 1703057

$Pt_{68}Cu_{32}$ nanoalloy	0.5 M KOH + 0.5 M CH_3CH_2OH	2.33	Nanoscale, **2017**, *9*, 2963-2968
Pt black-PbO_2	0.1 M KOH + 0.1 M CH_3CH_2OH	1.162	*New J. Chem.*, **2017**, *41*, 12123
PdCo@NPNCs	1 M KOH + 1 M CH_3CH_2OH	1.245	*J. Mater. Chem. A*, **2017**, *5*, 10876
Au@(Pt + Pd)/C	1 M NaOH + 1 M C_2H_5OH	8.99	*Chem. Commun.*, **2016**, *52*, 374
Pd_2S/C	0.5 M KOH + 0.5 M CH_3CH_2OH	0.162	*J. Power Sources* **2016**, *336*, 1.
Pd_3Sn_1/NG	1 M KOH + 1 M CH_3CH_2OH	3.0	*RSC Adv. 2016, 6, 19314*
$PdCu_2$	0.1 M KOH + 0.1 M CH_3CH_2OH	1.60	*ACS Appl. Mater. Interfaces* **2016**, *8*, 34497.
PdCo NTAs/CFC	1 M KOH + 1 M CH_3CH_2OH	1.49	*Angew. Chem. Int. Ed*. **2015**, *54*, 3669
Pd–PEDOT/GE	1.0 M NaOH + 1.0 M ethanol	4.50	*J. Mater. Chem. A* **2015**, *3*, 1077.

Pd/CB	1.0 M NaOH + 1.0 M ethanol	5.00	*Int. J. Hydrogen Energy* **2015**, *40*, 12382.
Pt-Pd (1:3)/RGO/GC	1 M KOH + 1 M CH_3CH_2OH	1.487	*ACS Appl. Mater. Interfaces* **2014**, *6*, 3607
Pd@CN	1 M KOH + 1 M CH_3CH_2OH	2.52	*Chem. Commun.*, **2014**, *50*, 12637
Pt-Pd CANs	0.5 M KOH + 1 M CH_3CH_2OH	1.08	J. Mater. Chem. A, **2014**, *2*, 13840
Pd-Ag nanoparticles	1 M KOH + 1 M CH_3CH_2OH	1.6	*J. Power Sources* **2014**, *263*, 13.
$Pt_{55}Pd_{45}$ bimetallic alloy nanowires	1 M KOH + 1 M CH_3CH_2OH	1.02	*Adv. Mater.* **2012**, 24, 2326
$Bi_{38}@Pt_{63}/C$	0.3 M C_2H_5OH + 0.5 M NaOH	4.8	*Electrochim. Acta* **2017**, 258, 933
$Pt_{50}Bi_{50}/C$	1 M KOH + 1 M CH_3CH_2OH	0.017	*Electrochem. Commun.* **2011, 1**3, 143.

$Pt_{55}Pd_{38}Bi_7$/C	1 M KOH + 1 M CH_3CH_2OH	2.3	*RSC Adv.,* **2016**, 6, 58336.
$Pd_{95}Bi_5$/C	1 M KOH + 1 M CH_3CH_2OH	0.018	*Int. J. Hydrogen. Eenerg.* **2011,** 36, 10522.
$Pd_{20}Bi_1$/C	1 M KOH + 1 M CH_3CH_2OH	5.67	*Electrochim. Acta* **2013**, 99, 22

5.4. Conclusion

In summary, the core-skin PtBi@Pt was successfully prepared by the single Pt atoms self-assembling on the surface of PtBi intermetallic using the SAS method. Rather than utilizing compressive strain to enhance the EOR activity, the tensile strain of Pt-skin surface of PtBi@Pt was realized to achieve a very high mass activity of 9.01 mA μg_{Pt}^{-1}, which is 8.26 times higher than that of Pt/C towards the EOR. Remarkably, the *in-situ* FTIR spectra and DFT results demonstrate that PtBi@Pt has better selectivity towards the EOR, which mainly proceeds via the C1 pathway, while PtBi/SA Pt and Pt/C mainly go through the C2 pathway. Such Pt-skin surface synthesized from a general approach is promotional to enhance the catalytic activity and selectivity toward these multimetal active sites chemical reactions.

Chapter 6

6. π -electron assisting preparation of single-atom sites on a heterogeneous support as bi-functional electrocatalysts towards full water splitting

6.1. Introduction

Single-atom catalysts (SACs) hold a great promise for maximizing catalytic efficiency of supported metals by achieving the ultimate utilization of every single atom.[241,242, 243-246] Multifarious single atoms have been fabricated and demonstrated their ultimate size effects, such as Pt_1[247-254], Ru_1[255,256], Ir_1[257], Fe_1[258,259] and Pd_1[250,260-263]. Significantly, various single atoms show remarkable catalytic activity and selectivity toward a variety of electrocatalytic reactions, including hydrogen evolution reaction (HER)[12], oxygen evolution reaction (OER)[264,265], oxygen reduction reaction (ORR)[249,255], CO oxidation reaction[247,253,266], CO_2 reduction reaction [250], water gas shift reaction[257], and hydrogenation[261] with a high efficiency. It is noteworthy that the same foreign isolated substitutions can be tuned to show distinguishing catalytic activities via anchoring on different supports. For instance, Yang *et al*. via anchoring single-atom Pt catalyst on two different supports of titanium carbide and titanium nitride toward ORR reaction, which shown the oxygen reduction current density of Pt_1/TiC was almost two times

larger than that of Pt_1/TiN at all potential ranges, suggesting a higher selectivity on producing H_2O_2 [267]. It is believed that the strong metal support interactions (SMSI) can change the physical orbital science, band gap, electronic density, and surface chemistry of the SACs, thus exhibiting different catalytic selectivity for a wide variety of chemical reactions. On the other hand, electrochemical water splitting is regarded as the most efficient and clean technology for high-purity hydrogen generation. It can be utilized to convert intermittent renewable energy such as solar and wind into chemical energy stored by hydrogen fuel as well.[268,269] The overall water splitting involves active electrocatalysis on anodic OER and cathodic HER. Nevertheless, it is rare that a catalyst is able to simultaneously and efficiently accelerate both OER and HER. Typically, Ir and Ru-based catalysts show superior performance for OER, while Pt-based catalyst exhibits high activity toward HER.[270,271] It is thus ideal but extremely challenging to construct a bi-functional catalyst with synergistic dual active sites that can simultaneously promote HER and OER.

Herein, zeolitic imidazolate framework-67 (ZIF-67) can serve as an ideal precursor to fabricate single metal atoms. It possesses unique π-electrons in the pentagon imidazole as aggregation inhibitors, which can initially bond with metal ions via strong π conjunction, thus successfully stabilize the single metal atom species. Moreover, the ZIF-67 can transform into a heterogeneous support with Co nanoparticles dispersed in N-doped porous carbon (Co/NC). This unique Co/NC support provides two distinct domains for generally anchoring various single metal ions (M_1= Pt_1, Ir_1, Pd_1, Ru_1, Fe_1, and Ni_1), leading to the formation of a serials of M_1@Co/NC catalysts. As shown in Figure 6-1, in a M_1@Co/NC catalyst, both of Co and NC can serve as substrates for single atoms, respectively, which subsequently corresponds to two different active

sites of M_1@Co and M_1@NC, simultaneously accelerating OER and HER. Moreover, the M_1@Co/NC catalysts demonstrate unique three dimensional (3D) isolated atomic dispersion of various metals by virtue of the distinctive tunneling effects of ZIF-67 structure. Significantly, the obtained Ir_1@Co/NC catalyst displays the highest activity toward overall water splitting, achieving an applied potential of 1.603 V vs. reversible hydrogen electrode (RHE) with 10 mA cm^{-2} in 1.0 M KOH solution. The catalytic activities are further clarified by the density functional theory (DFT) calculations, indicating that the $IrNC_3$ are responsible for the efficient HER capability while the Ir@CoO (Ir) site is beneficial for the OER.

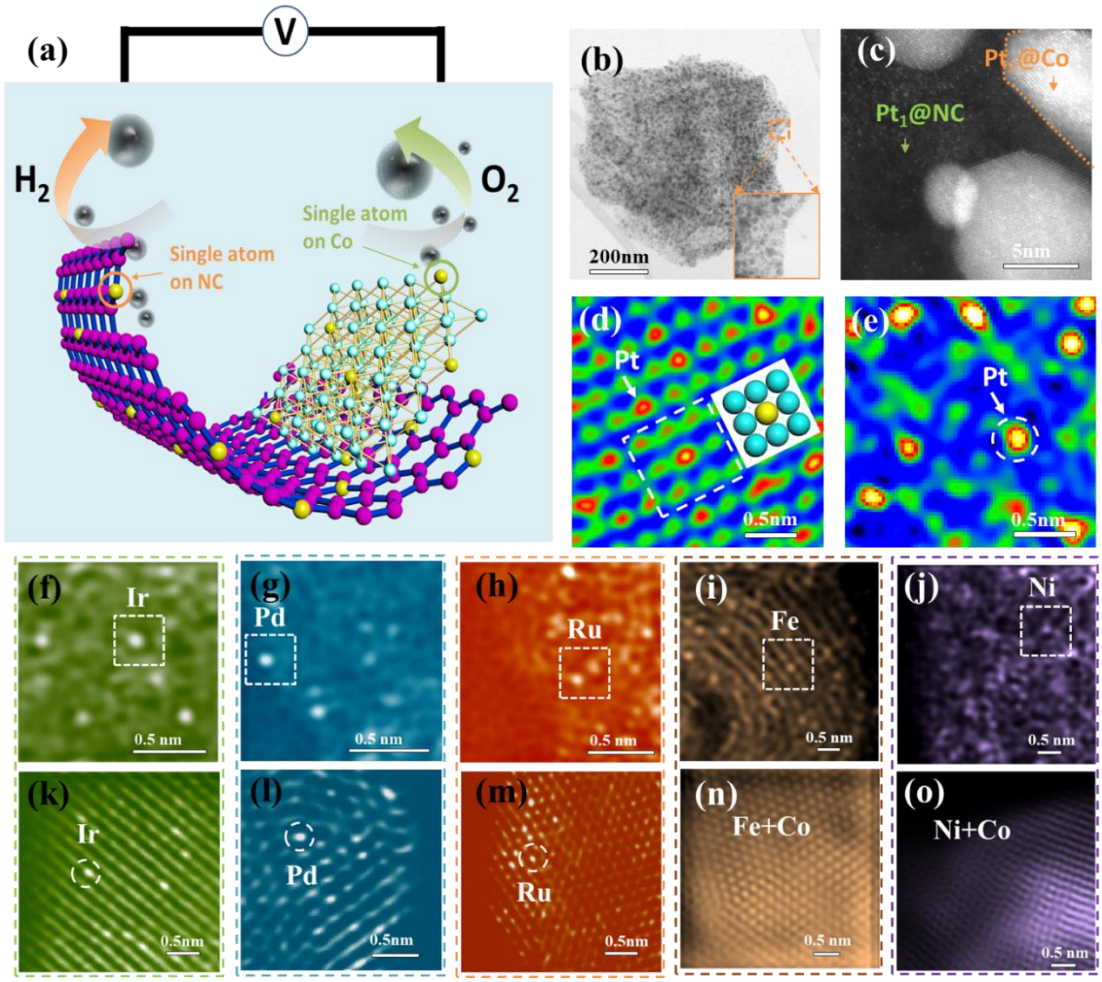

Figure 6-1. Detailed atomic resolution HAADF-STEM characterization and composition of M_1@Co/NC. (a) The illustration of the working mechanism of the prepared electrodes. (b) Annular bright field image (ABF)-STEM images of Pt_1@Co/NC with low magnification. (c) HAADF-STEM image of Pt_1@Co/NC with high magnification. (d) HAADF-STEM image of Pt_1@Co region, (e) FFTI-HAADF image of Pt_1@NC area. FFTI-HAADF images of (f) Ir_1, (g) Pd_1, (h) Ru_1, (i) Fe_1, and (j) Ni_1 on NC (above) and their corresponding FFTI-HAADF images on Co particles (below).

6.2. Experimental Section

6.2.1. Materials

Platinum(II) acetylacetonate ($C_{10}H_{14}O_4Pt$, 99%), Iridium(II) acetylacetonate ($C_{10}H_{14}O_4Ir$, 99%), Palladium(II) acetylacetonate ($C_{10}H_{14}O_4Pd$, 99%), Ruthenium (III) acetylacetonate ($C_{15}H_{21}O_6Ru$, 97%), Iron (III) acetylacetonate ($C_{15}H_{21}O_6Fe$, 99%), Nickel (II) acetylacetonate ($C_{10}H_{14}O_4Ni$, 99%), Cobalt(II) nitrate hexahydrate ($Co(NO_3)_2$ $6H_2O$, ACS reagent grade, ≥ 98%), 2-methylimidazole ($C_4H_6N_2$, 99%), Nafion@117 solution (5 wt %, dispersed in a binary solvent of water and lower aliphatic alcohols), and commercial Pt black (20 wt. % Pt loading on Vulcan XC72) and IrO_2 were purchased from Sigma-Aldrich. All the chemical reagents were used as received without any further purification.

6.2.2. Materials Preparation

6.2.2.1. Synthesis of ZIF-67

In a typical synthesis, 2-methylimidazole (1.97 g) was dissolved in a mixed solution of 30 ml methanol and 10 ml ethanol (solution A). $Co(NO_3)_2 \cdot 6H_2O$ (1.746 g) was dissolved in another mixed solution of 30 ml methanol and 10 ml ethanol. 0.125 mmol K_2PtCl_4 was dissolved in 2.56 ml deionized water (solution B). Solution A and solution B were then mixed under continuous stirring for 10 seconds, and the final solution was kept for 20 h at room temperature. The purple precipitate was collected by centrifugation, washed in ethanol several times, and dried at 80 °C.

6.2.2.2. Synthesis of (Pt, Ir, Pd, Ru, Fe, and Ni)$_1$@Co/CN

In a typical synthesis, 100 mg ZIF-67 powders mixed with 50 ml ethanol by ultra-sonification for 30 mins to form a homogeneous dispersion. 0.0075 mmol platinum (II) acetylacetonate, iridium (II) acetylacetonate, palladium acetylacetonate, ruthenium (III) acetylacetonate, nickel (II) acetylacetonate, and iron (III) acetylacetonate were then added into the dispersion with rigorously stirring until ethanol were evaporated out, forming ZIF-67-Pt/Ir/Pd/Ru/Fe/Ni mixtures respectively. Finally, the mixture was annealed at 600 °C (Pt/Ir/Pd/Ru)/700 °C (Fe/Ni) under argon for 2 h. These resultant products were denoted as (Pt/Ir/Pd/Ru/Fe/Ni)$_1$@Co/CN.

6.2.3. Characterization

The high-angle annular dark-field scanning TEM (HAADF-STEM) images and the scanning TEM energy dispersive X-ray spectroscopy (STEM-EDS) data were acquired on the transmission electron microscopy system (TEM, JEOL ARM-200F,

200 kV). The XRD patterns were collected by powder X-ray diffraction (XRD; GBC MMA diffractometer) with Cu Kα radiation at a scan rate of 3 ° min^{-1}. The bonding on Pt_1@Co/CN was determined by XPS (PHOIBOS 100 Analyser from SPECS, Berlin, Germany; Al Kα X-rays). The loading mass was determined by the inductively coupled plasma optical emission spectrometry (ICP-AES, IRIS Intrepid ER/S, Thermo Elemental). The Fourier transform infrared spectroscopy (FTIR) was performed at room temperature on a Shimadzu Prestige-21. The Raman spectroscopy was used to determine the length of bond on Jobin Yvon HR800. The secondary ion mass spectrometer (SIMS) Cameca IMS 5FE7 was applied to determine the surface and near surface composition and cluster in materials. X-ray absorption spectroscopy (XAS) experiments were carried out at the applied X-ray absorption fine structure spectroscopy (XAFS) beamline P65 at the PETRA III (Deutsches Elektronen-Synchrotron, DESY, Hamburg). The storage rings of PETRA III were operated at the electron energy of 6 GeV with a beam current of 100 mA. XAS spectra were recorded in quick-XAFS (QXAFS) method in transmission mode using an ionization chamber of Pt foil. The intensity of the monochromatic X-ray beam was monitored respectively by three consecutive ionization detectors. All the XAS spectra were processed using DEMETER software package. The data was normalized and analyzed via using Athena and Artemis software.

6.2.4. Density Function Calculation (DFT)

All the density functional theory (DFT) calculations were performed with the Vienna Ab-initio Simulation Package (VASP)[272-275]. The projector augmented wave (PAW) potentials[276] and Perdew-Burke-Ernzerhof (PBE) exchange-correlation functional[277] were adopted in the calculations with a plane wave kinetic energy cutoff of 520 eV.

The spin-polarization was also took into account and the energy converge criteria was set to be 10^{-5} eV, and the force was converged to less than 0.05 eV/Å on each ion.

A 6×6 supercell with a periodic boundary condition along the x-y plane was employed to model the infinite graphene sheet. The vacuum space was set 15 Å in the z direction, which was used to avoid the interactions between periodic images. K-space was sampled using a 3×3×1 Gamma-Centered grid. The single atom Ir is modelled as a four-coordinated structure, which is $IrNC_3$ and IrC_4.

To simulate surfaces, we applied three-dimensional slab models in this work. The (111) surface of Co was represented by a p(5×5) slab (a = 12.53 Å, b = 12.53 Å and c = 25.00 Å) with four-atomic-layer, in which Co atom on the surface was substituted by Ir atom, which is Ir-Co. During the structural optimization, the bottom two layers were kept fixed, while the other layers were allowed to relax. K-space was sampled using a 3×3×1 Gamma-Centered grid.

At about 0.2 V versus RHE, CoO layer would be generated on the surface of metal Co, while at about 1.9 V versus RHE, Co_2O_3 would be generated on the surface of Co. In the reality, 1.5V was added in the experiment. In the result, the adsorption energies of oxygen-based intermediates on the (100) surface of CoO were calculated, also in which Co atom on the surface was substituted by Ir atom, which is called Ir_1@CoO. The (100) surface of CoO was represented by p(4×4) slab with four layers thick. And the optimized lattice constants are a = b = 12.07 and c = 21.40 Å. During the structural optimization, the bottom two layer was kept fixed, while the top layers were allowed to relax. K-space was sampled using a 3×3×1 Gamma-Centered grid.

The mechanism of OER is assumed to proceed through four consecutive proton and electron transfer steps with HO*, O*, and HOO* intermediates, as shown below.

$$H_2O + * \rightarrow HO^* + H^+ + e^- \quad (1)$$

$$HO^* \rightarrow O^* + H^+ + e^- \quad (2)$$

$$H_2O + O^* \rightarrow HOO^* + H^+ + e^- \quad (3)$$

$$HOO^* \rightarrow O_2(g) + * + H^+ + e^- \quad (4)$$

where * represents the surface active site. The free energy of the various intermediates 298.15 K can be calculated by the following equation:

$$\Delta G = \Delta E + \Delta ZPE - T\Delta S - eU \quad (5)$$

where ΔE is the total energy change derived from DFT calculations, ΔZPE, ΔS, U are the zero point energy changes, the entropy changes and the applied electrode voltage, respectively, T is the temperature at 298.15 K. At a pH ≠ 0, the free energy of H^+ ions are corrected by the concentration dependence of the free energy: $\Delta G_{pH(pH)} = -kTln10 \cdot pH$.

The free energy for H* adsorption was calculated to evaluate the activity of HER according to the following equation:

$$\Delta G_{H^*} = \Delta E_{H^*} + \Delta ZPE - T\Delta S - \Delta G(pH) \quad (6)$$

ΔE_{H^*} is the adsorption energy of an H* at the active site.

First principle density functional theory (DFT) calculations have been performed to evaluate the most favorable sites of metal adsorption in ZIF67. The adsorption processes of six types of metals, i.e., Pt, Pd, Ir, Ru, Fe, Ni are examined

computationally. Meanwhile, three types of potential adsorption sites are identified depending on its nearest neighboring atoms with metal as N Site, Co Site and C Site. For all calculations, the Perdew-Burke-Ernzerhof (PBE) functional and projector augmented-wave (PAW)[278-280] method are adopted using the Vienna ab initio simulation package (VASP). The dispersive van der Waals interactions between the MoS_2 and BMLs were included using the DFT-D2 method of Grimme[281,282]. In each calculation, an energy cutoff of 500 eV were adopted while higher cutoff will have and energy difference of less than 0.01 eV. When performing the structure optimizations, the system is regarded as converged when the force per atom is less than 0.01 eV/Å.

6.2.5. Electrochemical Measurements

Before the glassy carbon electrode (GCE) was used, it was consecutively polished with 1.0 and 0.05 μm alumina powder, rinsed with deionized water, and sonicated first in ethanol and then in water. Electrochemical experiments were carried out in 1 M KOH by using a computer-controlled potentiostat (Princeton 2273 and 616, Princeton Applied Research) in a conventional three-electrode cell at room temperature. Typically, working electrodes were prepared by mixing the catalyst with deionized water + isopropanol + 5% Nafion® (v/v/v = 4/1/0.05). The loading mass on the rotating disk electrode (RDE) was calculated as 163 μg cm^{-2}. A Pt wire was used as the counter electrode and Ag/AgCl (KCl, 3M) was used as the reference electrode, with all potentials referred to reversible hydrogen electrode (RHE). Thus, the potential with respect to RHE can be calculated as follows: E(RHE) = E(Ag/AgCl) + 0.059 × pH + 0.210. Before testing, flowing N_2 was bubbled through the electrolyte in the cell to achieve an N_2-saturated solution. The HER and OER tests were carried out in N_2-

saturated 1 M KOH solution respectively with a scan rate of 10 mV s^{-1}. The overall water splitting test was performed in a two-electrode system. The catalyst ink modified on carbon fibre was used as both the cathode and anode in overall water splitting. The loading mass on carbon fibre is 0.2 mg/cm^2. Accelerated durability tests were performed at room temperature in 1 M KOH solution via constant voltage electrolysis at an applied potential of 1.6 V (Vs. RHE).

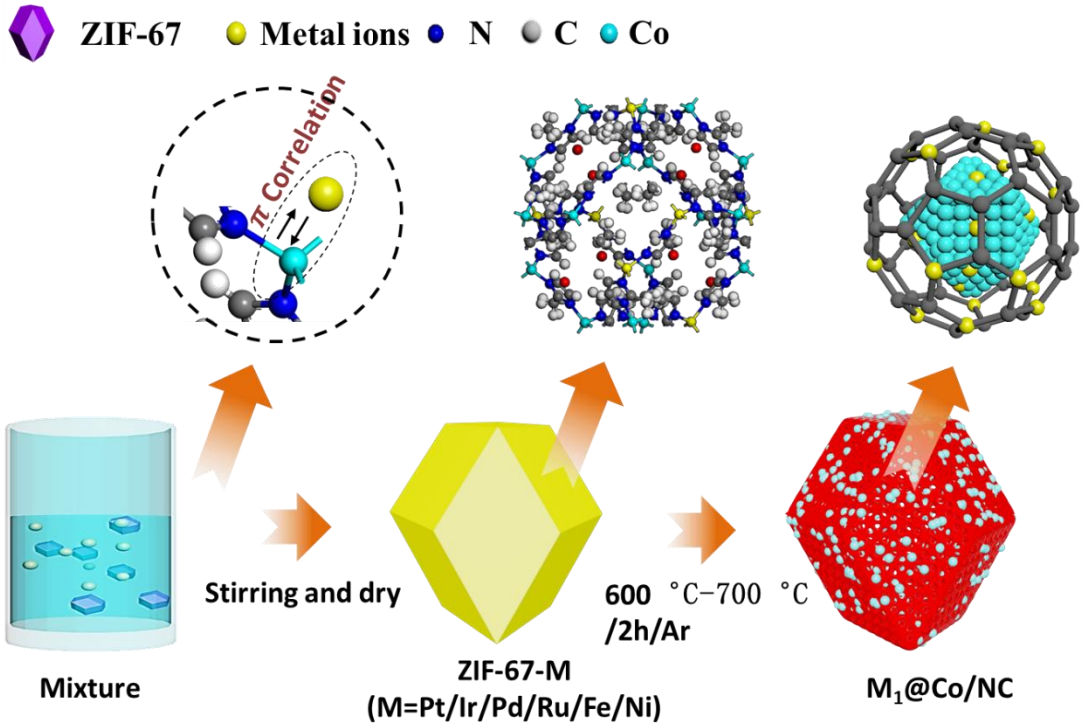

Figure 6-2. Schematic illustration of the formation of M_1@Co/NC.

6.3. Results and Discussion

As illustrated in Figure 6-2, when adding various metal ions (M^{2+}, M=Pt/Ir/Pd/Ru/Fe/Ni) into the ZIF-67 dispersion, a serials of ZIF-67-M mixtures can be formed via strong coordination of M^{2+} with imidazole pentagon via electron absorption under continual stirring. During pyrolysis at 600-700 ^oC under Ar

atmosphere, ZIF-67 precursor transforms into the heterogeneous Co/NC support; Simultaneously, the coordinated M^{2+} are reduced into metal single atoms (M_1) through the carbonization of the organic linkers, leading to the formation of isolated M_1 embedded in the Co and NC domains of the support (M_1@Co/NC). The high angle annular dark field (HAADF) image of scanning transmission electron microscopy (STEM) with a low magnification shows that the representative Pt_1@Co/NC (2.28 wt% Pt, confirmed by inductively coupled plasma optical emission spectrometry (ICP-AES)) exhibits a rough dodecahedral shape without any striking-contrast particles observed on the surface (Figure 6-1b). The high-magnification HAADF image of the Pt_1@Co/NC verifies that high-density Pt single atoms are uniformly dispersed on both Co nanoparticles and C matrices without agglomeration during the high-temperature annealing process of the ZIF-67-Pt mixture (Figure 6-1c).

The intensity mapping of high-resolution HAADF image demonstrates a highly contrast of electronic intensity of different atoms, that is, the high energy atoms correspond to red color and the low energy atoms show a gradient change to the blue color. The red spots, as shown in Figure 6-1d, correspond to the isolated Pt single atoms on the Co nanoparticles, which evidently occupy the position of Co atoms as illustrated in the white box. Hence, this portion of Pt_1 is stabilized by alloying with Co atoms to form single atom alloys (SAAs). It is believed that the alloyed Pt_1@Co SAAs can exhibit geometric and electronic structures different from those of the single atoms that are prepared by anchoring on the support. [262,283,284] Thus, the Pt_1@Co are expected to show low energy barrier, high selectivity and activity for catalytic reactions.[285] Furthermore, the fast Fourier transform inversed high resolution HAADF (FFTI-HAADF) image clearly shows a high-density of bright isolated Pt atoms dispersed on

the carbon layer (Figure 6-1e). More importantly, this synthetic strategy can be generalized for various metals, including iridium (Ir), palladium (Pd), Ruthenium (Ru), iron (Fe), and nickel (Ni) based on the abovementioned Co-alloying and N-coordination interactions. The bright contrast single atoms of Ir (2.2 wt%, Ir_1@Co/NC), Pd (1.9 wt%, Pd_1@Co/NC), Ru (2.0 wt%, Ru_1@Co/NC), Ni (1.8 wt%, Ni_1@Co/NC), and Fe (1.3 wt%, Fe_1@Co/NC) are uniformly dispersed on the Co/NC support without any particles observed (Figure 6-3).

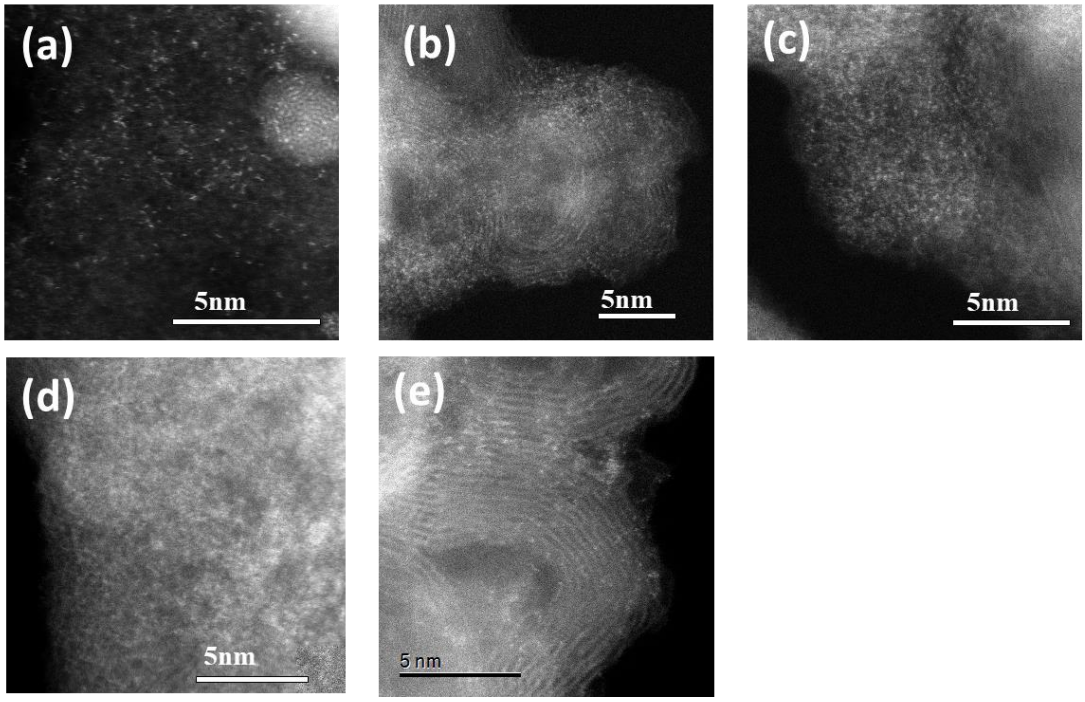

Figure 6-3. HAADF images for different M_1@Co/NC with single-atom (a) Ir, (b) Pd, (c) Ru, (d) Ni, and (e) Fe at low magnification.

Moreover, as shown in Figure 6-1f-j, the high resolution HAADF images show that single atoms of Ir, Pd, Ru, Fe, and Ni are isolated in nitrogen doped carbon matrix (white rectangle), indicating the highly strong coordination effect between C/N groups and metal ions. Also, as shown in the images below (Figure 6-1f-j), these single atoms Ir_1, Pd_1, Ru_1, Fe_1, and Ni_1, similar with Pt_1, are successfully doped on Co crystal

without agglomeration. The STEM-energy dispersive spectroscopy (EDS) element mapping further confirmed that the expected elements Pt, C, N and Co uniformly distributed over the entire architecture (Figure 6-4). Similarly, the single atoms (Ir_1/Pd_1/Ru_1/Fe_1/Ni_1) were uniformly dispersed in the substrates (Co/NC) (Figure 6-5, 6-6, 6-7, 6-8, 6-9).

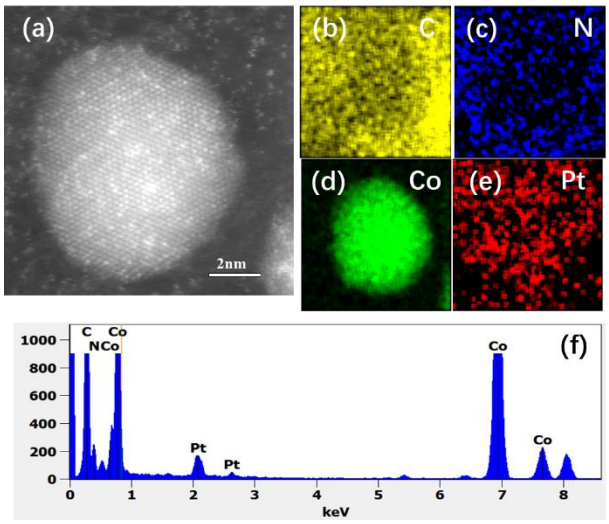

Figure 6-4. HAADF image and STEM-EDS of Pt_1@Co/NC. (a) HAADF image; (b-e) elemental mapping of Pt_1@Co/NC; (f) EDS. The STEM-EDS elemental mapping shows the expected Pt/Co/C/N were dispersed over the architecture. Also, the characteristic Pt peak was observed in the EDS, indicating the existence of Pt atoms.

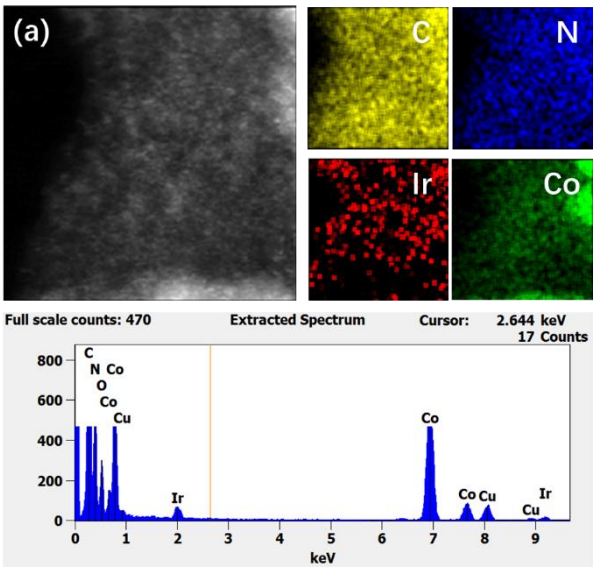

Figure 6-5. HAADF image and STEM-EDS of Ir_1@Co/CN. (a) HAADF image; (b-e) elemental mapping; (f) EDS.

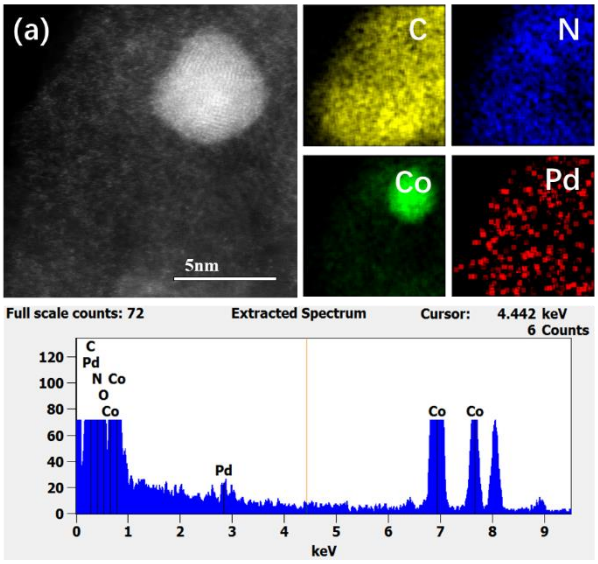

Figure 6-6. HAADF image and STEM-EDS of Pd_1@Co/CN. (a) HAADF image; (b-e) elemental mapping; (f) EDS.

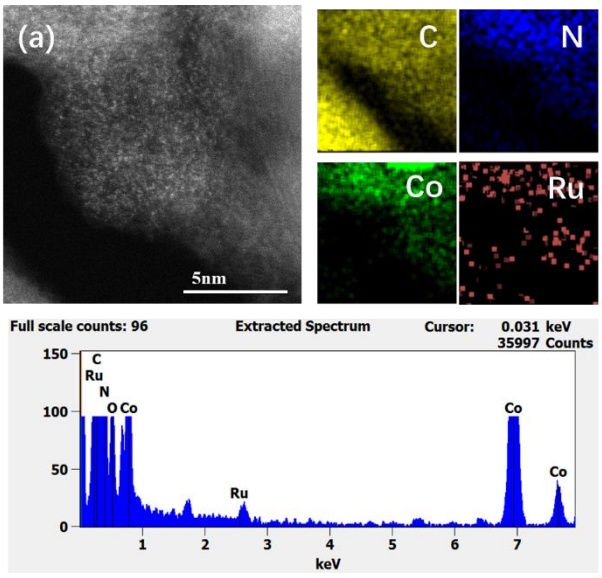

Figure 6-7. HAADF image and STEM-EDS of Ru_1@Co/CN. (a) HAADF image; (b-e) elemental mapping; (f) EDS.

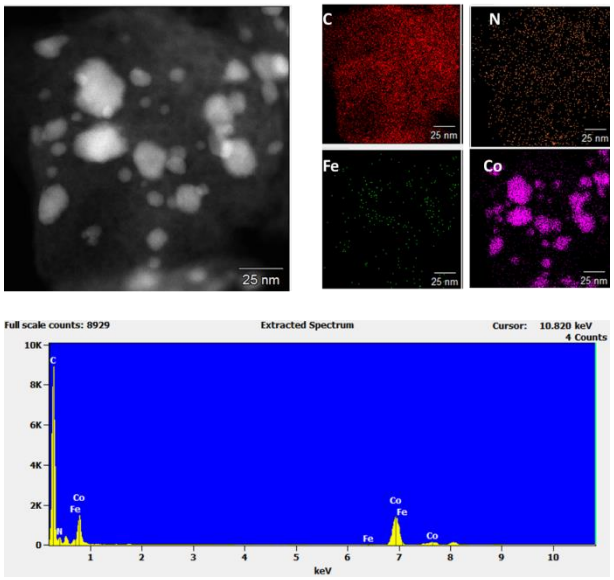

Figure 6-8. HAADF image and STEM-EDS of Fe_1@Co/CN. (a) HAADF image; (b-e) elemental mapping; (f) EDS.

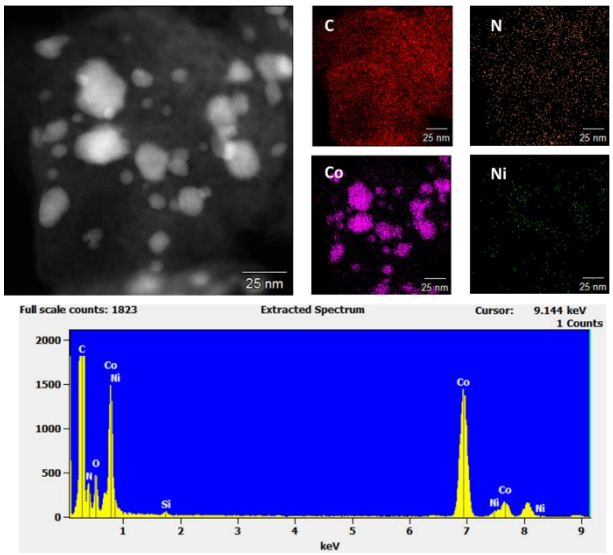

Figure 6-9. HAADF image and STEM-EDS of Ni_1@Co/CN. (a) HAADF image; (b-e) elemental mapping; (f) EDS.

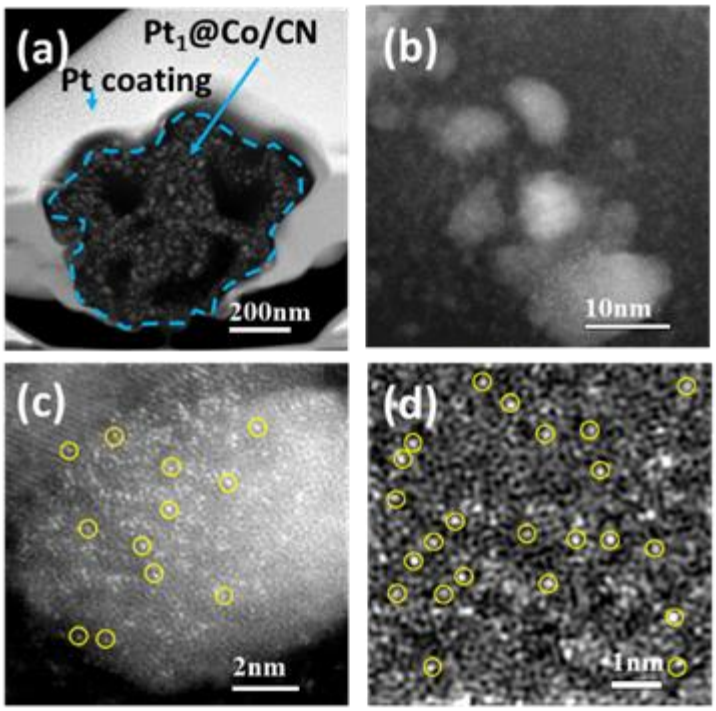

Figure 6-10. The HAADF images of the sectional view of Pt1@Co/NC with low magnification (a) and high magnification (b). The FFTI-HAADF image of Pt single atoms on Co (c) and C (d).

In addition, as a representative sample, we investigate the dispersion of Pt_1 single atoms in the Pt_1@Co/NC *via* the focus ion beam scanning electron microscopy (FIB-SEM) and the secondary ion mass spectrometer (SIMS). The FIB-SEM is applied to cut the Pt_1@Co/NC, which could provide its sectional view via STEM (Figure 6-10). The corresponding HAADF images display the existence of uniform and high density isolated Pt atoms over the cross section of Pt_1@Co/NC (Figure 6-10b), indicating the 3D isolated atomic dispersion of Pt. Also, the single Pt atoms anchored on both of Co and NC (Figure 6-10c and d) indicates that, besides the surface, the single Pt atoms can be embedded in multiple inner layers of the Co/NC support, which is conducive to expose more active sites for water splitting. This is the first time to realize a 3D single atom dispersion, which is ascribed to the easy accessibility of zeolitic structure and numerous functional organic group anchored on each tunnel. The 3D radial dispersion of Pt_1 is further analyzed via SIMS, which is a powerful tool to verify the element dispersion from the surface to depth (Figure 6-11). With time-sputtering from 0s to 600s, the depth profiling of Pt_1@Co/NC shows that the permanent and uniform signals of main elements (C, Co, Pt), indicating that Pt_1 has fascinating vertical dispersion (Figure 6-12).

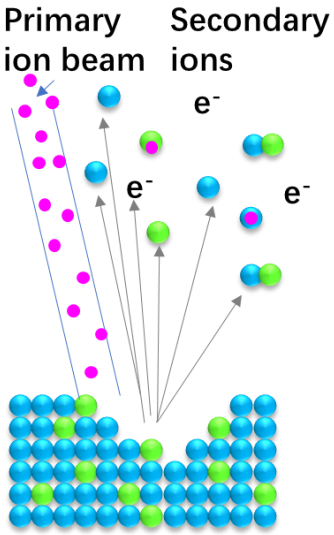

Figure 6-11. The brief working mechanism of SIMS. The primary ion beam is sputtering on the surface of specimens and meanwhile, the ejected secondary ions are collected and analyzed. With extending the sputtering time, the analyzed depth will increase.

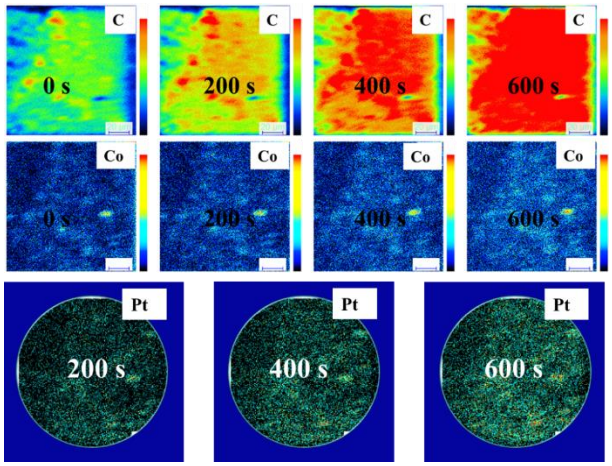

Figure 6-12. Time profiling of ions images of Pt, C and Co capturing on the same region of Pt_1@Co/NC. With the increase of sputtering time, both of C and Co keep shows their locally high counts, indicating these two elements have a depth-elemental dispersion.

Furthermore, the X-ray diffraction pattern (XRD) patterns of all M_1@Co/NC samples are well consistent with the Co/NC, only showing three peaks at 44.2 °, 51.5 °, and 75.9 °, which are indexed to be (111), (200), and (202) planes of Co (Figure 6-13), respectively. No other metals phases are formed in these M_1@Co/NC, further implying that the loaded metals are very likely to be atomically dispersed in the support without forming nanoclusters/nanoparticles with M-M stacking. In addition, thermogravimetric analysis (TGA) indicates that the mass ratio of Co and C in the Co/NC support is 65% and 35%, respectively (Figure 6-14).

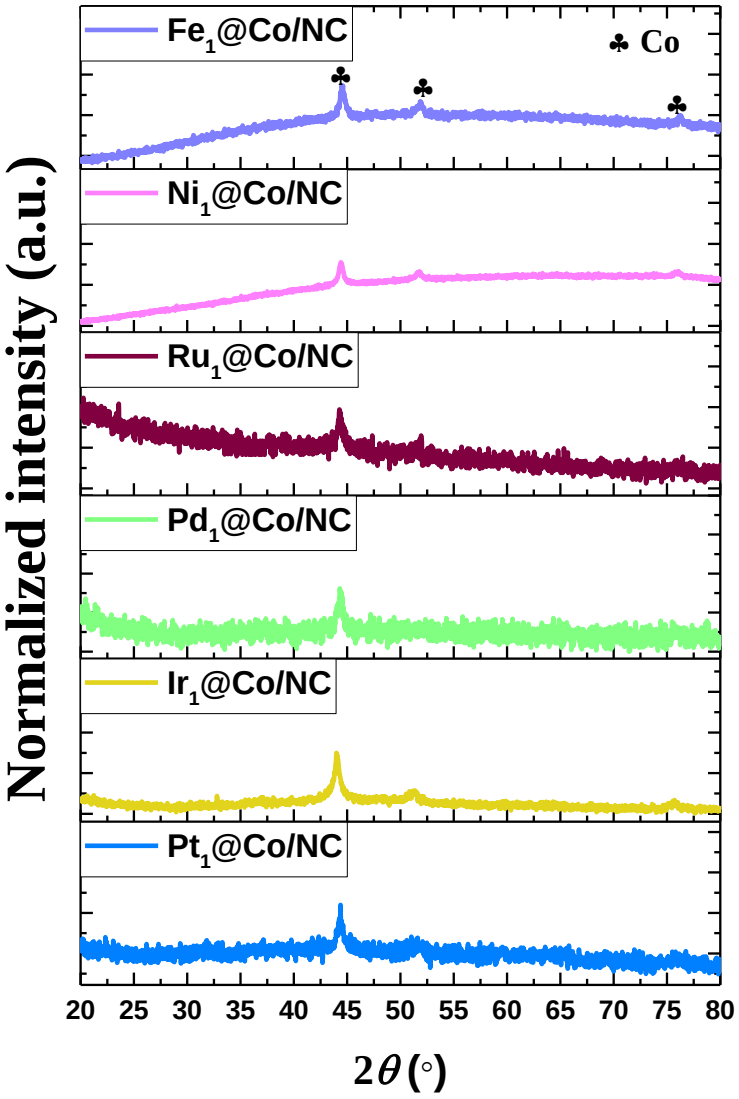

Figure 6-13. XRD patterns of Pt_1@Co/NC, Ir_1@Co/NC, Pd_1@Co/NC, Fe_1@Co/NC, Ni_1@Co/NC, and Ru_1@Co/NC.

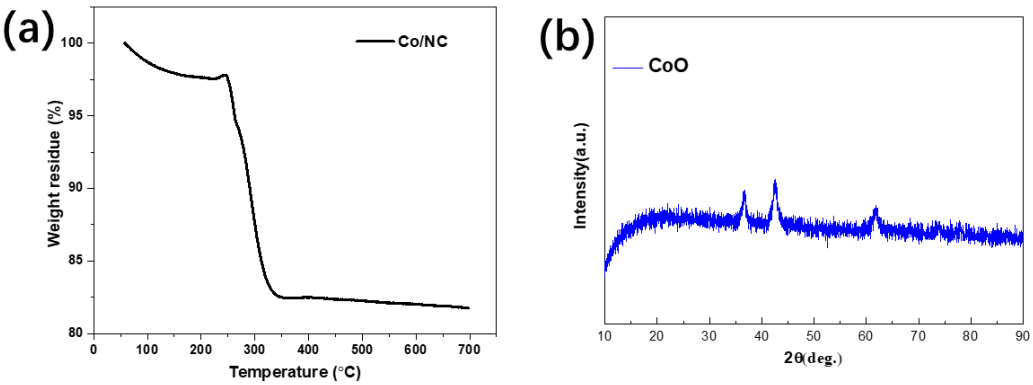

Figure 6-14. TGA curves of Co/NC performed in the air. The XRD pattern of resulting product shows the Co particle were oxidized to cobalt oxide (CoO). The calculation of mass ratio is based on the TGA curves and XRD result.

We, thus, have successfully developed a general strategy to synthesize 3D-dispersed single atoms, including precious elements and transition elements, on the heterogeneous support, which can lead to dual active sites with alternative electronic properties towards different catalytic reactions.

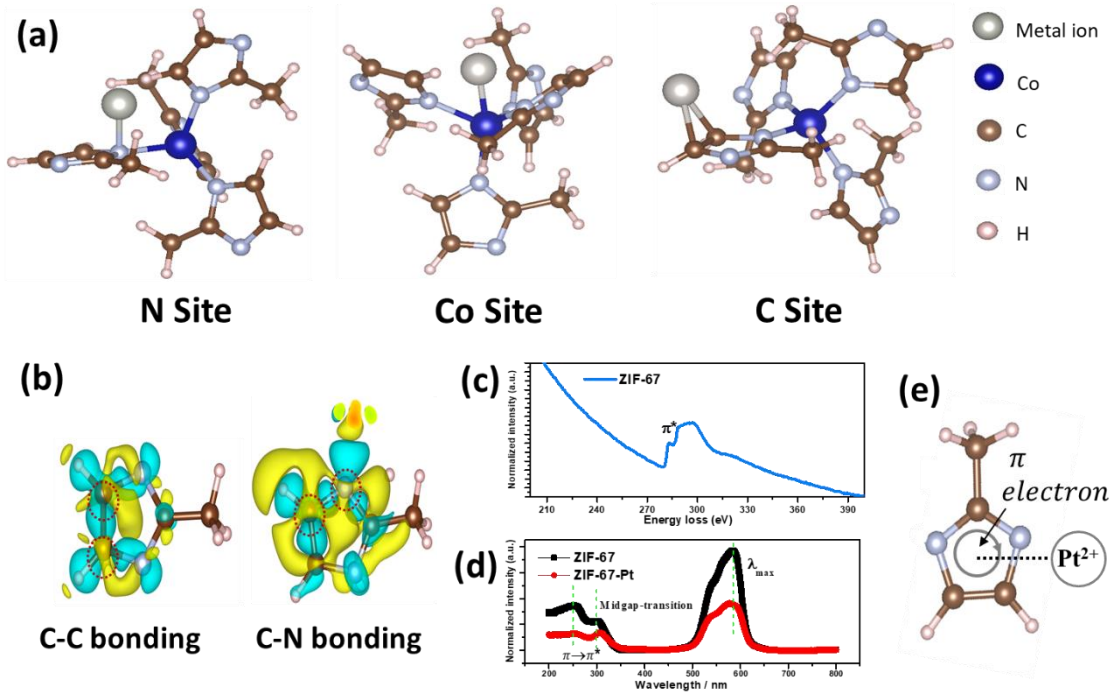

Figure 6-15. The confirmation of the Pt-π bond at the initial stage on imidazole group by DFT, UV-vis, and EELS. (a) Atomic configurations of three adsorption sites: N site; Co site; C site. (b) Calculated charge redistribution of C-C bond and C-N bond in ZIF-67. The calculated two atoms in bond are denoted by red circles. The yellow and blue iso-surface indicates gain or loss of electron density due to bond formation. (c) The EELS spectra of ZIF-67. (d) The Uv-vis spectra of ZIF-67 and ZIF-67-Pt. (e) The illustration of the correlation between Pt cation and π electrons.

Table 6-1. Calculated adsorption energy (eV/atom) of metals at different sites.

Metal	N Site	C Site	Co Site
Pt	-3.42	-3.22	-3.09
Pd	-2.22	-1.87	-1.79
Ir	-4.05	-3.52	-2.74

Ru	-3.61	-3.28	-3.00
Fe	-1.52	-0.90	-0.82
Ni	-2.37	-2.01	-1.94

DFT calculations are performed to evaluate the favorable sites of metal adsorption in ZIF-67. The ZIF-67 possesses 3D staggered structure so that the correlated metal ion on pentagon imidazole can isolate each other without aggregation. The adsorption processes for six types of metals, including Pt, Pd, Ir, Ru, Fe, and Ni, are examined computationally. Meanwhile, three types of potential adsorption sites are identified depending on its nearest neighboring atoms with metal as N site, Co site and C site (Figure 6-15a). The calculated adsorption energy of metals at different sites are demonstrated (Table 6-1). It can be seen that for all metals, due to the fact that electronegativity of N is higher than that of C, the electron will be polarized to N atoms more than C atoms, which determines that N serves as the most favorable adsorption site. Meanwhile, Co site is the most unfavorable adsorption site for metal atoms, which is mainly due to the great coulomb repulsion between metal ions. The adsorption mechanism can be further speculated by understanding the deformation charge density. As can be inferred from Figure 6-15b, both C-C and C-N bonds can cause charge redistribution of all five atoms in the pentagon rings. That indicates the fact the conjugated π bond exist in such pentagon C-N substructures of ZIF-67. Additionally, the EELS spectrum indicates the existence of π electron on ZIF-67, further confirming that the delocalized π electron are significant in absorbing metal ions (Figure 6-15c). Moreover, three prominent peaks are observed in the UV−vis spectrum of ZIF-67: 257

nm ($\pi \rightarrow \pi^*$), 303 nm (midgap transition), and at 582 nm (λ_{max}) (Figure 6-15d). In contrast, the ZIF-67-Pt with Pt ion adsorption leads to slight blue-shift of the λ_{max} (582 → 579 nm), while a slight red-shift is observed in the midgap transition (303 → 308 nm) and π transition, suggesting its P-type doping nature (basic nature, doping).[286,287] The EXAFS fitting curve of ZIF-67-Pt mixture suggests that the Pt_1 are sit on the top the pentagon ring and binding with five nitrogen/carbon atoms (Figure 6-16). The FFTI-HAADF image and color mapping of the ZIF-67-Pt mixture at 25 ℃ also shows a clear evidence that the bright contrast Pt ions were trapped on the edges of the pentagon of 2-methylimidazole (Figure 6-17), indicating that Pt ions are initially anchored in the imidazole group before the thermal treatment. In addition, the Raman spectroscopy was applied to further determine the length, symmetry of bonds between Pt and N. Comparing with the pure ZIF-67, the Raman spectroscopy of ZIF-67-Pt shows a clearly positive peak shift of 66.4 cm^{-1}, indicating the length of metal-N bond become shorter due to a higher polarized bond (Figure 6-18)[288,289], which is consistent with the shorter theoretical bonding length of Pt-N (1.950 Å) than Co-N (2.207 Å) (Figure 6-19). Particularly, a control sample (Pt-Co/NC) was synthesized from the mixture consisted of the as-obtained Co/NC and Pt ions. Due to the absence of imidazole groups in the Co/NC substrate, the mixed Pt ions are severely aggregated into the formation of Pt particles but no isolated Pt atoms dispersed after annealing (Figure 6-20), implying that the imidazole groups of ZIF-67 play a key role in preparing Pt single atoms. Thus, these results point out the delocalized π electrons in imidazole groups are the most critical for single atoms, which serve as anchoring sites to initially form a strong bonding with the M ions and keep them isolated through the thermal carbonization (Figure 6-15e).

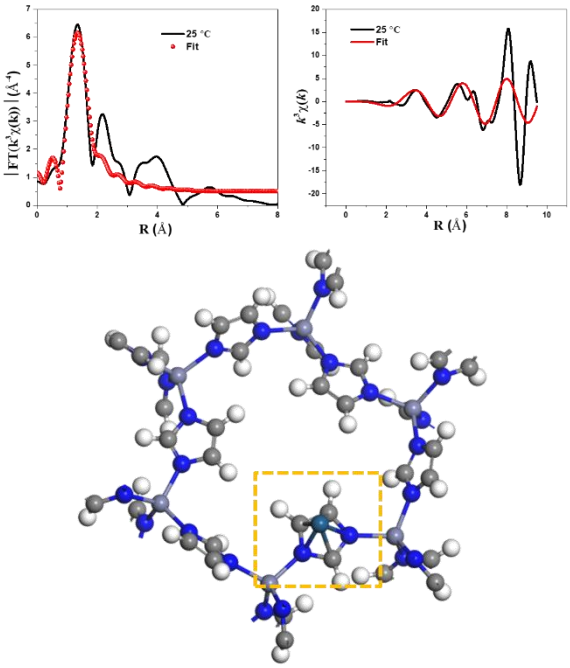

Figure 6-16. The EXAFS fitting curves of ZIF-67-Pt obtained at 25 °C and its corresponding fitting model.

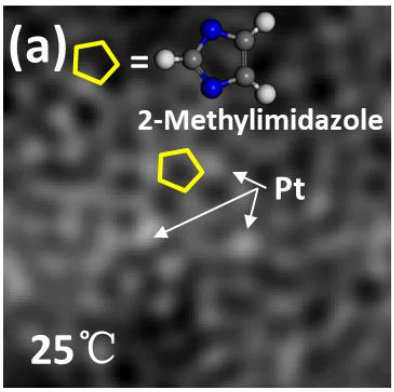

Figure 6-17. (a) FFTI-HAADF of ZIF-67-Pt.

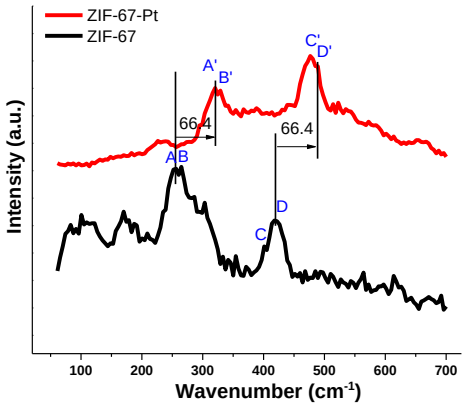

Figure 6-18. Raman spectra of ZIF-67 and ZIF-67-Pt. If points at 253.4 cm^{-1}, 266.8 cm^{-1}, 399.7 cm^{-1}, and 410.4 cm^{-1} on ZIF-67 were set as A, B, C, and D, similar peaks A', B', C', and D' also can be found at 319.8 cm^{-1}, 333.2 cm^{-1}, 466.1 cm^{-1}, and 476.8 cm^{-1}, which have a consistently 66.4 positive shift.

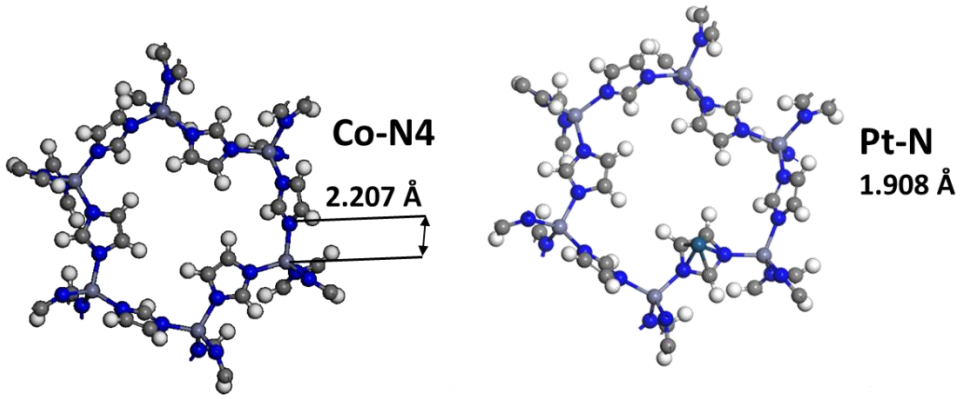

Figure 6-19. The theoretical atomic structure of ZIF-67 and ZIF-67-Pt.

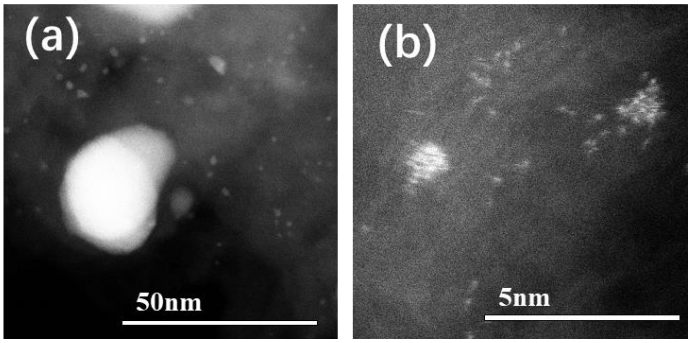

Figure 6-20. HAADF images of Pt-Co/CN.

The evolution of Pt_1@Co/NC along with temperature was monitored in the range of room temperature (RT) to 600 ºC. The valance of Pt speciation obtained in different temperatures can be determined from the normalized Pt L_3-edge X-ray absorption near edge structure (XANES). The observation in Figure 6-21 suggests that Pt (II) were initially reduced during RT to 150 ℃ but gradually oxidized into a maximum positive valence state from 300 to 450 ℃, and then re-reduced to form Pt single atoms by the further increased temperature at 600 ℃. Also, the absorption threshold of Pt L_3-edge in Pt_1@Co/NC is close to that in ZIF-67-Pt precursor at RT, implying the similar Pt valence state of approximately +2. Notably, the X-ray photoelectron spectroscopy (XPS) of Pt_1@Co/NC shows two typical fitting peaks of Pt^{2+}, which is well consistent with the analysis of XANES (Figure 6-22). Similarly, the oxidized valence status are also observed *via* the XPS analysis on Ir_1@Co/NC, Pd_1@Co/NC, and Ru_1@Co/NC (Figure 6-23). To investigate the coordination environment of Pt_1, extended X-ray absorption fine structure (EXAFS) analysis was performed.

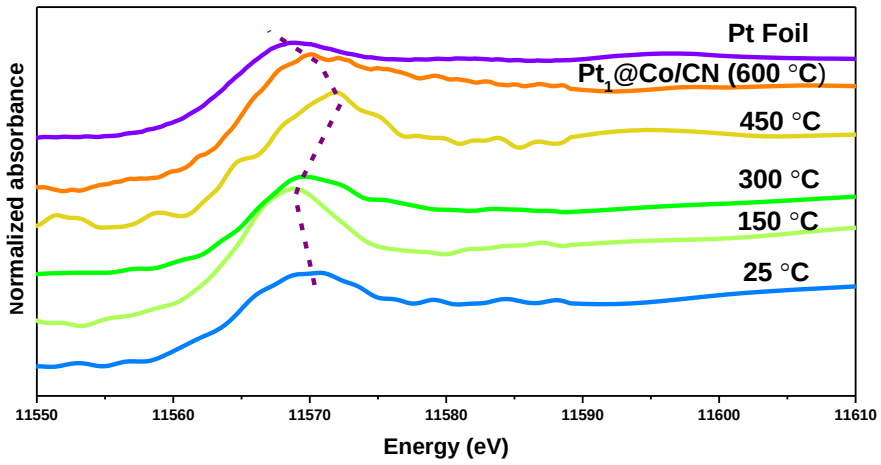

Figure 6-21. The normalized XANES spectra of ZIF-67-Pt mixture at different temperatures.

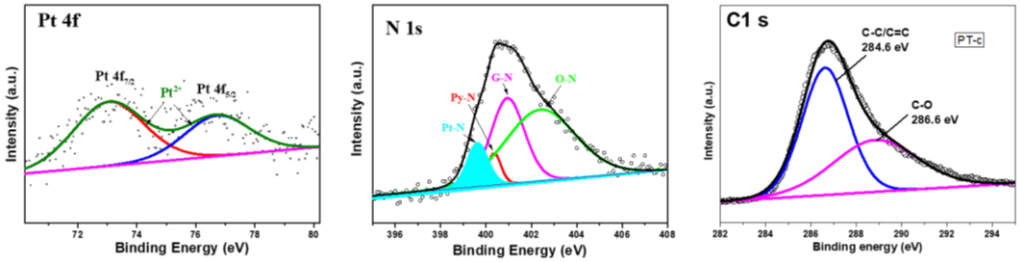

Figure 6-22. High resolution Pt 4f, N 1s, C 1s XPS spectra of Pt_1@Co/NC.

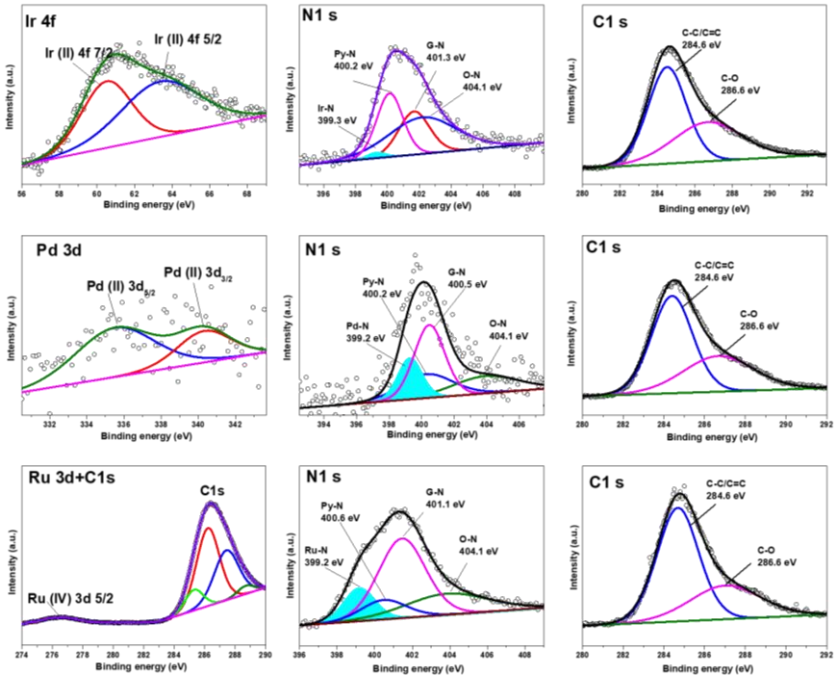

Figure 6-23. High resolution Ir 4f, N 1s, C 1s XPS spectra of Ir_1@Co/NC, Pd 3d, N 1s, C 1s XPS spectra of Pd_1@Co/NC, Ru 3d, N 1s, C 1s XPS spectra of Ru_1@Co/NC.

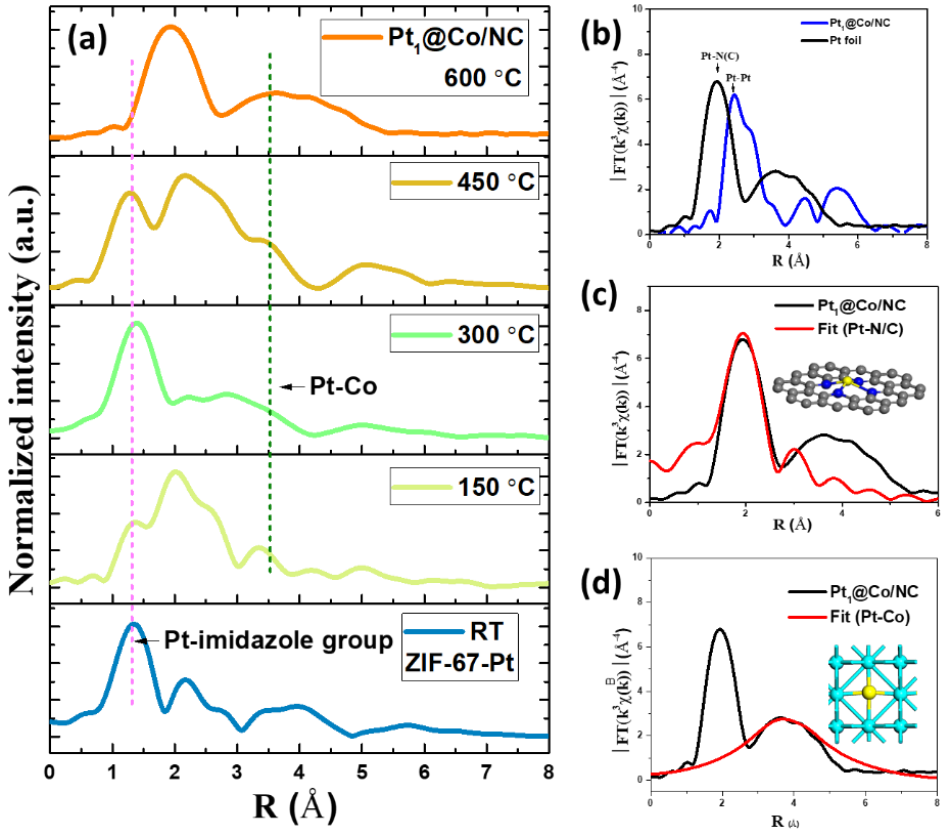

Figure 6-24. The local structure of the Pt single atoms in Pt_1@Co/NC by EXAFS. (a) The K^3-weighted Frourier transform (FT) spectra from EXAFS of ZIF-67-Pt mixture at different temperatures. (b) The K^3-weighted Frourier transform (FT) spectra from EXAFS. Δk = 2.3-9.0 $Å^{-1}$ for Pt_1@Co/NC; but Δk = 3.0-10.45 $Å^{-1}$ for Pt foil; EXAFS fitting of Pt-N/C shell (c), and Pt-Co shell (d) in R-space for Pt_1@Co/NC. The inset is the model of the fitted structures of Pt-N/C shell and Pt-Co shell.

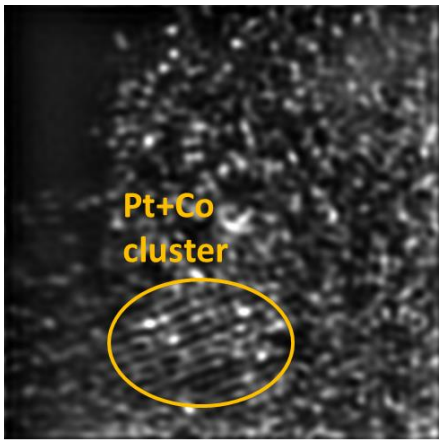

Figure 6-25. The HAADF image of Pt_1@Co/NC obtained at 300 °C.

The K^3-weighted FT spectra from EXAFS of these samples obtained in different temperature, as shown in Figure 6-24a**,** points out that the Pt^{2+} ions are bonded with low coordination numbers (purple dash line) before 600 ℃ and formed Pt-Co bond with a high coordination numbers in a long R space (Green dash line) from 300 to 600 ℃, which is consistent with the STEM result (Figure 6-25). Notably, a potential contribution from Pt-N(C) (1.9 Å) distance is detected without characteristic Pt-Pt distance (2.4 Å) by EXAFS (Figure 6-24b), indicating that the Pt has no characteristic Pt-Pt bonds, but exhibits low-atomic number neighbor in the first shell. Additionally, the EXAFS fitting suggests a coordination number of about 4 with N(C) (Figure 6-24c, Table 6-2), suggesting that the Pt atoms sit on the top of 4 N(C) atoms, which is in

good agreement with the speculation of HAADF. As the Pt-N and Pt-C bonds have a similar characteristic peak, they cannot be distinguished by EXAFS fitting[12]. The increasing temperature leads to the formation of Co nanoparticles in N-doped C. The best-fitting results of K-space and Fourier transforms in R space of Pt foil are also displayed in Figure 6-26. On the other hand, the scattering path of Pt-Co at 3.544 Å was fitted and shows a high consistence of Pt-6Co model in R space, as well as the K-space (Figure 6-24d, Figure 6-27), indicating the single Pt atoms are doped in the space of Co octahedral. Based on the above analysis, the local atomic structure around isolated Pt atoms can be confirmed to be coordinated with four-fold N/C atoms on a porous carbon matrix and alloyed in the center of Co octahedral.

Table 6-2. EXAFS data fitting results of Pt_1@Co/NC

Sample	Shell	N	R (Å)	σ2 ×102	ΔE_0 (eV)	r-factor (%)
Pt_1@Co/NC	Pt-C/N	12	1.93	0.26	7.7	2.5
	Pt-Co	6	3.54	0.3	3.4	1.8

N, the coordination number of the absorber-backscatter pair; R, the average absorber-backscatter distance; σ^2, the Debye-waller factor; ΔE_0, the innerpotential correction.

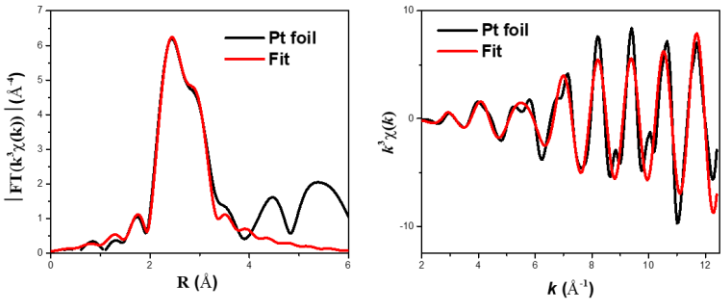

Figure 6-26. The EXAFS fitting curves of Pt foil.

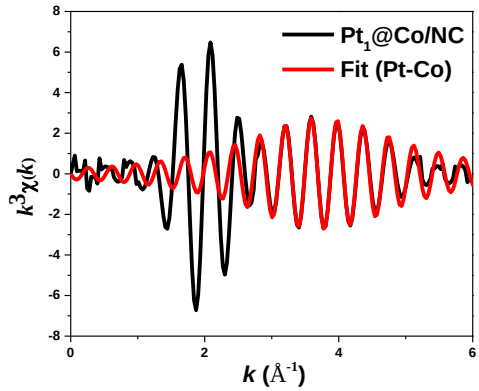

Figure 6-27. The EXAFS fitting curves of Pt-Co path of Pt_1@Co/NC in K space.

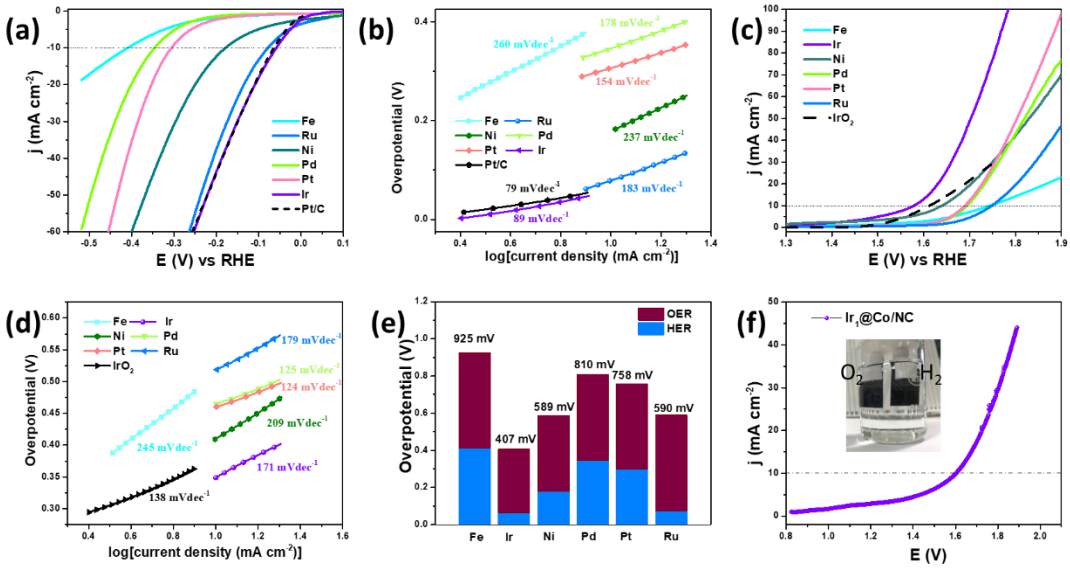

Figure 6-28. (a, c) Polarization curves of HER and OER of Pt_1@Co/NC, Ir_1@Co/NC, Pd_1@Co/NC, Ru_1@Co/NC, Ni_1@Co/NC, Fe_1@Co/NC, and commercial Pt/C, IrO_2 electrodes. (b, d) The corresponding Tafel slopes obtained from the polarization curves (a, c), respectively. (e) The overall over-potential of the corresponding electrodes obtained at 10 mA cm^{-2}. (f) The polarization curves of overall water splitting with the Ir_1@Co/NC catalyst. Inset is the image of two electrode system which is producing bubbles of H_2 and O_2 at an applied potential of 1.4V (Vs RHE).

The electrochemically catalyzed HER and OER with the M_1@Co/NC are evaluated in N_2-saturated 1.0 M KOH solutions *via* using a typical three-electrode cell at room temperature. The linear sweep voltammetry (LSV) curves of the Pt_1@Co/NC, Ir_1@Co/NC, Pd_1@Co/NC, Ru_1@Co/NC, Ni_1@Co/NC, and Fe_1@Co/NC electrodes are shown in Figure 6-28a with a scan rate of 10 mV s^{-1} for HER. It is evident that both Ir_1@Co/NC and Ru_1@Co/NC shows the most positive onset potential, particularly the Ir_1@Co/NC electrode exhibits a similar polarization curve with commercial Pt/C, which required 0.06 V to deliver the 10 mA cm^{-2} current density. Notably, the over-potentials (η) achieving a 10 mA cm^{-2} current density increase in the sequence: Fe_1@Co/NC < Pd_1@Co/NC < Pt_1@Co/NC < Ni_1@Co/NC < Ru_1@Co/NC < Ir_1@Co/NC, indicating that the Ir_1@Co/NC achieves a more fascinating HER performance. The Tafel plots as shown in Figure 6-28b, which is derived from the polarization curves (Figure 4a), indicates that the electrode of Ir_1@Co/NC (89 mV dec^{-1}) has a the lowest Tafel slope than Ru_1@Co/NC (183 mV dec^{-1}), Fe_1@Co/NC (260 mV dec^{-1}), Pd_1@Co/NC (178 mV dec^{-1}), Pt_1@Co/NC (154 mV dec^{-1}), and Ni_1@Co/NC (237 mV dec^{-1}). Particularly, the catalyst Ir_1@Co/NC shows a comparable Tafel slope with Pt/C (79 mV dec^{-1}), suggesting a favorable HER kinetic via a Volmer-Heyrovsky pathway.

On the other hand, the polarization curves as shown in Figure 6-28c revealed that the Ir_1@Co/NC presented a superior OER catalytic activity. The over-potentials delivering a current density of 10 mA cm^{-2} are in the followed sequence: Ir_1@Co/NC (343 mV) > IrO2 (385 mV) > Ni_1@Co/NC (410 mV) > Pt_1@Co/NC (458 mV) > Pd_1@Co/NC (463 mV) > Ru_1@Co/NC (515 mV) > Fe_1@Co/NC (515 mV). Also, Ir_1@Co/NC shows a Tafel slope of 171 mV dec^{-1}, which is better than Ni_1@Co/NC (209 mV dec^{-1}),

Ru_1@Co/NC (179 mV dec^{-1}), and Fe_1@Co/NC (245 mV dec^{-1}), indicating Ir_1@Co/NC had a better OER kinetic due to a possibly high exchange current density (6-28d). The Pt_1@Co/NC (124 mV dec^{-1}) and Pd_1@Co/NC (125 mV dec^{-1}), however, presented a faster exchange current, which is near to the commercial IrO_2. As summarized in Figure 6-28e, the overall over-potentials of HER and OER indicate that Ir_1@Co/NC (407 mV) had a lower over-potential than these other electrodes (Fe_1@Co/NC (925 mV), Ni_1@Co/NC (589 mV)), Pt_1@Co/NC (758 mV), Pd_1@Co/NC (810 mV), and Ru_1@Co/NC (590 mV), suggesting that the Ir_1@Co/NC is a highly efficient bi-functional catalyst to achieve excellent performance with an low overall potential window in water splitting. Accordingly, we integrate two Ir_1@Co/NC electrodes loaded on carbon paper (1.2 cm*1 cm) as water electrolysis anode and cathode in the electrolyte of 1.0 M KOH solution. It is clearly observed that the hydrogen and oxygen bubbles are formed when the applied potential is higher than 1.4 V (inset image, Figure 6-28f). Also, the current density can achieve 10 mA cm^{-2} with a potential of 1.603 V, which is consistent with the supposed potential window. It is of highly significance that the Ir_1@Co/NC catalyst can conduct a stable long-term overall water splitting over 5 h with a set potential of 1.61 V via constant voltage electrolysis (Figure 6-29). The comparison of overpotentials and mass activities of reported overall water-splitting catalysts based on noble metals indicates that Ir_1@Co/NC shows overwhelming mass activity with a comparable overall potential at current density of 10 mA cm^{-2}, regardless of acid and base electrolytes (Table 6-3).

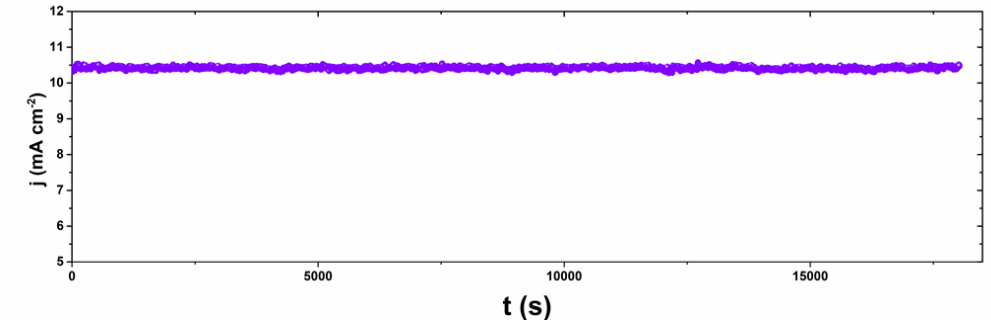

Figure 6-29. The stability test of Ir_1@Co/NC at 1.61 V Vs. RHE.

Table 6-3. The summary of the water splitting activity of recently reported bi-functional noble metal based catalysts.

Catalyst	Electrolyte	Mass activity mA cm^{-2} $\mu g_{noble\ metal}^{-1}$	Overall potential at 10 mA cm^{-2}	Reference
Pt/CC–Ir/CC	0.5 M H_2SO_4	0.06	1.65	290
Ir/GF	0.5 M H_2SO_4	0.2	1.55	290
Ru_2Ni_2 SNs/C	1.0 M KOH	0.12	1.58	291
IrW/C	0.5 M H_2SO_4	0.33	1.48	292
$IrNi_{0.57}Fe_{0.82}$	0.5 M $HClO_4$	0.05	1.64	293
$IrNi_{0.68}$	0.5 M HClO5	0.05	1.69	293
IrCoNi/CFP	0.5 M H_2SO_4	1	1.64	294
Pt-CoS_2/ CC	1.0 M KOH	0.27	1.55	295
IrNi NCs	0.1 M $HClO_4$	0.8	1.58	296

Ir NCs	0.1 M $HClO_4$	0.8	1.6	296
Ir_1@Co/NC	1.0 M KOH	**2.27**	**1.6**	This work

DFT calculations were performed to elucidate the electrocatalytic mechanism of the Ir_1@Co/NC towards accelerated HER and OER. The local structure of Ir_1 on Co/NC is confirmed via the fitting of EXAFS, similar with the coordination environment with Pt, in which the Ir_1 are formed four-fold N/C atoms on a porous carbon matrix and alloyed in the center of Co octahedral (Figure 6-30). Additionally, the XPS result suggests that the atomic ratio of C and N is around 4.82 (Figure 6-31), which means that $IrNC_3$ and IrC_4 are the most supposed model for a four-coordination structure, as shown in Figure 6-32a-d.

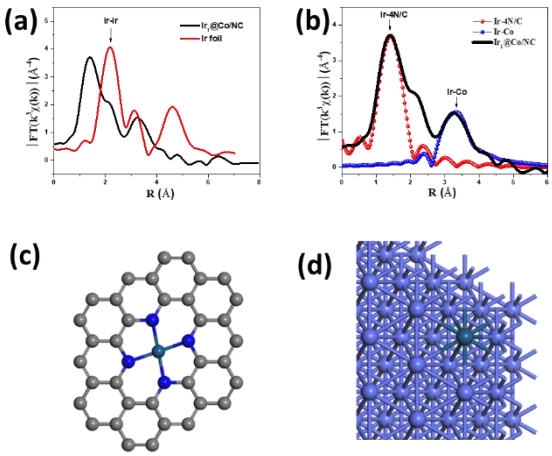

Figure 6-30. The K^3-weighted Frourier transform (FT) spectra from EXAFS for Ir_1@Co/NC and Ir foil (a); EXAFS fitting of Ir-N/C shell and Ir-Co shell (b) in R-space for Ir_1@Co/NC. The inset is the model of the fitted structures of Ir-N/C shell and Ir-Co shell.

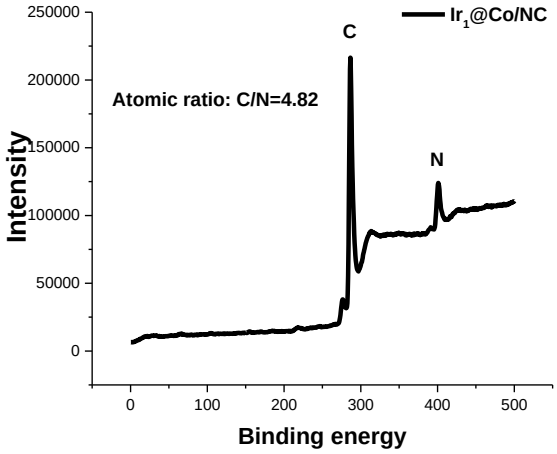

Figure 6-31. The XPS spectrum of Ir_1@Co/NC.

To simulate Co surface, we applied three-dimensional slab models in this work. The (111) surface of Co was represented by a p(5×5) slab (a = 12.53 Å, b = 12.53 Å and c = 25.00 Å) with four-atomic-layer, in which a Co atom on the surface was substituted by a Ir atom, which corresponds to Ir_1@Co as shown in Figure 6-32e and f. Additionally, it is well known that an oxidation layer would be easily generated on the Co surface forming CoO layers with an applied potential of OER, which is typically higher than 1.23 V (Vs. RHE).[294,297,298] Thus, the adsorption energies of oxygen-based intermediates on the (100) surface of CoO are calculated as well, in which a Co atom on the surface is substituted by a Ir atom (denoted as Ir_1@CoO) in Figure 6-32g and h.

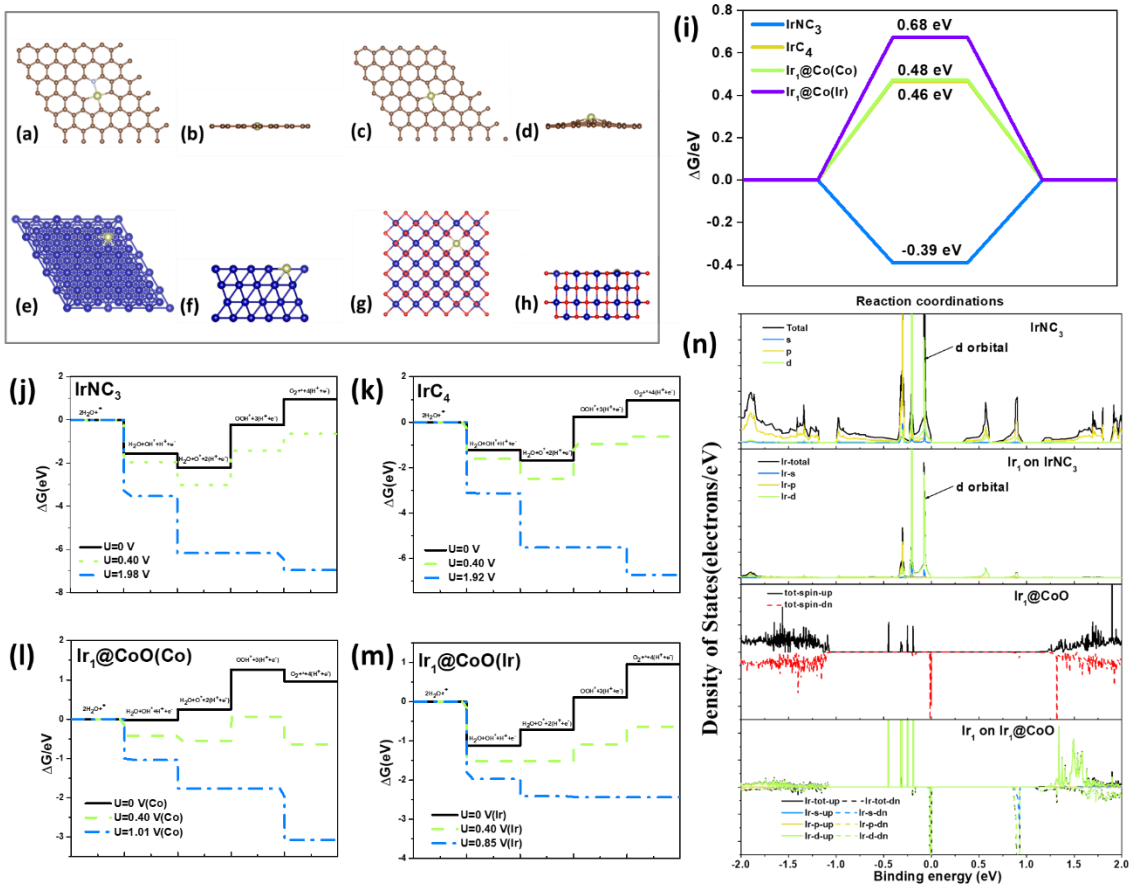

Figure 6-32. DFT calculation of the structured Ir_1 coordination. (a, c, e, g)Top views of $IrNC_3$, IrC_4, Ir@Co, and Ir@CoO respectively; (b, d, g, h) side views of $IrNC_3$, IrC_4, Ir_1@Co, and Ir_1@CoO respectively; gray, white, yellow, blue and red balls represent C, N, Ir, Co and O atoms. (i) The free energy diagrams for HER at pH=14 on $IrNC_3$, IrC_4, Ir_1@Co (Co) and Ir_1@Co (Ir). The reaction free energies of the intermediates on (j) $IrNC_3$, (k) IrC_4, (m) and (l) Ir_1@CoO(Co) and (n) Ir_1@CoO(Ir) (n) at pH = 14.

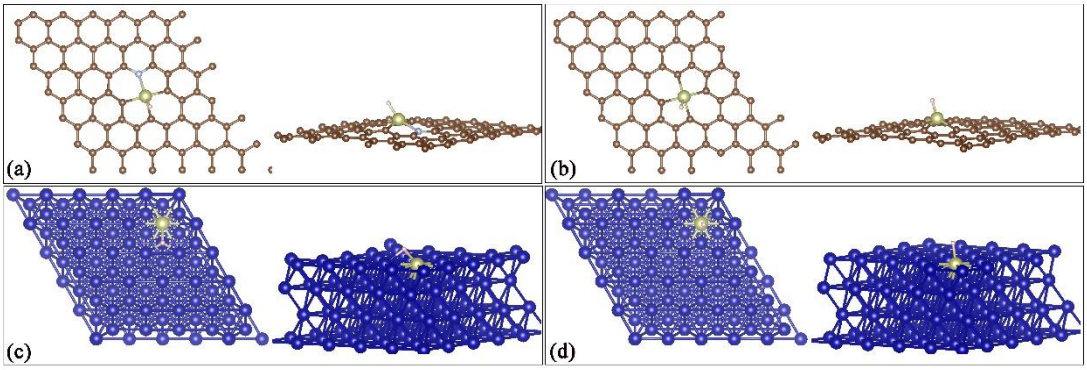

Figure 6-33. (a) The optimized structures of H adsorptions on (a) $IrNC_3$, (b) IrC_4, (c) Ir-Co(Co) and (d) Ir-Co(Ir).

It is ideal that the free energy of H* adsorption for a good HER catalyst should be close to zero, which is beneficial for both adsorption of H* and desorption of H_2. The optimized geometry of adsorption structure of H* intermediates on $IrNC_3$, IrC_4, Ir_1@Co (Co) and Ir_1@Co (Ir) model were shown in Figure 6-33. Figure 6-32i shows the free energy change of H* adsorption (ΔG_{H^*}) for the Ir_1@Co on the $IrNC_3$, IrC_4, Ir_1@Co (Co), and Ir_1@Co (Ir), respectively. Two possible H* adsorption configurations on of Co site (0.48 eV) and Ir (0.68 eV) site show large positive values and are far away from the neutral position, indicating that the Ir_1@Co has a high barrier of the rate determining step in alkaline solution. In comparison, single atom Ir_1 on a four-fold carbon structure shows they are in favor of the adsorption and dissociation of water molecules, showing a smaller ΔG_{H^*}. Impressively, compared with IrC_4 (0.46 eV), the $IrNC_3$ shows a smallest free energy of (-0.39 eV), indicating that trace of nitrogen atom can weaken the H* adsorption, leading to a low energy barrier for H* detachment.

The OER performance was also computed on the four possible catalytic sites and their free energies of the intermediates are plotted at pH=14, showing the different values

applied in different potential *U* (Figure 6-34). It is known that four elementary steps are involved in producing O_2 as shown in Figure 6-32j-m. Amongst, the third step, of which an O* reacts with another H_2O molecule to produce an OOH*, are the determined step. Variety of η are applied to decrease the uphill of free energy obtained at the equilibrium potential (U=0.40 V). In particular, the over-potential needed is 1.58 V (Figure 6-32j), 1.52 V (Figure 6-32k), 0.61 V (Figure 6-32l), and 0.45 V (Figure 6-32m) at pH = 14 for $IrNC_3$, IrC_4, Ir_1@CoO (Co), and Ir_1@CoO (Ir), respectively, indicating that the single atom Ir structured on the Co particles are the most efficient catalytic site in generating oxygen (Figure 6-34). Significantly, the same free energy ΔG_{H^*} of the fourth and final steps (Figure 6-32m) means that the Ir_1@CoO (Ir) can straight to producing OOH* and O_2 without any further decreased free energy ΔG_{H^*}. Also, comparing with $IrNC_3$, IrC_4, and Ir_1@CoO (Co), Ir_1@CoO (Ir) has the lowest free energy at the final step, implying the O_2 can be easily desorbed from the surface, decreasing the poisoning effect. The computational calculation confirmed that the single atom Ir structured on the heterogeneous substrate can facilitate the transfer from H_2O molecule to H_2 and O_2 in alkaline solution, thus simultaneously promoting the OER and HER. Particularly, one part Ir_1@CoO (Ir) shows the lowest computed over-potential of 0.45 V on OER while the other part Ir_1@NC_3 has the smallest free energy of 0.39 V on producing H_2. Also, as illustrated by the projected density of states (PDOS) in Figure 6-32h, both of the free atom Ir_1 doped NC and CoO shows a higher and narrow occupied states, which is majorly attributed by their *d* orbitals near Fermi level. This reveals that the single atom Ir_1 can effectively improve the *d*-electron domination near the Fermi level and promote the electron transfer, leading to a higher conductivity and enhanced catalytic activity as well. Also, being alloyed with Co, Ir_1 can

immediately weaken the adsorption energy with oxygen, resulting in reduced barrier of OER and improving the ability of accelerating the water splitting[294].

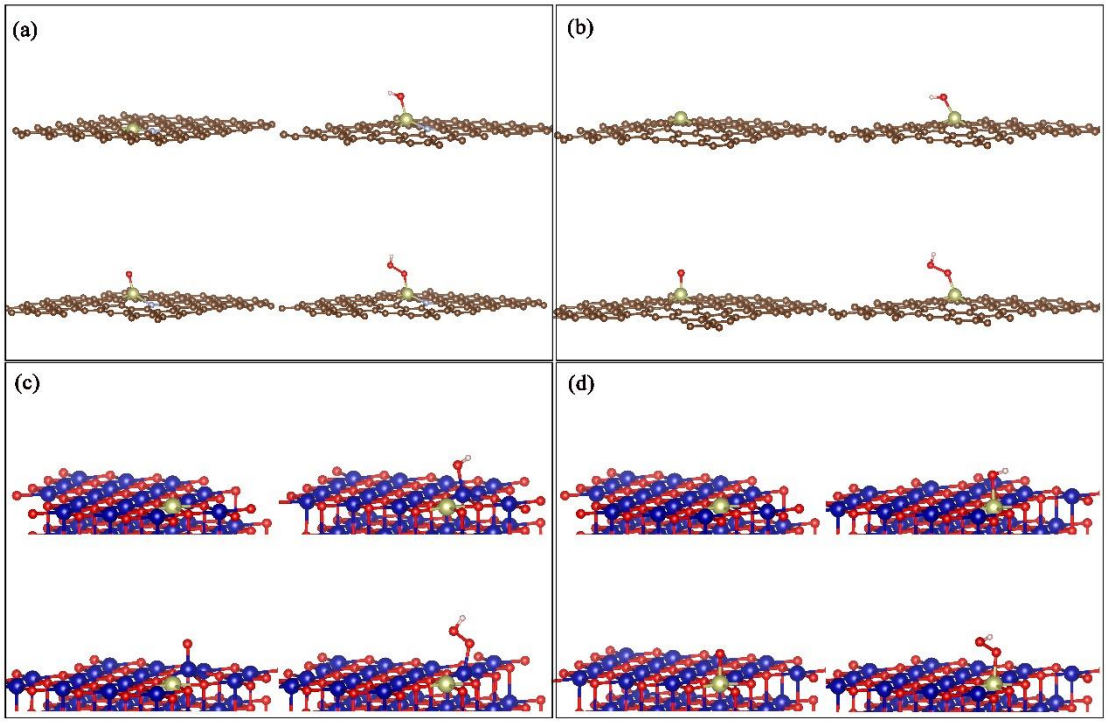

Figure 6-34. (a) The optimized structures of HO, O, and HOO adsorptions on (a) $IrNC_3$, (b) IrC_4, (c) Ir_1@CoO (Co), and (d) Ir_1@CoO (Ir).

In order to experimentally verify the activity differences of Ir1 anchored on distinct substrates, a control sample Ir_1@NC has been prepared (Fig. 6-35). In contrast to Ir_1@Co/NC, the Ir_1@NC shows a minor decrease of the overpotential for HER but a serious fading towards OER (Fig. 6-36), confirming that the Ir single atom on carbon matrix is mainly responsible for the high HER performance and the Co component in the support can also assist in improving the HER ability due to the enhanced conductivity. The results are well consistent with our experimental reulsts and DFT calculations.

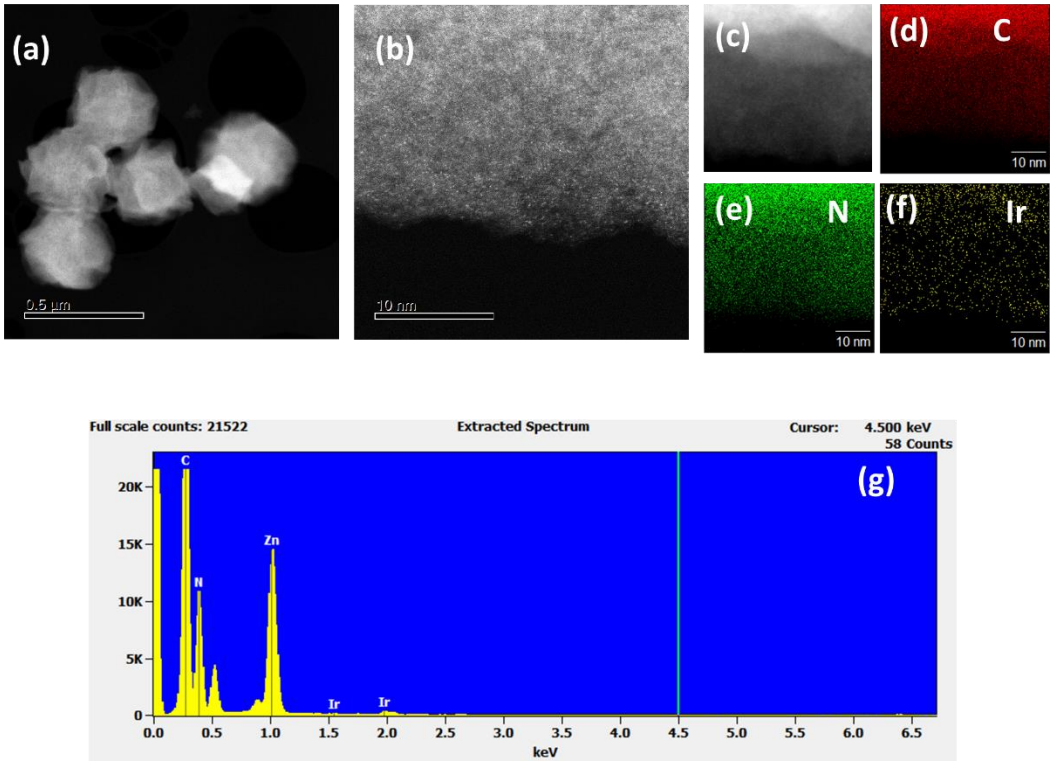

Figure 6-35. The HAADF image of Ir_1@NC with low resolution (a) and high resolution (b). (c-f) The elemental mapping images of Ir_1@NC. (g) The EDS spectrum of Ir_1@NC. The ZIF-8 has been selected as host materials to anchor Ir single atoms. The HAADF images and elemental mapping, EDS spectrum as well confirms that Ir single atom has been successfully prepared on nitrogen doped carbon matrix. Please note that the Ir_1@NC will be leached in the 1M HCl acid before it is being used to test HER.

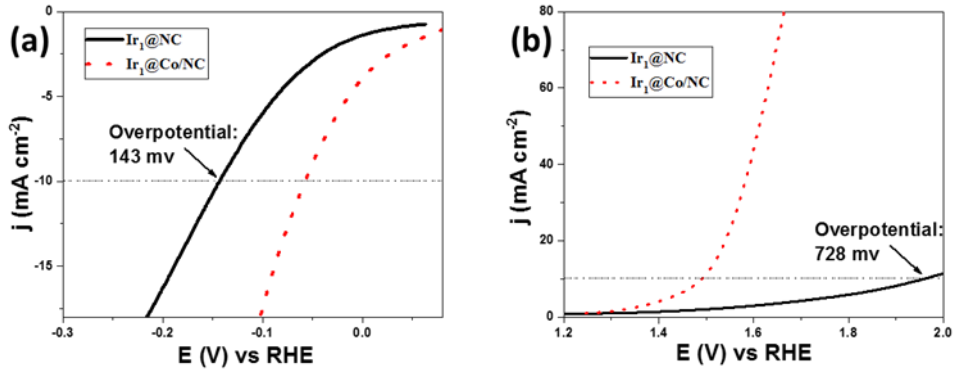

Figure 6-36. The performance comparisons of Ir_1@NC and Ir_1@Co/NC for (a) HER and (b) OER.

6.4. Conclusion

In sum, through coordinating with the π electrons on imidazole group of ZIF-67, the bonding metals ions (Pt^{2+}/Ir^{2+}/Pd^{2+}/Ru^{2+}/Ni^{2+}/Fe^{2+}) can be stabilized as isolated single atoms anchored on the heterogeneous substrate, composed of nitrogen doped carbon matrix and cobalt nanoparticles, via a facile pyrolysis process. The formation mechanism and high reactivity of these atomically dispersed atoms are systematically explored by control experiments and DFT calculations. The high accessibility of numerous tunnels on ZIF-67 frameworks leads to unique 3D dispersion of single atoms, thus achieving an ultrahigh density of active sites. Such fascinating structures of the high active materials, such as Ir_1@Co/NC, enable them as superior catalysts on reaction electrodes for HER and OER. The DFT calculations build a variety of possible Ir_1 active sites, showing that Ir_1@CoO (Ir) are responsible for the high OER performance, while the $Ir_1@NC_3$ leads to the superior HER efficiency. Such a synergistic structure simultaneously accelerate an efficient and stable ability on overall water splitting. This work sheds light on the synthesis of various single-atom catalysts with the high-efficiency and multifold active sites.

Chapter 7

7. General Conclusions and Outlook

7.1. General Conclusions

In this doctoral thesis work, the recent developments and the underlying mechanisms for various SACs fabrication and corresponding electrocatalytic applications are summarized, which lead to a better understanding of the role of single-atom species, supports selection, and SMSI effects for catalytic properties.

For instance, ZIF-67 was the excellent option being selected as support to anchor single atoms, owing to the easy accessibility and numerous ligands dispersed on the architectural structures. Also, , through coordinating with the π electrons on imidazole group of ZIF-67, the bonding metals ions (Pt^{2+}/Ir^{2+}/Pd^{2+}/Ru^{2+}/Ni^{2+}/Fe^{2+}) can be stabilized as isolated single atoms anchored on the heterogeneous substrate, composed of nitrogen doped carbon matrix and cobalt nanoparticles, via a facile pyrolysis process. Thus, we successfully build dual catalytic abilities via anchoring single atoms on alternative active sites, simultaneously promoting the HER and OER, on one material with efficient, stable, cheap characteristics. With the further control the thermal conditions, the combination between bimetallic structure and single atom can be prepared to show a synergistic effect on catalytic reaction. We demonstrate the synthesis of a quasi-Pt-allotrope: Pt_3Co nanospheres with an internal hollow structure (H-PtCo), which, in turn, are surrounded by an N-doped carbon shell with single-atom Pt anchored to it (Pt_1N-C). The intermetallic H-PtCo with its internal cavities and

uneven surface can expose abundant active sites and efficiently achieve high ORR activity. In addition, through tuning the self-assembling of the single atoms of Pt, the core-skin PtBi@Pt was successfully prepared on the surface of PtBi intermetallic using the SAS method, demonstarting a facinating EOR performance.

Specifically, owing to the synergistic effects between the hollow PtCo alloy cores and Pt single atoms/N co-doped C shells, the H-PtCo@Pt_1N-C shows the mass activity of H-PtCo@Pt_1N-C is 1.2 mA μg_{Pt}^{-1} at 0.9 V vs. reversible hydrogen electrode (RHE), which is one of the most remarkable ORR performance among all reported Pt-Co/C systems. After 10000 cycles, the mass activity of H-PtCo@Pt_1N-C at 0.9 V remains 1.26 mA μg_{Pt}^{-1} without any fade. These results indicate that H-PtCo@Pt_1N-C can boost the ORR activity with greatly enhanced durability. More importantly, the single atoms Pt in shells forming Pt-NC_3 is confirmed that they are favorable to prompt ORR performance via the DFT calculation. Also, when tested in tetraethylene glycol dimethyl ether (TEGDME) and dimethylsulfoxide (DMSO)-based organic electrolytes, the discharge overpotential of H-PtCo@Pt_1N-C was only 0.05 V, indicating that this sample has an efficient ORR capability in organic electrolytes as well. The tensile strain of Pt-skin surface of PtBi@Pt was realized to achieve a very high mass activity of 9.01 mA μg_{Pt}^{-1}, which is 8.26 times higher than that of Pt/C towards the EOR. Remarkably, the *in-situ* FTIR spectra and DFT results demonstrate that PtBi@Pt has better selectivity towards the EOR, which mainly proceeds via the C1 pathway, while PtBi/SA Pt and Pt/C mainly go through the C2 pathway. It is novel that the M_1 can simultaneously anchor on two distinct domains of the hybrid support, four-fold N/C atoms (M_1@NC) and center of Co octahedral (M_1@Co), which are expected to serve as bifunctional electrocatalysts towards HER and OER, respectively. Amongst, a

catalyst of Ir_1 exhibits the most excellent water splitting performance, showing a low applied potential of 1.603 V to achieve 10 mA cm^{-2} in 1.0 M KOH solution with cycling over 5 h. The density functional theory (DFT) calculations speculate that the Ir_1@Co (Ir) sites can accelerate the OER and Ir_1@ NC_3 sites are responsible for the enhanced HER, clarifying the unprecedented performance of this bi-functional catalyst toward full water splitting.

7.2. Outlook

Single atoms have become a new frontier in the catalysis field, which possess the maximum atomic utilization efficiency and have an unsaturated coordination environment. With their unique electronic and structural properties, metal single atoms usually show outstanding catalytic performance towards various chemical reactions. It is challenging, however, to synthesize stable single metal-atom catalysts because of their high surface energy and tendency towards aggregation. Thus, it is exceedingly difficult to fabricate a large range of metal single atoms on the same support. More research should focus on a new strategy for the surface modification of the support, in which the formation of surface uncapped defects on the carbonaceous support is vital to successfully stabilize the single metal-atom species through N-coordination without aggregation.

For future research, it is essential to develop more SACs with high thermal/chemical stability and excellent catalytic performance. It is should be pointed out that the current loading ratio of SACs is relatively low. In order to enhance the catalytic performance of various SACs, it is urgent to explore various strategies to achieve high loading ratio, such as developing synthesis methods and modifying the surface of supports.

Manipulating strong interactions between SACs and supports with abundant anchoring sites would hold great promise for this target. On the other hand, the understanding of the catalytic mechanism and performance based on the interactions between SACs and supports should be further deepened at the atomic scale by employing SACs as model systems with the aid of theoretical calculation and in situ characterization. Moreover, we believe the synergistic effect of different types of SACs is very critical in optimizing catalytic performance for diverse reactions. It opens a new avenue for structure design and material synthesis, in which a series of binary/ternary/multi-phase SACs are waiting to be explored. The further study on optimal doping levels and ratios is also significant and meaningful. Therefore, more efforts on the applications of SACs could be extended to a wide range of useful catalytic reactions for energy generation, water purification, gas emission control, and production of chemicals. Research along this SACs direction is expected to be very interesting and fruitful.

References

1 J. Liu, *Acs Catalysis* 2016, **7**, 34.

2 a) J. M. Thomas, R. Raja, D. W. Lewis, *Angewandte Chemie International Edition* 2005, **44**, 6456; b) B. Qiao, A. Wang, X. Yang, L. F. Allard, Z. Jiang, Y. Cui, J. Liu, J. Li, T. Zhang, *Nature chemistry* 2011, **3**, 634; c) M. Ranocchiari, C. Lothschütz, D. Grolimund, J. A. van Bokhoven, presented at Proc. R. Soc. A 2012.

3 L. Wang, L. Huang, F. Liang, S. Liu, Y. Wang, H. Zhang, *Chinese Journal of Catalysis* 2017, **38**, 1528.

4 a) S. Tauster, S. Fung, R. L. Garten, *J. Am. Chem. Soc.* 1978, 100, 170; b) S. J. Tauster, *Accounts of Chemical Research* 1987, **20**, 389.

5 A. Bruix, J. A. Rodriguez, P. J. Ramírez, S. D. Senanayake, J. Evans, J. B. Park, D. Stacchiola, P. Liu, J. Hrbek, F. Illas, *Journal of the American Chemical Society* 2012, **134**, 8968.

6 V. E. Henrich, P. A. Cox, *The surface science of metal oxides*, Cambridge university press, 1996.

7 C. T. Campbell, *Nature chemistry* 2012, **4**, 597.

8 P. Hu, Z. Huang, Z. Amghouz, M. Makkee, F. Xu, F. Kapteijn, A. Dikhtiarenko, Y. Chen, X. Gu, X. Tang, *Angewandte Chemie* 2014, **126**, 3486.

9 O. Lopez-Acevedo, K. A. Kacprzak, J. Akola, H. Häkkinen, *Nature chemistry* 2010, 2, 329.

10 a) S. Dahl, A. Logadottir, R. Egeberg, J. Larsen, I. Chorkendorff, E. Törnqvist, J. K. Nørskov, *Physical Review Letters* 1999, 83, 1814; b) J. K. Nørskov, T. Bligaard, B. Hvolbæk, F. Abild-Pedersen, I. Chorkendorff, C. H. Christensen, *Chem. Soc. Rev.* 2008, **37**, 2163.

11 a) A. Wang, J. Li, T. Zhang, *Nature Reviews Chemistry* 2018, 2, 65; b) Y. Chen, Z. Huang, Z. Ma, J. Chen, X. Tang, *Catalysis Science & Technology* 2017, 7, 4250; c) C. Zhu, S. Fu, Q. Shi, D. Du, Y. Lin, *Angewandte Chemie International Edition* 2017, **56**, 13944.

12 Tokura, Y. & Nagaosa, N. *Science* **288**, 462-468 (2000).

13 Häkkinen, H., Abbet, S., Sanchez, A., Heiz, U. & Landman, U. *Angewandte Chemie International Edition* **42**, 1297-1300 (2003).

14 Muller, D. A. *et al. Nature* **399**, 758 (1999).

15 Campbell, C. T. *Surface science reports* **27**, 1-111 (1997).

16 Umebayashi, T., Yamaki, T., Itoh, H. & Asai, K. *Journal of Physics and Chemistry of Solids* **63**, 1909-1920 (2002).

17 Chien, C.-H., Chiou, S. H., Guo, G. & Yao, Y.-D. *Journal of magnetism and magnetic materials* **282**, 275-278 (2004).

18 O'Connor, N. J., Jonayat, A., Janik, M. J. & Senftle, T. P. *Nature Catalysis* **1**, 531 (2018).

19 Dresselhaus, M. S., Dresselhaus, G. & Eklund, P. C. (Elsevier, 1996).

20 Zhang, Y., Zhang, Y., Zhang, D. & Liu, C. *The Journal of Physical Chemistry B* **110**, 4671-4674 (2006).

21 Shi Kam, N. W., Jessop, T. C., Wender, P. A. & Dai, H. *Journal of the American Chemical Society* **126**, 6850-6851 (2004).

22 Steele, B. C. & Heinzel, A. in *Materials For Sustainable Energy: A Collection of Peer-Reviewed Research and Review Articles from Nature Publishing Group* 224-231 (World Scientific, 2011).

23 Lefèvre, M. & Dodelet, J.-P. *Electrochimica Acta* **48**, 2749-2760 (2003).

24 Stoyanov, S. R., Titov, A. V. & Král, P. *Coordination Chemistry Reviews* **253**, 2852-2871 (2009).

25 Jasinski, R. A new fuel cell cathode catalyst. *Nature* **201**, 1212 (1964).

26 Fei, H. *et al. Nature communications* **6**, 8668 (2015).

27 Zhu, Y. *et al. ACS Catalysis* **8**, 10004-10011 (2018).

28 Zhang, C. *et al. ACS nano* **11**, 6930-6941 (2017).

29 Yin, P. *et al. Angewandte Chemie International Edition* **55**, 10800-10805 (2016).

30 Zhao, C. *et al. Journal of the American Chemical Society* **139**, 8078-8081 (2017).

31 Chen, Y. *et al. Angewandte Chemie International Edition* **56**, 6937-6941 (2017).

32 Wang, X. *et al. Journal of the American Chemical Society* **139**, 9419-9422 (2017).

33 Li, X. *et al. Journal of the American Chemical Society* **140**, 12469-12475, doi:10.1021/jacs.8b05992 (2018).

34 Casanovas, J., Ricart, J. M., Rubio, J., Illas, F. & Jiménez-Mateos, J. M. *Journal of the American Chemical Society* **118**, 8071-8076 (1996).

35 Liu, J. *et al. Nature communications* **8**, 15938 (2017).

36 Duchesne, P. N. *et al. Nature materials* **17**, 1033 (2018).

37 Greiner, M. T. *et al. Nature chemistry* **10**, 1008 (2018).

38 Yue, Q., Chang, S., Qin, S. & Li, J. *Physics Letters A* **377**, 1362-1367 (2013).

39 Rodriguez, J. A. & Goodman, D. W. *Science* **257**, 897-903 (1992).

40 Cotton, F. A., Murillo, C. A. & Walton, R. A. (Springer Science & Business Media, 2005).

41 Bruix, A. *et al. Journal of the American Chemical Society* **134**, 8968-8974 (2012).

42 Fu, Q., Saltsburg, H. & Flytzani-Stephanopoulos, M. *Science* **301**, 935-938 (2003).

43 Novotný, Z. *et al. Physical review letters* **108**, 216103 (2012).

44 Bliem, R. *et al. Science* **346**, 1215-1218 (2014).

45 Bliem, R. *et al. ACS Nano* **8**, 7531-7537, doi:10.1021/nn502895s (2014).

46 Novotny, Z. *et al. Physical Review B* **87**, 195410 (2013).

47 Parkinson, G. S. *et al. Nature materials* **12**, 724 (2013).

48 Bliem, R. *et al. ACS nano* **8**, 7531-7537 (2014).

49 Qiao, B. *et al. ACS Catalysis* **5**, 6249-6254 (2015).

50 Dvořák, F. *et al. Nature communications* **7**, 10801 (2016).

51 Jones, J. *et al.* Thermally stable single-atom platinum-on-ceria catalysts via atom trapping. *Science* **353**, 150-154 (2016).

52 Moses-DeBusk, M. *et al. Journal of the American Chemical Society* **135**, 12634-12645 (2013).

53 Zhang, Z. *et al. Nature Communications* **8**, 16100 (2017).

54 Cui, X. *et al. ACS central science* **3**, 580-585 (2017).

55 Narula, C. K., Allard, L. F., Stocks, G. & Moses-DeBusk, M. *Scientific reports* **4**, 7238 (2014).

56 Li, Z.-Y., Yuan, Z., Li, X.-N., Zhao, Y.-X. & He, S.-G. *Journal of the American Chemical Society* **136**, 14307-14313 (2014).

57 Lin, J. *et al. Journal of the American Chemical Society* **135**, 15314-15317 (2013).

58 Qiao, B. *et al. Nano Research* **8**, 2913-2924 (2015).

59 Lin, J. *et al. Chemical Communications* **51**, 7911-7914 (2015).

60 Wei, H. *et al. Nature communications* **5**, ncomms6634 (2014).

61 Qiao, B. *et al. Nature Chemistry* **3**, 634 (2011).

62 Liu, P. *et al. Science* **352**, 797-800 (2016).

63 DeRita, L. *et al. Journal of the American Chemical Society* **139**, 14150-14165 (2017).

64 Gu, X.-K. *et al. ACS Catalysis* **4**, 3886-3890 (2014).

65 Wang, C. *et al. ACS Catalysis* **6**, 210-218 (2015).

66 Huang, Z. *et al. Angewandte Chemie* **124**, 4274-4279 (2012).

67 Ding, K. *et al. Science* **350**, 189-192 (2015).

68 Wang, L. *et al. Angewandte Chemie International Edition* **56**, 4712-4718 (2017).

69 Wang, J. *et al. ChemSusChem* **9**, 784-790 (2016).

70 Deng, J. *et al. Energy & Environmental Science* **8**, 1594-1601 (2015).

71 Liu, G. *et al. Nature chemistry* **9**, 810 (2017).

72 Yang, S., Kim, J., Tak, Y. J., Soon, A. & Lee, H. *Angewandte Chemie International Edition* **55**, 2058-2062 (2016).

73 Yang, S., Tak, Y. J., Kim, J., Soon, A. & Lee, H. *ACS Catalysis* **7**, 1301-1307 (2017).

74 Wang, H. *et al. Nano letters* **12**, 141-144 (2011).

75 Sun, S. *et al. Scientific reports* **3**, 1775 (2013).

76 Yan, H. *et al. Journal of the American Chemical Society* **137**, 10484-10487 (2015).

77 Qiu, H. J. *et al. Angewandte Chemie International Edition* **54**, 14031-14035 (2015).

78 Zhang, X. *et al. Nature communications* **4**, 1924 (2013).

79 Malta, G. *et al. Science* **355**, 1399-1403 (2017).

80 Vilé, G. *et al. Angewandte Chemie International Edition* **54**, 11265-11269 (2015).

81 Li, X. *et al. Advanced Materials* **28**, 2427-2431 (2016).

82 Zheng, Y. *et al. Journal of the American Chemical Society* **139**, 3336-3339 (2017).

83 Tao, L. *et al. Nano Energy* **41**, 417-425 (2017).

84 Zhang, H. *et al. Journal of the American Chemical Society* **139**, 14143-14149 (2017).

85 Kyriakou, G. *et al. Science* **335**, 1209-1212 (2012).

86 Boucher, M. B. *et al. Physical Chemistry Chemical Physics* **15**, 12187-12196 (2013).

87 Lucci, F. R. *et al. Nature communications* **6**, 8550 (2015).

88 Pei, G. X. *et al. ACS Catalysis* **7**, 1491-1500 (2017).

89 Shan, J. *et al. Applied Catalysis B: Environmental* **205**, 541-550 (2017).

90 Lou, Y. & Liu, J. *Industrial & Engineering Chemistry Research* **56**, 6916-6925 (2017).

91 Guzman, J. & Gates, B. C. *Journal of Catalysis* **226**, 111-119 (2004).

92 Yang, M., Allard, L. F. & Flytzani-Stephanopoulos, M. *Journal of the American Chemical Society* **135**, 3768-3771 (2013).

93 Chen, M. & Goodman, D. *Science* **306**, 252-255 (2004).

94 Matthey, D. *et al. Science* **315**, 1692-1696 (2007).

95 Kwak, J. H. *et al. Science* **325**, 1670-1673 (2009).

96 Bruix, A. *et al. Angewandte Chemie International Edition* **53**, 10525-10530 (2014).

97 Liu, J.-C., Wang, Y.-G. & Li, J. *Journal of the American Chemical Society* **139**, 6190-6199 (2017).

98 Branda, M. M., Ferullo, R. M., Causà, M. & Illas, F. *The Journal of Physical Chemistry C* **115**, 3716-3721, doi:10.1021/jp111427j (2011).

99 Yu-Yao, Y.-F. & Kummer, J. *Journal of Catalysis* **106**, 307-312 (1987).

100 Liang, J.-X. *et al. The Journal of Physical Chemistry C* **118**, 21945-21951, doi:10.1021/jp503769d (2014).

101 Boccuzzi, F., Chiorino, A., Manzoli, M., Andreeva, D. & Tabakova, T. *Journal of Catalysis* **188**, 176-185 (1999).

102 Liang, J.-X. *et al. The Journal of Physical Chemistry C* **118**, 21945-21951 (2014).

103 Li, F., Li, Y., Zeng, X. C. & Chen, Z. *ACS Catalysis* **5**, 544-552 (2014).

104 Li, X.-N., Yuan, Z. & He, S.-G. *Journal of the American Chemical Society* **136**, 3617-3623 (2014).

105 Lee, C., Wei, X., Kysar, J. W. & Hone, J. *Science* **321**, 385-388 (2008).

106 Zhang, C. *et al. Advanced Energy Materials*, 1703487 (2018).

107 Zhang, B. *et al. Angewandte Chemie International Edition* **55**, 8319-8323 (2016).

108 Li, X. *et al. Journal of the American Chemical Society* **140**, 12469-12475 (2018).

109 Zheng, Y. & Qiao, S.-Z. *National Science Review* (2018).

110 Zheng, Y. *et al. Nature communications* **5**, 3783 (2014).

111 Gao, G. *et al. Journal of Catalysis* **332**, 149-155 (2015).

112 Liu, J. *et al. Science* **347**, 970-974 (2015).

113 Gao, G., Jiao, Y., Waclawik, E. R. & Du, A. *Journal of the American Chemical Society* **138**, 6292-6297 (2016).

114 Tak, Y. J., Jang, W., Richter, N. A. & Soon, A. *Physical Chemistry Chemical Physics* **17**, 9680-9686 (2015).

115 Back, S. & Jung, Y. *ACS Energy Letters* **2**, 969-975 (2017).

116 Guo, X. *et al.* Direct, *Science* **344**, 616-619 (2014).

117 Kwak, J. H., Kovarik, L. & Szanyi, J. n. *ACS Catalysis* **3**, 2094-2100 (2013).

118 Wang, C., Yang, M. & Flytzani-Stephanopoulos, M. *AIChE Journal* **62**, 429-439 (2016).

119 Guan, H. *et al. AIChE Journal* **63**, 2081-2088 (2017).

120 Guo, L.-W. *et al. Nature communications* **7**, 13481 (2016).

121 Therrien, A. J. *et al. Nature Catalysis* **1**, 192 (2018).

122 Li, L. *et al. Journal of catalysis* **299**, 90-100 (2013).

123 Nie, L. *et al. Science* **358**, 1419-1423 (2017).

124 Kim, J., Kim, H. E. & Lee, H. *ChemSusChem* **11**, 104-113 (2018).

125 Zhu, C., Fu, S., Shi, Q., Du, D. & Lin, Y. *Angewandte Chemie International Edition* (2017).

126 Bayatsarmadi, B., Zheng, Y., Vasileff, A. & Qiao, S. Z. *Small* (2017).

127 Cui, X. *et al. Angewandte Chemie International Edition* **55**, 6708-6712 (2016).

128 Zitolo, A. *et al. Nature communications* **8**, 957 (2017).

129 Chen, Y. *et al. Angewandte Chemie* **129**, 7041-7045 (2017).

130 Zitolo, A. *et al. Nature materials* **14**, 937 (2015).

131 Wu, H. *et al. Energy & Environmental Science* **9**, 3736-3745 (2016).

132 Cheng, N. *et al. Nature communications* **7**, 13638 (2016).

133 Boucher, M. B., Goergen, S., Yi, N. & Flytzani-Stephanopoulos, M. *Physical Chemistry Chemical Physics* **13**, 2517-2527 (2011).

134 Si, R. & Flytzani-Stephanopoulos, M. *Angewandte Chemie* **120**, 2926-2929 (2008).

135 Boucher, M. B. *et al. The Journal of Physical Chemistry C* **115**, 1261-1268 (2010).

136 Yi, N., Si, R., Saltsburg, H. & Flytzani-Stephanopoulos, M. *Applied Catalysis B: Environmental* **95**, 87-92 (2010).

137 Yi, N., Si, R., Saltsburg, H. & Flytzani-Stephanopoulos, M. *Energy & Environmental Science* **3**, 831-837 (2010).

138 Kim, Y. T. *et al. Angewandte Chemie* **118**, 421-425 (2006).

139 Campbell, C. T., Parker, S. C. & Starr, D. E. *Science* **298**, 811-814 (2002).

140 Parker, S. C. & Campbell, C. T. *Physical Review B* **75**, 035430 (2007).

141 Farmer, J. A. & Campbell, C. T. *Science* **329**, 933-936 (2010).

142 Yang, M. *et al. Science* **346**, 1498-1501 (2014).

143 Yang, M. *et al. Journal of the American Chemical Society* **137**, 3470-3473 (2015).

144 Rim, K. T. *et al. The Journal of Physical Chemistry C* **113**, 10198-10205 (2009).

145 Bliem, R. *et al. Proceedings of the National Academy of Sciences* **113**, 8921-8926 (2016).

146 Horch, S. *et al. Nature* **398**, 134 (1999).

147 Zhang, L. *et al. ACS Catalysis* **5**, 6563-6572 (2015).

148 Liu, W. *et al. Chemical Science* **7**, 5758-5764 (2016).

149 Hu, P. *et al. Angewandte Chemie* **126**, 3486-3489 (2014).

150 Wei, H. *et al. Chemical science* **8**, 5126-5131 (2017).

151 Pei, G. X. *et al. Acs Catalysis* **5**, 3717-3725 (2015).

152 Feng, Q. *et al. Journal of the American Chemical Society* **139**, 7294-7301 (2017).

153 Kwak, J. H., Kovarik, L. & Szanyi, J. n. *ACS catalysis* **3**, 2449-2455 (2013).

154 Matsubu, J. C., Yang, V. N. & Christopher, P. *Journal of the American Chemical Society* **137**, 3076-3084 (2015).

155 Cheng, M.-J., Clark, E. L., Pham, H. H., Bell, A. T. & Head-Gordon, M. *ACS Catalysis* **6**, 7769-7777 (2016).

156 Back, S., Lim, J., Kim, N.-Y., Kim, Y.-H. & Jung, Y. *Chemical science* **8**, 1090-1096 (2017).

157 Sarfraz, S., Garcia-Esparza, A. T., Jedidi, A., Cavallo, L. & Takanabe, K. Cu–Sn bimetallic catalyst for selective aqueous electroreduction of CO2 to CO. *ACS Catalysis* **6**, 2842-2851 (2016).

158 Yang, H. B. *et al. Nature Energy* **3**, 140 (2018).

159 Genovese, C. *et al. Nature communications* **9**, 935 (2018).

160 Siahrostami, S. *et al. Nature materials* **12**, 1137 (2013).

161 Verdaguer-Casadevall, A. *et al. Nano letters* **14**, 1603-1608 (2014).

162 a) L. Chen, X. Dong, Y. Wang, Y. Xia, *Nature communications* 2016, **7**, 11741; b) K. Luo, M. R. Roberts, R. Hao, N. Guerrini, D. M. Pickup, Y.-S. Liu, K. Edström, J. Guo, A. V. Chadwick, L. C. Duda, *Nature chemistry* 2016, **8**, 684; c) Q. Jia, J. Li, K. Caldwell, D. E. Ramaker, J. M. Ziegelbauer, R. S. Kukreja, A. Kongkanand, S. Mukerjee, *ACS Catalysis* 2016, **6**, 928; d) J. Greeley, I. Stephens, A. Bondarenko, T. P. Johansson, H. A. Hansen, T. Jaramillo, J. Rossmeisl, I. Chorkendorff, J. K. Nørskov, *Nature Chemistry* 2009, **1**, 552.

163 a) K. Jiang, D. Zhao, S. Guo, X. Zhang, X. Zhu, J. Guo, G. Lu, X. Huang, *Science Advances* 2017, **3**, e1601705; b) X. Huang, E. Zhu, Y. Chen, Y. Li, C. Y. Chiu, Y. Xu, Z. Lin, X. Duan, Y. Huang, *Advanced Materials* 2013, **25**, 2974.

164 V. R. Stamenkovic, B. Fowler, B. S. Mun, G. Wang, P. N. Ross, C. A. Lucas, N. M. Marković, *Science* 2007, **315**, 493.

165 D. Wang, H. L. Xin, R. Hovden, H. Wang, Y. Yu, D. A. Muller, F. J. DiSalvo, H. D. Abruña, *Nature Materials* 2013, **12**, 81.

166 I. Dutta, M. K. Carpenter, M. P. Balogh, J. M. Ziegelbauer, T. E. Moylan, M. H. Atwan, N. P. Irish, *The Journal of Physical Chemistry C* 2010, **114**, 16309.

167 D. Y. Chung, S. W. Jun, G. Yoon, S. G. Kwon, D. Y. Shin, P. Seo, J. M. Yoo, H. Shin, Y.-H. Chung, H. Kim, *Journal of the American Chemical Society* 2015, **137**, 15478.

168 X.-F. Yang, A. Wang, B. Qiao, J. Li, J. Liu, T. Zhang, *Accounts of Chemical Research* 2013, **46**, 1740.

169 a) M. Crespo-Quesada, A. Yarulin, M. Jin, Y. Xia, L. Kiwi-Minsker, *Journal of the American Chemical Society* 2011, 133, 12787; b) D. Wang, Y. Yu, H. L. Xin, R. Hovden, P. Ercius, J. A. Mundy, H. Chen, J. H. Richard, D. A. Muller, F. J. DiSalvo, *Nano Letters* 2012, **12**, 5230.

170 N. Tian, Z.-Y. Zhou, S.-G. Sun, Y. Ding, Z. L. Wang, *science* 2007, **316**, 732.

171 a) L. Dubau, J. Durst, F. Maillard, L. Guétaz, M. Chatenet, J. André, E. Rossinot, *Electrochimica Acta* 2011, **56**, 10658; b) C. Cui, L. Gan, M. Heggen, S. Rudi, P. Strasser, *Nature Materials* 2013, **12**, 765; c) L. Dubau, F. Maillard, M. Chatenet, J. André, E. Rossinot, *Electrochimica Acta* 2010, **56**, 776.

172 M. Gummalla, S. C. Ball, D. A. Condit, S. Rasouli, K. Yu, P. J. Ferreira, D. J. Myers, Z. Yang, *Catalysts* 2015, **5**, 926.

173 X. Wang, M. Vara, M. Luo, H. Huang, A. Ruditskiy, J. Park, S. Bao, J. Liu, J. Howe, M. Chi, *Journal of the American Chemical Society* 2015, **137**, 15036.

174 a) J. Tang, Y. Yamauchi, *Nature Chemistry* 2016, **8**, 638; b) R. R. Salunkhe, C. Young, J. Tang, T. Takei, Y. Ide, N. Kobayashi, Y. Yamauchi, *Chemical Communications* 2016, **52**, 4764; c) W. Zhang, X. Jiang, Y. Zhao, A. Carné-Sánchez, V. Malgras, J. Kim, J. H. Kim, S. Wang, J. Liu, J.-S. Jiang, *Chemical Science* 2017, **8**, 3538; d) C. Young, J. Wang, J. Kim, Y. Sugahara, J. Henzie, Y. Yamauchi, *Chemistry of Materials* 2018, **30**, 3379; e) C. Wang, Y. V. Kaneti, Y. Bando, J. Lin, C. Liu, J. Li, Y. Yamauchi, *Materials Horizons* 2018, **5**, 394.

175 Y.-X. Wang, J. Yang, S.-L. Chou, H. K. Liu, W.-x. Zhang, D. Zhao, S. X. Dou, *Nature Communications* 2015, **6**, 8689.

176 N. Liu, H. Wu, M. T. McDowell, Y. Yao, C. Wang, Y. Cui, *Nano Letters* 2012, **12**, 3315.

177 Z. Zhang, Y. Zhu, H. Asakura, B. Zhang, J. Zhang, M. Zhou, Y. Han, T. Tanaka, A. Wang, T. Zhang, *Nature Communications* 2017, **8**, 16100.

178 G. Kresse, J. Furthmüller, *Physical review B* 1996, **54**, 11169.

179 J. P. Perdew, K. Burke, M. Ernzerhof, *Physical Review Letters* 1996, **77**, 3865.

180 J. K. Nørskov, J. Rossmeisl, A. Logadottir, L. Lindqvist, J. R. Kitchin, T. Bligaard, H. Jonsson, *The Journal of Physical Chemistry B* 2004, **108**, 17886.

181 B. Y. Xia, Y. Yan, N. Li, H. B. Wu, X. W. D. Lou, X. Wang, *Nature Energy* 2016, **1**, 15006.

182 W. Zhang, X. Jiang, X. Wang, Y. V. Kaneti, Y. Chen, J. Liu, J. S. Jiang, Y. Yamauchi, M. Hu, *Angewandte Chemie International Edition* 2017.

183 D. Gebauer, A. Völkel, H. Cölfen, *Science* 2008, **322**, 1819.

184 S. Fu, C. Zhu, Q. Shi, D. Du, Y. Lin, *Catalysis Science & Technology* 2016, **6**, 5052.

185 K. Stańczyk, R. Dziembaj, Z. Piwowarska, S. Witkowski, *Carbon* 1995, **33**, 1383.

186 L. Bu, S. Guo, X. Zhang, X. Shen, D. Su, G. Lu, X. Zhu, J. Yao, J. Guo, X. Huang, *Nature Communications* 2016, **7**, 11850.

187 M. Liu, R. Zhang, W. *Chen, Chem. Rev*. 2014, **114**, 5117.

188 Y. G. Guo, J. S. Hu, L. J. Wan, *Adv. Mater*. 2008, **20**, 2878.

189 Z. Wu, Y. Lv, Y. Xia, P. A. Webley, D. Y. Zhao, *J. Am. Chem. Soc*. 2012, **134**, 2236.

190 C. Guo, Y. Zheng, J. Ran, F. Xie, M. Jaroniec, S. Z. Qiao, *Angew. Chem. Int. Ed*. 2017, **56**, 8359.

191 W. Du, G. Yang, E. Wong, N. A. Deskins, A. I. Frenkel, D. Su, X. Teng, *J. Am. Chem. Soc*. 2014, **136**, 10862.

192 N. Erini, R. Loukrakpam, V. Petkov, E. A. Baranova, R. Yang, D. Teschner, Y. Huang, S. R. Brankovic, P. Strasser, *ACS Catal*. 2014, **4**, 1859.

193 B. W. Zhang, T. Sheng, Y. X. Wang, X. M. Qu, J. M. Zhang, Z. C. Zhang, H. G. Liao, F. C. Zhu, S. X. Dou, Y. X. Jiang, S. G. Sun, *ACS Catal*. 2017, **7**, 892.

194 A. Ferre-Vilaplana, C. Buso-Rogero, J. M. Feliu, E. Herrero, *J. Phys. Chem. C*. 2016, **120**, 11590.

195 Y. Wang, S. Zou, W. B. Cai, *Catalysts.* 2015, **5**, 1507.

196 L. Jiang, L. Colmenares, Z. Jusys, G. Q. Sun, R. J. Behm, Electrochim. *Acta* 2007, **53**, 377.

197 W. Huang, X. Y. Ma, H. Wang, R. Feng, J. Zhou, P. N. Duchesne, P. Zhang, F. Chen, N. Han, F. Zhao, J. Zhou, W. B. Cai, Y. Li, *Adv. Mater*. 2017, **29**, 1703057.

198 A. Kowal, M. Li, M. Shao, K. Sasaki, M. B. Vukmirovic, J. Zhang, N. S. Marinkovic, P. Liu, A. I. Frenkel, R. R. Adzic, *Nat. Mater*. 2009, **8**, 325.

199 T. Sheng, Y. F. Xu, Y. X. Jiang, L. Huang, N. Tian, Z. Y. Zhou, I. Broadwell, S. G. Sun, *Acc. Chem. Res.* 2016, **49**, 2569.

200 C. Bianchini, P. K. Shen, *Chem. Rev.* 2009, **109**, 4183.

201 B. W. Zhang, H. L. Yang, Y. X. Wang, S. X. Dou, H. K. Liu, *Adv. Energy Mater*. 2018, **0**, 1703597.

202 A. L. Strickler, A. Jackson, T. F. Jaramillo, *ACS Energy Letters* 2017, **2** (1), 244.

203 P. Wang, K. Jiang, G. Wang, J. Yao, X. Huang, *Angew. Chem. Int. Ed.* 2016, **55** (41), 12859.

204 Z. Niu, N. Becknell, Y. Yu, D. Kim, C. Chen, N. Kornienko, G. A. Somorjai, P. Yang, *Nat. Mater.* 2016, **15**, 1188.

205 A. Oh, H. Baik, D. S. Choi, J. Y. Cheon, B. Kim, H. Kim, S. J. Kwon, S. H. Joo, Y. Jung, K. Lee, *ACS Nano* 2015, **9** (3), 2856.

206 V. R. Stamenkovic, B. Fowler, B. S. Mun, G. F. Wang, P. N. Ross, C. A. Lucas, N. M. Markovic, *Science* 2007, **315** (5811), 493.

207 V. R. Stamenkovic, B. S. Mun, M. Arenz, K. J. J. Mayrhofer, C. A. Lucas, G. Wang, P. N. Ross, N. M. Markovic, *Na. Mater.* 2007, **6** (3), 241.

208 C. Chen, Y. J. Kang, Z. Y. Huo, Z. W. Zhu, W. Y. Huang, H. L. Xin, J. D. Snyder, D. G. Li, J. A. Herron, M. Mavrikakis, M. F. Chi, K. L. More, Y. D. Li, N. M. Markovic, G. A. Somorjai, P. D. Yang, V. R. Stamenkovic, *Science* 2014, **343** (6177), 1339.

209 L. Bu, N. Zhang, S. Guo, X. Zhang, J. Li, J. Yao, T. Wu, G. Lu, J. Y. Ma, D. Su, X. Huang, *Science* 2016, **354** (6318), 1410.

210 C. Young, J. Wang, J. Kim, Y. Sugahara, J. Henzie, Y. Yamauchi, *Chemistry of Materials* 2018, **30**, 3379.

211 M. Li, Z. Zhao, T. Cheng, A. Fortunelli, C.-Y. Chen, R. Yu, Q. Zhang, L. Gu, B. V. Merinov, Z. Lin, E. Zhu, T. Yu, Q. Jia, J. Guo, L. Zhang, W. A. Goddard, Y. Huang, X. Duan, *Science* 2016, **354**, 1414.

212 C. Li, M. Iqbal, J. Lin, X. Luo, B. Jiang, V. Malgras, K. C. W. Wu, J. Kim, Y. Yamauchi, *Accounts of Chemical Research* 2018, **51**, 1764.

213 C. Li, B. Jiang, Z. Wang, Y. Li, M. S. A. Hossain, J. H. Kim, T. Takei, J. Henzie, Ö. Dag, Y. Bando, Y. Yamauchi, *Angewandte Chemie* 2016, **128**, 12938.

214 E. C. Tyo, S. Vajda, *Nat Nano* 2015, **10**, 577.

215 S. Yao, X. Zhang, W. Zhou, R. Gao, W. Xu, Y. Ye, L. Lin, X. Wen, P. Liu, B. Chen, E. Crumlin, J. Guo, Z. Zuo, W. Li, J. Xie, L. Lu, C. J. Kiely, L. Gu, C. Shi, J. A. Rodriguez, D. Ma, *Science* 2017, **357**, 389.

216 Z. L. Wang, K. Sun, J. Henzie, X. Hao, C. Li, T. Takei, Y.-M. Kang, Y. Yamauchi, *Angewandte Chemie* 2018, **57**, 5848.

217 Rao, L.; Jiang, Y.-X.; Zhang, B.-W.; Cai, Y.-R.; Sun, S.-G. *Phys. Chem. Chem. Phys.* 2014, **16** (27), 13662.

218 Kresse, G.; Hafner, *J. Phys. Rev. B* 1993, **48**, 13115.

219 Kresse, G.; Hafner, *J. Phys. Rev. B* 1996, **54**, 13115.

220 Blochl, P. E. *Phys. Rev. B* 1994, **50**, 17953.

221 Kresse, G.; Joubert, D. *Phys. Rev. B* 1999, **59**, 1758.

222 Alavi, A.; Hu, P.; Deutsch, T.; Silvestrelli, P. L.; Hutter, *J. Phys. Rev. Lett.* 1998, **80**, 3650.

223 Michadelides, A.; Liu, Z. P.; Zhang, C. J.; Alavi, A.; King, D. A.; Hu, P. *J. Am. Chem. Soc.* 2003, **125**, 370.

224 Liu, Z. P.; Hu, P. *J. Am. Chem. Soc.* 2003, **125**, 1958.

225 D. Deng, X. Chen, L. Yu, X. Wu, Q. Liu, Y. Liu, H. Yang, H. Tian, Y. Hu, P. Du, R. Si, J. Wang, X. Cui, H. Li, J. Xiao, T. Xu, J. Deng, F. Yang, P. N. Duchesne, P. Zhang, J. Zhou, L. Sun, J. Li, X. Pan, X. Bao, *Sci. Adv.* 2015, **1** (11).

226 W. Liu, L. Zhang, X. Liu, X. Liu, X. Yang, S. Miao, W. Wang, A. Wang, T. Zhang, *J. Am. Chem. Soc.* 2017, **139**, 10790.

227 H. Wei, X. Liu, A. Wang, L. Zhang, B. Qiao, X. Yang, Y. Huang, S. Miao, J. Liu, T. Zhang, *Nat. Commun.* 2014, **5**, 5634.

228 X. L. Ji, K. T. Lee, R. Holden, L. Zhang, J. J. Zhang, G. A. Botton, M. Couillard, L. F. Nazar, *Nat. Chem.* 2010, **2** (4), 286.

229 D. Volpe, E. Casado-Rivera, L. Alden, C. Lind, K. Hagerdon, C. Downie, C. Korzeniewski, F. J. DiSalvo, H. D. Abruña, *J. Electrochem. Soc.* 2004, **151**, A971.

230 B. Qiao, A. Wang, X. Yang, L. F. Allard, Z. Jiang, Y. Cui, J. Liu, J. Li and T. Zhang, *Nat. Chem.* 2011, **3**, 634.

231 P. Liu, Y. Zhao, R. Qin, S. Mo, G. Chen, L. Gu, D. M. Chevrier, P. Zhang, Q. Guo, D. Zang, B. Wu, G. Fu and N. Zheng, *Science* 2016, **352**, 797.

232 H. Li, L. Wang, Y. Dai, Z. Pu, Z. Lao, Y. Chen, M. Wang, X. Zheng, J. Zhu, W. Zhang, R. Si, C. Ma and J. Zeng, Nat. *Nanotechnol.* 2018, **13**, 411.

233 J. Liu, M. Jiao, L. Lu, H. M. Barkholtz, Y. Li, Y. Wang, L. Jiang, Z. Wu, D. J. Liu, L. Zhuang, C. Ma, J. Zeng, B. Zhang, D. Su, P. Song, W. Xing, W. Xu, Y. Wang, Z. Jiang, G. Sun, *Nat. Commun.* 2017, **8**, 15938.

234 B. W. Zhang, Y. X. Jiang, J. Ren, X. M. Qu, G. L. Xu, S. G. Sun, *Electrochim. Acta* 2015, **162**, 254.

235 A. Chen, P. Holt-Hindle, *Chem. Rev.* 2010, **110**, 3767.

236 C. W. Xu, H. Wang, P. K. Shen, S. P. Jiang, *Adv. Mater.* 2007, **19**, 4256.

237 S. Fu, C. Zhu, D. Du, Y. Lin, *ACS Appl. Mater. Interfaces* 2015, **7**, 13842.

238 Y. Qin, M. Luo, Y. Sun, C. Li, B. Huang, Y. Yang, Y. Li, L. Wang, S. Guo, *ACS Catal.* 2018, **8**, 5581.

239 Z. Y. Zhou, Q. Wang, J. L. Lin, N. Tian, S. G. Sun, Electrochim. *Acta* 2010, **55**, 7995.

240 T. Sheng, W. F. Lin, C. Hardacre, P. Hu, Phys. *Chem. Chem. Phys.* 2014, **16**, 13248.

241 Bell, A. T. The impact of nanoscience on heterogeneous catalysis. *Science* **299**, 1688-1691 (2003).

242 Yang, X.-F. *et al.* Single-atom catalysts: a new frontier in heterogeneous catalysis. *Accounts of Chemical Research* **46**, 1740-1748 (2013).

243 Zhang, L. *et al.* Platinum-based nanocages with subnanometer-thick walls and well-defined, controllable facets. *Science* **349**, 412-416 (2015).

244 Zhu, C., Fu, S., Shi, Q., Du, D. & Lin, Y. *Angewandte Chemie* (2017).

245 Dhiman, M. & Polshettiwar, V. *ChemCatChem* **10**, 881-906 (2018).

246 Kim, Y. T. *et al. Angewandte Chemie* **118**, 421-425 (2006).

247 Qiao, B. *et al. Nature chemistry* **3**, 634 (2011).

248 Zhang, B. *et al. Angewandte Chemie International Edition* **55**, 8319-8323 (2016).

249 Liu, J. *et al. Nature communications* **8**, 15938 (2017).

250 Gao, G., Jiao, Y., Waclawik, E. R. & Du, A. *Journal of the American Chemical Society* **138**, 6292-6297 (2016).

251 Jones, J. *et al. Science* **353**, 150-154 (2016).

252 Li, X. *et al. Advanced Materials* **28**, 2427-2431 (2016).

253 Moses-DeBusk, M. *et al. Journal of the American Chemical Society* **135**, 12634-12645 (2013).

254 Dvořák, F. *et al. Nature communications* **7**, 10801 (2016).

255 Zhang, C. *et al. ACS nano* **11**, 6930-6941 (2017).

256 Wang, X. *et al. Journal of the American Chemical Society* **139**, 9419-9422 (2017).

257 Lin, J. *et al. Journal of the American Chemical Society* **135**, 15314-15317 (2013).

258 Chen, Y. *et al. Angewandte Chemie International Edition* **56**, 6937-6941 (2017).

259 Zhang, H. *et al. Journal of the American Chemical Society* **139**, 14143-14149 (2017).

260 Antolini, E. *Energy & Environmental Science* **2**, 915-931 (2009).

261 Vilé, G. *et al. Angewandte Chemie International Edition* **54**, 11265-11269 (2015).

262 Kyriakou, G. *et al. Science* **335**, 1209-1212 (2012).

263 Yan, H. *et al. Journal of the American Chemical Society* **137**, 10484-10487 (2015).

264 Li, X. *et al. Chemical Communications* **52**, 13233-13236 (2016).

265 Zheng, Y. *et al. Journal of the American Chemical Society* **139**, 3336-3339 (2017).

266 Li, F., Li, Y., Zeng, X. C. & Chen, Z. *ACS Catalysis* **5**, 544-552 (2014).

267 Yang, S., Tak, Y. J., Kim, J., Soon, A. & Lee, H. *ACS Catalysis* **7**, 1301-1307 (2017).

268 Nocera, D. G. The artificial leaf. *Accounts of chemical research* **45**, 767-776 (2012).

269 Turner, J. A. Sustainable hydrogen production. *Science* **305**, 972-974 (2004).

270 Lee, Y., Suntivich, J., May, K. J., Perry, E. E. & Shao-Horn, Y. *The journal of physical chemistry letters* **3**, 399-404 (2012).

271 Tian, J., Liu, Q., Asiri, A. M. & Sun, X. *Journal of the American Chemical Society* **136**, 7587-7590 (2014).

272 Kresse, G. & Furthmüller, J. *Computational materials science* **6**, 15-50 (1996).

273 Kresse, G. & Furthmüller, J. *Physical review B* **54**, 11169 (1996).

274 Kresse, G. & Hafner, J. *Physical Review B* **48**, 13115 (1993).

275 Kresse, G. & Hafner, J. *Physical Review B* **49**, 14251 (1994).

276 Kresse, G. & Joubert, D. *Physical Review B* **59**, 1758 (1999).

277 Perdew, J. P., Burke, K. & Ernzerhof, M. *Physical review letters* **77**, 3865 (1996).

278 Hohenberg, P. & Kohn, W. *Physical Review* **136**, B864-B871, doi:10.1103/PhysRev.136.B864 (1964).

279 Kohn, W. & Sham, L. J. *Physical Review* **140**, A1133-A1138 (1965).

280 Blöchl, P. E. *Physical Review B* **50**, 17953-17979, doi:10.1103/PhysRevB.50.17953 (1994).

281 Grimme, S. Semiempirical. *Journal of Computational Chemistry* **27**, 1787-1799, doi:10.1002/jcc.20495 (2006).

282 Grimme, S., Antony, J., Ehrlich, S. & Krieg, H. *The Journal of Chemical Physics* **132**, 154104, doi:10.1063/1.3382344 (2010).

283 Lucci, F. R. *et al. Nature communications* **6**, 8550 (2015).

284 Pei, G. X. *et al. ACS Catalysis* **7**, 1491-1500 (2017).

285 Bu, L. *et al. Nature communications* **7**, 11850 (2016).

286 Zheng, D. *et al. Royal Society open science* **5**, 171928 (2018).

287 Ullah, H., Shah, A.-u.-H. A., Bilal, S. & Ayub, K. *The Journal of Physical Chemistry C* **118**, 17819-17830 (2014).

288 Brogan, M. S., Dines, T. J. & Cairns, J. A. *Journal of the Chemical Society, Faraday Transactions* **90**, 1461-1466 (1994).

289 Schejn, A. *Stability and cytotoxicity evaluation*, Université de Lorraine, (2015).

290 Zhang, J. *et al. Nano Energy* **40**, 27-33 (2017).

291 Ding, J., Shao, Q., Feng, Y. & Huang, X. *Nano Energy* **47**, 1-7 (2018).

292 Lv, F. *et al. ACS central science* **4**, 1244-1252 (2018).

293 Fu, L., Cheng, G. & Luo, W. *Journal of Materials Chemistry A* **5**, 24836-24841 (2017).

294 Feng, J. *et al. Advanced Materials* **29**, 1703798 (2017).

295 Han, X. *et al. Advanced Energy Materials* **8**, 1800935 (2018).

296 Pi, Y., Shao, Q., Wang, P., Guo, J. & Huang, X. *Advanced Functional Materials* **27**, 1700886 (2017).

297 Reier, T. *et al. Journal of the American Chemical Society* **137**, 13031-13040 (2015).

298 Chen, C. H. *et al. Advanced Materials* **20**, 1205-1209 (2008).

Appendix A: Publications

1. ***Wei-Hong Lai***, Bin-Wei Zhang, Zhenpeng Hu, Xi-Ming Qu, Yan-Xia Jiang, Yun-Xiao Wang, Jia-Zhao Wang, Hua Kun Liu, Shu-Lei Chou. The Quasi-Pt-Allotrope Catalyst: Hollow PtCo@single-Atom Pt_1 on Nitrogen-Doped Carbon toward Superior Oxygen Reduction. ***Advanced Functional Materials***. 2019,1807340.
2. ***Wei-Hong Lai***, Yun-Xiao Wang, Yong Wang, Minghong Wu, Jia-Zhao Wang, Hua-Kun Liu, Shu-Lei Chou, Jun Chen, and Shi-Xue Dou. Morphology tuning of inorganic nanomaterials across multiple dimensions through balancing electrolytic dissociation and supersaturation. ***Nature Chemistry***. Accepted in principle.
3. ***Wei-Hong Lai,*** Li-Fu Zhang, Wei-Bo Hua, Sylvio Indris, Zi-chao Yan, Zhe Hu, Binwei Zhang, Yani Liu, Li Wang, Min Liu, Rong Liu, Yun-Xiao Wang, Jia-Zhao Wang,* Zhenpeng Hu, Hua-Kun Liu, Shu-Lei Chou,* Shi-Xue Dou. General π-electron-assisted strategy for single-atom (Ir, Pt, Ru, Pd, Fe, and Ni) electrocatalysts with bi-functional active sites toward highly efficient water splitting. ***Angewandte Chemie International Edition***, 2019, DOI: 10.1002/ange.201904614.
4. ***Wei-Hong Lai,*** *et al*. Atomic-local environments for single-atom catalysts: electronic correlation, synthesis, and activity. Submitted to ***Advanced Energy Materials.***
5. Yunxiao Wang, ***Wei-Hong Lai (Equal author)***, Yun-Xia Wang, Shu-Lei Chou, Xinping Ai, Hanxi Yang, Yuliang Cao. Sulfur-based electrodes via multi-

electron reactions for room-temperature sodium-ion storage. ***Angewandte Chemie***. 2019, DOI: 10.1002/ange.201902552.

6. Binwei Zhang, ***Wei-Hong Lai (Equal author)***, Tian Sheng, Ximing Qu, Yunxiao Wang, Long Ren, Lei Zhang, Yi Du, Yanxia Jiang, Shi-Gang Sun, Shixue Dou. Ordered Platinum-Bismuth Intermetallic Clusters with Pt-skin for High Efficient Electrochemical Ethanol Oxidation Reaction. ***Journal of Materials Chemistry A***. 2019, accepted.
7. Yun-Xiao Wang, Jianping Yang, ***Weihong Lai***, Shu-Lei Chou, Qin-Fen Gu, Hua Kun Liu, Dongyuan Zhao, Shi Xue Dou. Achieving high-performance room-temperature sodium–sulfur batteries with S@ interconnected mesoporous carbon hollow nanospheres. ***Journal of the American Chemical Society***. 2016, 138, 16576-16579.
8. Zhe Hu, Zhixin Tai, Qiannan Liu, Shi-Wen Wang, Huile Jin, Shun Wang, ***Weihong Lai***, Mingzhe Chen, Lin Li, Lingna Chen, Zhanliang Tao, Shu-Lei Chou. Ultrathin 2D TiS2 Nanosheets for High Capacity and Long‐Life Sodium Ion Batteries. ***Advanced Energy Materials***. 2019, 9, 1803210.
9. Chunling Zhu, Zhuoxun Yin, ***Weihong Lai***, Yue Sun, Lina Liu, Xitian Zhang, Yujin Chen, Shu-Lei Chou. Fe-Ni-Mo Nitride Porous Nanotubes for Full Water Splitting and Zn-Air Batteries. ***Advanced Energy Materials***. 2018, 8, 1802327.
10. Bin-Wei Zhang, Tian Sheng, Yun-Dan Liu, Yun-Xiao Wang, Lei Zhang, ***Wei-Hong Lai***, Li Wang, Jianping Yang, Qin-Fen Gu, Shu-Lei Chou, Hua-Kun Liu, Shi-Xue Dou. Atomic cobalt as an efficient electrocatalyst in sulfur cathodes for superior room-temperature sodium-sulfur batteries. ***Nature Communications***. 2018, 9, 4082-4093.

11. Mingzhe Chen, David Cortie, Zhe Hu, Huile Jin, Shun Wang, Qinfen Gu, Weibo Hua, Enhui Wang, ***Weihong Lai***, Lingna Chen, Shu-Lei Chou, Xiao-Lin Wang, Shi-Xue Dou. A Novel Graphene Oxide Wrapped $Na_2Fe_2(SO_4)_3$/C Cathode Composite for Long Life and High Energy Density Sodium-Ion Batteries. ***Advanced Energy Materials***. 2018, 8, 1800944.

12. Yaru Liang, ***Wei-Hong Lai***, Zongcheng Miao, Shu-Lei Chou. Nanocomposite materials for the sodium–ion battery: a review. ***Small***. 2018, 14, 1702514.

13. Yun-Xiao Wang, Binwei Zhang, ***Weihong Lai***, Yanfei Xu, Shu-Lei Chou, Hua-Kun Liu, Shi-Xue Dou. Sodium-Sulfur Batteries: Room-Temperature Sodium-Sulfur Batteries: A Comprehensive Review on Research Progress and Cell Chemistry. ***Advanced Energy Materials.*** 2017, 7, 1770140.

14. Bin-Wei Zhang, Yun-Dan Liu, Yun-Xiao Wang, Lei Zhang, Ming-Zhe Chen, ***Wei-Hong Lai***, Shu-Lei Chou, Hua-Kun Liu, Shi-Xue Dou. In Situ Grown S Nanosheets on Cu Foam: An Ultrahigh Electroactive Cathode for Room-Temperature Na-S Batteries. ***ACS Applied materials & interfaces***. 2017, 9, 24446-24450.

15. Chun-Sheng Li, Yan Sun, ***Wei-Hong Lai***, Jia-Zhao Wang, Shu-Lei Chou. Ultrafine Mn3O4 Nanowires/Three-Dimensional Graphene/Single-Walled Carbon Nanotube Composites: Superior Electrocatalysts for Oxygen Reduction and Enhanced Mg/Air Batteries. ***ACS Applied materials & interfaces***, 2016, 8 (41), 27710–27719.

16. Nv Wang, Yuan Gao, Yun-Xiao Wang, Kai Liu, ***Weihong Lai***, Yemin Hu, Yong Zhao, Shu-Lei Chou, Lei Jiang. Nanoengineering to Achieve High Sodium

Storage: A Case Study of Carbon Coated Hierarchical Nanoporous TiO_2 Microfibers. ***Advanced Science***. 2016, 3, 1600013.

17. ***Weihong Lai***, Min Liu, Chunyan Li, Hongli Suo, Ming Yue .Recovery of a composite powder from NdFeB slurry by co-precipitation. ***Hydrometallurgy***. 2014, 150, 27-33.

Appendix B: Conferences & Activities

1. The 2016 International Symposium on Next-Generation Batteries, North Wollongong, Australia, Aug. 9th to 12th, 2016.
2. 2018 INTERNATIONAL SYMPOSIUM ON ADVANCED MATERIALS & SUSTAINABLE TECHNOLOGIES, Brisbane, Australia, 22-25 July, 2018.

Appendix C: Scholarships & Awards

1. 2015-2019: Matching Scholarship & International Postgraduate Tuition Award, UOW.